MELT MIGRATION DYNAMICS AND TRACE ELEMENT FRACTIONATION BENEATH MID-OCEAN RIDGES

BY
BODA LIU
B.SC., GEOLOGY, PEKING UNIVERSITY, BEIJING, 2013

A DISSERTATION SUBMITTED IN PARTIAL FULFILLMENT OF THE REQUIREMRENTS FOR THE DEGREE OF DOCTOR OF PHILOSOPHY IN THE DEPARTMENT OF EARTH, ENVIRONMENTAL, AND GEOLOGICAL SCIENCES AT BROWN UNIVERSITY

PROVIDENCE, RHODE ISLAND

MAY 2018

This dissertation by Boda Liu is accepted in its present form by the Department of Earth, Environmental, and Planetary Sciences as satisfying the dissertation requirement for the degree of Doctor of Philosophy

Date_____ _____
Yan Liang, Ph.D., Advisor

Recommended to the Graduate Council

Date_____ _____
E. Marc Parmentier, Ph.D., Reader

Date_____ _____
Donald Forsyth, Ph.D., Reader

Date_____ _____
Alberto Saal, Ph.D., Reader

Date_____ _____
Greg Hirth, Ph.D., Reader

Date_____ _____
Mark Behn, Ph.D., External Reader

Approved by the Graduate Council

Date_____ _____
Andrew G. Campbell
Dean of the Graduate School

BODA LIU

324 Brook Street, Box 1846
Providence, RI 02912

Phone: +1(401)316-7722
Email: boda_liu@brown.edu

Education

Ph.D., Geological Sciences, Brown university, expected 2018

B.Sc., Geology, Peking University, 2013

Research Interests

Melting of heterogeneous mantle; trace element and isotope fractionation; geodynamics of partially molten mantle; geochemical inverse problems; high-order numerical methods

Publications

Liu B, Liang Y. (2017) The prevalence of kilometer-scale heterogeneity in the source region of MORB upper mantle, *Science Advances*, 3(11). doi: http://dx.doi.org/10.1126/sciadv.1701872

Liu B, Liang Y. (2017) An introduction of Markov chain Monte Carlo method to geochemical inverse problems: Reading melting parameters from REE abundances in abyssal peridotites. *Geochimica et Cosmochimica Acta*, **203:** 216-234. doi: http://dx.doi.org/10.1016/j.gca.2016.12.040

Liang Y, **Liu B**. (2016) Simple models for disequilibrium fractional melting and batch melting with application to REE fractionation in abyssal peridotites. *Geochimica et Cosmochimica Acta*, **173:** 181-197. doi: http://dx.doi.org/10.1016/j.gca.2015.10.020

Liang Y, **Liu B**. Stretching chemical heterogeneity by melt migration in an upwelling mantle: An analysis based on time-dependent batch and fractional melting models (submitted to *Earth and Planetary Science Letters*)

Liu B, Liang Y. Smearing and mixing of chemical heterogeneities by melt migration in an upwelling mantle: Application to Pb, Hf, Nd, Sr isotope systems (in preparation)

Liu B, Liang Y. A 2D double-porosity model for melting and melt migration beneath mid-ocean ridges (in preparation)

Abstracts

Liu B, Liang Y. (2017) A 2D double-porosity model for melting and melt migration beneath mid-ocean ridges. AGU Fall Meeting, poster presentation: DI51B-0313

Liang Y, **Liu B**. (2017) Size-sensitive mixing of chemical heterogeneities by melting and melt migration beneath mid-ocean ridges. AGU Fall Meeting, poster presentation: V51D-0402

Liu B, Liang Y. (2016) Effects of size and shape of mantle source on the fractionation of isotopes during melting of a heterogeneous mantle: a time-dependent study. AGU fall meeting, oral presentation: DI14A-06

Liu B, Liang Y. (2015) Application of Markov chain Monte Carlo method to mantle melting: an example from REE abundances in abyssal peridotites. AGU fall meeting, poster presentation: V11B-3065

Liang Y, **Liu B**. (2015) Can LREE enriched patterns in clinopyroxenes in abyssal peridotites be produced by melting of a depleted mantle source? AGU Fall Meeting, poster presentation: V11B-3059

Honors & Awards

- Dissertation Fellowship, Brown University, 2018
- First Year Fellowship, Brown University, 2013
- Honorable Mention, "Interdisciplinary Contest in Modeling", The Consortium for Mathematics and Its Applications of U.S., 2012
- Zengxianzi Fellowship, Peking University, 2010-2012

Teaching Experience

- Teaching Assistant, Brown University, GEOL0250: Computational Approaches to Modelling and Quantitative Analysis in Natural Sciences: An Introduction, Fall 2016
- Teaching Assistant, Brown University, GEOL1620: Continuum Physics of the Solid Earth, Spring 2016
- Teaching Assistant, Brown University, GEOL0350: Mathematical Methods of Fluid and Solid Geophysics and Geology, Fall 2015

Research & Instrumental Experience

Numerical and Statistical modeling:

- Implementation of the Discontinuous Galerkin method using deal.II library
- Parallel computation on multi-core CPU (C++)
- alphaMELTs thermodynamic model for mantle melting
- Markov chain Monte Carlo Method (C++)
- Geodynamics modeling using ASPECT

Instrumental experience:

- Magnetic mineral separation
- Electron microprobe
- LA-ICP-MS

Professional Experience

- Research Assistant, Brown University, September 2013 - present
- Member of American Geophysical Union, September 2015 – present

Invited Talks

- Woods Hole Oceanographic Institution, Seeing the size of chemical heterogeneities under mid-ocean ridges, January 2018
- Peking University, Reading melting parameters from REE abundances in abyssal peridotites, January 2018

Acknowledgement

I would like to thank my advisor Prof. Yan Liang, for the patient guidance and encouragement. The joy and enthusiasm he has for the research was contagious and motivational for me. I have been extremely fortunate to have Liang who cared so much about my work, and who responded to my questions and queries so promptly.

It has been my honor to work with such a group of excellent geologists. I would like to thank Marc Parmentier, Don Forsyth, Greg Hirth, Alberto Saal for their valuable comments and encouragement, and Mark Behn for reading my thesis and attending my defense. Chapter 1 starts from a project of Don's course and Chapter 3 benefits from lots of insightful discussions with Marc, Don, Greg, and Colleen in the melt seminar. I would also like to thank Steve Parman and Reid Cooper for giving me the knowledge I need to think about igneous petrology and thermodynamics. My thanks go out especially to Professor Chi-Wang Shu for answering questions about numerical methods. My sincere thanks also go to Soumen Mallick and Joe Boesenberg who gave me access to the laboratory facilities and provided unfailing support and assistance.

I want to thank my fellow DEEPS graduate students, Chenguang Sun, Lijing Yao, Nick Dygert, Mary Peterson, Kei Shimizu, Colin Jackson, Ben Chilson-Parks, Jack Krantz, Taka Kanaya, Yinsui Zheng, Qing Li, Jenna Palmer, Junlin Hua and many others for the stimulating discussions and for all the fun we have had in the past five years.

I would particularly like to thank Dongkun Zhang and Wei Zhang for being my buddies in the past twelve years, from studying hard together at high school in Wuhan to making dumplings together in Providence.

I would like to thank my parents for their support, encouragement and sacrifice. Without being brought to those trips to embrace the beauty of nature since I was seven, I would never have been so curious about the Earth and this thesis would never have been written.

Lastly, the small heterogeneity that looks like a sailboat in Figure 2-1 is for you, Jingfan. Thanks for your encouragement, inspiration, and all the magics.

Table of contents

List of Tables

List of Figures

Introduction

The objective of this thesis is to use first order geochemical and geophysical observations to understand melt generation and migration processes beneath mid-ocean ridge spreading centers. First-order observations are building blocks of the current understanding of the Earth. However, individual observation is a finite perspective. Conclusions drawn from one set of observations may not be fully respected by other theories motivated by different observations. This thesis believes that the power of two observations is greater than one, the more the better, and we can deepen the understanding of a geological system by synthesizing existing observations that are not easily combined. Such a philosophy will be expressed in the context of mid-ocean ridges (MOR) because a wide range of observations are available. In following paragraphs, examples will be outlined for how models and interpretation methods are improved to extract insights from a combination of existing observations.

In Chapter 1, I examine an important geochemical problem to mantle melting beneath mid-ocean ridges: if chemical disequilibrium is needed to explain the observed rare earth elements (REE) in clinopyroxene (cpx) in abyssal peridotites. I read three pieces of information from concentrations of REE in cpx in abyssal peridotites. They are: the degree of melting, the melt porosity, and the extent of chemical disequilibrium. Observations of concentrations of REE in clinopyroxene (cpx) in abyssal peridotites has been used to constrain the first two parameters since the seminal work of Johnson et al. (1990). The importance of disequilibrium melting has also been recognized shortly after (Qin, 1992; Iwamori, 1993; Van Orman, 2002). The difficulty in modeling the effect of chemical disequilibrium is the coupling of grain scaler diffusion to tectonic scale melt

migration. For that reason, the data of REE concentration in cpx has not been fully utilized to test the effect of chemical disequilibrium. In the paper published in *Geochimica et Cosmochimica Acta* 203:216-234, I developed a simple model that can predict concentrations of REE given the set of these three parameters. I implemented an inversion method, called Markov chain Monte Carlo method, to directly acquire the most probable estimate and uncertainty intervals of these three parameters. The main conclusion is a robust correlation between the degree of melting and the extent of disequilibrium. This correlation can be used to deduce the grain size of cpx and the potential temperature once the temperature-dependence of the diffusivity of REE and the melt productivity during decompression melting are known.

In Chapter 2, I examine an important but previously unknown question on magma genesis beneath mid-ocean ridges: how the size and shape of mantle heterogeneity affect the correlation of isotope ratios in mid-ocean ridge basalts (MORB) and abyssal peridotites. The size of chemical heterogeneities has been inferred from both geochemical and geophysical perspectives to be a wide spectrum of scales, from centimeters (Warren and Shimizu, 2010) to thousands of kilometers (Hart, 1984; Garnero and McNamara, 2008). In a paper published in *Science Advances* 3 (11), I have put some constraints on the spectrum of scales by studying the effect of the size of chemical heterogeneities on these two sets of geochemical observations. Results show that the observed difference in $^{143}Nd/^{144}Nd$ in MORB and abyssal peridotites cannot be produced if most chemical heterogeneities are smaller than 1 km, and the observed range of $^{143}Nd/^{144}Nd$ in MORB cannot be produced if most chemical heterogeneities are larger than 60 km. These two constraints can be

combined with the estimate of the enrichment of Nd in heterogeneities to put tighter constraints on the size of chemical heterogeneities.

The purpose of Chapter 3 is to build a platform for assimilating as many geochemical and geophysical observations as possible. Any mid-ocean ridge model should be able to explain these first order observations. These include fine scale petrological features (Kelemen et al., 2000; Holtzman et al., 2003), crustal thickness, compositions of MORB and residues (Elliott and Spiegelman, 2003; Lundstrom, 2003; Warren, 2016; White and Klein, 2014), and geophysical interpretations of melt distributions (Baba et al., 2006; Yang et al., 2007; Key et al., 2013). By applying the approach of "double-porosity model", I am able to capture fine scale petrological features and make internally-consistent predictions of some other observations such as the crustal thickness, the REE pattern in the pooled melt and abyssal peridotites, excesses of (^{230}Th/^{234}U) and (^{226}Ra/^{230}Th) in MORB, the depth of high porosity region beneath the ridge axis. These predictions are compared with real observations to obtain constraints on processes beneath mid-ocean ridges. Practices as such have improved the understanding of rock fabric-facilitated melt focusing and produced a preliminary constraint on the depth of the beginning of melt extraction.

The fusion of these three chapters naturally leads to a roadmap beyond this thesis. Future studies should deal with melt migration in channels (like Chapter 3), be time-dependent (like Chapter 2), be able to interpret with robustness (like Chapter 1), and always be strongly constrained by observations (all Chapters). One potential project would be applying a parametrized model for major elements to the 2D double porosity model. The first-order observation of major element correlations in the MORB could be a strong test for the melt focusing process predicted by Chapter 3. Another potential project would be

applying a time-dependent ridge model to the East Pacific Rise (EPR). The well-accumulated geophysical and geochemical observations at EPR could provide tighter constraints on both the dynamics of melt migration and the nature of mantle source heterogeneities.

References

Baba, K., A. D. Chave, R. L. Evans, G. Hirth and R. L. Mackie (2006). "Mantle dynamics beneath the East Pacific Rise at 17°S: Insights from the Mantle Electromagnetic and Tomography (MELT) experiment." Journal of Geophysical Research: Solid Earth (1978–2012) **111**(B2).

Elliott, T. and M. Spiegelman (2003). "Melt migration in oceanic crustal production: a U-series perspective." Treatise on geochemistry **3**: 465-510.

Garnero, E. J. and A. K. McNamara (2008). "Structure and Dynamics of Earth's Lower Mantle." Science **320**(5876): 626-628.

Harmon, N., D. W. Forsyth and D. S. Weeraratne (2009). "Thickening of young Pacific lithosphere from high-resolution Rayleigh wave tomography: A test of the conductive cooling model." Earth and Planetary Science Letters **278**(1): 96-106.

Hart, S. R. (1984). "A large-scale isotope anomaly in the Southern Hemisphere mantle." Nature **309**: 753.

Holtzman, B. K., D. L. Kohlstedt, M. E. Zimmerman, F. Heidelbach, T. Hiraga and J. Hustoft (2003). "Melt Segregation and Strain Partitioning: Implications for Seismic Anisotropy and Mantle Flow." Science **301**(5637): 1227-1230.

Iwamori, H. (1993). "A model for disequilibrium mantle melting incorporating melt transport by porous and channel flows." Nature **366**(6457): 734-737.

Johnson, K. T. M., H. J. B. Dick and N. Shimizu (1990). "Melting in the oceanic upper mantle: An ion microprobe study of diopsides in abyssal peridotites." Journal of Geophysical Research: Solid Earth **95**(B3): 2661-2678.

Kelemen, P. B., M. Braun and G. Hirth (2000). "Spatial distribution of melt conduits in the mantle beneath oceanic spreading ridges: Observations from the Ingalls and Oman ophiolites." Geochemistry, Geophysics, Geosystems **1**(7): n/a-n/a.

Key, K., S. Constable, L. Liu and A. Pommier (2013). "Electrical image of passive mantle upwelling beneath the northern East Pacific Rise." Nature **495**(7442): 499-502.

Liu, B. and Y. Liang (2017). "An introduction of Markov chain Monte Carlo method to geochemical inverse problems: Reading melting parameters from REE abundances in abyssal peridotites." Geochimica et Cosmochimica Acta **203**: 216-234.

Liu, B. and Y. Liang (2017). "The prevalence of kilometer-scale heterogeneity in the source region of MORB upper mantle." Science Advances **3**(11).

Lundstrom, C. C. (2003). "Uranium-series disequilibria in mid-ocean ridge basalts: observations and models of basalt genesis." Reviews in Mineralogy and Geochemistry **52**(1): 175-214.

Qin, Z. (1992). "Disequilibrium partial melting model and its implications for trace element fractionations during mantle melting." Earth and Planetary Science Letters **112**(1): 75-90.

Van Orman, J. A., T. L. Grove and N. Shimizu (2002). "Diffusive fractionation of trace elements during production and transport of melt in Earth's upper mantle." Earth and Planetary Science Letters **198**(1): 93-112.

Warren, J. M. (2016). "Global variations in abyssal peridotite compositions." Lithos **248–251**: 193-219.

Warren, J. M. and N. Shimizu (2010). "Cryptic Variations in Abyssal Peridotite Compositions: Evidence for Shallow-level Melt Infiltration in the Oceanic Lithosphere." Journal of Petrology **51**(1-2): 395-423.

CHAPTER 1

Application of Markov chain Monte Carlo method to geochemical inverse problems

Boda Liu and Yan Liang

Department of Earth, Environmental and Planetary Sciences

Brown University, Providence, Rhode Island 02912

Published in Geochimica et Cosmochimica Acta **203**: 216-234, 2017

Abstract

Markov chain Monte Carlo (MCMC) simulation is a powerful statistical method in solving inverse problems that arise from a wide range of applications. In Earth sciences applications of MCMC are primarily in the field of geophysics. The purpose of this study is to introduce MCMC to geochemical inverse problems related to trace element fractionation during mantle melting. MCMC method has several advantages over least squares methods in deciphering melting processes from trace element abundances in basalts and mantle rocks. Here we use MCMC to invert for extent of melting, fraction of melt present during melting, and extent of chemical disequilibrium between the melt and residual solid from REE abundances in clinopyroxene in abyssal peridotites from Mid-Atlantic Ridge, Central Indian Ridge, Southwest Indian Ridge, Lena Trough, and American-Antarctic Ridge. We consider two melting models: one with exact analytical solution and the other without. We solve the latter numerically in a chain of melting models according to the Metropolis-Hastings algorithm. The probability distribution of inverted melting parameters depends on assumptions of the physical model, knowledge of mantle source composition, and constraints from actual REE data. Results from MCMC inversion are consistent with and carry more information than previous results based on nonlinear least squares inversion. We show that chemical disequilibrium is likely to play an important role in fractionating LREE in residual peridotites during partial melting beneath mid-ocean ridge spreading centers. MCMC is well suited for more complicated but physically more realistic melting problems that do not have analytical solutions.

1. Introduction

The abundances and distributions of trace elements in primitive basalts and residual peridotites are important to understanding mantle source compositions and mantle melting processes. During partial melting, abundances of a trace element in interstitial melt and residual solid are redistributed or fractionated in accordance with its solid-melt partition coefficient, extent of melting, and style of melt extraction. Interpretations of the trace element data, therefore, depend critically on melting models, melting parameters, and mantle source composition. Simple melting models that have frequently been used in the interpretation of trace element data in basalts and residual peridotites include batch melting, incremental batch melting, fractional melting, and dynamic melting models (e.g., Shaw, 2000 and references therein). A common feature of these simple melting models is that they all have explicit analytical solutions relating melt or residual solid compositions to the degree of melting experienced by the solid. In more complicated but physically more realistic melting models, such as double porosity melting models and disequilibrium melting models (Qin, 1992; Iwamori, 1993b, 1994; Lundstrom, 2000; Ozawa, 2001; Jull et al., 2002; Van Orman et al., 2002; Liang and Parmentier, 2010; Liang and Peng, 2010), there are no analytical solutions to the mass conservation equations governing the fractionation of trace elements in partial melt and residual solid, except a few special cases. Numerical methods are used to solve the governing transport equations (Richter, 1986; Jull et al., 2002; Spiegelman and Kelemen, 2003).

Interpretations of basalt and peridotite trace element data typically follow one of the two approaches or methods (Allegre and Minster, 1978): direct method and inverse method. In the direct approach, one calculates trace element abundances in the melt and

residual solid or mineral (often clinopyroxene) for a range of melting parameters (e.g., 0-20% melting, 0-2% trapped melt in the dynamic melting model) using several melting models for a group of trace elements in question (e.g., REE and HFSE). Results from the forward calculation are then compared with measured trace element data on a spider diagram, element vs. element diagrams (e.g., Ti vs. Zr), or element vs. element ratio diagrams (e.g., Sm/Yb vs. Yb). The model is deemed acceptable or successful if part or all of the observed trace element data in samples included in the study can be explained or bracketed by those predicted by the forward model calculation. If the melting model fails to explain part of the observed data (e.g., LREE enrichment in residual clinopyroxene), additional processes such as late-stage melt impregnation or mantle metasomatism are invoked and further tested. Such forward modeling followed by direct comparison with measured data has been widely used in the interpretation of trace element data from primitive basalts and residual peridotites (e.g., Langmuir et al., 1977, 2006; McKenzie, 1985; Johnson et al., 1990; Kelemen et al., 1997; Niu and Hékinian, 1997; Shimizu, 1998; Lundstrom, 2000; Hellebrand et al., 2002; Jull et al., 2002; Van Orman et al., 2002; Spiegelman and Kelemen, 2003; Niu, 2004; Kelley et al., 2006; Liang and Parmentier, 2010; Brunelli et al., 2006, 2014).

In the inverse approach, the melting parameters are extracted from measured trace element data through least squares analysis (Allegre and Minster, 1978; Minster and Allegre, 1978; Hofmann and Feigenson, 1983; McKenzie and O'Nions, 1991; Albarède, 1996; Zou, 2007). Here one minimizes a Chi-square defined by the measured trace element concentrations and those predicted by the melting model and weighted by data quality. Early applications of the inverse method to mantle melting follow the strategies outlined

in Minster and Allegre (1978) and Hofmann and Feigenson (1983). Given the relatively poor knowledge of mineral-melt partition coefficients, melting reaction, and mantle composition and mineralogy at the time, these early studies used the batch melting model and incompatible trace element ratios and abundances in basalts to invert for bulk solid-melt partition coefficients and mantle mineralogy (Feigenson et al., 1983; Hofmann and Feigenson, 1983; Ormerod et al., 1991; Feigenson and Carr, 1993). McKenzie and coworkers (McKenzie and O'Nions, 1991; Watson and McKenzie, 1991; White et al., 1992; Watson, 1993; Tainton and McKenzie, 1994; McKenzie and O'Nions, 1995; McKenzie and O'Nions, 1998; McKenzie et al., 2004) applied Backus and Gilbert (1968)'s optimization technique (for a summary see Parker, 1977) to invert melt fraction and distribution in a melting column from REE abundances in basalts. In a more restricted case in which the melting model has explicit analytical function, the nonlinear least squares method (also called the linearized least squares method, abbreviated as "LS" hereafter, Tarantola, 2005) is very useful in inverting all model parameters simultaneously. There is only a few mantle melting studies that took the nonlinear least squares approach. Liang and Peng (2010) used nonlinear least squares method and a steady-state double porosity model to invert the degree of melting and melt suction rate from REE and Y abundances in residual clinopyroxene from the Central Indian Ridge using data reported by Hellebrand et al. (2002). LREE abundances in half of the sample set are too high to be consistent with the steady-state model. Liang and Liu (2016) further examined this problem using a disequilibrium perfect fractional melting model. They showed that small extent of chemical disequilibrium, due to slow diffusion of LREE in clinopyroxene, can explain the elevated LREE abundances in residual clinopyroxenes in the abyssal peridotites. They also noted a

positive correlation between the degree of melting and the extent of chemical disequilibrium and attributed it to an increase in melting rate and a decrease in REE diffusion rate along the melting path. However, given the highly nonlinear nature of the melting problem and the simplified melting model used, it is not clear if this is a robust observation for decompressional melting along a melting column when additional melting parameters are considered. For example, in a more general case of dynamic melting, a small fraction of melt is retained in the melting column, which may affect the interpretation of other melting parameters through nonlinear trade-offs. Although it is straightforward to develop a disequilibrium dynamic melting model by relaxing model assumptions, the governing mass conservation equations are nonlinear and do not have explicit analytical solutions (e.g., Liang, 2003), which limits application of the nonlinear least squares inversion method. If more complicated melting models are used to interpret trace element data, robust inversion methods are needed.

The purposes of this study are twofold: (1) to introduce Markov chain Monte Carlo method (MCMC) to geochemical inverse problems related to trace element fractionation during mantle melting, and (2) to further test the robustness of the positive correlation between the degree of melting and the extent of chemical disequilibrium noted earlier. Very often, conservation equations for trace element fractionation during concurrent melting, melt migration and melt-rock interaction do not have analytical solutions and hence cannot be easily solved using least squares inversion methods. MCMC is a powerful statistical method for solving inverse problems that arise from a wide range of applications, such as physics, chemistry, computational biology, computer science, financial engineering, among others (Robert and Casella, 2004; Liu, 2008). In Earth sciences applications of

MCMC are primarily in the field of geophysics (Sambridge and Mosegaard, 2002). MCMC method has several advantages over the least squares method in inverting melting parameters from trace element abundances in basalts and mantle rocks. First, MCMC can handle any model or equation that has no explicit analytical solution. Second, MCMC can take advantage of prior knowledge of the system in question (e.g., based on previous studies, we know mantle melting is near fractional) and further improve the estimation of model parameters based on new observations in hand, an important feature that nonlinear least squares inversion methods do not have. Third, MCMC can find multiple global minimums in nonlinear problems that may pose a challenge to nonlinear least squares analysis. And finally, MCMC can provide insights into uncertainties of model parameters with nonlinear trade-off.

The remaining of this paper is organized as follows. In Section 2, we outline the procedure of MCMC. In Section 3, we use two melting models and abyssal peridotite data from Central Indian Ridge to highlight the advantages of MCMC: the disequilibrium fractional melting model which has explicit analytical solution, and a more general model of disequilibrium dynamic melting that has no analytical solution. In Sections 4, we use MCMC and the disequilibrium dynamic melting model to invert melting parameters from REE and Y abundances clinopyroxene in abyssal peridotites from four additional ridge systems: Mid-Atlantic Ridge, Southwest Indian Ridge, Lena Trough, and American-Antarctic Ridge. We show that a robust positive correlation between the degree of melting and the extent of disequilibrium for REE in clinopyroxene exists in abyssal peridotites from Southwest Indian Ridge and Central Indian Ridge and discuss our results in the context of

adiabatic mantle melting in Section 5. And finally in Section 6, we outline potential applications of MCMC to more general cases of mantle melting.

2. Markov chain Monte Carlo Method

Markov chain Monte Carlo method was first introduced by Metropolis et al. (1953) to study macroscopic equilibrium. The method was generalized by Hastings (1970) for more flexible implementation. The MCMC approach uses the posterior distribution to estimate the probability of model parameter given data as constraints. Here posterior distribution is the distribution of unknown model parameters based on the observed data. By randomly generating trial models and accepting or rejecting the trial model in accordance with a transition probability, Metropolis-Hastings algorithm produces a chain of models whose distribution converges to posterior distribution, i.e., the desired parameters that reproduce the observed data.

1.1. The estimate of model parameters: Posterior distribution

To estimate a model parameter is to determine the probability distribution of model parameter (i.e., their best-estimated values and associate uncertainties) given the data as constraints. For example, REE abundances in an abyssal peridotite may suggest that 10% melting is more likely to explain the observed REE data than 5% melting. In other words, the degree of melting (F) has higher probability at 10% than 5%. There exists a posterior distribution that specifies the probability of F within a range of values. There are two ways to describe posterior distribution: (1) a probability density function characterized by a finite number of parameters and (2) a sample set consisting of a large number of model parameters belonging to the posterior distribution. The nonlinear least squares method

utilizes the former with a normal distribution (characterized by two parameters: the mean and the standard deviation), whereas MCMC resorts to the latter which is more general. The mean and standard deviation of the sample of model parameters acquired by MCMC are consistent with the nonlinear least squares method if the posterior distribution is a normal distribution.

Let **m** be a vector of model parameters. In the case of disequilibrium fractional melting model mentioned in Section 3.2 below, **m** = (F, ε), where ε is the extent of chemical disequilibrium. Let **C** be the data or concentration vector with each component C_i as the concentration of element i. In Bayesian statistics, the posterior probability of a model, p(**m**|**C**), is proportional to the product of the data-independent prior probability of this model, $\theta(\mathbf{m})$, and the likelihood of the model in observing the data, L(**C**|**m**) (Grandis et al., 1999; Sambridge and Mosegaard, 2002; Robert and Casella, 2004; Tarantola, 2005; Korenaga and Karato, 2008), viz.,

$$p(\mathbf{m}|\mathbf{C}) = A \cdot L(\mathbf{C}|\mathbf{m}) \cdot \theta(\mathbf{m}) \tag{1-1}$$

$$\int p(\mathbf{m}|\mathbf{C})\, d\mathbf{m} = 1 \tag{1-2}$$

where the bold letters are vectors; A is a constant which forces p(**m**|**C**) to satisfy Eq. (1-2). (Since we will only use ratios of p(**m**|**C**) in MCMC, the constant A will be set as 1.) In terms of notation, the vertical bar "|" stands for a conditional probability. For example, p(**m**|**C**) reads the probability of **m** given the observation **C**. The prior distribution of model θ(**m**) reflects the understanding of model before analyzing data. In the simple cases considered in the next section where only the bounds of each model parameter are known,

the prior probability $\theta(\mathbf{m})$ is constant within a model space restricted by those bounds, we take $\theta(\mathbf{m}) = 1$. The likelihood of observing $\mathbf{C}$ given model parameter $\mathbf{m}$ is a function of misfit Chi-squares, $X^2(\mathbf{C}, \mathbf{m})$,

$$L\left(\mathbf{d}|\mathbf{m}\right) = \exp\left(-\frac{X^2\left(\mathbf{C},\mathbf{m}\right)}{2}\right), \tag{1-3}$$

$$X^2\left(\mathbf{C},\mathbf{m}\right) = \sum_i \left(\frac{\log\left(C_i^{predict}\left(\mathbf{m}\right)\right) - \log\left(C_i\right)}{\sqrt{\left(\frac{\delta C_i^0}{C_i^0}\right)^2 + \left(\frac{\delta C_i}{C_i}\right)^2}} \right)^2, \tag{1-4}$$

where $C_i^{predict}\left(\mathbf{m}\right)$ is the concentration of element i predicted by model parameter $\mathbf{m}$ (e.g., we can calculate $C_i^{predict}\left(\mathbf{m}\right)$ as the prediction of disequilibrium fractional melting model using Eq. (1-6) or a more complicated model such as Eqs. (1-8) and (1-9) below); C_i^0 is the concentration of element i in the mantle source; δC_i^0 is the variation in the concentration of element i in the mantle source; δC_i is the uncertainty in the measured concentration of element i. Here for purpose of demonstration, we assume the relative source variation $\delta C_i^0 / C_i^0$ dominates the relative uncertainty of measurement $\delta C_i / C_i$. The posterior probability is greater if the Chi-square is smaller, i.e. the model fits the data with smaller overall residue is more probable.

1.2. Implementation of MCMC through Metropolis-Hastings algorithm

To obtain the posterior distribution defined by Eqs. (1-1) to (1-4), we carry out MCMC simulations using the following steps (Hastings, 1970; Sambridge and Mosegaard, 2002; Robert and Casella, 2004; Liu, 2008):

Step 1. Start from any model $\mathbf{m_0}$. Calculate predicted observation $\mathbf{C}^{\mathbf{predict}}(\mathbf{m_0})$. Calculate the likelihood function $L(\mathbf{m_0}|\mathbf{C})$ according to Eqs. (1-3) and (1-4).

Step 2. Suppose $\mathbf{m_k}$ is the current model (if this step follows Step 1, k = 0). Choose a temporary model $\mathbf{m_{temp}}$ randomly. Calculate predicted observation $\mathbf{C}^{\mathbf{predict}}(\mathbf{m_{temp}})$. Calculate the likelihood function $L(\mathbf{m_{temp}}|\mathbf{C})$ according to Eqs. (1-3) and (1-4).

- if the ratio $p(\mathbf{m_{temp}}|\mathbf{C}) / p(\mathbf{m_k}|\mathbf{C}) > 1$, accept $\mathbf{m_{temp}}$ as $\mathbf{m_{k+1}}$.
- else, generate a uniformly distributed random number, t, between 0 and 1.
  - if $p(\mathbf{m_{temp}}|\mathbf{C}) \; p(\mathbf{m_k}|\mathbf{C}) > t$ or the iteration of Step 2 has reached a pre-defined maximum number (2000 in this study), accept $\mathbf{m_{temp}}$ as $\mathbf{m_{k+1}}$.
  - else, go to Step 2.

Step 3. Continue to Step 2 until a sufficient number (at least 1000) of accepted models are produced.

The set of accepted models converges to the posterior distribution after sufficient numbers of accepted model are collected. However, the exact number can only be determined empirically. In this study, we use the Metropolis-Hastings algorithm to acquire a sample set consisting of at least 1000 models. There are alternative algorithms to implement MCMC (Robert and Casella, 2004; Liu, 2008). For example, “Gibbs Sampling”, which, in its basic form is a special case of the Metropolis-Hastings algorithm, is more

desirable for models with a large number of parameters (e.g., there are 18 fitting parameters in the olivine rheology model of Korenaga and Karato, 2008).

The result of MCMC simulations following the procedure outlined in the preceding section is a set of accepted models ($\mathbf{m_0}, \mathbf{m_1}, \ldots, \mathbf{m_n}$) representing the posterior distribution of model parameters, e.g., F and ε in the case of disequilibrium fractional melting. Among these models, there is one model called "the most probable model" whose probability in reproducing the observed data is the greatest, designated as $\mathbf{m_{MP}} = (F_{MP}, \varepsilon_{MP})$ or $(F_{MP}, \varepsilon_{MP}, \alpha_{MP})$ for the two melting models considered in the next section. In general, the probability distribution of F is not normal or symmetric. To facilitate comparison with normal distribution, we use σ_- and σ_+ as lower and upper standard deviation of F. The probability that an F randomly chosen from $(F_0, F_1, \ldots, F_n)$ (F_i belongs to $\mathbf{m_i}$) falls into the interval $[F_{MP} - \sigma_-, F_{MP} + \sigma_+]$ is 68%. The derivation of σ_- and σ_+ is presented in Appendix A. For convenience, we use the notation $F_{MP-\sigma_-}^{+\sigma_+}$ to describe a non-normal posterior distribution of F. We use this notation for all parameters in the model. In the special case of normal distribution, $\sigma_- = \sigma_+$. We recover the mean and standard deviation of F, viz., $F_{mean} \pm \sigma$.

As for the nonlinear least squares method, the estimate of a model parameter, say F, has a symmetric form because the method implicitly assumes a normal distribution of F characterized by the mean (F_{LS}) and the standard deviation (σ_{LS}). Since the nonlinear least squares method proceeds through iteration to find F_{LS} which fits the data with the smallest overall residue, F_{LS} is expected to be the same as F_{MP} if the iteration converges. The standard deviation obtained by the nonlinear least squares method does not have to be the

same as σ_- or σ_+ unless the posterior distribution is normal. We will compare results in these three formats ($F_{MP}{}^{+\sigma_+}_{-\sigma_-}$, $F_{mean} \pm \sigma$, $F_{LS} \pm \sigma_{LS}$) in a case study in section 3.2.

3. Case Studies

3.1. Data and source composition

To demonstration the advantages of MCMC, we consider REE and Y abundances in clinopyroxene (cpx) in abyssal peridotites from several major ridges. To focus on melting history, we have adopted Warren (2016)'s identification of "residual abyssal peridotites" and excluded samples that show textural evidence of refertilization. We further choose samples with at least 8 reported trace elements (REE and Y) in cpx. This procedure leads to a data set of 135 samples (summarized in Table 1, data from Johnson et al., 1990, Hellebrand et al., 2002; Salters and Dick, 2002; Hellebrand and Snow, 2003; Brunelli et al., 2006; Brunelli and Seyler, 2010; Lassiter et al., 2014; Mallick et al., 2014). Melting history of each sample is encapsulated by multiple incompatible trace element abundances in cpx. Concentrations of the selected trace elements in cpx will be regarded as a data vector **C** in MCMC as described in Section 2. For simplicity, we consider melting of the depleted MORB mantle or DMM (Workman and Hart, 2005) in spinel peridotite field, and we recognize that trace element and isotope compositions of mantle sources beneath mid-ocean ridge spreading centers vary among different ridge systems. Following Liang and Liu (2016), we exclude La in our data if the chondrite-normalized ratio $(La/Ce)_N > 2$. We consider two disequilibrium melting models: one with analytical solution and the other without. The former allows us to compare with results from direct nonlinear least squares inversion. The latter melting model is more general as it has one additional model

parameter. Our goal in this section is to demonstrate the procedure and advantage of MCMC through two case studies of a subset of data from the Central Indian Ridge. In Section 4, we further expand case study two by considering trace element data from other ridge systems listed in Table 1.

3.2. Case study one: Melting model with explicit analytical solution

Disequilibrium melting happens when diffusion in residual minerals for a trace element of interest cannot keep up with melting of the minerals. It can be characterized by a disequilibrium parameter ε which is defined as the ratio of melting rate relative to chemical exchange rate,

$$\varepsilon = \frac{\Gamma}{\rho_s (1-\phi) R} , \tag{1-5}$$

where ρ_s is the density of the solid; ϕ is the porosity; Γ is the melting rate of the bulk solid; and R is the exchange rate coefficient. During disequilibrium fractional melting, the concentration of a trace element in a residual mineral (e.g., cpx), $C(\mathbf{m})$, is given by the simple expression (Liang and Liu, 2016),

$$C(\mathbf{m}) = C_s^0 \frac{k_{cpx}}{k_0} \left(1 - \frac{\varepsilon + k_p}{\varepsilon + k_0} F\right)^{\frac{1-k_p}{k_p+\varepsilon}} , \tag{1-6}$$

where F is the degree of melting; k_0 is the bulk partition coefficient at the onset of melting; k_p is the bulk partition coefficient calculated according to melting reaction; k_{cpx} is the cpx-melt partition coefficient; C_s^0 is the concentration the trace element in the mantle source. Eq. (1-6) reduces to the familiar equilibrium non-modal perfect fractional melting model

when $\varepsilon = 0$. It is obtained under the assumption that diffusion rates in residual minerals are the same for the element of interest.

Liang and Liu (2016) used Eq. (1-6) and a nonlinear least squares method to invert for F and ε from REE and Y abundances in cpx in 22 abyssal peridotites from the Central Indian Ridge (CIR, Hellebrand et al., 2002). To compare with their results and to test the new inversion method, here we conduct MCMC simulations for the 22 samples from CIR using the same mineral-melt partition coefficients, melting reaction and starting mantle composition as in their study. For diffusion limited mass transfer, ε is inversely proportional to the diffusion coefficient in the mineral. Following their study, we scale ε_{REE} for REE and Y to that of La (designated as ε_{La} hereafter) according to their diffusion coefficients (D) in cpx, viz.,

$$\varepsilon_{REE} = \frac{D_{La}}{D_{REE}} \varepsilon_{La}, \tag{1-7}$$

where temperature-dependent REE + Y diffusion coefficients for cpx are from or interpolated from diffusivity data reported in Van Orman et al. (2002). For shorthand notation, we set $\varepsilon = \varepsilon_{La}$ hereafter. Hence, the model in MCMC simulations has two unknown model parameters: degree of melting and extent of disequilibrium for La, designated as $\mathbf{m} = (F, \varepsilon)$.

We choose the prior distribution as a uniform distribution in a two-dimension model space. In other words, any $\mathbf{m} = (F, \varepsilon)$ in the model space has the same prior probability. The bound for F is less than the degree of melting when cpx is exhausted ($F < 18\%$, Baker and Stolper, 1994). The bound for ε is [0, 0.05] according to previous inversion

results and reference value at reasonable physical conditions (Liang and Liu, 2016). Fig. 1-1 displays results of 6231 MCMC simulations for sample ANTP126-2 following the steps outlined in section 2.2. Here the observed data are shown as yellow circles and each gray line represents an REE pattern calculated using accepted **m** from MCMC simulation. Those REE patterns predicted by models within the asymmetric confidence interval ([F_{MP}- σ_-, F_{MP}+ σ_+] and [ε_{MP} - σ_-, ε_{MP} + σ_+]) define a region enclosing the data (Fig. 1-1). The prediction with the most probable model is the best fit to the data (red line in Fig. 1-1). Figs. 1- 2a and 1-2b display marginal distributions of F and ε, respectively. The marginal distribution of ε is skewed: σ_+ of ε is larger than σ_- of ε. The normal distribution derived from nonlinear least squares inversion is markedly narrower than the MCMC accepted models in the histogram. The inconsistency between sample mean and the most probable model also indicates asymmetry of posterior distribution of ε. In a plot of ε vs. F, accepted models scatter around a near ellipse figure centered at most probable model (Fig. 1-3). Positive trade-off between F and ε is demonstrated as the NE-SW trending of the accepted models. The ranges of asymmetric uncertainty estimate (σ_+ and σ_-) are larger than or comparable to 68% confidence ellipses for normal distribution. Figures similar to Fig. 1-3 for the 22 CIR samples are presented in Supplementary Figure S1-1. For a few samples, the uncertainty range characterized by σ_+ and σ_- are greater than the range of 95% confidence ellipse derived from direct nonlinear least squares inversion (e.g., samples ANTP87-5, ANTP87-9, ANTP89-2, ANTP89-5, ANTP89-8, ANTP89-15). The nonlinear least squares method cannot describe asymmetric probability distribution of ε and may lead to underestimate of uncertainty.

The most probable model derived from MCMC is not necessarily a good fit to the data. The most probable model still cannot fit sample CIRCE93-7 which exhibits a "hump shape" REE pattern. The probability of the most probable model is effectively zero ($p = 1 \cdot 10^{-14}$ according to Eq. 1-1), which means that the melting model (Eq. 1-6) cannot explain this sample. A more general model involving refertilization by a small amount of melt produced in the lower part of the melting column, as suggested by Hellebrand et al. (2002), can explain the observed REE data. To avoid samples affected by refertilization and other post-melting processes (discussed in Section 5.3), any sample that has the probability less than $1 \cdot 10^{-4}$ for the most probable model will be excluded.

For all samples, the model estimates from nonlinear least squares inversion are consistent with those derived from the most probable model (Fig. 1-4). But the means of accepted models show systematic deviation from the most probable model and the nonlinear least squares results (Fig. 1-4). For $F_{MP} > 15\%$, F_{mean} is smaller than F_{MP} and F_{LS}, whereas for $F_{MP} < 15\%$, ε_{mean} is greater than ε_{MP} and ε_{LS}. Since the model represents the most probable physical condition given the data constraint, we recommend using F_{MP} over F_{mean}. For later discussion, the estimate of the model parameter will be presented in the asymmetric form, $F_{MP}^{+\sigma_+}_{-\sigma_-}$ and $\varepsilon_{MP}^{+\sigma_+}_{-\sigma_-}$.

3.3. Case study two: Melting model without explicit analytical solution

The preceding example demonstrates the procedure of MCMC and its advantage in estimating meaningful uncertainties for model parameters. In this section, we demonstrate another important advantage of MCMC using a disequilibrium dynamic melting model that does not have an explicit analytical solution. Nonlinear least squares inversion of such a

problem is considerably challenging, if not impossible. Here we show that MCMC is well suited for this class of inverse problems.

The dynamic or continuous melting model has been widely used to study trace element fractionation during mantle melting (e.g., Langmuir et al., 1977; McKenzie, 1985; Zou, 1998; Shaw, 2000). Here we consider a more general case of dynamic melting by allowing chemical disequilibrium between residual minerals and interstitial melt. In nondimensional form, the governing mass conservation equations for a trace element in the interstitial melt (C_f) and residual solid (C_s) are given by two coupled ordinary differential equations (a derivation is presented in Appendix B). In terms of the degree of melting, we have

$$(1-F)\varepsilon\alpha\frac{dC_f}{dF} = \varepsilon\left(C_s^p - C_f\right) + \left(C_s - kC_f\right) \tag{1-8}$$

$$(1-F)\varepsilon\frac{dC_s}{dF} = -\varepsilon\left(C_s^p - C_s\right) - \left(C_s - kC_f\right) \tag{1-9}$$

$$\alpha = \frac{\rho_f \phi V_f}{\rho_s (1-\phi) V_s} \tag{1-10}$$

where ε is defined by Eq. (1-5); α is the mass flux ratio between the melt and the residual solid; C_s^p is the concentration of bulk solid calculated according to melting reaction; k is the bulk partition coefficient (Appendix). To be consistent with equilibrium dynamic melting models of Zou (1998) and Shaw (2000), we assume that dynamic melting starts at $F = f_p$ before which melting takes place as equilibrium batch melting. Hence the initial melt and solid compositions at $F = f_p$ are

$$C_f = \frac{C_s^0}{k_0 + f_p\left(1 - k_P\right)}\ , \tag{1-11}$$

$$C_s = \frac{C_s^0}{k_0 + f_p\left(1 - k_P\right)} \frac{k_0 - k_P f_p}{1 - f_p}\ , \tag{1-12}$$

where C_s^0 is the concentration of the source; and f_p is a function of α (Shaw, 2000), viz.

$$f_p = \frac{\alpha}{1+\alpha}. \tag{1-13}$$

The disequilibrium dynamic melting model has three parameters (F, ε, α). It recovers the equilibrium dynamic melting when ε = 0, the disequilibrium perfect fractional melting when α = 0. For incompatible trace element, the concentration in residue at a given F increases with α or ε (Liang and Liu, 2016). Since there is no explicit analytical solution to Eqs. (1-8) and (1-9), here we invert the melting parameters through MCMC simulations. Our observations include REE and Y abundances in cpx in the 22 abyssal peridotites from CIR. We solve Eqs. (1-8) and (1-9) numerically using the third-order Runge Kutta method (Shu and Osher, 1988), starting from the initial conditions prescribed by Eqs. (1-11) and (1-12).

The prior bounds for model parameters are $f_p < F < 0.18$, $0.0002 < \varepsilon < 0.05$, and $0.0005 < \alpha < 0.04$. The upper bound for F and ε are the same as in case study one in section 3.2. The lower bound for F is the onset of dynamic melting (Eq. 1-13). The upper bound for α is equivalent to a scenario in which there is 2% porosity and the melt percolates two times faster than the solid. The non-zero lower bounds for ε and α are for the consideration

of numerical stability in solving Eqs. (1-8) and (1-9). These upper and lower bounds are conservative with respect to the most probable models.

Supplementary Figure S1-2 and Table S1 summarize our simulation results. Fig. 1-5 shows results of MCMC simulations for three samples: one with effectively zero α (ANTP126-2), one with effectively zero ε (ANTP89-1), and one with intermediate α and ε (sample CIRCE93-4). These model parameters are not from normal distributions (Figs. 1- 6 and 1-7). Fig. 1-6 displays the asymmetric marginal distributions of F, ε, and α for sample ANTP126-2. The most probable model deviates from the peak of marginal distribution as a result of 3D to 1D projection. This is further illustrated in Fig. 1-7 for the three samples displayed in Fig. 1-5. Even when projected on F – ε and ε – α planes, accepted models as points of $\mathbf{m} = (F, \varepsilon, \alpha)$ clearly display nonlinear trade-offs. There is a broad negative correlation between ε and α in Figs. 1-7b, 1-7e and 1-7h. The distribution near the origin on the ε-α plane is considerably sparser than the region where α and ε are greater than 0.01 (Fig. 1-7b). Thus, equilibrium fractional melting is unlikely for sample ANTP126-2. Further, the ε-α correlation is not characterized by an ellipse expected in a bimodal normal distribution. The probability distribution is denser near ε axis than near α axis (Fig. 1-7b). The most probable model has small α and relatively large ε, which is clearly shown in Fig. 1-7c. Therefore, sample ANTP126-2 is better represented by a model that is closer to disequilibrium fractional melting than equilibrium dynamic melting. (The converse is true for sample 89-1.) Figs. 1- 7d, 1-7e, and 1-7f are from a model with both ε and α greater than 0.01, i.e., an intermediate case that cannot be represented by known analytical solutions (i.e., the disequilibrium factional melting model ($\alpha = 0$, $\varepsilon > 0$) or the equilibrium dynamic melting model ($\varepsilon = 0$, $\alpha > 0$)). Estimate of ε in case study one only

considers the $\alpha = 0$ plane in F - ε - α space. Because there exists trade-offs between ε and α, case study one would overestimate ε. The trade-off between the extent of disequilibrium and the extent of incomplete melt extraction has been noted by previous studies (Qin, 1992; Iwamori, 1993b; Van Orman et al., 2002). The preceding examples demonstrate that with MCMC simulations it possible to target the most probable combination of ε and α for individual sample. Similar figures summarizing MCMC simulations for all the samples included in this study are presented in Supplementary Figure S1-2.

Fig. 1-8 compares results from case studies one and two for the CIR samples. In general, ε estimated in case study two (unfilled circles) are smaller, especially for those samples with F less than 13%. This is largely due to the negative trade-off between ε and α in the disequilibrium dynamic melting model, i.e., the product $\varepsilon\alpha$ in Eq. (1-8). The lower values of ε in the disequilibrium dynamic melting model are compensated by α which is absent in the disequilibrium perfect fractional melting model. (For the same reason, values of α derived from the equilibrium dynamic melting model would be higher than values obtained from the disequilibrium dynamic melting model.) Therefore, values of ε derived from the more general melting model in case study two are more reliable than values derived from the disequilibrium fractional melting model in case study one and the equilibrium dynamic melting model.

4. Application to Abyssal Peridotites from other Selected Ridge Systems

One of the major motivations for our MCMC study is the positive correlation between F and ε derived from nonlinear least squares inversion of REE and Y abundances in cpx in abyssal peridotites from CIR using the disequilibrium fractional melting model (Liang and Liu, 2016). This positive correlation is further confirmed in the present study through the

application of a more general melting model with more robust error estimate (Fig. 1-8). An interesting question is if similar correlation between F and ε also exists in abyssal peridotites from other ridge systems. In this section, we expand case study two in Section 3.3 to include peridotites from Vema Lithospheric Section (VLS, 35 samples, Brunelli et al., 2006), Kane Fracture Zone and Saint Paul Fracture Zone (KSP, 9 samples, Brunelli and Seyler, 2010; Mallick et al., 2014) at Mid-Atlantic Ridge, South West Indian Ridge (SWIR, 35 samples, Warren, 2007), Lena Trough at Arctic Ocean (LT, 25 samples, Hellebrand and Snow, 2003; Lassiter et al., 2014), and American-Antarctica Ridge (AAR, 9 samples, Johnson et al., 1990). The spreading rate of SWIR, LT, and AAR is less than 20 mm/yr, which is slower than CIR (30-51 mm/yr) while the spreading rate of VLS and KSP at Mid-Atlantic Ridge (25-31 mm/yr) is at the lower end of CIR (Argus and Gordon, 1991; DeMets et al., 2010).

Supplementary Table S1 summarizes results from MCMC simulations based on the disequilibrium dynamic melting model (Eqs. 1-8 to 1-13). Supplementary Figure S1-2 present MCMC simulations of individual samples. Similar to case study one, samples potentially affected by post-melting processes are excluded according to a threshold probability ($p < 0.03$). As a result of this filtering, thirty four out of 135 samples are disqualified. REE abundances in these samples are likely affected by secondary processes such as melt refertilization (discussed in section 5.3). As a precaution, we exclude these samples in the interpretation of the disequilibrium dynamic melting model. If we only consider the most probable model, samples from all ridge systems considered in this study except two samples from SWIR (EDUL-6B-1-3 and EDUL-23-2-8 from SWIR, Seyler et al., 2011) show a positive correlation between F and ε for La, although the range of

variation differs among localities (Fig. 1-9). The lower bound of ε for these two samples still lie on the trend of the rest of 25 samples from SWIR (magenta squares in Fig. 1-9). A model on the F – ε trend still produces acceptable fit (Fig. 1-9 and Fig. 1-S2). . Samples from CIR show strong positive trends even when uncertainties are considered (Figs. 1- 9a and 1-9d). The F – ε trend in SWIR has higher ε values than the F – ε trend in CIR.

5. Discussion

5.1. The positive correlation between F and ε

We have demonstrated in the preceding sections that the positive correlations between F and ε for La in cpx in abyssal peridotites is a robust feature of mantle melting beneath the mid-ocean ridge spreading centers. To the first order, the positive correlation is consistent with the predicted ε as a function of F at a given mantle potential temperature (Fig. 1-10). Our inverted disequilibrium parameter ε is the ratio of the melting rate to the solid-melt diffusive exchange rate for La in cpx (Eq. 1-5). The melting rate is proportional to solid upwelling rate (V_s) and melt productivity (dF/dz) along the melting column. The diffusive exchange rate is inversely proportional to the time scale of La diffusion in cpx. Liang and Liu (2016) presented a simple equation relating ε to these parameters, viz.,

$$\varepsilon = \frac{V_s d^2}{15(1-F)D}\frac{dF}{dz} \quad , \tag{1-14}$$

where d is the average grain size of cpx; D is the diffusivity of the trace element of interest in cpx; z is the vertical distance above the depth at the onset of melting. In the calculation below, we take V_s as half of the local spreading rate (Argus and Gordon, 1991; DeMets et al., 2010). The grain size of starting mantle is not known. Here we assume that the grain

size of cpx at the onset of melting (d_0) is 1.5 mm and decreases during melting (in proportion to cpx volume reduction). Asimow et al. (1997, 2001) demonstrated that one can use the thermodynamic model pMELTS to calculate melt productivity along a melting column. Fig. 1-10 displays calculated disequilibrium parameter for La (ε_{La}) along three melting paths using pMELT (Ghiorso et al., 2002; Smith and Asimow, 2005) for anhydrous melting of a DMM source (Workman and Hart, 2005). The calculated ε_{La} is smaller for higher potential temperature as a result of strong temperature dependent diffusivity. The disequilibrium parameter ε_{La} varies by one order of magnitude over the range of potential temperatures considered (1280°C to 1340°C). The increase of ε_{La} at lower F is due to increasing melt productivity and decreasing diffusion rate, while the decrease of ε_{La} at higher F is due to grain size reduction of cpx during melting. The latter is not well constrained. In case study two, we assume ε_{La} to be constant along the melting column. Thus the inverted ε should be regarded as an average value during disequilibrium melting. For the convenience of comparison, we also calculate the average of ε_{La} at a given F as the arithmetic mean of ε_{La} from the onset of melting to F. Fig. 1-10 shows that the average ε_{La} (dashed lines) increases but lags behind the instantaneous ε_{La} at lower F. As F further increases, the average ε_{La} levels off.

5.2. Variation of ε at a given F

There are considerable variations of ε for La at a given F among samples from the same ridge segments, which cannot be explained by any single melting path in Fig. 1-10. Possible factors responsible for observed variations of ε at a given F include, but are not limited to (see Section 5.3 below), grain size variation among segments and grain size distribution in a single segment, upwelling rate, and potential temperature. In the following

discussion, "variation in ε" refers to "variations of ε for La at a given F" unless stated otherwise. We first consider variations in upwelling rate.

According to Eq. (1-14), ε is proportional to local upwelling rate (and hence spreading rate). Thus, the inverted ε from ridges of different spreading rate are not directly comparable. To facilitate comparison, we renormalize ε from different ridges to a common or reference spreading rate V_0 (= 30 mm/yr). The results are shown in Fig. 1-10. If the variation in ε is due to upwelling rate only, Fig. 1-10 would plot all scaled inversion results on the same trend. However, results shown in Fig. 1-10 still contain considerable variations in ε. High ε and low F is common for samples from ridges with ultra-slow spreading rate (SWIR, LT, and AAR), while ridges with intermediate spreading rate (CIR) show lower ε and higher F. Two data sets from the slow spreading Mid-Atlantic Ridge (VLS and KSP) are plotted between CIR and ultra-slow spreading ridges. This is further illustrated in Fig. 1-11b where samples with large ε/F ratios are from ultra-slow spreading ridges (SWIR, LT, AAR), while samples with small ε/F ratios are from intermediate-slow spreading ridge (CIR). In general, ε increases with grain size (d_0) and decreases with potential temperature (T_p). Different local ε-F trends suggest factors other than upwelling rate contribute to the bulk part of the variation in ε. Interestingly, the average degree of melting in each bin of spreading rate is positively correlated with spreading rate (Fig. 1-11a). If this positive correlation between F and spreading rate is due to increasing potential temperature, faster spreading ridges would also have smaller ε (due to higher diffusion rate in cpx). Indeed, both the average and maximum ε in each bin decreases with the spreading rate (Fig. 1-11b).

A reduction of potential temperature from 1310°C to 1280°C can explain the observed difference in ε between SWIR and CIR (Fig. 1-10). Such variations in potential temperature agree with the ranges of potential temperatures inferred from independent studies (Niu and O'Hara, 2008; Dalton et al., 2014). Many abyssal peridotite samples are from fracture zones. In the Vema Lithospheric Section at Mid-Atlantic Ridge, inverted ε increases progressively to the east, although the trend is rather weak (Fig. 1-12). Such local variation of ε could, in part, be attributed to temperature as geodynamic modeling justifies such temperature perturbation as a result of transform fault effect (Morgan and Forsyth, 1988; Roland et al., 2010). If the most probable ε indeed increases 10 fold along this 250 km long fracture zone, this would require a temperature increase of ~60 °C. However, it is important to note that sharp variation in ε also exists in a single transform fault (three fold difference between two samples, ANTP89-17 and ANTP89-2 within 25 km from Marie Celeste TF in CIR, Hellebrand et al., 2002). If the observed variation in ε is due to potential temperature alone, the temperature profile of one sample during melting may be 30°C higher than the temperature profile of another sample 30 km away, which means that at the same ridge section potential temperature could differ by 30°C. In a thermal model of transform fault (Morgan and Forsyth, 1988; Roland et al., 2010), sharp horizontal temperature gradient is difficult to extent to the depth of initial melting (~60 km). Considering a 60 km mantle column upwelling at a rate of 15mm/yr, the characteristic length scale of thermal conduction during decompression melting is 11 km (assuming thermal diffusivity of 1×10^{-6} m^2/s, Turcotte and Schubert, 2002). Therefore, it is not likely that 30°C horizontal temperature difference within 30km can persist from the onset of

melting to the end of melting. So, temperature can only account for inter-ridge and smooth along-fault variation of ε.

For the sharp along-fault variation, the grain size variation is a simple explanation, as ε is very sensitive to grain size (Eq. 1-14). Unfortunately, clinopyroxene which is the dominant host for REE in spinel peridotites is almost exhausted in residual abyssal peridotites (Warren, 2016). If the grain size is extrapolated back to the source, the uncertainty is expected to increase further. Here, we provide an estimate of initial grain size of cpx by attributing the local variation of ε at a given F solely to grain size variation after correction for upwelling rate. The factor that regresses inverted data to each predicted melting trend shown in Fig. 1-10 is proportional to the grain size squared according to Eq. (1-15). Thus, the grain size of the source is derived for each sample at a presumed potential temperature,

$$d = \sqrt{\frac{\varepsilon_{La} \cdot V_0 / V_{sp}}{\varepsilon^0_{Tp}}} \cdot d_0, \tag{1-15}$$

where ε^0_{Tp} is the average ε calculated on a melting path with potential temperature T_p and reference grain size (d_0 = 1.5 mm) and reference upwelling rate (V_s = 15mm/yr).

Only samples from the VLS at MAR (Brunelli et al., 2006) and the Marie Celeste TF at CIR (Hellebrand et al., 2002) are used to estimate grain size because there is a relatively large dataset within a single transform fault (26 in VLS and 9 in Marie Celeste TF) where we assume the potential temperature is constant. Fig. 1-13 demonstrates that larger grain size is required to compensate faster diffusivity at higher potential temperature. Given three choices of potential temperature, the average grain size ranges from 0.56 mm

to 2.55 mm in these two locations. The grain size distribution in these two locations cannot be discriminated statistically given the same potential temperature. In other words, there could be no difference in grain size and potential temperature between these two locations although the spreading rates between the two locations are somewhat different (Marie Celeste TF, 41 mm/yr; VLS, 28 mm/yr). The average grain size of each potential temperature is distinct. The potential temperature or the average grain size could be estimated given the knowledge of the other.

5.3. Other processes

A number of factors or processes not considered in this study can also affect trace element abundances in residual peridotites: (1) source heterogeneity, (2) shallow level refertilization, and (3) subsolidus reequilibration. In Liang and Liu (2016), we assessed the effects of (1) and (2) using available Nd isotope data from VLS (12 samples). Fig. 1-14 includes 7 additional samples from SWIR, Kane Fracture Zone, and Saint Paul Fracture Zone. There is no obvious correlation between ε and $^{143}Nd/^{144}Nd$. The latter is a measure of source heterogeneity. It is possible that variations in major element composition (hence mineral proportion) and non-uniform grain size distribution also contribution to the observed variations in ε. These effects should be considered in future studies.

Shallow level melt refertilization by small degree melt produced in the lower part of the melting column has been suggested by Hellebrand et al. (2002) and Brunelli et al. (2006) to account for elevated LREE patterns in residual cpx in some abyssal peridotites from CIR and VLS. We note that refertilization can account for the 31 cpx samples excluded in this study (for examples see Hellebrand et al, 2002; Brunelli et al, 2006; Liang

and Liu, 2016). According to Sun and Liang (2014), HREE in cpx could be elevated by a factor of 2 during subsolidus exchange with orthopyroxene in spinel harzburgite at low temperatures. A correction of HREE to lower values could increase the estimate of F because HREE are more depleted than they appear. The estimate of ε could also increase because there will be more LREE enrichment relative to HREE (see Fig. 1-5 of Liang and Liu, 2016).

6. Summary and outlook

The present study is motivated primarily by the positive correlation between F and ε_{La} derived from nonlinear least squares inversion of REE and Y abundances in cpx in abyssal peridotites from CIR using the disequilibrium perfect fractional melting model. To test the robustness of this correlation for melting beneath mid-ocean ridge spreading centers, we have to consider more general melting models and to better assess uncertainties of inverted melting parameters. Most physically more realistic melting models for trace element do not have explicit analytical solutions, which poses considerable challenge to nonlinear least squares analysis. This leads us naturally to the MCMC method. Here we demonstrated the procedures of MCMC simulations and its advantages in studying geochemical inverse problems through two case studies of disequilibrium mantle melting. We introduced MCMC method to interpret geochemical observations as consequences of the model with unknown physical parameters. We showed that melting parameters inverted through MCMC simulations are consistent with those obtained from direct nonlinear least squares inversions. However, the nonlinear least squares method cannot describe the asymmetric posterior distribution. The uncertainty derived from nonlinear least squares method could be underestimated.

Reading REE data from cpx in abyssal peridotites through MCMC simulations and the disequilibrium dynamic melting model has led to new insights into the melting processes beneath mid-ocean ridge spreading centers. We found that disequilibrium dynamic melting model can explain REE patterns in cpx in 101 out of 135 residual abyssal peridotites considered in this study. The positive correlation between F and ε_{La} has been confirmed by the disequilibrium dynamic melting model and additional data from several ultra-slow to intermediate spreading centers around the world. We suggest that the positive correlation between F and ε_{La} is a natural consequence of decompressional melting beneath the mid-ocean ridge spreading center that results from continuous competition between melting and diffusive exchange between the minerals and the melt. More isotope and petrological data are needed to assess the role of mantle source heterogeneity on the variations of ε at a given F. The variation in ε at a given F is unlikely caused by variations in upwelling velocity or spreading rate alone. The combination of potential temperature and grain size distribution of cpx can explain the ε-F trend, although additional factors and processes such as mantle source heterogeneity, shallow level refertilization, and subsolidus reequilibration may also have contributed to the observed REE patterns in the peridotites. In VLS of MAR or the Marie Celeste TF at CIR, the average grain size may increase from 0.56 mm to 2.55 mm to accommodate increasing potential temperature.

For purpose of demonstration, we considered two simple disequilibrium fractional melting models by assuming constant mineral-melt REE partition coefficients and diffusion coefficients, by treating non-modal melting as a simple melting reaction with constant coefficients, and by simplifying the physics of melting extraction with a constant porosity or melt-to-solid mass flux ratio (i.e., the dynamic melting model). These

assumptions and simplifications, which have been widely used in geochemical studies of mantle melting, can be relaxed or eliminated within the framework of MCMC which does not require explicit analytical solutions for the conservation equations. This unique feature of MCMC allows us to use self-consistent melting models to better constrain melting parameters from trace element abundances in residual minerals and basalts in the future. For example, in a more realistic scenario of adiabatic mantle melting, one can use a thermodynamic model to calculate residual mineral proportions and major element compositions along a melting path. Results from the thermodynamic modeling can be used to calculate temperature-, pressure- and mineral composition-dependent mineral-melt REE partition coefficients and diffusion coefficients based on parameterized lattice strain models for REE partitioning and Arrhenius relations for REE diffusion in pyroxenes. Furthermore, independent geophysical observations and modeling could be used as prior knowledge in MCMC simulations. The present study treated α as a free parameter within a reasonable range. We can put tighter constraints on α by considering the melt fraction as observed by tomography studies. Finally, for the one-dimensional steady-state problem considered in this study, it is also straightforward to include the physics of melt migration as part of the MCMC simulations. The melt fraction, melt and solid velocities, and melting rate are related to each other through mass, momentum and energy conservation equations (e.g., McKenzie, 1984). This will eliminate the model-dependent parameter α in our inversion, which will enable us to further constrain the relationship between F and ε in the melting model. One of the advantages of MCMC is that we do not have to know the exact value of porosity and velocities of the melt and the solid a priori. The uncertainty in these

physical parameters can be circumvented by solving forward models with a range of values. The data will automatically converge those parameters to the most probable values.

The ability to handle nonlinear problems with many parameters or unknowns through MCMC simulations allows the possibility of further expanding the simple one-dimensional steady-state melting problem considered in the present study to more complicated but geologically more realistic cases that are time-dependent and/or multidimensional. For example, the chemistry of basalt is related not only to the melting processes but also the subsequent mixing happened under a permeability barrier or in the sub-axial magma chamber. These melting and mixing processes involves multiple parameters, including but are not limited to the shape of the melting regime, the frequency of replenishment, the rate and proportion of crystallization. Through applications of MCMC to basalt geochemistry, we could make estimate on the most probable parameters that best explain the observed data. Another potential application of MCMC is the variation of isotopic and trace element heterogeneity in basalts. The variation of $^{143}Nd/^{144}Nd$ in present day samples is a result of time-integrated process of mantle evolution and melt extraction and has been widely used to fingerprint mantle source heterogeneity (e.g., DePaolo, 1988; Hofmann, 1997). With the flexibility of MCMC in incorporating multiple dataset and in handling conservation equations that do not have explicit analytical solutions, it is possible to quantify processes involved in melting and melt migration in a chemically and lithologically heterogeneous mantle by integrating major element, trace element, and isotope data in basalts and residual peridotites with geophysical observations and the physics and thermodynamics of melt migration.

Acknowledgments

We would like to thank Don Forsyth for advice on MCMC method, Reid Cooper and Greg Hirth for discussion regarding clinopyroxene grain size in mantle rocks, Jessica Warren for sharing her unpublished SWIR data, and Nick Dygert for a careful reading of an earlier version of this paper. This paper benefited from thoughtful review comments by Paul Asimow, Haibo Zou, an anonymous reviewer, and the associate editor Dmitri Ionov. This work was supported by US National Science Foundation grants OCE-115567 and EAR-1624516 and by NASA grant SSERVI NNA14AB01A.

References

Albarède, F. (1996). Introduction to geochemical modeling, Cambridge University Press.

Allegre, C. and J. Minster (1978). "Quantitative models of trace element behavior in magmatic processes." Earth and Planetary Science Letters **38**(1): 1-25.

Anders, E. and N. Grevesse (1989). "Abundances of the elements: Meteoritic and solar." Geochimica et Cosmochimica Acta **53**(1): 197-214.

Argus, D. F. and R. G. Gordon (1991). "No-net-rotation model of current plate velocities incorporating plate motion model NUVEL-1." Geophysical Research Letters 18(11): 2039-2042.

Backus, G. and F. Gilbert (1968). "The Resolving Power of Gross Earth Data." Geophysical Journal of the Royal Astronomical Society **16**(2): 169-205.

Brunelli, D. and M. Seyler (2010). "Asthenospheric percolation of alkaline melts beneath the St. Paul region (Central Atlantic Ocean)." Earth and Planetary Science Letters **289**(3–4): 393-405.

Brunelli, D., M. Seyler, A. Cipriani, L. Ottolini and E. Bonatti (2006). "Discontinuous melt extraction and weak refertilization of mantle peridotites at the Vema Lithospheric Section (Mid-Atlantic Ridge)." Journal of Petrology **47**(4): 745-771.

Dalton, C. A., C. H. Langmuir and A. Gale (2014). "Geophysical and geochemical evidence for deep temperature variations beneath mid-ocean ridges." Science **344**(6179): 80-83.

DeMets, C., R. G. Gordon and D. F. Argus (2010). "Geologically current plate motions." Geophysical Journal International **181**(1): 1-80.

DePaolo, D. J. (1980). "Crustal growth and mantle evolution: inferences from models of element transport and Nd and Sr isotopes." Geochimica et Cosmochimica Acta **44**(8): 1185-1196.

Feigenson, M. D. and M. J. Carr (1993). "The Source of central-american lavas - inferences from geochemical inverse modeling." Contributions to Mineralogy and Petrology **113**(2): 226-235.

Feigenson, M. D. and M. J. Carr (1983). "Case studies on the origin of basalt .II. The transition from tholeiitic to alkalic volcanism on Kohala Volcano, Hawaii." Contributions to Mineralogy and Petrology **84**(4): 390-405.

Ghiorso, M. S., M. M. Hirschmann, P. W. Reiners and V. C. Kress (2002). "The pMELTS: A revision of MELTS for improved calculation of phase relations and major element partitioning related to partial melting of the mantle to 3 GPa." Geochemistry, Geophysics, Geosystems **3**(5): 1-35.

Glueckauf, E. (1955). "Theory of chromatography. Part 10.—Formula for diffusion into spheres and their application to chromatography." Transactions of the Faraday Society **51**: 1540-1551.

Grandis, H., M. Menvielle and M. Roussignol (1999). "Bayesian inversion with Markov chains—I. The magnetotelluric one-dimensional case." Geophysical Journal International **138**(3): 757-768.

Hastings, W. K. (1970). "Monte Carlo sampling methods using Markov chains and their applications." Biometrika **57**(1): 97-109.

Hellebrand, E., J. Snow, S. Mostefaoui and P. Hoppe (2005). "Trace element distribution between orthopyroxene and clinopyroxene in peridotites from the Gakkel Ridge: a SIMS and NanoSIMS study." Contributions to Mineralogy and Petrology **150**(5): 486-504.

Hellebrand, E. and J. E. Snow (2003). "Deep melting and sodic metasomatism underneath the highly oblique-spreading Lena Trough (Arctic Ocean)." Earth and Planetary Science Letters **216**(3): 283-299.

Hellebrand, E., J. E. Snow, P. Hoppe and A. W. Hofmann (2002). "Garnet-field Melting and Late-stage Refertilization in 'Residual' Abyssal Peridotites from the Central Indian Ridge." Journal of Petrology **43**(12): 2305-2338.

Hofmann, A. W. and M. D. Feigenson (1983). "Case studies on the origin of basalt .I. Theory and reassessment of grenada basalts." Contributions to Mineralogy and Petrology **84**(4): 382-389.

Iwamori, H. (1993). "A model for disequilibrium mantle melting incorporating melt transport by porous and channel flows." Nature **366**(6457): 734-737.

Iwamori, H. (1994). "^{238}U-^{230}Th-^{226}Ra and ^{235}U-^{231}Pa disequilibria produced by mantle melting with porous and channel flows." Earth and Planetary Science Letters **125**(1–4): 1-16.

Johnson, K. T. M., H. J. B. Dick and N. Shimizu (1990). "Melting in the oceanic upper mantle: An ion microprobe study of diopsides in abyssal peridotites." Journal of Geophysical Research: Solid Earth **95**(B3): 2661-2678.

Jull, M., P. B. Kelemen and K. Sims (2002). "Consequences of diffuse and channelled porous melt migration on uranium series disequilibria." Geochimica et Cosmochimica Acta **66**(23): 4133-4148.

Korenaga, J. and S.-I. Karato (2008). "A new analysis of experimental data on olivine rheology." Journal of Geophysical Research: Solid Earth **113**(B2): B02403.

Lassiter, J. C., B. L. Byerly, J. E. Snow and E. Hellebrand (2014). "Constraints from Os-isotope variations on the origin of Lena Trough abyssal peridotites and implications for the composition and evolution of the depleted upper mantle." Earth and Planetary Science Letters **403**: 178-187.

Liang, Y. (2003). "On the thermo-kinetic consequences of slab melting." Geophysical Research Letters **30**(24): 2270.

Liang, Y. and B. Liu (2016). "Simple models for disequilibrium fractional melting and batch melting with application to REE fractionation in abyssal peridotites." Geochimica et Cosmochimica Acta **173**: 181-197.

Liang, Y. and E. M. Parmentier (2010). "A Two-Porosity Double Lithology Model for Partial Melting, Melt Transport and Melt–rock Reaction in the Mantle: Mass Conservation Equations and Trace Element Transport." Journal of Petrology **51**(1-2): 125-152.

Liang, Y. and Q. Peng (2010). "Non-modal melting in an upwelling mantle column: Steady-state models with applications to REE depletion in abyssal peridotites and the dynamics of melt migration in the mantle." Geochimica et Cosmochimica Acta **74**(1): 321-339.

Liu, J. S. (2008). Monte Carlo strategies in scientific computing, Springer Science & Business Media.

Lundstrom, C. (2000). "Models of U-series disequilibria generation in MORB: the effects of two scales of melt porosity." Physics of the Earth and Planetary Interiors **121**(3–4): 189-204.

Mallick, S., H. J. B. Dick, A. Sachi-Kocher and V. J. M. Salters (2014). "Isotope and trace element insights into heterogeneity of subridge mantle." Geochemistry, Geophysics, Geosystems **15**(6): 2438-2453.

McKenzie, D. (1984). "The generation and compaction of partially molten rock." Journal of Petrology **25**(3): 713-765.

McKenzie, D. and R. K. O'Nions (1991). "Partial melt distributions from inversion of rare earth element concentrations." Journal of Petrology **32**(5): 1021-1091.

McKenzie, D. and R. K. O'Nions (1995). "The source regions of ocean island basalts." Journal of Petrology **36**(1): 133-159.

McKenzie, D. and R. K. O'Nions (1998). "Melt production beneath oceanic islands." Physics of the Earth and Planetary Interiors **107**(1–3): 143-182.

McKenzie, D., A. Stracke, J. Blichert-Toft, F. Albarede, K. Gronvold and R. K. O'Nions (2004). "Source enrichment processes responsible for isotopic anomalies in oceanic island basalts." Geochimica et Cosmochimica Acta **68**(12): 2699-2724.

Metropolis, N., A. W. Rosenbluth, M. N. Rosenbluth, A. H. Teller and E. Teller (1953). "Equation of state calculations by fast computing machines." The Journal of Chemical Physics **21**(6): 1087-1092.

Minster, J. F. and C. J. Allegre (1978). "Systematic use of trace-elements in igneous processes .III. inverse problem of batch partial melting in volcanic suites." Contributions to Mineralogy and Petrology **68**(1): 37-52.

Morgan, J. P. and D. W. Forsyth (1988). "Three-dimensional flow and temperature perturbations due to a transform offset: Effects on oceanic crustal and upper mantle structure." Journal of Geophysical Research: Solid Earth **93**(B4): 2955-2966.

Niu, Y. and M. J. O'Hara (2008). "Global correlations of ocean ridge basalt chemistry with axial depth: a new perspective." Journal of Petrology **49**(4): 633-664.

Ormerod, D. S., N. W. Rogers and C. J. Hawkesworth (1991). "Melting in the lithospheric mantle - inverse modeling of alkali-olivine basalts from the big pine volcanic field, California." Contributions to Mineralogy and Petrology **108**(3): 305-317.

Ozawa, K. (2001). "Mass balance equations for open magmatic systems: Trace element behavior and its application to open system melting in the upper mantle." Journal of Geophysical Research: Solid Earth **106**(B7): 13407-13434.

Parker, R. L. (1977). "Understanding inverse theory." Annual Review of Earth and Planetary Sciences **5**: 35.

Qin, Z. (1992). "Disequilibrium partial melting model and its implications for trace element fractionations during mantle melting." Earth and Planetary Science Letters **112**(1): 75-90.

Richter, F. M. (1986). "Simple models for trace element fractionation during melt segregation." Earth and Planetary Science Letters **77**(3–4): 333-344.

Robert, C. and G. Casella (2004). Monte Carlo statistical methods, Springer Science & Business Media.

Roland, E., M. D. Behn and G. Hirth (2010). "Thermal-mechanical behavior of oceanic transform faults: Implications for the spatial distribution of seismicity." Geochemistry, Geophysics, Geosystems **11**(7): n/a-n/a.

Salters, V. J. M. and H. J. B. Dick (2002). "Mineralogy of the mid-ocean-ridge basalt source from neodymium isotopic composition of abyssal peridotites." Nature **418**(6893): 68-72.

Sambridge, M. and K. Mosegaard (2002). "Monte Carlo methods in geophysical inverse problems." Reviews of Geophysics **40**(3): 1009.

Seyler, M., D. Brunelli, M. J. Toplis and C. Mével (2011). "Multiscale chemical heterogeneities beneath the eastern Southwest Indian Ridge (52°E–68°E): Trace element compositions of along-axis dredged peridotites." Geochemistry, Geophysics, Geosystems **12**(9).

Shaw, D. M. (2000). "Continuous (dynamic) melting theory revisited." The Canadian Mineralogist **38**(5): 1041-1063.

Shu, C.-W. and S. Osher (1988). "Efficient implementation of essentially non-oscillatory shock-capturing schemes." Journal of Computational Physics **77**(2): 439-471.

Spiegelman, M. and P. B. Kelemen (2003). "Extreme chemical variability as a consequence of channelized melt transport." Geochemistry, Geophysics, Geosystems **4**(7): n/a-n/a.

Sun, C. and Y. Liang (2014). "An assessment of subsolidus re-equilibration on REE distribution among mantle minerals olivine, orthopyroxene, clinopyroxene, and garnet in peridotites." Chemical Geology **372**(0): 80-91.

Tainton, K. M. and D. McKenzie (1994). "The generation of kimberlites, lamproites, and their source rocks." Journal of Petrology **35**(3): 787-817.

Tarantola, A. (2005). Inverse problem theory and methods for model parameter estimation. Philadelphia, PA, Society for Industrial and Applied Mathematics.

Turcotte, D. L. and G. Schubert (2002). Geodynamics, Cambridge University Press.

Van Orman, J. A., T. L. Grove and N. Shimizu (2002). "Diffusive fractionation of trace elements during production and transport of melt in Earth's upper mantle." Earth and Planetary Science Letters **198**(1): 93-112.

Warren, J. M. (2007). Geochemical and rheological constraints on the dynamics of the oceanic upper mantle, Massachusetts Institute of Technology.

Warren, J. M. (2016). "Global variations in abyssal peridotite compositions." Lithos **248–251**: 193-219.

Watson, S. (1993). "Rare earth element inversions and percolation models for Hawaii." Journal of Petrology **34**(4): 763-783.

Watson, S. and D. McKenzie (1991). "Melt generation by plumes - A Study of hawaiian volcanism." Journal of Petrology **32**(3): 501-537.

White, R. S., D. McKenzie and R. K. O'Nions (1992). "Oceanic crustal thickness from seismic measurements and rare earth element inversions." Journal of Geophysical Research: Solid Earth **97**(B13): 19683-19715.

Workman, R. K. and S. R. Hart (2005). "Major and trace element composition of the depleted MORB mantle (DMM)." Earth and Planetary Science Letters **231**(1–2): 53-72.

Zou, H. (1998). "Trace element fractionation during modal and nonmodal dynamic melting and open-system melting: a mathematical treatment." Geochimica et Cosmochimica Acta **62**(11): 1937-1945.

Zou, H. (2007). Quantitative geochemistry, World Scientific.

Appendix

1. Procedure for finding σ_- and σ_+ for parameter F from a set of accepted models

To determine σ_- and σ_+ for parameter F from a set of accepted models, we use the following steps outlined below. First, we sort $\mathbf{m_i}$ according to F and obtain a set ($\mathbf{m_{F0}}$, $\mathbf{m_{F1}}$,…, $\mathbf{m_{Fn}}$) which has ascending F (F_{F0}, F_{F1},…, F_{FN}). Second, we make the histogram of F with 100 bins. The center of each bin consists of (F_{b1}, F_{b2},…, F_{b100}). Third, we approximate the histogram of F with a smooth marginal probability density of F, $p_F(F)$. Fourth, we sort (F_{b1}, F_{b2},…, F_{b100}) with ascending order of $p_F(F)$ and obtain a set (F_{bp1}, F_{bp2},…, F_{bp100}). Fifth, we find the smallest index i such that,

$$\sum_{j=i}^{100} p_F\left(F_{bpj}\right) \le 68\% \cdot \sum_{j=1}^{100} p_F\left(F_{bpj}\right). \tag{A1-1}$$

The minimum and maximum among (F_{bpi}, F_{bp2},…, F_{bp100}) are F_{lower} and F_{upper} respectively. Finally, we obtain σ_- and σ_+ for parameter F as:

$$\sigma_- = F_{MP} - F_{lower} \text{ or } 0 \text{ if } F_{MP} < F_{lower}, \tag{A1-2}$$

$$\sigma_+ = F_{upper} - F_{MP} \text{ or } 0 \text{ if } F_{MP} > F_{upper}, \tag{A1-3}$$

where F_{MP} is the F of the most probable model $\mathbf{m_{MP}}$ among ($\mathbf{m_0}$, $\mathbf{m_1}$,…, $\mathbf{m_n}$).

2. Derivation of the disequilibrium dynamic melting model

We consider concurrent melting and melt segregation in a steady-state, upwelling double porosity mantle column in which part of the melt generated in the matrix (lherzolite/harzburgite) is extracted or sucked into nearby melt channels (high-porosity dunites or melt-filled dikes). Our primary interest in the present study is the concentration

of a trace element in the partial melt and constituent residual minerals in the matrix. In one-dimension, the mass conservation equations governing spatial variations of the melting column and concentrations of a trace element in the matrix melt and minerals are given by the following set of equations (e.g., McKenzie, 1984; Iwamori, 1993a; Liang and Parmentier, 2010):

$$\frac{d\left(\rho_s\left(1-\phi\right)w_j V_s\right)}{dz} = -\Gamma p_j, \tag{A1-4}$$

$$\frac{d\left(\rho_f \phi V_f\right)}{dz} = \Gamma\left(1-S\right), \tag{A1-5}$$

$$\frac{d\left(Flux_{ch}\right)}{dz} = \Gamma S, \tag{A1-6}$$

$$\frac{d\left(\rho_s\left(1-\phi\right)w_j V_s C_s^j\right)}{dz} = -\Gamma p_j C_s^j - \rho_s\left(1-\phi\right)w_j R_j\left(C_s^j - k_j C_f\right), \tag{A1-7}$$

$$\frac{d\left(\rho_f \phi V_f C_f\right)}{dz} = \sum_j \Gamma p_j C_s^j - \Gamma R C_f + \rho_s\left(1-\phi\right)\sum_j w_j R\left(C_s^j - k_j C_f\right), \tag{A1-8}$$

$$\frac{dF}{dz} = \frac{\left(1-F\right)\Gamma}{\rho_s\left(1-\phi\right)V_s} \tag{A1-9}$$

where ρ_s and ρ_f are densities of the solid and the melt, respectively; ϕ is the porosity of the residual solid matrix; w_j is the mass fraction of mineral j in the matrix (j = olivine, clinopyroxene, orthopyroxene, and spinel, respectively); V_s is the upwelling velocity of the solid; V_f is the velocity of the melt; z is the height above initial melting depth; Γ is the melting rate of the bulk solid; p_j is the stoichiometric weight fraction of phase j in the melting reaction; S is the melt suction rate; $Flux_{ch}$ is the melt flux in channel; F is the

degree of melting; C_s^j is the concentration in mineral j; k_j and R_j are the partition coefficient and the exchange rate coefficient for the trace element of interest between mineral j and melt, respectively. The sum of w_j or p_j over j from 1 to 4 is one.

Eqs. (A1-4) and (A1-5) are mass conservations equations for the matrix, while Eq. (A1-6) is the mass conservation equation for the channel melt (McKenzie, 1984; Iwamori, 1993a; Liang and Parmentier, 2010). Eqs. (A1-7) and (A1-8) are mass conservation equations for a trace element in mineral j and interstitial melt in the matrix, accounting for incongruent melting of the matrix (first terms on the RHS of Eqs. (A1-7) and (A1-8), and diffusive exchange among the minerals and the melt (last terms on the RHS of Eqs. A1-7 and A1-8). Following earlier work (Glueckauf, 1955; McKenzie, 1984; Navon and Stolper, 1987; Liang and Liu, 2016), here we use linear kinetics to approximate steady-state diffusive exchange between mineral j and its surrounding melt. For simplicity, we neglect diffusion and dispersion in the melt (see Liang, 2008 for a discussion of this assumption). Finally, Eq. (A1-9) describe variations of the degree of melting of the solid matrix that upwells along the melting column (Liang and Peng, 2010).

The bulk solid concentration and the bulk partition coefficient are given by the usual expressions,

$$C_s = \sum_j x_j C_s^j, \qquad \text{(A1-10)}$$
$$k = \sum_j w_j k_j,$$

whereas the bulk solid concentration participated in melting reaction is calculated according to reaction coefficients of non-modal melting,

$$C_s^p = \sum_j p_j C_s^j. \qquad \text{(A1-11)}$$

Figure Captions

Figure 1-1 Comparison between observed (circles) and model derived (lines) REE + Y patterns in residual clinopyroxene in spinel lherzolite. The observed data are from an abyssal peridotite from the Central Indian Ridge (Hellebrand et al., 2002, their sample ANTP126-2). Individual lines are calculated using the disequilibrium fractional melting model (Eq. 1-2) through MCMC simulations. Concentrations in clinopyroxene are normalized by CI chondrite (Anders and Grevesse, 1989).

Figure 1-2 Histograms displaying MCMC simulation results of sample ANTP126-2 for the degree of melting (F, panel a) and the disequilibrium parameter for La in clinopyroxene (ε, panel b) obtained using the disequilibrium fractional melting model (Eq. 1-6). Black solid line: most probable model. Black dashed line: upper/lower σ about the most probable model. Red curves correspond to the normal distribution parameterized by nonlinear least squares inversion. Subscripts 'MP' and 'LS' refer to most probable model parameter from MCMC simulations and results of nonlinear least squares method.

Figure 1-3 Plot of accepted model parameters for sample ANTP126-2 in F-ε plane. Red error bars correspond to the most probable model with upper/lower σ. Blue error bars correspond to mean ± σ. Also shown are results from nonlinear least squares inversion (ellipses). The larger ellipse corresponds to 95% confidence level, while the smaller ellipse corresponds to 68.2% confidence level. The 68.2% confidence eclipse underestimates the uncertainty of ε and F.

Figure 1-4 Comparison of melting parameters derived through MCMC simulations and nonlinear least squares inversion of REE + Y in residual clinopyroxenes in abyssal peridotites from the Central Indian Ridge (data from Hellebrand et al., 2002). (a) Degree of melting (F). (b) Disequilibrium parameter for La in clinopyroxene. Subscripts 'MP' and 'LS' refer to most probable model parameter from MCMC simulations and results of nonlinear least squares method. See text for discussion.

Figure 1-5 Comparison between observed (circles) and model derived REE + Y patterns in clinopyroxene in abyssal peridotites. Three samples from the Central Indian Ridge (Hellebrand et al., 2002) are shown as examples of disequilibrium fractional melting (a), disequilibrium dynamic melting (b), and equilibrium dynamic melting (c). Individual curves are calculated using the disequilibrium dynamic melting model (Eqs. 1-8 and 1-9) through MCMC simulations. The most probable model parameters are listed under the sample name.

Figure 1-6 Histograms displaying MCMC simulation results of sample ANTP126-2 for the degree of melting (F, panel a), the disequilibrium parameter for La in clinopyroxene (ε, panel b), and the mass flux ratio or fraction of melt retained (α, panel c) obtained using the disequilibrium dynamic melting model (Eqs. 1-8 and 1-9). Solid line: most probable model. Dashed line: uncertainty interval about the most probable model. Notice the most probable model parameter may lie on the bound of uncertainty interval.

Figure 1-7 Plots of accepted model parameters for three samples in F-ε plane (a, d, g), ε-α plane (b, e, h), and F-ε-α space (c, f, i). Model parameters are derived from MCMC simulations using the disequilibrium dynamic melting model (Eqs. 1-8 and 1-9).

Red error bars correspond to the maximum probability model with upper/lower σ. Blue error bars correspond to the symmetric format of mean ± σ. In the 3D space, the gold shade is the range of 10% best models.

Figure 1-8 Comparison of the most probable melting parameters (F and ε_{La}) derived from MCMC simulations using the disequilibrium perfect fractional melting model (Eq. 1-6) and the disequilibrium dynamic melting model (Eqs. 1-8 and 1-9) for samples from the Central Indian Ridge in the two case studies discussed in text. Results for a given sample from the two case studies are connected by a dashed line. The disequilibrium fractional melting model in case one overestimates ε when F is smaller than 13%.

Figure 1-9 Plots of inverted F and the disequilibrium parameter ε for samples from selected ridges (see Table 1 for data source). The arrows and magenta squares in (a) suggest a model closer to the main trend can explain these two samples. The REE pattern derived from the on-trend model for can be found in the supplementary Figure S2. Samples from SWIR and CIR show robust positive trends. Number of samples from each ridge system (N) is given in the figure legend.

Figure 1-10 Variations of the calculated disequilibrium parameter ε for La as a function of F along adiabat melting paths for three choices of potential temperatures (curves). Calculation of ε is detailed in section 5.1. In general, ε increases with initial grain size and decreases with potential temperature. Dashed lines are arithmetic average of ε from the onset of melting to F. To compare inverted results with calculation of ε, we use spreading rate to correct the most probable ε. Number of samples from each ridge system (N) is given in the figure legend.

Figure 1-11 Plots of inverted degree of melting F (panel a) and normalized disequilibrium parameters ε_{La} (V_0 / V_{sp}) /F (b) as a function of spreading rate. ε_{La} increases with grain size and decreases with potential temperature (marked by arrows in panel b). The magenta bar represents the average over the interval of spreading rate.

Figure 1-12 Variations of ε along the Vema Lithospheric Section at Mid-Atlantic Ridge (Brunelli et al., 2006). The gray arrow shows a trend of increasing ε toward east side of VLS.

Figure 1-13 The grainsize distribution of samples from VLS (a, c, e) and Marie Celeste TF at CIR (b, d, f) given potential temperature of 1280°C, 1310°C, or 1340°C. Above each plot is the mean and the standard deviation of the mean acquired by bootstrap resampling. Blue and red curves are fits of normal distribution.

Figure 1-14 Plot of ε against $^{143}Nd/^{144}Nd$ for 19 samples from the Mid-Atlantic ridge (VLS and KSP) and the Southwest Indian Ridge (SWIR) shows no correlation between source heterogeneity and ε.

Figures

Figure 1-1 Comparison between observed (circles) and model derived (lines) REE + Y patterns in residual clinopyroxene in spinel lherzolite.

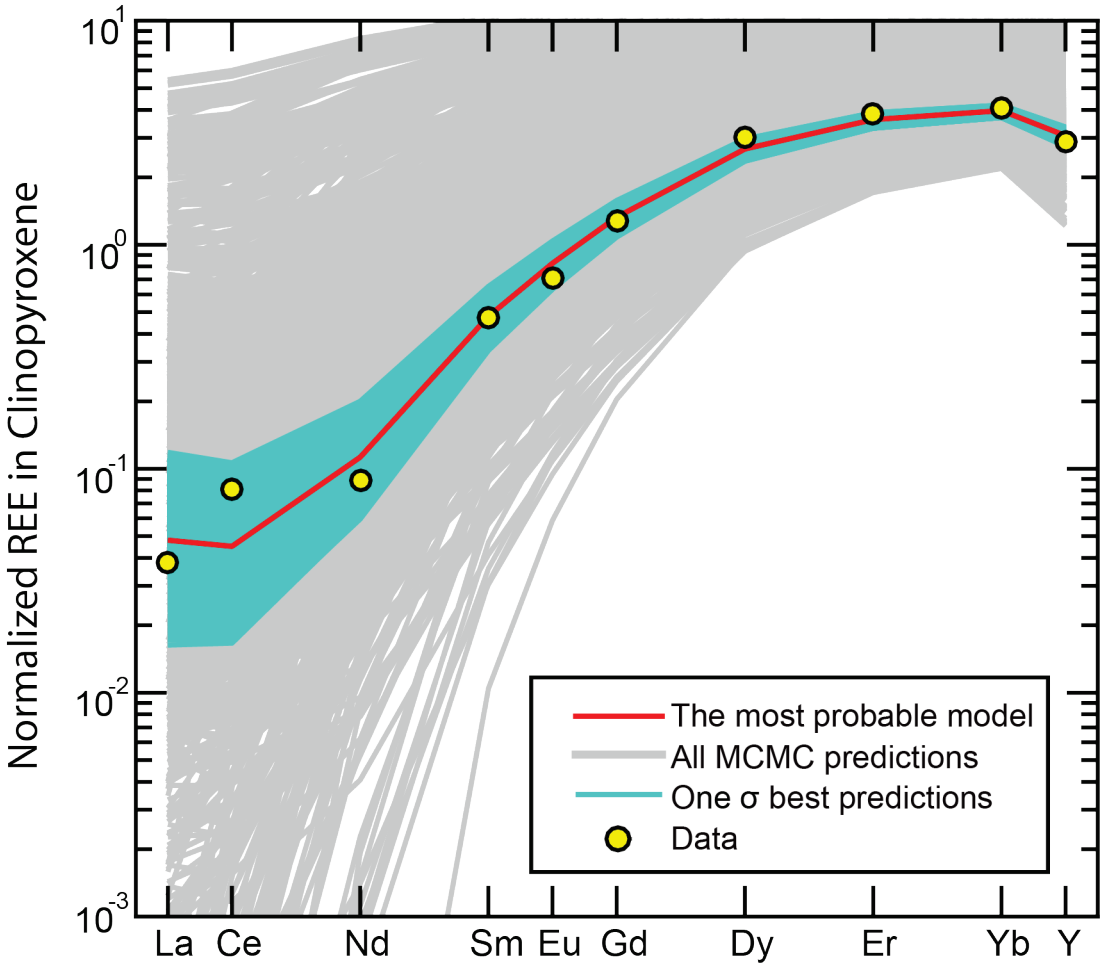

Figure 1-2 Histograms displaying MCMC simulation results of sample ANTP126-2 for F and ε obtained using the disequilibrium fractional melting model

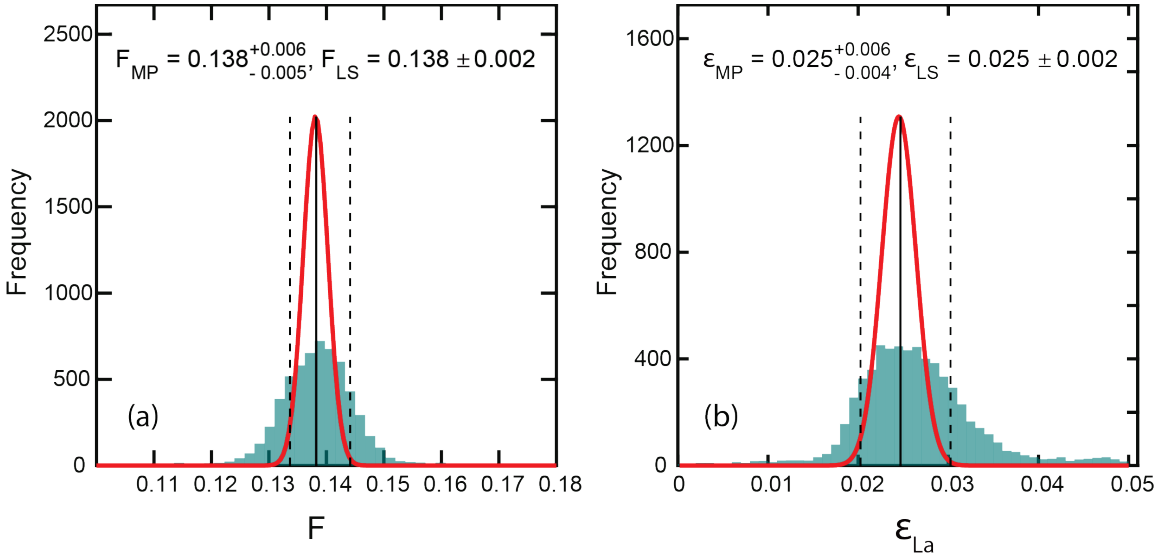

Figure 1-3 Plot of accepted model parameters for sample ANTP126-2 in F-ε plane

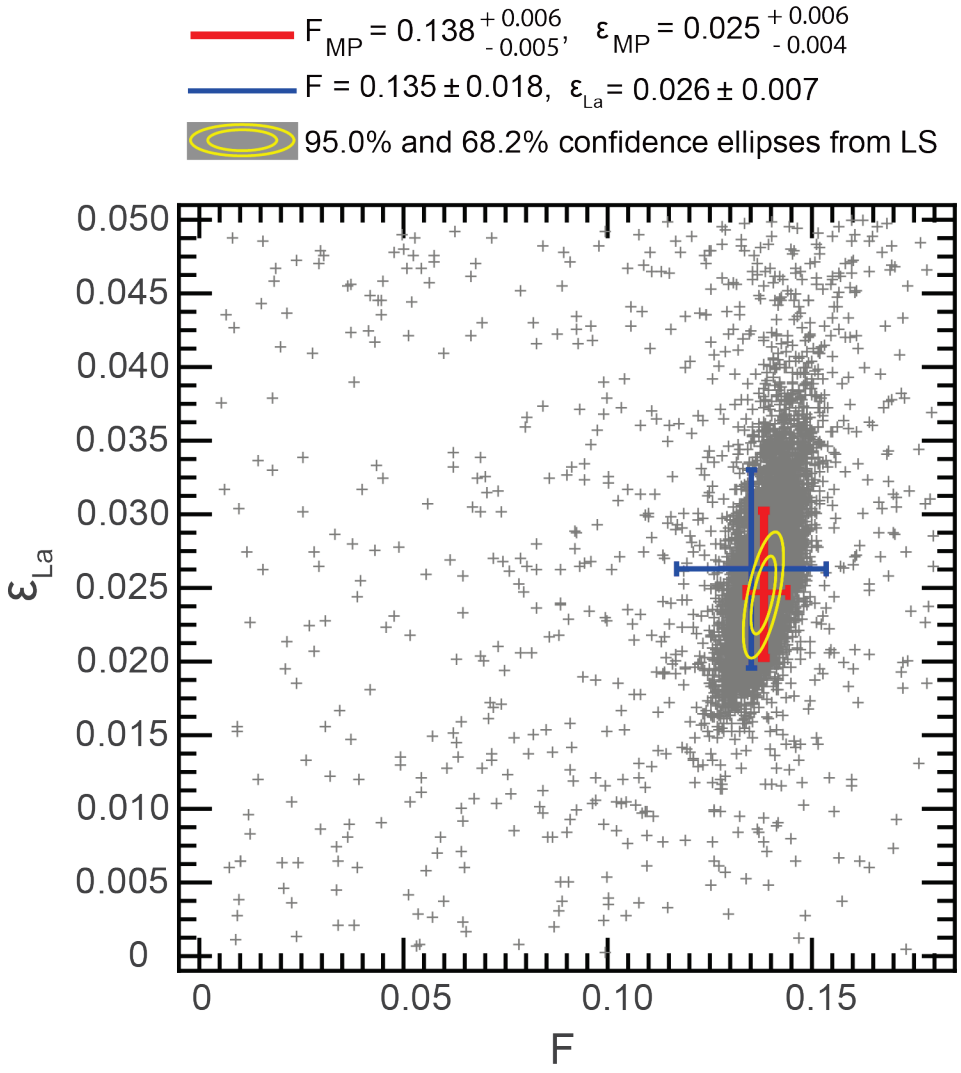

Figure 1-4 Comparison of melting parameters derived through MCMC simulations and nonlinear least squares inversion of REE + Y in residual clinopyroxenes in abyssal peridotites from the Central Indian Ridge

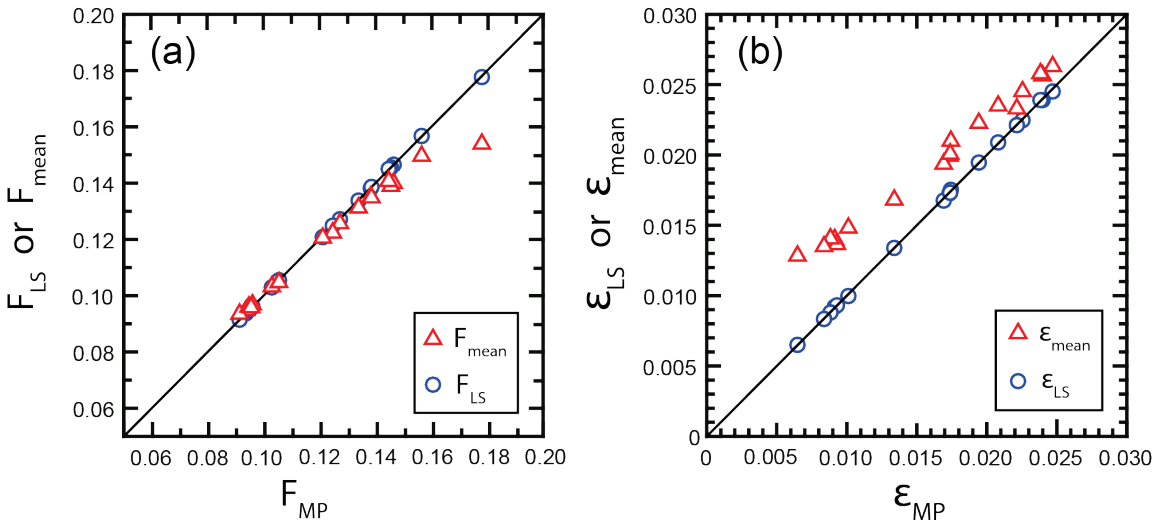

Figure 1-5 Comparison between observed (circles) and model derived REE + Y patterns in clinopyroxene in abyssal peridotites

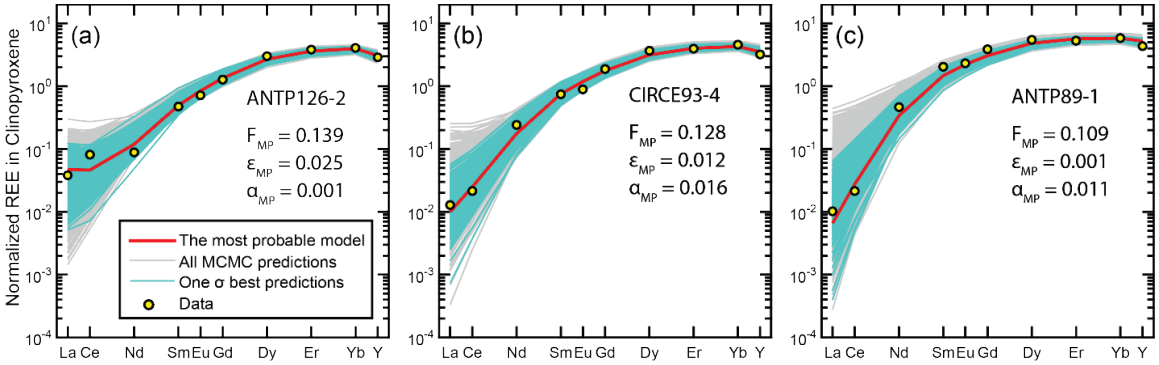

Figure 1-6 Histograms displaying MCMC simulation results of sample ANTP126-2 for F, ε, and α obtained using the disequilibrium dynamic melting model

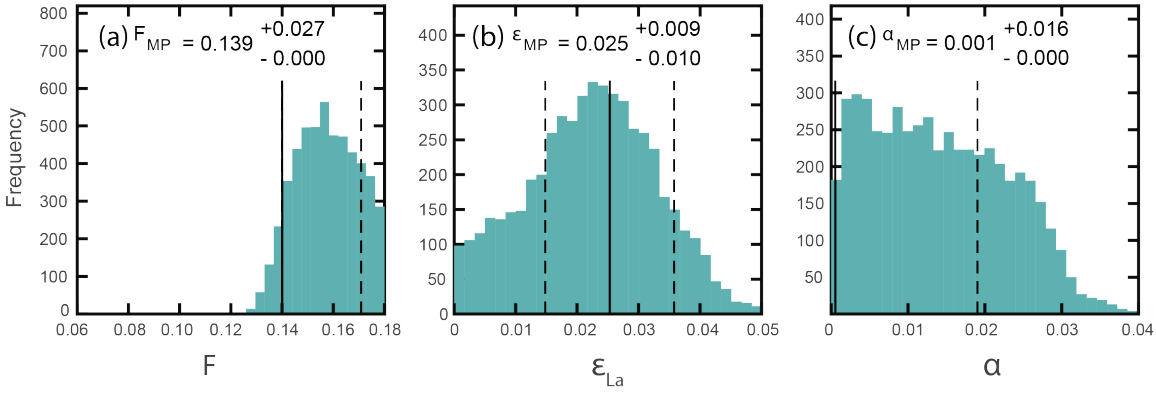

Figure 1-7 Plots of accepted model parameters in parameter spaceS for three samples

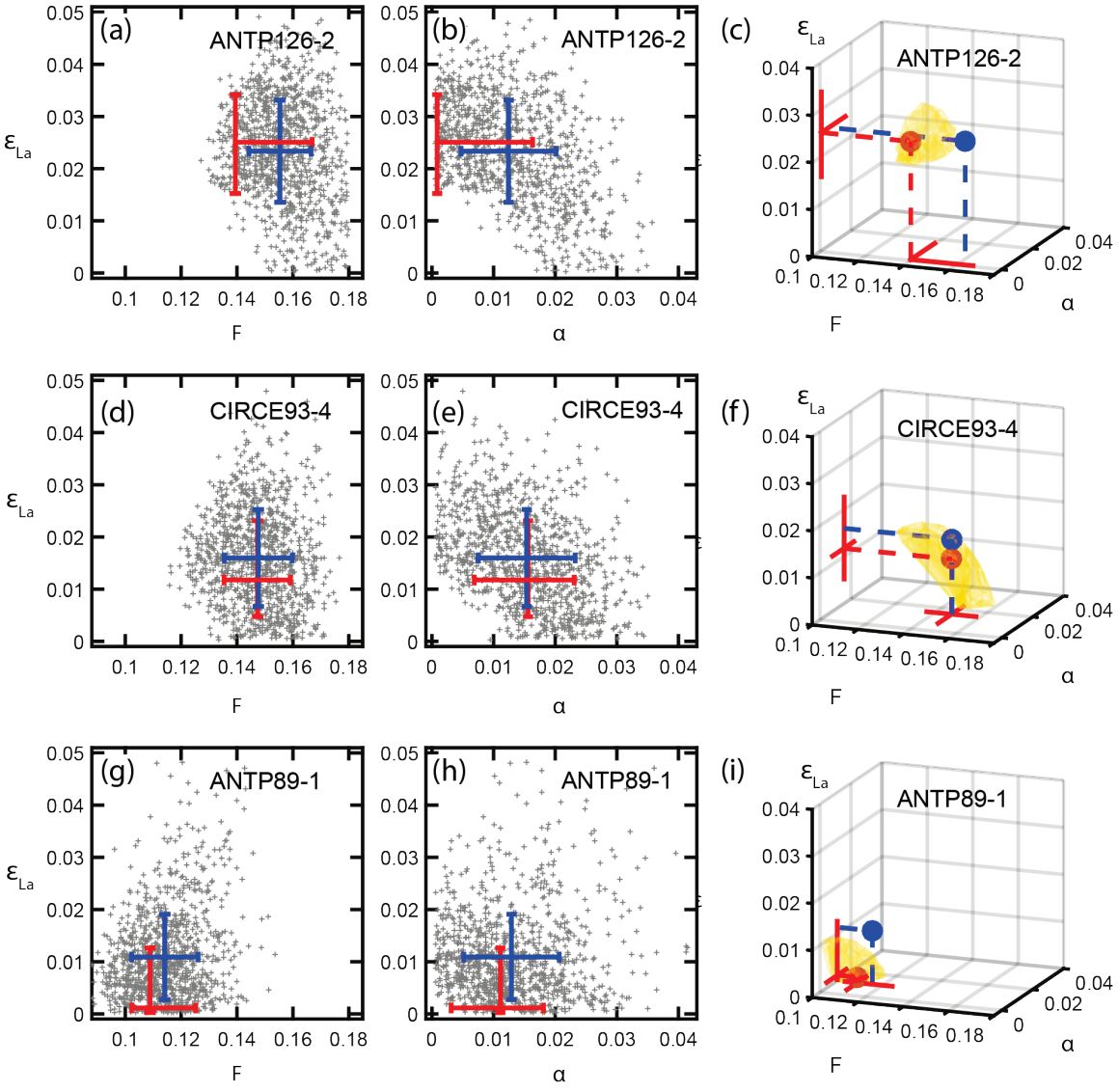

Figure 1-8 Comparison of the most probable melting parameters (F and ε_{La}) derived from MCMC simulations using the disequilibrium perfect fractional melting model and the disequilibrium dynamic melting model

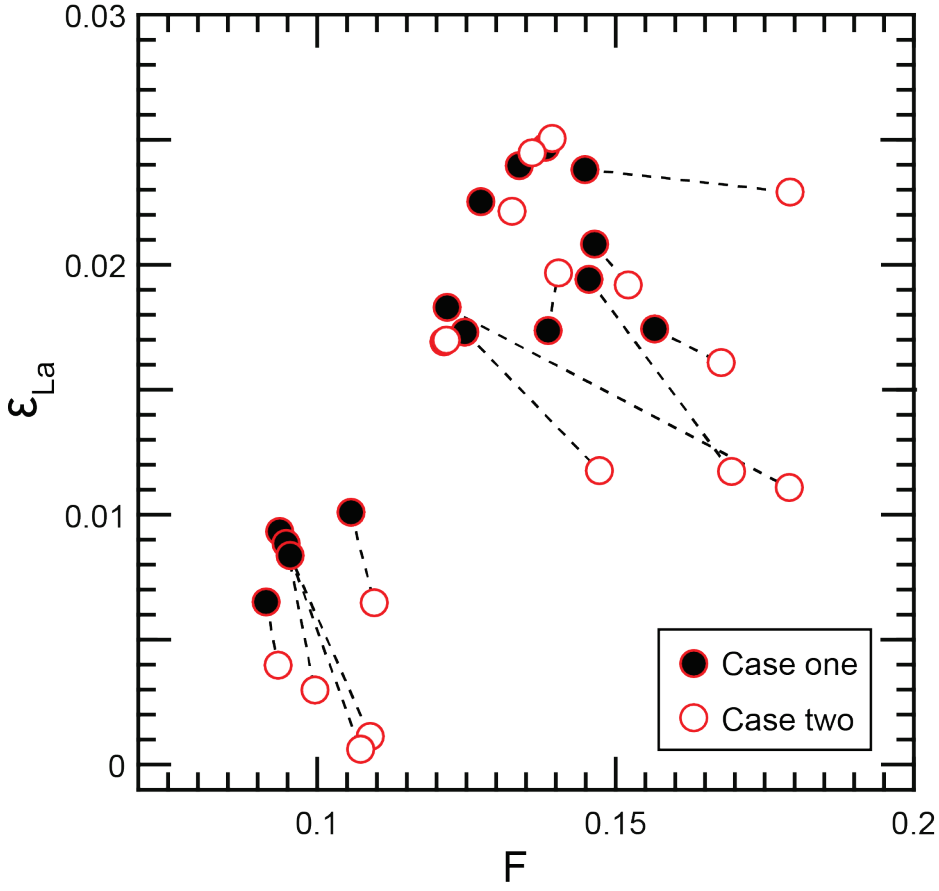

Figure 1-9 Plots of inverted F and the disequilibrium parameter ε for samples from selected ridges

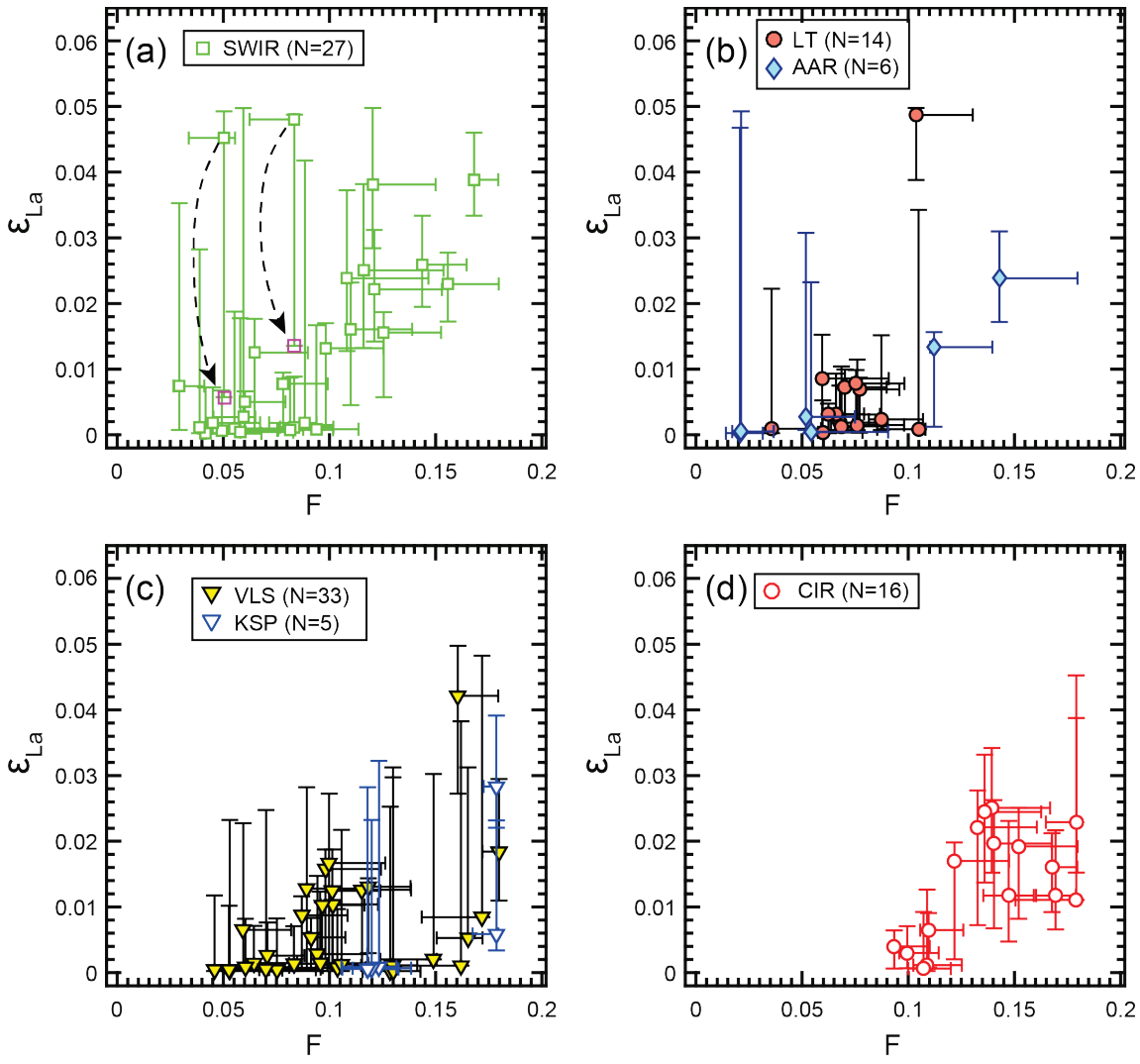

Figure 1-10 Variations of the calculated disequilibrium parameter ε for La as a function of F along adiabat melting paths for three choices of potential temperatures

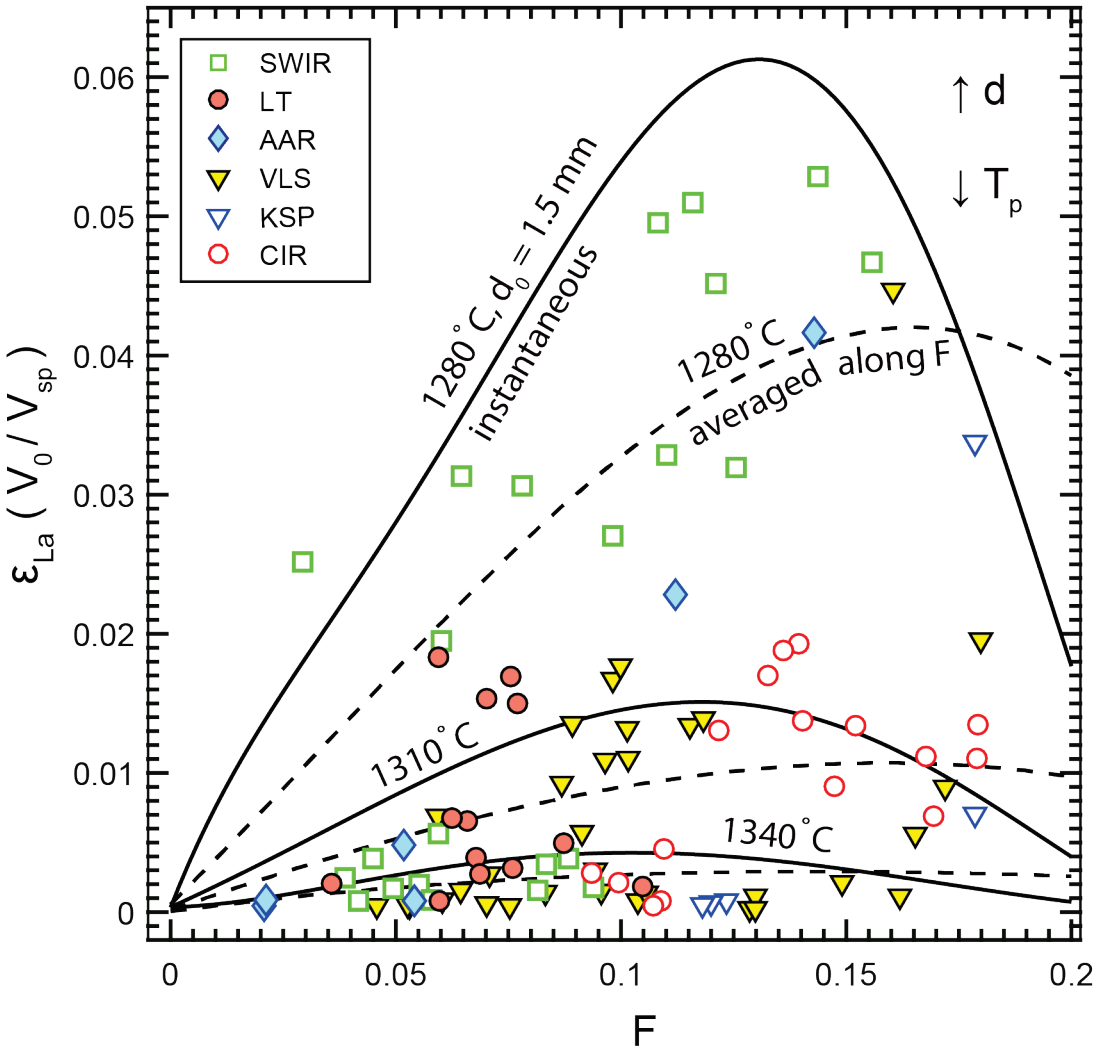

Figure 1-11 Plots of inverted degree of melting and normalized disequilibrium parameters as a function of spreading rate

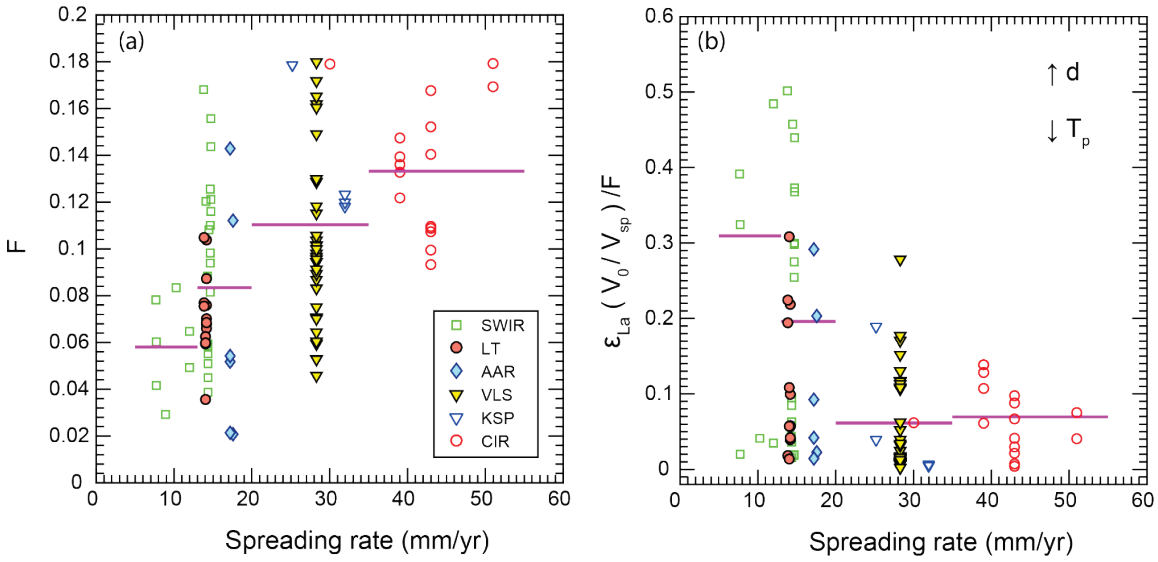

Figure 1-12 Variations of ε along the Vema Lithospheric Section at Mid-Atlantic Ridge

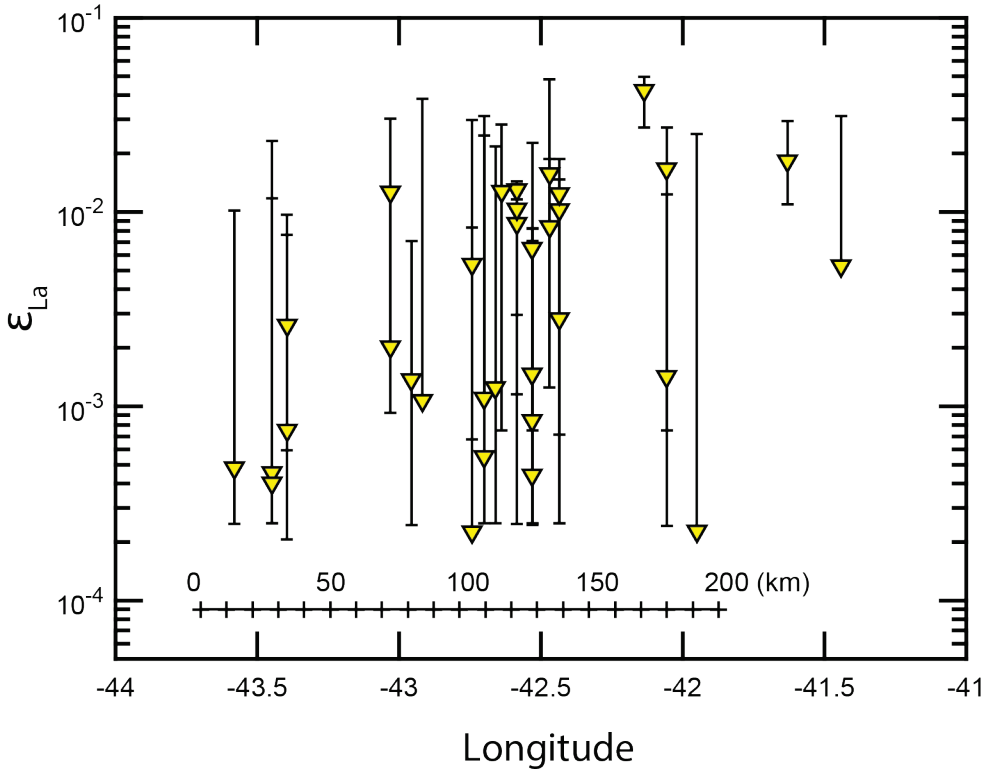

Figure 1-13 The grainsize distribution of samples from VLS and Marie Celeste TF at CIR given potential temperature

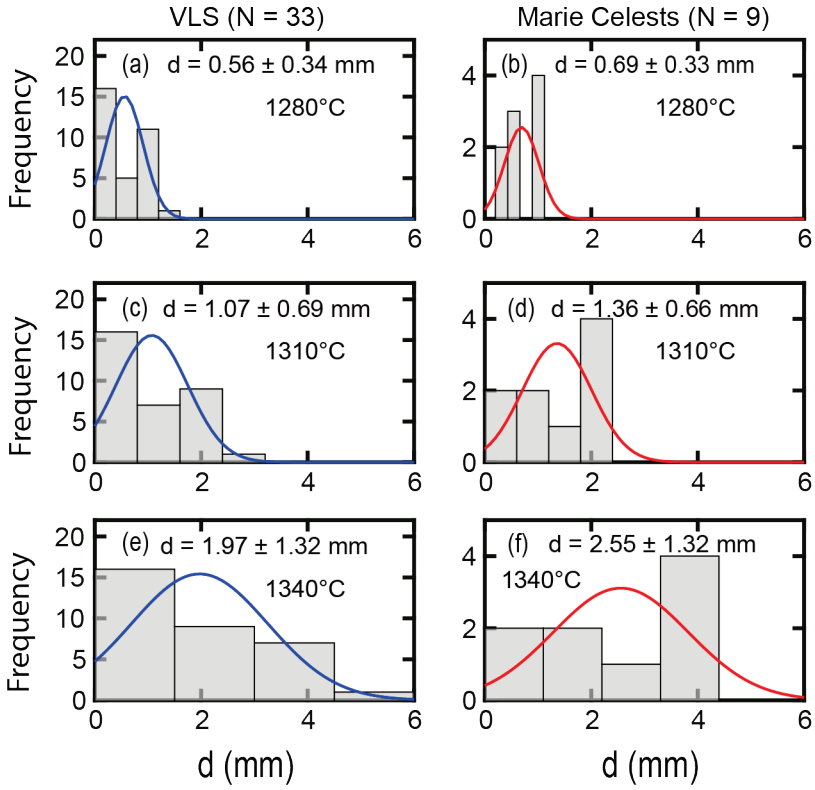

Figure 1-14 Plot of ε against $^{143}Nd/^{144}Nd$ for 19 samples from the Mid-Atlantic ridge and the Southwest Indian Ridge

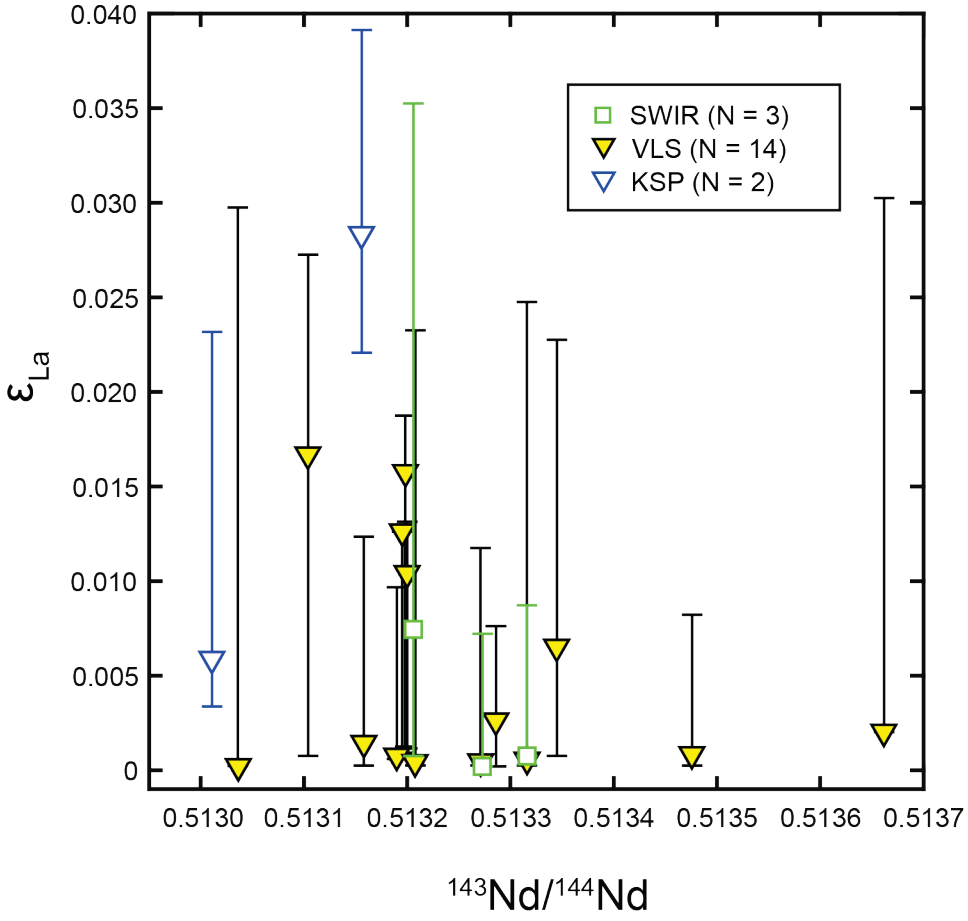

Tables

Table 1-1 List of key symbols

Symbol	Description
$\mathbf{C}$, C_{i}	$\mathbf{C}$ is an array of observed multiple trace element concentrations, C_i
C_{f}	Concentration of a trace element in the instantaneous melt
C_{s}^{0}	Concentration of the bulk solid at the onset of melting
d	Mineral grain size
d_0	Reference grain size, 1.5mm
D	Diffusivity of the element of interest in the mineral
D_{La}, D_{REE}	Diffusivity of La or REE in the mineral
F	Degree of melting experienced by the bulk solid
$F_{LS} \pm \sigma_{LS}$	The estimate of F and uncertainty obtained using the nonlinear least squares method
$F_{MP-\sigma_-}^{+\sigma_+}$	The most probable estimate of F_{MP} and asymmetric uncertainties σ_+ and σ_-
$F_{mean} \pm \sigma$	The average and standard deviation of all accepted F from MCMC simulations
f_p	Degree of melting at the onset of dynamic melting, defined in Eq. (1-15)
k, k_{cpx}	Bulk solid-melt or cpx-melt partition coefficient
k_0	Bulk solid-melt partition coefficient at the onset of melting
k_p	Bulk solid-melt partition coefficient for the melting reaction
$L(\mathbf{C}\|\mathbf{m})$	Likelihood of observing $\mathbf{C}$ given the model, $\mathbf{m}$. Defined in Eq. (1-3)
$\mathbf{m}$	A vector of model parameters
$p(\mathbf{m}\|\mathbf{C})$	Posterior probability of a model, $\mathbf{m}$, given observation $\mathbf{C}$, defined in Eq. (1-1)
R	The mineral-melt exchange rate constant, defined in Eq. (1-7)
T_p	Potential temperature
V_f, V_s	Velocity of the melt or the solid
V_{sp}	Spreading rate
V_0	Reference spreading rate, 30 mm/yr
z	Vertical coordinate, measured from the base of the melting column
α	The ratio between the melt and solid mass or mass flux ratio, Eq. (1-11)

$\theta(\mathbf{m})$	The data-independent prior probability of the model, $\mathbf{m}$
ε	Element specific disequilibrium parameter, Eq. 5 and Eq. 16
$\varepsilon_{La}, \varepsilon_{REE}$	Disequilibrium parameter for La or REE
ε_{Tp}^{0}	ε averaged along a melting path with reference grain size and spreading rate
ϕ_f	Porosity
Γ	Melting rate of the bulk solid
ρ_f, ρ_s	Density of the melt or the solid
$\chi^2(\mathbf{C}, \mathbf{m})$	Chi-square of observation $\mathbf{C}$ given the model, $\mathbf{m}$

Table 1-2 List of sample locations and sources

Sample location	Number of samples	Data sources
Southwest Indian Ridge (SWIR)	35	Salters and Dick (2002); Warren (2007); Seyler et al. (2011); Mallick et al. (2014)
Lena Trough (LT) at Arctic Ridge	25	Hellebrand and Snow (2003); Lassiter et al. (2014)
American-Antarctic Ridge (AAR)	9	Johnson et al. (1990)
Vema Lithospheric Section (VLS) at Mid-Atlantic Ridge	35	Brunelli et al. (2006)
Kane FZ & St. Paul FZ (KSP) at Mid-Atlantic Ridge	9	Brunelli and Seyler (2010); Mallick et al. (2014)
Central Indian Ridge (CIR)	22	Hellebrand et al. (2002)

Supplementary Materials

Figure S1-1 Results from case study one for 22 samples from CIR. Download link:

https://ars.els-cdn.com/content/image/1-s2.0-S0016703717300029-mmc2.pdf

Figure S1-2 Results using the disequilibrium dynamic melting model for 135 samples from selected ridges. Download link:

https://ars.els-cdn.com/content/image/1-s2.0-S0016703717300029-mmc3.pdf

Table S1-1 List of the most probable melting parameters (F, ε, α) for all 135 samples in case study two. Down load link:

https://ars.els-cdn.com/content/image/1-s2.0-S0016703717300029-mmc1.xlsx

CHAPTER 2

The prevalence of kilometer-scale heterogeneity in the source region of MORB mantle

Boda Liu and Yan Liang

Department of Earth, Environmental and Planetary Sciences

Brown University, Providence, Rhode Island 02912

Published in Science Advances **3**(11), 2017

Abstract

The source regions of mid-ocean ridge basalts (MORB) are heterogeneous, consisting of chemically and lithologically distinct domains of variable size. Partial melting of such heterogeneous mantle sources gives rise to diverse isotopic compositions of MORB and abyssal peridotites. Variations in radiogenic isotope ratios in MORB are attributed to mixing of melts derived from enriched and depleted mantle components. But melt mixing alone cannot fully account for the difference between the average $^{143}Nd/^{144}Nd$ in abyssal peridotites and their spatially associated MORB. Here we show that the more depleted Nd isotope composition in abyssal peridotites is a natural consequence of melt-migration induced mixing or smearing in the melting column. Sub-kilometer scale enriched mantle components or heterogeneities are significantly damped or homogenized in both the residue and erupted melt during their transit through the melting region. Heterogeneities having larger size and higher incompatible trace element abundance are more resistive to the mixing processes. The size-sensitive mixing depends on a parameter called the enrichment strength which is the product of the heterogeneity size and the ratio between incompatible trace element abundance in the enriched and depleted mantle sources. Observed Nd-Hf isotope variations in MORB and abyssal peridotites can be reproduced if the enrichment strength is 20-60 km. These heterogeneities could be on the kilometer scale and have similar isotope ratios to but less incompatible trace element abundances than recycled oceanic crust.

1. Introduction

Isotopic compositions of basalts and residual peridotites have been widely used to fingerprinting mantle source compositions (Hofmann, 2003). Since melting cannot fractionate isotopes of heavy elements (e.g., $^{143}Nd/^{144}Nd$ or $^{176}Hf/^{177}Hf$), the extracted instantaneous melt would have the same isotopic composition as its residue (Ito and Mahoney, 2005; Stracke and Bourdon, 2009). An important observation is that the average $^{143}Nd/^{144}Nd$ in abyssal peridotites is higher than their spatially associated MORB (referred to as the "MORB-AP offset" hereafter, Fig. 2-1a). In individual locations where abyssal peridotites are sampled, such offset also exits (Fig. 2S-1). The MORB-AP offset becomes more noticeable if refertilized samples are excluded (Fig. 2-1a). The offset of the mean $^{143}Nd/^{144}Nd$ in all abyssal peridotites relative to MORB has been attributed to the preferential melting of isotopically enriched lithology (Salters and Dick, 2002; Liu et al., 2008) or higher Nd abundance in isotopically enriched melt (Warren et al., 2009). In the former case, radiogenic isotope ratio would correlate with the abundance of incompatible trace element in the residue. However, existing data does not demonstrate such a correlation at global or local scale (Fig. S2-2). Instead, the lack of correlation between incompatible trace elements, such Yb and $^{143}Nd/^{144}Nd$ in residual clinopyroxene, suggests that an isotopically distinct source could have experienced variable degrees of melting (Fig. S2-2). In the latter case, residues inherit both the isotope ratio of enriched and depleted sources while extracted melts are mixtures of the two sources. Since melts derived from the enriched lithology generally have higher incompatible trace element abundance, the isotope signature of the melt would be dominated by the enriched component. Although mixing has been widely used to explain variations in radiogenic isotope ratios observed in

MORB and abyssal peridotites (Zindler and Hart, 1986; Carlson, 1995; Hofmann, 1997; Hofmann, 2003), it is difficult to distinguish if the mixing happens in the mantle source (e.g., a mixed mantle source) before partial melting or during melt extraction and aggregation.

To distinguish where and when mixing takes place during melting and melt migration in the mantle, one should consider the physical size of mantle source heterogeneity and the rate of chemical exchange between the partial melt and its coexisting residue. During decompression melting of a spatially heterogeneous mantle, melts generated in the lower part of the melting column percolate upward and may encounter a residue of different isotopic composition. Chemical exchange then takes place, which tends to restore chemical and isotopic equilibrium between the melt and the residual solid (Fig. 2-2). Recent studies have suggested that small extent of chemical disequilibrium should be present during decompression melting beneath mid-ocean ridge spreading centers (Qin, 1992; Iwamori, 1993; Van Orman et al., 2002; Liang and Liu, 2016; Liu and Liang, 2017), as the rates of Nd and Hf diffusion in pyroxene are relatively slow compared to the rate of melting (Van Orman et al., 2001; Bloch and Ganguly, 2014). The effective percolation velocity of a trace element in the partially molten mantle depends on its partition coefficient(McKenzie, 1984; Navon and Stolper, 1987). Chromatographic fractionation during melt percolation in the mantle can result in decoupling of Sr, Nd, and Hf isotope ratios in residual peridotites when there are spatial variations in these trace elements and isotopes in the mantle source(Navon and Stolper, 1987). The extent of fractionation depends on the degree of chemical disequilibrium between the percolating melt and residual solid and the size of mantle source heterogeneity.

In this study, we use a simplified double-porosity ridge model to investigate how the size and composition of mantle source heterogeneity affect the variation and correlation of Nd and Hf isotopes in basalts and residual peridotites during decompression melting of a two-component mantle beneath mid-ocean ridge spreading centers (Fig. 2-1b). The enriched component (Chauvel et al., 2008) has distinct isotope signature as well as higher concentrations of Nd and Hf than the depleted component (Salters and Stracke, 2004; Workman and Hart, 2005). We focus on the roles of the size and trace element abundances of heterogeneities under constraints of $^{143}Nd/^{144}Nd$ and $^{176}Hf/^{177}Hf$ systematics in MORB and abyssal peridotites. We are not considering Sr isotope in this study because Sr is less resistive to hydrothermal alteration than Nd and Hf in peridotites (Frisby et al., 2016).

2. Pesudo-2D double porosity model

We will use a pesudo-2D double porosity model to simulate the isotope ratios ($^{143}Nd/^{144}Nd$ and $^{176}Hf/^{177}Hf$) of the residue and the pooled melt. The pesudo-2D ridge model consists of nine melting columns with maximum degree of melting 2%, 4%, …, 18% stacked together as half of the triangular melting region. In each of these melting columns, we model the spatial and temporal variations of $^{143}Nd/^{144}Nd$ and $^{176}Hf/^{177}Hf$ heterogeneity during concurrent melting and melt migration using a 1D disequilibrium double-porosity model which is built on previous studies (Lundstrom, 2000; Liang and Parmentier, 2010; Liu and Liang, 2017). We assume that the physical state of the system is at steady state. Darcy's law constrains the velocity difference between the melt and solid residue. The diffusion of Nd and Hf in clinopyroxene limits the rate of chemical exchange between the matrix melt and the residue (Navon and Stolper, 1987). The time-dependent mass conservation equations for ^{143}Nd, ^{144}Nd, ^{176}Hf, and ^{177}Hf are solved using a Runge-Kutta

Discontinuous Galerkin method (Cockburn and Shu, 1998). The error for an isotope is 10^{-9} ppm (Supplementary Table S2-1). The time-dependent boundary condition has a Gaussian shaped enrichment with a background value of DMM and a peak value of a specific EM. Gaussian peaks of EM signature are placed randomly in the ambient DMM. The composition of DMM varies within extreme values from Salters and Stracke (2004) and Workman and Hart (2005). The isotope ratios of EM are related to the age of recycled oceanic crust (1-3 Ga) and the proportion of sediments in the crust (0-10%). The abundance of trace element in EM is determined by mixing recycled oceanic crust and DMM. The range of trace element abundance in EM is from 3 to 12 times of DMM. The DMM composition is from a bivariate normal distribution within the range of extreme values (Salters and Stracke, 2004; Workman and Hart, 2005). In the ridge model, all residue with degrees of melting between 5% and 18%, equivalent to the degree of melting of abyssal peridotites (Liu and Liang, 2017), are included. Channel melt and matrix melt from all melting columns are assumed to mix instantaneously below the permeability barrier and form the pooled melt. The composition of magma chamber is modeled using pooled melt as input (DePaolo, 1996). See the Appendix for the detailed model setup and the numerical method.

3. Results

3.1. Stretching and smearing isotopic heterogeneity by melt migration

A key result of the present study is that an enriched isotopic signal in the mantle source can be significantly deformed by melt-migration induced stretching and smearing during decompression melting in the mantle. This can be illustrated using a simple 1D double-porosity model that treats the melting column as two overlapping continua

consisting of low-porosity residual peridotites and high-porosity interconnected channels (Kelemen et al., 1997; Lundstrom, 2000; Liang and Parmentier, 2010). It has been suggested that replacive dunites observed in the mantle sections of ophiolites and massif peridotites may serve as high-porosity pathways for efficient melt extraction in the mantle (Kelemen et al., 1997). To model the spatial and temporal evolution of the enriched isotopic signal in the melting column, we use a time-dependent advection-reaction model which includes the effect of slow diffusion in pyroxene to calculate Nd and Hf concentrations and their isotopic ratios in the melts and the solids. To distinguish melts and solids in the two continua, we refer the low-porosity continuum as the matrix and the high-porosity continuum as the channel in the description below. During decompression melting, the porosity and the velocity of the matrix melt increase while the velocity of the matrix solid decreases along the melting column (Fig. S2-3), giving rise to increasing velocity difference between the matrix melt and the matrix solid. Without loss of generality, we consider spatial and temporal variations of two Gaussian-shaped isotopic heterogeneities (4.4 and 1.1 km long) embedded in the background mantle (Fig. 2-2). Nd and Hf abundances in the enriched source are five times more than in the background mantle.

After entering the melting column, the isotope signature in a layer of enriched heterogeneity splits into three distinct signals: one in the slow-moving matrix solid, one in the slightly faster matrix melt (Fig. 2-2), and the third in the much faster channel melt (Supplementary Movie S2-1). As the enriched melt percolates upward, its size as marked by Nd and Hf isotope ratios increases due to the upward acceleration of the matrix melt while its amplitude decreases due to the diffusive exchange between the melt and the residue in the matrix. As the enriched melt percolates upward, it metasomatizes the residue

immediately ahead of the original heterogeneity, increasing the size of the enriched signal in the matrix solid. However, the enriched signal in the residue has larger amplitude and lags behind that in the matrix melt (cf. blue and red curves at 0.65 Myr in Fig. 2-2). Hence the residue could record more extreme enriched isotopic signals and larger isotope ranges than the matrix melt. Larger disequilibrium in Hf isotope between the matrix melt and matrix solid is expected (Fig. 2-2c) because the diffusion of Hf in pyroxene is slower than that of Nd(Van Orman et al., 2001; Bloch and Ganguly, 2014). The Hf isotopic signal in the residue is more resistive to amplitude reduction than Nd. The stretching- and smearing-induced chemical deformation (i.e., shape change) of isotopic heterogeneity in the matrix melt and the residue is cumulative and accelerates upward in melting column (Fig. 2-2 and supplementary Movie S1). This chemical deformation is more effective to disperse smaller heterogeneities than larger ones (Fig. 2-2). Depending on Nd and Hf abundances in their sources, sub-kilometer heterogeneities may not survive their transit through the melting column.

During near fractional melting, most of the melt generated by decompression melting are extracted through high-porosity channels. In contrast to that in the matrix melt, the enriched signal in the channel melt is quickly dispersed throughout the melting column (in less than 0.06 Myr) by the much faster flow of the channel melt (Supplementary Movie S1). Continuous extraction of matrix melts to the channel results in mixing between the depleted matrix melt and the enriched channel melt. The enriched isotope ratio in the channel is therefore gradually diluted upward. It is very difficult to preserve and sample extreme isotope compositions of the channel melt unless the melting column is very short.

Isotopic signals of the channel melt and residual solid, therefore, are decoupled. This has important implications for the observed MORB-AP offset.

3.2. The importance of the size of mantle heterogeneity

To understand the MORB-AP offset, we first examine the effects of the size and composition of mantle heterogeneity on the isotope ratios in the residues and melts using the double-porosity ridge model (Fig. 2-1b). The triangular melting region consists of bundles of vertically upwelling double-porosity melting columns made of a low-porosity matrix and high-porosity channel. Melt generated in the matrix (blue regions in Fig. 2-1b) is extracted into nearby channels (green) and percolates upward until diverted and focused to the ridge axis along the base of the lithosphere where conductive cooling produces a permeability barrier (Sparks and Parmentier, 1991; Hebert and Montési, 2010). The channel melt and the remaining matrix melt are collected below the permeability barrier where lateral melt transport and extensive mixing of melt take place (Sparks and Parmentier, 1991). Melts derived from different melting columns are assumed to be well mixed to form pooled melt. The pooled melt is further mixed in a crustal magma chamber before eruption. The volume of the magma chamber is 1 km^2 per unit length of the ridge axis, which is on the upper end of geophysical observations(Sinton and Detrick, 1992).

Fig. 2-3 compares four cases of melting a two-component mantle that consists of variable proportion of depleted MORB mantle (DMM) and enriched mantle (EM). The isotopic ranges (Salters and Stracke, 2004; Chauvel et al., 2008) of EM and DMM are the same in the four cases. In each case, enriched heterogeneities of a specific size (2.2 or 8.9 km) are embedded randomly in the background DMM. The trace element abundance of EM is not well constraint. Here we consider two cases: one is 3 times and the other is 12

times that of DMM (Salters and Stracke, 2004). This enrichment factor is designated as "EMX" hereafter. The proportion of EM is adjusted so that the concentration-averaged isotope ratio of the source in each case fits the average of global MORB data. The concentration-averaged $^{143}Nd/^{144}Nd$ in the source, for example, is the total mass of ^{143}Nd in the source divided by the total mass of ^{144}Nd in the source. The calculated proportion of EM decreases from 11% to 3% as EMX increases from 3 to 12.

As demonstrated in the preceding section, melt-migration induced chemical deformation of a heterogeneous mantle source will produce a range of isotope ratios in the residue. If the size of heterogeneity and the enrichment factor are large (e.g., 8.9 km and EMX = 12, Fig. 2-3d), the residue presents a wide range of isotope ratios in between DMM and EM in the source. The residue has little modification of the isotopic composition compared to the source. Since DMM has more than 96% volume fraction in the source, the most common isotope signature of the residue is that of DMM. If the size of heterogeneity and the enrichment factor are small (e.g., 2.2 km and EMX = 3, Fig. 2-3a), the $^{143}Nd/^{144}Nd$ of residue no longer resembles the source. Melt migration induced smearing or mixing has produced a significant amount of residue with intermediate $^{143}Nd/^{144}Nd$ which converges to the concentration-averaged value of the source. Increasing Nd abundance in EM makes the enriched source more resistive to mixing and thus favors the preservation of original mantle source $^{143}Nd/^{144}Nd$ in the residue (cf. Figs. 2-3a and 2-3c or Figs. 2-3b and 2-3d). Mixing of $^{176}Hf/^{177}Hf$ in the residue also occurs for the small and less enriched heterogeneities (Fig. 2-3a) but at a smaller extent compared to $^{143}Nd/^{144}Nd$. This is due to the slower diffusion of Hf in pyroxene (Figs. 2-2b and 2-2d). Thus, the most common $^{176}Hf/^{177}Hf$ in the residue does not converge to the concentration average of the source. The

residue has a most common $^{176}Hf/^{177}Hf$ in between DMM and the concentration average of the source.

Mixing of partial melts derived from a wide range of depth takes place in the high-porosity channel network during melt migration in the mantle and accumulation of melts in the magma chamber process (Fig. 2-1b). Increasing the abundance of trace element in the enriched heterogeneity could partly offset the dilution effect. Since the chemical signal in the matrix melt is already damped, the composition of channel melt will inherit the size-sensitive mixing effect in the matrix. Since the channel melt is a mixture of all melts extracted from the matrix, all enriched chemical signals in a melting column are integrated in the channel. As the size of heterogeneity increases, the isotopic enrichment in the channel would be less diluted (supplementary Movie S1). Consequently, the channel melt will be mixed less and samples a wider range of isotopic variability if the size of heterogeneity is larger.

The pooled melt mixes channel melt from all melting columns in the triangular melting region. Thus, the composition of pooled melt will also inherit the size-sensitive mixing effect and be further mixed under the permeability barrier. As the size and the enrichment decrease, mixing and dilution in the matrix and channel melts strengthens, which makes the isotopic composition of pooled melt to converge to the concentration average of the source. Magma chamber process leads to further homogenization, but this effect is very small due to the small magma chamber residence time which is defined as the ratio between magma chamber volume and the melt volume flux (DePaolo, 1996). In Nd-Hf isotopic space, the erupted melt has a wide range of composition around the concentration average of the source or the average MORB in all cases unless the

enrichment is high and the size is large (Fig. 2-3d). The range of melt composition shrinks as the size of heterogeneity decreases. Increasing the trace element abundance of EM or EMX could enlarge the range of compositions in the erupted melt. In all cases, the erupted melt does not represent either the EM or the DMM source. The entire field of EM and part of the depleted isotope ratios of DMM are underrepresented in the erupted melt.

The relation between the isotope ratios in the erupted melt and the residue changes systemically with the size and the enrichment factor. In a case of large size and high enrichment (Fig. 2-3d: 8.9 km and EMX = 11.9), the erupted malt peaks at roughly the same $^{143}Nd/^{144}Nd$ as the residue. Hence there is no MORB-AP offset in this case. As the size or the enrichment decreases, the composition of erupted melt converges to the concentration average while the composition of the residue peaks at DMM-like $^{143}Nd/^{144}Nd$. The MORB-AP offset is produced. When the size is small and the enrichment of EM is low (Fig. 2-3a: 2.2 km and EMX = 3.04), both the melt and residue converge to the source-averaged $^{143}Nd/^{144}Nd$. The MORB-AP offset disappears. Interestingly, the most common $^{176}Hf/^{177}Hf$ in the residue is still higher than the erupted melt (Fig. 2-3a). Therefore, the $^{143}Nd/^{144}Nd$ MORB-AP offset as observed in natural samples should correspond to a set of moderate size and enrichment. As the Hf offset is seen more often than the Nd offset in our simulations, the residue could be plotted above the melt trend in Nd-Hf isotopic space (Fig. S2-7).

There is a trade-off between the size (L) and the enrichment factor (EMX) of EM in producing the Nd and Hf isotopic variations presented in the preceding section: the PDF of the erupted melt and the residue will not change so long as the product L*EMX remains the same. This is demonstrated in Figs. 2-3b and 2-3c (L*EMX = 27 km and 26 km,

respectively). We refer the product, L*EMX, as the enrichment strength. Figs. 2-4a and 2-4b summarize our simulation results for the most common $^{143}Nd/^{144}Nd$ in the residue and the erupted melt (color coded dots) for a wide range of EM size and enrichment factor. The range or variability of $^{143}Nd^{144}Nd$ (marked by vertical bars) is defined by half-height width of the PDF in the residue or erupted melt. If the enrichment strength is larger than 30 km (as in the case of Fig. 2-3d), the composition of the residue is almost the same as DMM. As the enrichment strength decreases to 10 km, either by reducing the size or the Nd abundance in EM, the enriched signals are smeared by melt migration-induced mixing, and the marginal PDF becomes broader and the peak location migrates to the concentration average of the source. As the enrichment strength decreases below 10 km (as in the case of 2-3a), strong mixing in the residue leads to narrowing of the marginal PDF. For the erupted melt, reducing the enrichment strength from 200 km to 1.8 km shrinks the marginal PDF (Fig. 2-4b). The $^{143}Nd/^{144}Nd$ of EM (lower than 0.51295) is underrepresented in the marginal PDF of erupted melt. The average DMM-like $^{143}Nd/^{144}Nd$ (0.5132) is within the half-height width of the marginal PDF of erupted melt only if the enrichment strength is larger than 80 km. At such large enrichment strength, the marginal PDF of erupted melt centers at a value larger than the concentration average of the source. If the enrichment strength is smaller than 80 km, the marginal PDF of melt is symmetric and centers around the source average.

The observed MORB-AP offset requires that the $^{143}Nd/^{144}Nd$ of melt is relatively well-mixed to represent the concentration average of EM and DMM while the $^{143}Nd/^{144}Nd$ of residue is not efficiently mixed so that the residue still has a DMM-like signature. To produce an MORB-AP offset (0.51306 vs. 0.51320), the enrichment strength should be

greater than 20 km. The abyssal peridotites seem to sample a wider range of $^{143}Nd/^{144}Nd$ than the locally associated MORB. The range of observed MORB composition requires an enrichment strength of 60 km. The range of melt composition will expand if the size of the magma chamber is smaller than used here or the mixing during melt pooling is not complete (see next section). Therefore, the enrichment strength of 60 km should be taken as an upper bound. The lower bound (20 km) of the enrichment strength for preserving MORB-AP offset varies only 2 times and the upper bound (60 km) for restricted range of melt composition is invariable for a range of model parameters (Fig. S2-5).

4. Discussion

4.1. Inefficient mixing during melt pooling

In our model, the pooled melt is a well-mixed aggregation of melts coming out of each melting column in the triangular melting region. This is likely an oversimplification of the mixing process during melt focusing because the isotopic variability of melt inclusions suggests incomplete mixing of mantle derived melts (Sobolev and Shimizu, 1993; Saal et al., 1998). We test a case in which melt focusing does not mix melts derived from vertical melt channels. The erupted melt is a collection of melts with different compositions before entering the magma chamber. We can sample the collection at a probability proportional to the melt flux to obtain a statistical representation of the melt collection (Fig. S2-6). As expected, the composition of the melt collection is more variable than the well-mixed pooled melt. The lowest degree (2%) channel melt in the melt collection is barely diluted by melt extraction and contributes to the most depleted isotope ratios in the source that pooled melt cannot sample. Due to the small volume proportion of such low degree melt in all melt generated in the melting region, the chance of sampling

extreme isotope ratios in the melt collection is very low. The marginal PDF of $^{143}Nd/^{144}Nd$ in the melt collection tends to peak at more depleted isotope ratios than the pooled melt (Fig. S2-6). For the case shown in Fig. S2-6, the peak of $^{143}Nd/^{144}Nd$ in the melt collection is indistinguishable from the residue while the pooled melt has noticeably lower $^{143}Nd/^{144}Nd$ than the residue. To produce the MORB-AP offset, some mixing during melt focusing or in the magma chamber is required. The relative low viscosity of basaltic melt favors rapid overturn and efficient homogenization in the magma chamber (Huber et al., 2009). The erupted melt is sufficiently, if not completely, mixed to approach the concentration averaged isotope ratios of the source. Since inefficient mixing during melt pooling makes it more difficult to produce the MORB-AP offset, the constraints for the enrichment strength could only become tighter.

4.2. The 20-60 km enrichment strength and the form of enriched heterogeneities

The Nd-Hf isotopic composition of the heterogeneity or EM is related to the unique elemental ratios in oceanic crust, including a small portion of sediments (Hofmann and White, 1982; Chauvel et al., 2008). The abundance of Nd in the recycled oceanic crust is 25 to 12 times higher than DMM, depending on the proportion of sediments, the age of recycling, the extent of subduction modification, and the choice of DMM composition (Stracke et al., 2003; Chauvel et al., 2008). The proportion of oceanic crust should be 3% to fit the average MORB (Fig. 2-3c and 2-3d). The subducted oceanic crust is likely thinned or stretched by mantle convection, resulting in a distribution of size and shape of the heterogeneity (van Keken et al., 2002). A significant amount of recycled crustal materials would melt before the onset of peridotite melting (Kogiso et al., 2004), producing melt with enriched incompatible trace element abundance and isotope ratios. Such enriched melt

could metasomatize the overlying depleted mantle, producing heterogeneities with a range of EMX. The isotope ratio of these metasomatized mantle is expected to be dominated by the recycled materials. The size of these metasomatized heterogeneities is expected to be larger than unmelted crustal materials due to percolation of small degree melts derived from them. Since the extent of melt-migration induced mixing after the onset of peridotite melting is scaled with the enrichment strength and the observed MORB-AP offset requires a moderate extent of mixing, the majority of heterogeneities cannot have an enrichment strength outside the range of 20-60km. The enrichment factor of EM could be in the range of 1 to 25. Therefore, the size of heterogeneities responsible for the observed isotope ratios in MORB and abyssal peridotites could be on the kilometer scale. Our model does not imply the absence of smaller heterogeneities in the mantle source, as the sub-kilometer class does not contribute to the observed MORB-AP offset. The size and composition of mantle heterogeneity are important to the interpretation of isotope and incompatible trace element data in basalts and residual peridotites and must be taken into consideration in geochemical studies of mantle derived rocks. Systematic studies of high-resolution spatially correlated mantle samples may help to constrain the size, distribution, and nature of chemical heterogeneities in the mantle.

Acknowledgments

We thank C. Huber, S. Mallick, and A. Saal for useful discussion. This paper benefited from thoughtful reviews by G. Ito, M. Jackson, and the associate editor C.-T. Lee. This work was supported by a grant from the U.S. NSF (EAR-1624516).

References

Albarède, F. (1993). "Residence time analysis of geochemical fluctuations in volcanic series." Geochimica Et Cosmochimica Acta **57**(3): 615-621.

Anders, E. and N. Grevesse (1989). "Abundances of the elements: Meteoritic and solar." Geochimica Et Cosmochimica Acta **53**(1): 197-214.

Bangerth, W., D. Davydov, T. Heister, L. Heltai, G. Kanschat, M. Kronbichler, M. Maier, B. Turcksin and D. Wells (2016). The deal.II Library, Version 8.4. Journal of Numerical Mathematics. **24:** 135.

Bangerth, W., R. Hartmann and G. Kanschat (2007). "deal.II—A general-purpose object-oriented finite element library." ACM Trans. Math. Softw. **33**(4): 24.

Bloch, E. and J. Ganguly (2014). "176Lu–176Hf and 147Sm–143Nd ages of the Martian shergottites: Evaluation of the shock-resetting hypothesis through diffusion kinetic experiments and modeling, and petrological observations." Earth and Planetary Science Letters **395**: 173-183.

Brunelli, D., M. Seyler, A. Cipriani, L. Ottolini and E. Bonatti (2006). "Discontinuous Melt Extraction and Weak Refertilization of Mantle Peridotites at the Vema Lithospheric Section (Mid-Atlantic Ridge)." Journal of Petrology **47**(4): 745-771.

Carlson, R. W. (1995). "Isotopic inferences on the chemical structure of the mantle." Journal of Geodynamics **20**(4): 365-386.

Chauvel, C., E. Lewin, M. Carpentier, N. T. Arndt and J.-C. Marini (2008). "Role of recycled oceanic basalt and sediment in generating the Hf-Nd mantle array." Nature Geoscience **1**(1): 64-67.

Cipriani, A., H. K. Brueckner, E. Bonatti and D. Brunelli (2004). "Oceanic crust generated by elusive parents: Sr and Nd isotopes in basalt-peridotite pairs from the Mid-Atlantic Ridge." Geology **32**(8): 657-660.

Cockburn, B. and C.-W. Shu (1989). "TVB Runge-Kutta local projection discontinuous Galerkin finite element method for conservation laws. II. General framework." Mathematics of computation **52**(186): 411-435.

Cockburn, B. and C.-W. Shu (1998). "The Runge–Kutta Discontinuous Galerkin Method for Conservation Laws V: Multidimensional Systems." Journal of Computational Physics **141**(2): 199-224.

DePaolo, D. J. (1996). "High-frequency isotopic variations in the Mauna Kea tholeiitic basalt sequence: Melt zone dispersivity and chromatography." Journal of Geophysical Research: Solid Earth **101**(B5): 11855-11864.

Frisby, C., M. Bizimis and S. Mallick (2016). "Seawater-derived rare earth element addition to abyssal peridotites during serpentinization." Lithos **248–251**: 432-454.

Glueckauf, E. (1955). "Theory of chromatography. Part 10.—Formulæ for diffusion into spheres and their application to chromatography." Transactions of the Faraday Society **51**: 1540-1551.

Hebert, L. B. and L. G. J. Montési (2010). "Generation of permeability barriers during melt extraction at mid-ocean ridges." Geochemistry, Geophysics, Geosystems **11**(12).

Hofmann, A. (1997). "Mantle geochemistry: the message from oceanic volcanism." Nature **385**(6613): 219-229.

Hofmann, A. (2003). "Sampling mantle heterogeneity through oceanic basalts: isotopes and trace elements." Treatise on geochemistry **2**: 61-101.

Hofmann, A. W. and W. M. White (1982). "Mantle plumes from ancient oceanic crust." Earth and Planetary Science Letters **57**(2): 421-436.

Huber, C., O. Bachmann and M. Manga (2009). "Homogenization processes in silicic magma chambers by stirring and mushification (latent heat buffering)." Earth and Planetary Science Letters **283**(1–4): 38-47.

Ito, G. and J. J. Mahoney (2005). "Flow and melting of a heterogeneous mantle: 1. Method and importance to the geochemistry of ocean island and mid-ocean ridge basalts." Earth and Planetary Science Letters **230**(1–2): 29-46.

Iwamori, H. (1993). "Dynamic disequilibrium melting model with porous flow and diffusion-controlled chemical equilibration." Earth and Planetary Science Letters **114**(2): 301-313.

Iwamori, H., D. McKenzie and E. Takahashi (1995). "Melt generation by isentropic mantle upwelling." Earth and Planetary Science Letters **134**(3): 253-266.

Kelemen, P. B., G. Hirth, N. Shimizu, M. Spiegelman and H. J. B. Dick (1997). "A Review of Melt Migration Processes in the Adiabatically Upwelling Mantle beneath Oceanic Spreading Ridges." Philosophical Transactions: Mathematical, Physical and Engineering Sciences **355**(1723): 283-318.

Keller, T., R. F. Katz and M. M. Hirschmann (2017). "Volatiles beneath mid-ocean ridges: Deep melting, channelised transport, focusing, and metasomatism." Earth and Planetary Science Letters **464**: 55-68.

Kogiso, T., M. M. Hirschmann and M. Pertermann (2004). "High-pressure Partial Melting of Mafic Lithologies in the Mantle." Journal of Petrology **45**(12): 2407-2422.

Liang, Y. (2003). "On the thermo-kinetic consequences of slab melting." Geophysical Research Letters **30**(24): 2270.

Liang, Y. and B. Liu (2016). "Simple models for disequilibrium fractional melting and batch melting with application to REE fractionation in abyssal peridotites." Geochimica Et Cosmochimica Acta **173**: 181-197.

Liang, Y. and E. M. Parmentier (2010). "A Two-Porosity Double Lithology Model for Partial Melting, Melt Transport and Melt–rock Reaction in the Mantle: Mass Conservation Equations and Trace Element Transport." Journal of Petrology **51**(1-2): 125-152.

Liang, Y. and Q. Peng (2010). "Non-modal melting in an upwelling mantle column: Steady-state models with applications to REE depletion in abyssal peridotites and the dynamics of melt migration in the mantle." Geochimica Et Cosmochimica Acta **74**(1): 321-339.

Liu, B. and Y. Liang (2017). "An introduction of Markov chain Monte Carlo method to geochemical inverse problems: Reading melting parameters from REE abundances in abyssal peridotites." Geochimica Et Cosmochimica Acta **203**: 216-234.

Liu, C.-Z., J. E. Snow, E. Hellebrand, G. Brugmann, A. von der Handt, A. Buchl and A. W. Hofmann (2008). "Ancient, highly heterogeneous mantle beneath Gakkel ridge, Arctic Ocean." Nature **452**(7185): 311-316.

Lundstrom, C. (2000). "Models of U-series disequilibria generation in MORB: the effects of two scales of melt porosity." Physics of the Earth and Planetary Interiors **121**(3–4): 189-204.

Mallick, S., H. J. B. Dick, A. Sachi-Kocher and V. J. M. Salters (2014). "Isotope and trace element insights into heterogeneity of subridge mantle." Geochemistry, Geophysics, Geosystems **15**(6): 2438-2453.

McKenzie, D. (1984). "The generation and compaction of partially molten rock." Journal of Petrology **25**(3): 713-765.

Navon, O. and E. Stolper (1987). "Geochemical Consequences of Melt Percolation: The Upper Mantle as a Chromatographic Column." The Journal of Geology **95**(3): 285-307.

Parzen, E. (1962). "On estimation of a probability density function and mode." The annals of mathematical statistics **33**(3): 1065-1076.

PetDB, www.earthchem.org/petdb.

Plank, T. and C. H. Langmuir (1992). "Effects of the melting regime on the composition of the oceanic crust." Journal of Geophysical Research: Solid Earth (1978–2012) **97**(B13): 19749-19770.

Qin, Z. (1992). "Disequilibrium partial melting model and its implications for trace element fractionations during mantle melting." Earth and Planetary Science Letters **112**(1): 75-90.

Ribe, N. M. (1985). "The deformation and compaction of partial molten zones." Geophysical Journal International **83**(2): 487-501.

Saal, A. E., S. R. Hart, N. Shimizu, E. H. Hauri and G. D. Layne (1998). "Pb Isotopic Variability in Melt Inclusions from Oceanic Island Basalts, Polynesia." Science **282**(5393): 1481-1484.

Salters, V. J. M. and H. J. B. Dick (2002). "Mineralogy of the mid-ocean-ridge basalt source from neodymium isotopic composition of abyssal peridotites." Nature **418**(6893): 68-72.

Salters, V. J. M. and A. Stracke (2004). "Composition of the depleted mantle." Geochemistry, Geophysics, Geosystems **5**(5): Q05B07.

Shaw, D. M. (2000). "Continuous (Dynamic) Melting Theory Revisited." The Canadian Mineralogist **38**(5): 1041-1063.

Shu, C.-W. and S. Osher (1988). "Efficient implementation of essentially non-oscillatory shock-capturing schemes." Journal of Computational Physics **77**(2): 439-471.

Sinton, J. M. and R. S. Detrick (1992). "Mid-ocean ridge magma chambers." Journal of Geophysical Research: Solid Earth **97**(B1): 197-216.

Sobolev, A. V. and N. Shimizu (1993). "Ultra-depleted primary melt included in an olivine from the Mid-Atlantic Ridge." Nature **363**(6425): 151-154.

Sparks, D. W. and E. M. Parmentier (1991). "Melt extraction from the mantle beneath spreading centers." Earth and Planetary Science Letters **105**(4): 368-377.

Stracke, A., M. Bizimis and V. J. M. Salters (2003). "Recycling oceanic crust: Quantitative constraints." Geochemistry, Geophysics, Geosystems **4**(3): n/a-n/a.

Stracke, A. and B. Bourdon (2009). "The importance of melt extraction for tracing mantle heterogeneity." Geochimica Et Cosmochimica Acta **73**(1): 218-238.

Stracke, A., J. E. Snow, E. Hellebrand, A. von der Handt, B. Bourdon, K. Birbaum and D. Günther (2011). "Abyssal peridotite Hf isotopes identify extreme mantle depletion." Earth and Planetary Science Letters **308**(3–4): 359-368.

The_MELT_Seismic_Team (1998). "Imaging the Deep Seismic Structure Beneath a Mid-Ocean Ridge: The MELT Experiment." Science **280**(5367): 1215-1218.

van Keken, P. E., E. H. Hauri and C. J. Ballentine (2002). "Mantle mixing: the generation, preservation, and destruction of chemical heterogeneity." Annual Review of Earth and Planetary Sciences **30**(1): 493-525.

Van Orman, J. A., T. L. Grove and N. Shimizu (2001). "Rare earth element diffusion in diopside: influence of temperature, pressure, and ionic radius, and an elastic model for diffusion in silicates." Contributions to Mineralogy and Petrology **141**(6): 687-703.

Van Orman, J. A., T. L. Grove and N. Shimizu (2002). "Diffusive fractionation of trace elements during production and transport of melt in Earth's upper mantle." Earth and Planetary Science Letters **198**(1): 93-112.

Wark, D. A. and E. B. Watson (1998). "Grain-scale permeabilities of texturally equilibrated, monomineralic rocks." Earth and Planetary Science Letters **164**(3–4): 591-605.

Warren, J. M., N. Shimizu, C. Sakaguchi, H. J. B. Dick and E. Nakamura (2009). "An assessment of upper mantle heterogeneity based on abyssal peridotite isotopic compositions." Journal of Geophysical Research: Solid Earth **114**(B12): B12203.

Workman, R. K. and S. R. Hart (2005). "Major and trace element composition of the depleted MORB mantle (DMM)." Earth and Planetary Science Letters **231**(1–2): 53-72.

Zindler, A. and S. Hart (1986). "Chemical Geodynamics." Annual Review of Earth and Planetary Sciences **14**: 493-571.

Appendix

1. Governing equations for 1D melting column

We consider concurrent melting and melt segregation in an upwelling double porosity mantle column in which part of the melt generated in the low-porosity matrix (lherzolite/harzburgite + melt) is extracted into nearby high-porosity dunite channels. Our primary interest in the present study is the spatial and temporal variations of a trace element and its isotope ratio in the partial melt and residual solid in the matrix and the channel network. For simplicity, we assume that the velocity and porosity of the matrix and channel are in steady state. In one-dimension, the evolution of the physical state of the melting column and the concentration of a trace element are governed by the following set of conservation equations (McKenzie, 1984; Ribe, 1985; Iwamori, 1993; Liang and Parmentier, 2010; Liang and Peng, 2010; Liang and Liu, 2016; Liu and Liang, 2017):

$$\frac{\partial\left(\rho_f \phi_m V_f^m\right)}{\partial z} = \Gamma_m\left(1-S\right), \tag{A2-1}$$

$$\frac{\partial\left[\rho_s\left(1-\phi_m\right)V_s^m\right]}{\partial z} = -\Gamma_m, \tag{A2-2}$$

$$\frac{\partial\left[\rho_f \phi_{ch} V_f^{ch} + \rho_s\left(1-\phi_{ch}\right)V_s^{ch}\right]}{\partial z} = \Gamma_m S\frac{1-\psi}{\psi} \tag{A2-3}$$

$$\phi_m\left(V_f^m - V_s^m\right) = \frac{k_\phi}{\eta_f}\left(1-\phi_m\right)\Delta\rho g, \tag{A2-4}$$

$$\begin{aligned}&\frac{\partial\left(\rho_f \phi_m C_f^m\right)}{\partial t} + \frac{\partial\left(\rho_f \phi_m V_f^m C_f^m\right)}{\partial z} \\ &= \Gamma_m C_s^p - \Gamma_m S C_f^m + \rho_s\left(1-\phi_m\right)R\left(C_s^m - k_m C_f^m\right),\end{aligned} \tag{A2-5}$$

$$\frac{\partial\left(\rho_s\left(1-\phi_m\right)C_s^m\right)}{\partial t}+\frac{\partial\left[\rho_s\left(1-\phi_m\right)V_s^m C_s^m\right]}{\partial z} = -\Gamma_m C_s^p-\rho_s\left(1-\phi_m\right)R\left(C_s^m-k_m C_f^m\right). \tag{A2-6}$$

$$\frac{\partial\left[\rho_f\phi_{ch}+k_{ch}\rho_s\left(1-\phi_{ch}\right)\right]C_f^{ch}}{\partial t}+\frac{\partial\left[\rho_f\phi_{ch}V_f^{ch}+k_{ch}\rho_s\left(1-\phi_{ch}\right)V_s^{ch}\right]C_f^{ch}}{\partial z} = \Gamma_m \mathrm{S}\frac{1-\psi}{\psi}C_f^m. \tag{A2-7}$$

where z is vertical distance above the solidus; ρ_s and ρ_f are densities of the solid and the melt; ϕ and ϕ_{ch} are porosities of the matrix and the channel; C_s^p is the bulk solid matrix concentration participated in the melting reaction(Liang and Liu, 2016); V_s^m and V_f^m are velocities of the solid and the melt in the matrix; V_s^{ch} and V_f^{ch} are velocities of the solid and the melt in the channel; ψ is the relative volume fraction of the channel; $\Delta\rho$ is the density contrast between the residue solid and the melt; g is the gravitational constant; η_f is the viscosity of the melt; k_ϕ is the permeability of the matrix; Γ_m is the melting rate of the bulk solid; S is the melt suction rate; C_s^m and C_f^m are concentrations in the residue solid or the melt in the matrix; C_s^i is the concentration in the constituent mineral i in the matrix; C_f^{ch} is the concentration in the channel melt; k_m and R are the partition coefficient and the exchange rate coefficient(Liang, 2003; Liang and Liu, 2016) for the trace element of interest between the matrix solid and the melt, respectively; k_{ch} is the bulk partition coefficient in the channel. Following ref.(Liang and

Liu, 2016), we make use of the simplifying assumption that mineral-melt exchange rate coefficients are the same among the minerals in residual matrix,

$$R = \frac{15 D_{diff}}{d^2}, \tag{A2-8}$$

where D_{diff} is the diffusivity of a trace element in clinopyroxene; d is the average grain size of clinopyroxene. The spatial coordinate, z, is related to the extent of melting experienced by the solid matrix through the material derivative(Liang and Peng, 2010),

$$\frac{dF}{dz} = \frac{(1-F)\Gamma_m}{\rho_s (1-\phi) V_s^m}, \tag{A2-9}$$

where F is the degree of melting.

Eqs. (A2-1) to (A2-3) are mass conservations equations for the matrix and the channel (McKenzie, 1984; Iwamori, 1993; Liang and Peng, 2010), while Eq. (A2-4) is the Darcy's law. Eqs. (A2-5) to (A2-7) are mass conservation equations for a trace element in the interstitial melt and mineral i in the matrix, accounting for incongruent melting of the matrix, melt extraction, and diffusive exchange among minerals and the melt. Following earlier works (Glueckauf, 1955; McKenzie, 1984; Navon and Stolper, 1987; Liang and Liu, 2016), we use linear kinetics to approximate steady-state diffusive exchange between mineral i and its surrounding melt. For simplicity, we neglect diffusion and dispersion in the melt (see Liang, 2008 for a discussion of this assumption) and assume that ϕ_{ch} and ψ are constant.

Boundary conditions at the bottom of the melting column, z = 0, are as follows:

$$\rho_f \phi_m V_f^m \mid_{z=0} = 0,\ \ \rho_s \left(1-\phi_m\right) V_s^m \mid_{z=0} = \rho_s V_0,\ \ \rho_f \phi_{ch} V_f^{ch} \mid_{z=0} = 0, \qquad \text{(A2-10)}$$

$$C_f^m \mid_{z=0} = \frac{C_s^0}{k_m},\ \ C_s^m \mid_{z=0} = C_s^0,\ \ C_s^i \mid_{z=0} = k_i \cdot C_f^m,\ C_f^{ch} \mid_{z=0} = \frac{C_s^0}{k_m}, \qquad \text{(A2-11)}$$

where V_0 is the upwelling velocity of the mantle before melting; C_s^0 is the concentration of a trace element in the mantle source. A detailed description of boundary conditions for Nd and Hf used in this study is presented in section 1.2 below. To simulate spatially distributed mantle heterogeneities, we consider time-dependent boundary conditions for the mantel source with Gaussian distributions,

$$C_s^0 = C^D + \sum_{n=1}^{N} \left(C_n^E - C^D\right) \cdot \exp\left(-\left(\frac{t-t_n}{\sigma_n}\right)^2\right), \qquad \text{(A2-12)}$$

where C^D is the concentration of an isotope in the depleted mantle (C^D could have multiple values as defined in Eq. (A2-15) below); C_n^E is the concentration of an isotope in the nth enriched heterogeneity that passes the solidus at time t_n; and σ_n is related to the size (l_n) and upwelling mantle velocity (V_0) through the expression,

$$\sigma_n = \frac{l_n}{4\sqrt{\pi} V_0}. \qquad \text{(A2-13)}$$

The proportion of enriched heterogeneities in the mantle source ($EM\%$) can be calculated from the amount of enriched and depleted materials passing through the solidus over the duration of the simulation (t_d). The fraction of N enriched heterogeneities in the mantle source passing through the solidus is,

$$EM\% = \frac{\sum_{n=1}^{N} \sqrt{\pi}\sigma_n}{t_d}. \tag{A2-14}$$

In Figs. 2-3, 2-4, S2-4, and S2-5, the depleted mantle has variable concentrations. This is implemented by dividing the boundary condition into multiple intervals within which the depleted mantle has a constant concentration,

$$C^D(t) = \begin{cases} C_1^D, & t_0^D < t < t_1^D \\ C_2^D, & t_1^D < t < t_2^D \\ & \cdots \\ C_M^D, & t_{M-1}^D < t < t_M^D \end{cases}, \tag{A2-15}$$

where C_m^D is the concentration of the depleted mantle within the interval $t_{m-1}^D < t < t_m^D$. For simplicity and numerical accuracy, we assume the interval to be sufficiently large compared to individual enriched heterogeneity so that we can solve each interval of C^D separately and superimpose solutions together. For example, if $C_{f\,m}^{ch}(t,z)$ is the solution of channel melt with boundary condition Eq. (A2-12) and $C^D(t) = C_m^D$, $t_{m-1}^D < t < t_m^D$, the solution of channel melt with variable DMM composition is,

$$C_f^{ch}(t,z) = \begin{cases} C_{f\,1}^{ch}(t,z), & t_0^D + t_{ch}(z) < t < t_1^D + t_{ch}(z) \\ C_{f\,2}^{ch}(t,z), & t_1^D + t_{ch}(z) < t < t_2^D + t_{ch}(z) \\ & \cdots \\ C_{f\,M}^{ch}(t,z), & t_{M-1}^D + t_{ch}(z) < t < t_M^D + t_{ch}(z) \end{cases}, \tag{A2-16}$$

where $t_{ch}(z)$ is the time it takes for the enriched heterogeneity in the source to advect to the height z in the channel.

We solve the conservation equations in two steps (section 1.1). We first solve the porosities and velocities from the steady-state mass conservation equations for the melt and solid (Eqs. A2-1 to A2-3) and Darcy's law (Eq. A2-4). Given porosities and velocities, we then solve the time-dependent conservation equations for trace elements in the double-porosity system from Eqs. (A2-5) to (A2-7), subject to the boundary conditions outlined above.

1.1. Porosity and velocity

We assume that the solid in the channel has the same velocity as the solid in the matrix,

$$V_s^{ch} = V_s^m. \tag{A2-17}$$

We will assume constant melting rate and integrate Eqs. (A2-1) to (A2-3) to obtain fluxes of the matrix and the channel functions of the degree of melting. The Darcy's law, Eq. (A2-4), becomes,

$$0 = -\left(1-\phi_m\right) g\Delta\rho + \frac{\eta_f \phi_m}{k_\phi}\left(\frac{\left(1-S\right)F\rho_s V_0}{\rho_f \phi_m} - \frac{\left(1-F\right)\rho_s V_0}{\rho_s\left(1-\phi_m\right)} \right). \tag{A2-18}$$

where the permeability is a function of average grain size (d) and porosity (Wark and Watson, 1998),

$$k_\phi = \frac{d^2 {\phi_m}^n}{C_\phi}. \tag{A2-19}$$

where C_ϕ is a constant. Substituting Eq. (A2-19) into Eq. (A2-18), we have an expression relating matrix porosity to degree of melting and melt suction rate (here we assume $\phi_m \ll 1$ and apply Boussinesq approximation), viz.,

$$0 = -\frac{g\Delta\rho}{V_0\eta_f}\frac{d^2{\phi_m}^n}{C_\phi} - (1-F)\cdot\phi_m + (1-S)F. \tag{A2-20}$$

It is convenient to cast Eq. (A2-20) into dimensionless form. The natural length scale, z_0, is the height of the melting column. The natural velocity scale is V_0, the upwelling velocity of the mantle before melting. The natural time scale is the advection time of solid mantle:

$$t_0 = \frac{z_0}{V_0}. \tag{A2-21}$$

The reference porosity, ϕ_0 is 0.1%. These scales suggest the following non-dimensionalization:

$$z = \mathrm{z}'\cdot z_0, \tag{A2-22}$$

$$V_s^m = V_s^{m'}V_0,\ V_f^m = V_f^{m'}V_0,\ V_f^{ch} = V_f^{ch'}V_0 \tag{A2-23}$$

$$\phi_m = \phi_m^{'}\cdot\phi_0, \phi_{ch} = \phi_{ch}^{'}\cdot\phi_0, \tag{A2-24}$$

where primes denote dimensionless variables. After dropping primes, the nondimensionalized equations are,

$$0 = -B\cdot{\phi_m}^n(1-\phi_m\phi_0)^2 - (1-F)\cdot\phi_m\phi_0 + (1-S)F(1-\phi_m\phi_0) \tag{A2-25}$$

$$V_f^m = \frac{F\left(1-\mathrm{S}\right)}{\phi_m \phi_0}, \tag{A2-26}$$

$$V_s^m = \frac{1-F}{1-\phi_m \phi_0}, \tag{A2-27}$$

$$V_f^{ch} = \frac{\left(1+S\frac{1-\psi}{\psi}F\right)-V_s^m}{\phi_{ch}\phi_0}, \tag{A2-28}$$

where B is the dimensionless buoyancy (Ribe, 1985),

$$B = \frac{g\Delta\rho d^2 {\phi_0}^n}{C_\phi V_0 \eta_f}. \tag{A2-29}$$

Eq. (A2-25) is solved numerically. Once we have the solution of ϕ_m, velocities can be derived from Eqs. (A2-1) to (A2-3). In the next section, we will treat these physical variables as known.

1.2. Trace element concentrations in the melt and solid

Isotope ratios are derived from solutions of individual isotopes, ^{143}Nd, ^{144}Nd, ^{176}Hf, and ^{177}Hf. The composition of the enriched heterogeneity depends on the age of recycling and the proportion of sediments (Chauvel et al., 2008). Compositions of EM are calculated using the model of Chauvel et al. (2008) after randomly selecting a recycling age (between 1 and 3 Ga) and a proportion of sediments (between 0 and 10%). The random composition of DMM used in Fig. 2-3, 2-4, S2-4, S2-5, and S2-6 is from a bivariate normal distribution of ^{143}Nd/^{144}Nd and ^{176}Hf/^{177}Hf with extreme values from literatures (Salters and Stracke,

2004; Workman and Hart, 2005). The correlation coefficient for bivariate normal distribution of $^{143}Nd/^{144}Nd$ and $^{176}Hf/^{177}Hf$ in DMM is 0.5.

To facilitate numerical solution of the conservation equations for trace elements, we make the following substitution for concentrations:

$$C_f = \phi_m \phi_0 C_f^m, \tag{A2-30}$$

$$C_s = \left(1 - \phi_m \phi_0\right) C_s^m, \tag{A2-31}$$

$$C^{ch} = \left[\phi_{ch}\phi_0 + k_{ch}\left(1 - \phi_{ch}\phi_0\right)\right] C_f^{ch}. \tag{A2-32}$$

Eqs. (A2-5) to (A2-7) then take the form

$$\frac{\partial C_f}{\partial t} + \frac{\partial\left(V_f^m C_f\right)}{\partial z} = F_0 \cdot \left(\frac{C_s}{1-\phi_m\phi_0}\frac{k_p}{k_m} - \mathrm{S}\frac{C_f}{\phi_m\phi_0}\right) + F_0 / D_a \cdot \left(\frac{C_s}{1-\phi_m\phi_0} - k_m \frac{C_f}{\phi_m\phi_0}\right), \tag{A2-33}$$

$$\frac{\partial C_s}{\partial t} + \frac{\partial\left(V_s^m C_s\right)}{\partial z} = -F_0 \cdot \frac{C_s}{1-\phi_m\phi_0}\frac{k_p}{k_m} - F_0 / D_a \cdot \left(\frac{C_s}{1-\phi_m\phi_0} - k_m \frac{C_f}{\phi_m\phi_0}\right), \tag{A2-34}$$

$$\frac{\partial C^{ch}}{\partial t} + \frac{\partial\left(V_e^{ch} C^{ch}\right)}{\partial z} = F_0 \cdot \mathrm{S}\frac{1-\psi}{\psi} C_f^m, \tag{A2-35}$$

where the effective velocity in the channel is the usual chromatography velocity (Navon and Stolper, 1987), viz.,

$$V_e^{ch} = \frac{\phi_{ch}\phi_0 V_f^{ch} + k_{ch}\left(1-\phi_{ch}\phi_0\right)V_s^{ch}}{\phi_{ch}\phi_{ch}\phi_0 + k_{ch}\left(1-\phi_{ch}\phi_0\right)}. \tag{A2-36}$$

Eqs. (A2-33) to (A2-35) have two dimensionless parameters:

$$F_0 = \frac{z_0 \Gamma_m}{\rho_s V_0}, \tag{A2-37}$$

$$Da = \frac{\Gamma_0}{\rho_s \left(1 - \phi_m \phi_0\right) R}, \tag{A2-38}$$

where F_0 is a reference degree of melting; Da is a Damköhler number describing the relative rates of melting and chemical exchange. In the case of constant melting rate, F_0 is the maximum degree of melting. Da is the same as ε in ref. (Liang and Liu, 2016).

The numerical scheme used to solve Eqs. (A2-33) to (A2-35) is a fourth-order Runge-Kutta Discontinuous Galerkin method (Shu and Osher, 1988; Cockburn and Shu, 1989; Cockburn and Shu, 1998). This high-order accurate numerical method is especially suitable for the advection dominant problem outlined above where accuracy is essential in computing Nd and Hf isotope ratios in the system. The software package used for implementation of the numerical scheme is deal.ii (Bangerth et al., 2007; Bangerth et al., 2016). Depending on the size of the enriched heterogeneity, we use 80 to 1280 cells in our simulations. The optimal order of accuracy is tested in a simpler advection-reaction system which has explicit analytical solutions (Liu and Liang, in preparation). Table S1 demonstrates the strong correlation between cell number and numerical errors. Here L_2 and L_∞ and are the Euclidean norm and the infinity norm of the difference between the analytical solution and the numerical solution (Cockburn and Shu, 1989). The numerical order is close to the optimal order of 4 which means that the error is proportional to h^4, where h is the cell size.

2. Modelling pooled melt and the magma chamber process

Erupted basalts are final products of mixed melts generated from a broad triangular melting region beneath the mid-ocean ridge spreading center (Fig. 2-1). As an end-member case, we assume that the matrix melt and channel melt at the top of each melting column are well mixed beneath the permeability barrier (Hebert and Montési, 2010). Because small amount of low degree melt may not erupt to the seafloor (Keller et al., 2017), we consider mixing of all melt which has a degree of melting between 2% and 18%. The channel melt flux and chemical flux are calculated using the expressions (Plank and Langmuir, 1992),

$$Flux^{pooled} = \int_{F=0.02}^{0.18} dF\left(\frac{L_x}{0.18}\right)\cdot\left[(1-\psi)\cdot\rho_f\phi_m\phi_0 V_f^m + \psi\cdot\rho_f\phi_{ch}\phi_0 V_f^{ch}\right], \quad \text{(A2-39)}$$

$$C_f^{pooled}\cdot Flux^{pooled} = \int_{F=0.02}^{0.18} dF\left(\frac{L_x}{0.18}\right)\cdot\left[(1-\psi)\cdot\rho_f\phi_m\phi_0 V_f^m C_f^m + \psi\cdot\rho_f\phi_{ch}\phi_0 V_f^{ch} C_f^{ch}\right], \quad \text{(A2-40)}$$

where $Flux^{pooled}$ is the flux of pooled melt derived from the triangular melting region; L_x is the dimensionless width of the triangular melting region; C_f^{pooled} is the concentration of the pooled melt.

In practice, we collect melt derived from multiple melting columns of variable extent of melting (2%, 4%, …, 18%),

$$Flux^{pooled} = \sum_{q=1}^{9}\left(\frac{L_x}{9}\right)\cdot\left[(1-\psi)\rho_f\phi_m\phi_0 V_f^m + \psi\rho_f\phi_{ch}\phi_0 V_f^{ch}\right], \quad \text{(A2-41)}$$

$$C_f^{pooled} \cdot Flux^{pooled} = \sum_{q=1}^{9}\left(\frac{L_x}{9}\right)\cdot\begin{bmatrix}(1-\psi)\cdot\rho_f\phi_m\phi_0 V_f^m\cdot C_f^m \\ +\psi\cdot\rho_f\phi_{ch}\phi_0 V_f^{ch}\cdot C_f^{ch}\end{bmatrix}, \quad \text{(A2-42)}$$

where solutions to the matrix porosity, velocities, and concentrations at the top of each melting column are taken from section 1.

Finally, melt compositions in a continuously sustained magma chamber are given by the mass balance equation and initial condition (Albarède, 1993),

$$\frac{d\left(\rho_f A\cdot C^{chamber}\right)}{dt} = C_f^{pooled}\cdot Flux^{pooled} - C^{chamber}\cdot Flux^{pooled}, \quad \text{(A2-43)}$$

$$C^{chamber}\big|_{t=0} = C_f^{pooled}\big|_{t=0}. \quad \text{(A2-44)}$$

where A is a measure of the relative size of the magma chamber in the plane perpendicular to the ridge; $C^{chamber}$ is the concentration of the melt in the magma chamber.

By choosing a horizontal length scale equal to the width of the melting region, L_x reduces to 1. We choose A to be 1/200 (or 1 km^2) based on the observation that the size of the magma chamber is small compared to the melting region (Sinton and Detrick, 1992; The_MELT_Seismic_Team, 1998). Eq. (A2-43) is integrated using Euler's scheme with time step of 1/2000.

3. Data compilation

We have compiled 96 published $^{143}Nd/^{144}Nd$ data of abyssal peridotites from Mid-Atlantic Ridge (Mallick et al., 2014), Southwest Indian Ridge (Salters and Dick, 2002; Warren et al., 2009; Mallick et al., 2014), and Mid-Cayman Rise (Mallick et al., 2014). If

the TiO_2 content in the spinel is larger than 0.12 wt.% or the La/Ce ratio normalized by CI chondrite (Anders and Grevesse, 1989) is greater than 2, the sample is considered refertilized or metasomatized (Mallick et al., 2014; Liang and Liu, 2016). The remaining 67 samples are referred to as residual abyssal peridotites. We use a geochemical database, PetDB, to choose any MORB data as the local MORB along the ridge within 550km of the dredge site of each residual abyssal peridotite. The data are summarized in Fig. S2-1. Fig. 2-1a combines all abyssal peridotites and their local MORB. To account for the different size of residual abyssal peridotite dataset and local MORB dataset, the frequency of local MORB is weighted by the number of local residual abyssal peridotite samples.

Figure Captions

Figure 2-1 (a) Histogram of $^{143}Nd/^{144}Nd$ in abyssal peridotites from Mid-Atlantic Ridge (Mallick et al., 2014) and Southwest Indian Ridge (Salters and Dick, 2002; Warren et al., 2009; Mallick et al., 2014), selected residual abyssal peridotites and spatially associated MORB (see data compilation). (b) Cartoon illustrating the double-porosity ridge model for melting and melt migration in a heterogeneous mantle beneath a mid-ocean spreading center.

Figure 2-2 Stretching and smearing of an enriched heterogeneity in an upwelling melting column. Spatial variations of (a and b) $^{143}Nd/^{144}Nd$ and (c and d) $^{176}Hf/^{177}Hf$ at three selected times are shown by blue (residue) and red lines (matrix melt). The initial size of the heterogeneity is 4.4 km (a and c) or 1.1 km (b and d). The initial Nd and Hf in the heterogeneity are five times more enriched than in the depleted mantle. Pairs of facing triangles are material markers that track the locations of major element particles in the residue at the selected times. The small reduction in the marker distance is due to partial melting (Fig. S2-3b). The degree of melting is linearly proportional to the vertical distance above the solidus ($z = 0$). The dashed lines mark the isotope ratio of the enriched endmember (see Supplementary Movie S2-1).

Figure 2-3 The effect of the size and trace element abundance of mantle heterogeneity on the variations of isotope ratios in the pooled melt, erupted melt, and residues (a to d). The enrichment factor (EMX), proportion of EM in the source, and the initial size of enriched heterogeneities are listed above each panel. Gray outlines at the

lower left and upper right corner are the range of isotope ratios of EM and DMM, respectively. Gray dots are global MORB data (PetDB). The pentagram is the average of global MORB. Contours show the probability density function of the composition of the erupted melt predicted by the model. Histograms show the marginal distribution of $^{143}Nd/^{143}Nd$ and $^{176}Hf/^{177}Hf$ in the source, residue, pooled melt, and erupted melt. Dashed lines on histograms mark the concentration average of the source.

Figure 2-4 Size-sensitive mixing for the residue and the melt. The $^{143}Nd/^{144}Nd$ of the residue (a) and the erupted melt (b) as a function of the enrichment strength of the heterogeneity (L*EMX). Colored dots are the $^{143}Nd/^{144}Nd$ at the peak of marginal distribution in the residue or the erupted melt. Vertical bars are the half-height width of the marginal distribution of $^{143}Nd/^{144}Nd$. The thick gray lines are the concentration average of the source. Dashed lines in (b) are the range of MORB. If the enrichment strength is smaller than 20 km (arrow in panel a), the peak of marginal distribution in the residue would converge to the source average, and no offset would be observed. If the enrichment strength is larger than 60 km (arrow in panel b), the range of isotopic compositions in the erupted melt would be larger than that observed in the MORB.

Supplementary figure captions

Figure S2-1 Histograms of Nd isotopes in abyssal peridotites (AP), residual abyssal peridotites and local MORB at (a) Mic-Cayman Ridge (Mallick et al., 2014), (b) Kane Fracture Zone from Mid-Atlantic Ridge (Mallick et al., 2014), (c) Vema Lithospheric Section from Mid-Atlantic Ridge (Cipriani et al., 2004), and (d) Southwest Indian Ridge (Salters and Dick, 2002; Warren et al., 2009).

Figure S2-2 (a) Correlation of Yb and Er in clinopyroxenes in abyssal peridotites. The composition of clinopyroxene in DMM (Salters and Stracke, 2004) is marked by the red cross. Gray crosses are the composition of clinopyroxene after 5%, 10% and 15% degree of melting. Data points with edges are residual abyssal peridotites. (b) Lack of correlation between the Yb concentration and $^{143}Nd/^{144}Nd$ in clinopyroxene. Abyssal peridotites with $^{143}Nd/^{144}Nd$ of 0.5132 could have melted for a wide range of degree of melting. Data includes the same sample set (Salters and Dick, 2002; Cipriani et al., 2004; Brunelli et al., 2006; Warren et al., 2009; Mallick et al., 2014) as Fig. S2-1 and more from Gakkel Ridge (Stracke et al., 2011). There is no locally associated MORB for Gakkel Ridge samples.

Figure S2-3 (a) Spatial variations of porosity in the 1D upwelling melting column. The four curves represent four choices of relative melt suction rate (S = 0.95, 0.90, 0.85 and 0.80), defined as the ratio of the rate of melt removal from the matrix to nearby high-porosity channels to the rate of matrix melting (Iwamori, 1993; Iwamori et al., 1995). Cases of perfect fractional melting and batch melting correspond to $S = 1$ and 0, respectively. Hence, we are considering near fractional melting in this study. (b) Spatial variations of residue and matrix melt velocities for four choices of melt

suction rate. V_0 is the solid upwelling rate at the solidus. At a given column height or degree of melting, the lesser the extent of melt extraction to channel is (i.e., smaller S), the higher the porosity and the faster the velocity of the melt in the matrix are. The velocity of the residue decreases upward to conserve mass.

Figure S2-4 The $^{176}Hf/^{177}Hf$ of the residue (a) and the erupted melt (b) as a function of the enrichment strength of the heterogeneity (L*EMX). Here, EMX is the concentration of Hf in EM normalized by DMM. Colored dots are the $^{176}Hf/^{177}Hf$ at the peak of marginal distribution in the residue or the erupted melt. Vertical bars are the half-height width of the marginal distribution of $^{176}Hf/^{177}Hf$. The thick gray line is the concentration average of the source.

Figure S2-5 The $^{143}Nd/^{144}Nd$ of the residue (a) and the erupted melt (b) as a function of the enrichment strength of the heterogeneity (L*EMX). Filled color dots and open symbols are the $^{143}Nd/^{144}Nd$ at the peak of marginal distribution in the residue or the erupted melt. Vertical bars are the half-height width of the marginal distribution of $^{143}Nd/^{144}Nd$. The thick gray lines are the concentration average of the source. The same results as Fig. 2-4 are plotted as fainted color and lines. The current figure includes more simulations with faster exchange rate (Da_{Nd} = 0.01, open squares) and more efficient melt extraction (S = 0.90, open circles).

Figure S2-6 The composition of melt collection, residues, pooled melt, and sources in the Hf-Nd isotope correlation diagram. The enrichment factor (EMX), proportion of EM in the source, and the initial size of enriched heterogeneities are listed at the top of this figure. Gray outlines at the lower left and upper right corner are the range

of isotope ratios of EM and DMM, respectively. Gray dots are MORB data. The pentagram is the MORB average. Dashed lines on histograms mark the concentration average of the source.

Figure S2-7 A comparison of the predicted compositions of the residue and erupted melt in a case with Hf offset but without Nd offset. Blue and red loops are contours of the probability density function of the residue and erupted melt. The enrichment factor (EMX), proportion of EM in the source, and the initial size of enriched heterogeneities are listed. Gray outlines at the lower left and upper right corner are the range of isotope ratios of EM and DMM respectively.

Figures

Figure 2-1 Histogram of $^{143}Nd/^{144}Nd$ in abyssal peridotites (a) and cartoon illustrating the double-porosity ridge model (b)

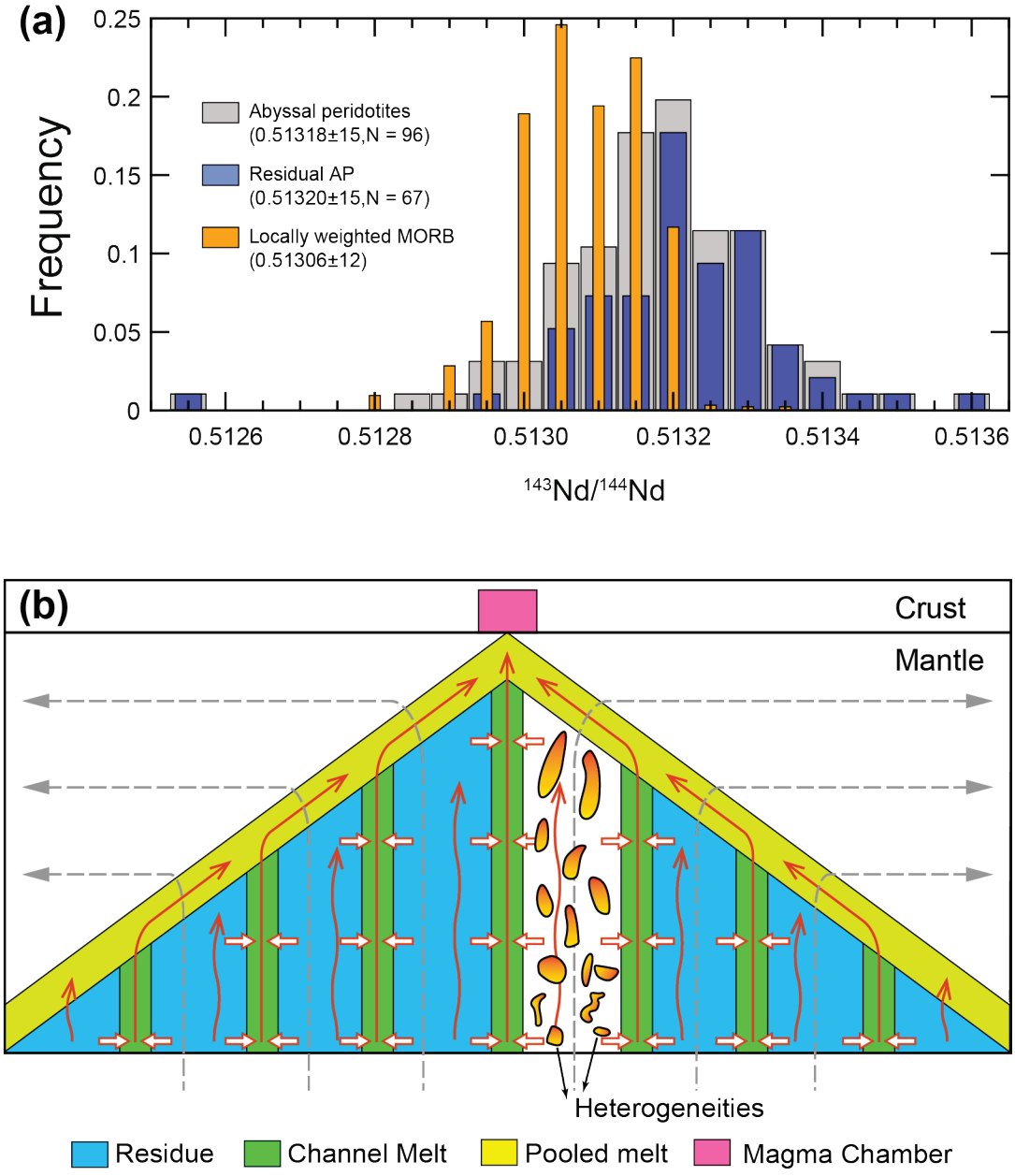

Figure 2-2 Stretching and dispersion of an enriched heterogeneity in an upwelling melting column

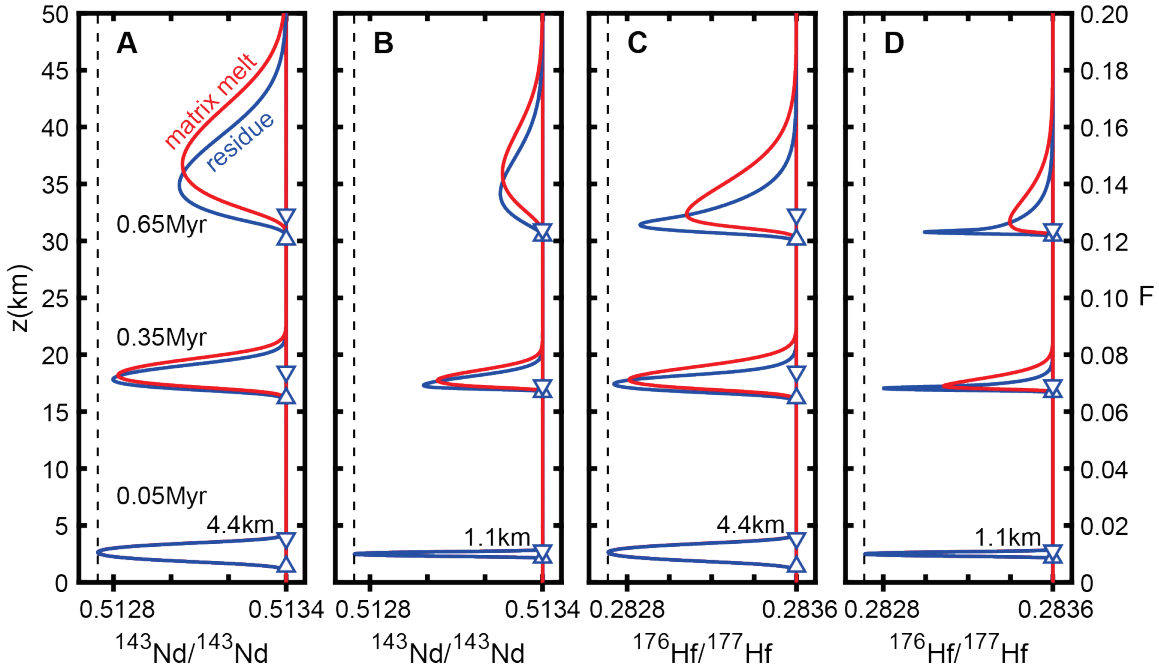

Figure 2-3 The effect of the size and trace element abundance of mantle heterogeneity on the variations of isotope ratios in the pooled melt, erupted melt, and residues

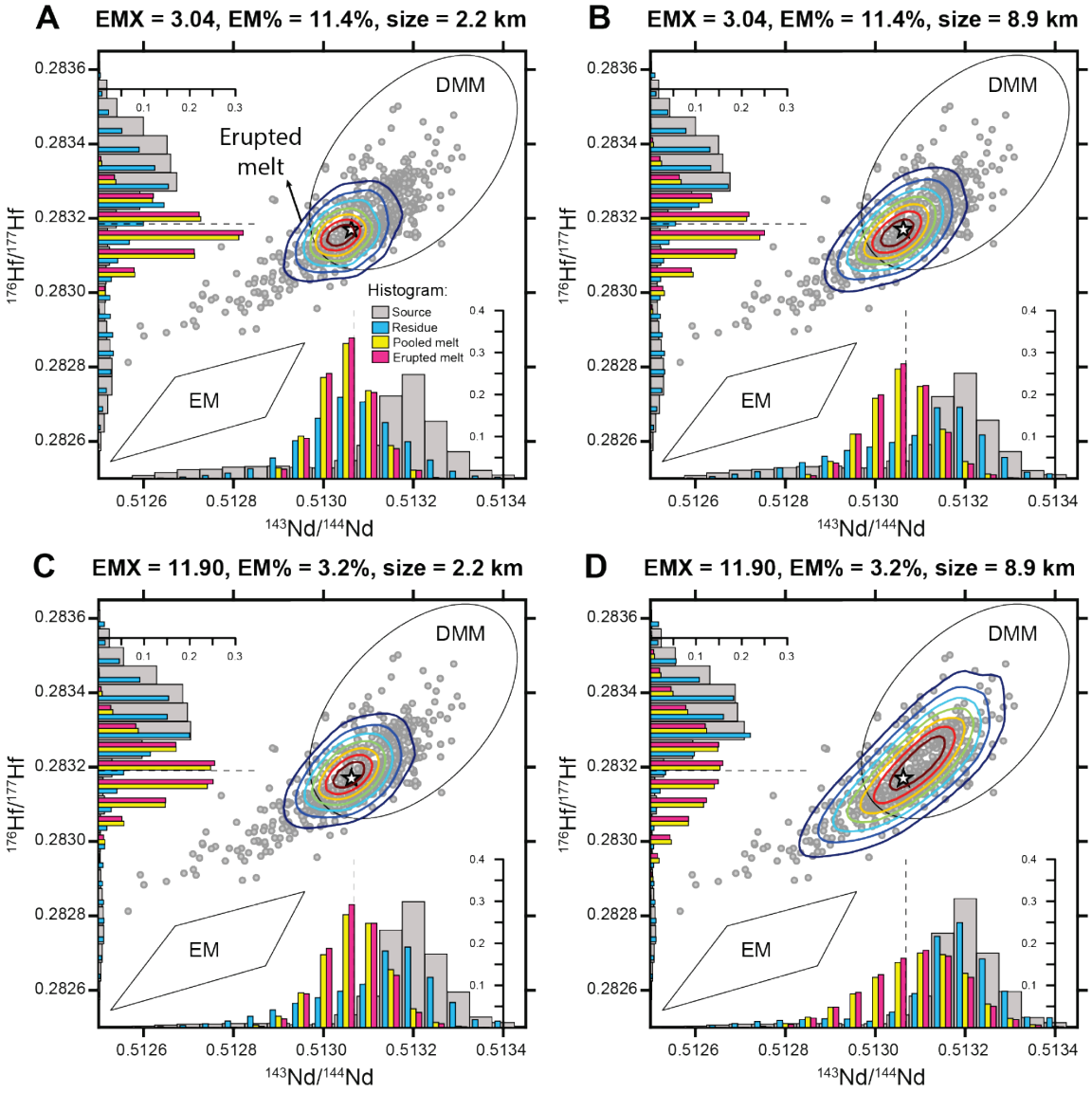

Figure 2-4 Size-sensitive mixing for the residue and the melt

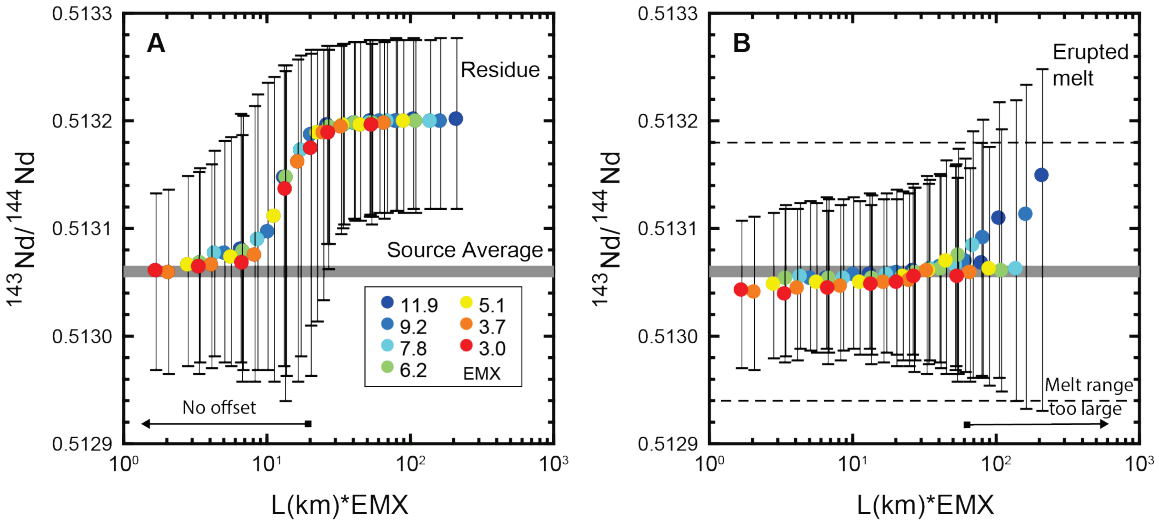

Figure S2-1 Histograms of Nd isotopes in abyssal peridotites, residual abyssal peridotites and local MORB at selected ridges

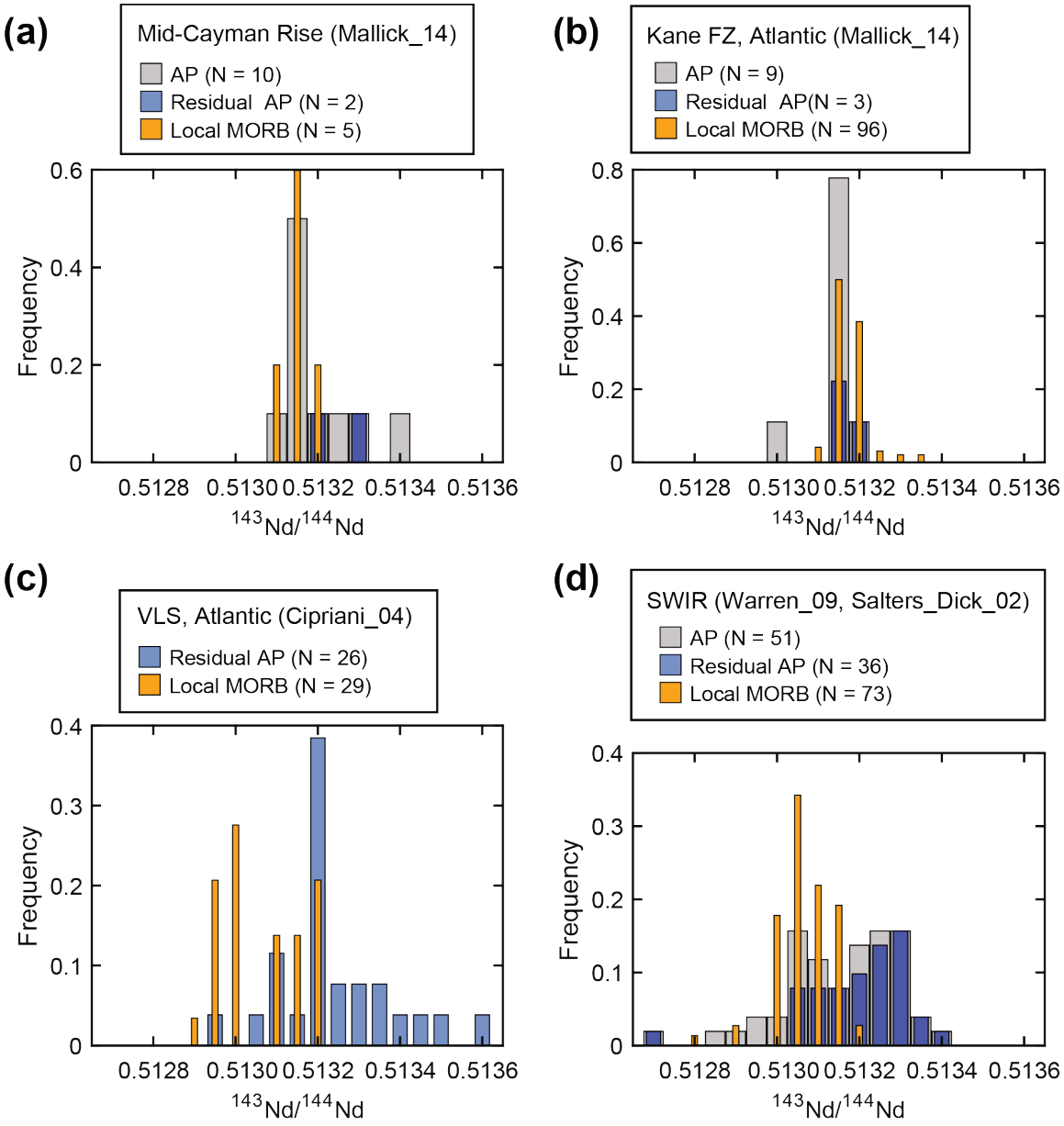

Figure S2-2 Correlation of Yb and Er in clinopyroxenes in abyssal peridotites(a) andlLack of correlation between the Yb concentration and $^{143}Nd/^{144}Nd$ in clinopyroxene (b)

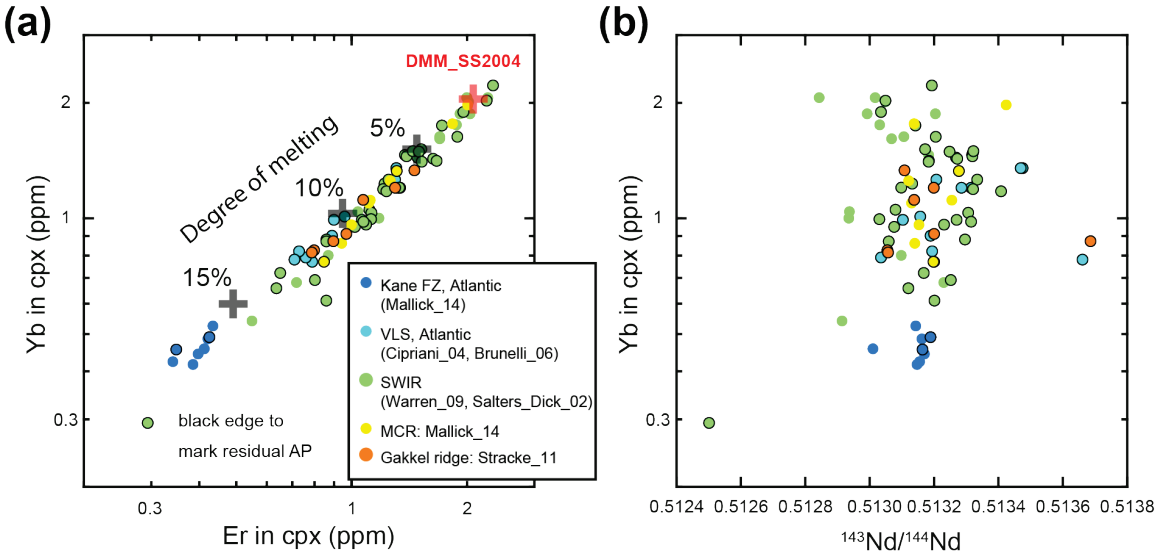

Figure S2-3 Spatial variations of porosity in the 1D upwelling melting column (a) and spatial variations of residue and matrix melt velocities for four choices of melt suction rate (b)

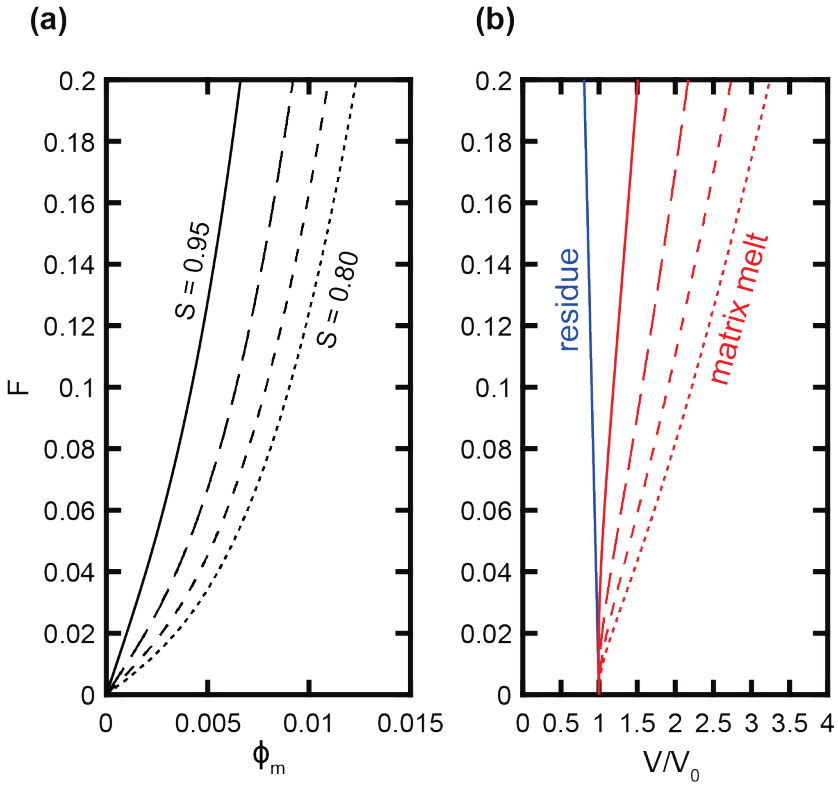

Figure S2-4 The $^{176}Hf/^{177}Hf$ of the residue (a) and the erupted melt (b) as a function of the enrichment strength of the heterogeneity

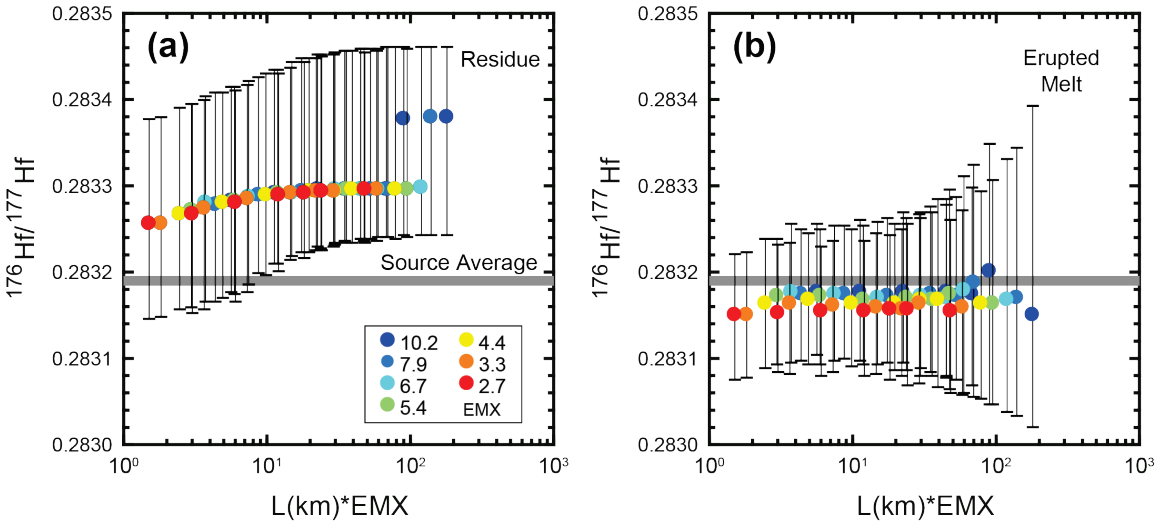

Figure S2-5 The $^{143}Nd/^{144}Nd$ of the residue (a) and the erupted melt (b) as a function of the enrichment strength of the heterogeneity (L*EMX)

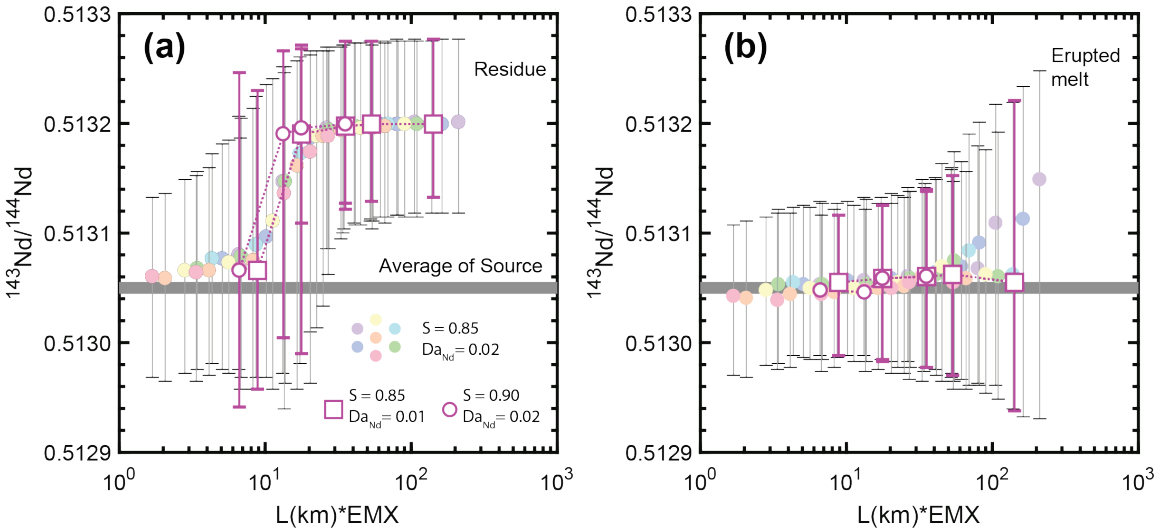

Figure S2-6 The composition of melt collection, residues, pooled melt, and sources in the Hf-Nd isotope correlation diagram

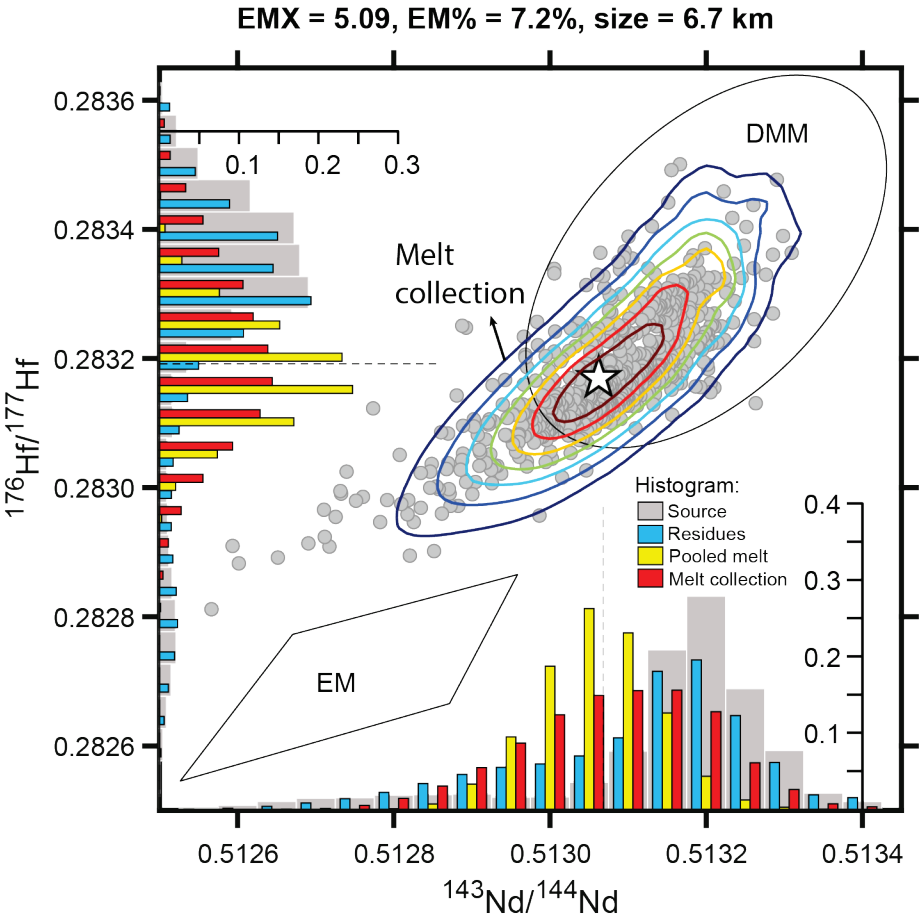

Figure S2-7 A comparison of the predicted compositions of the residue and erupted melt in a case with Hf offset but without Nd offset

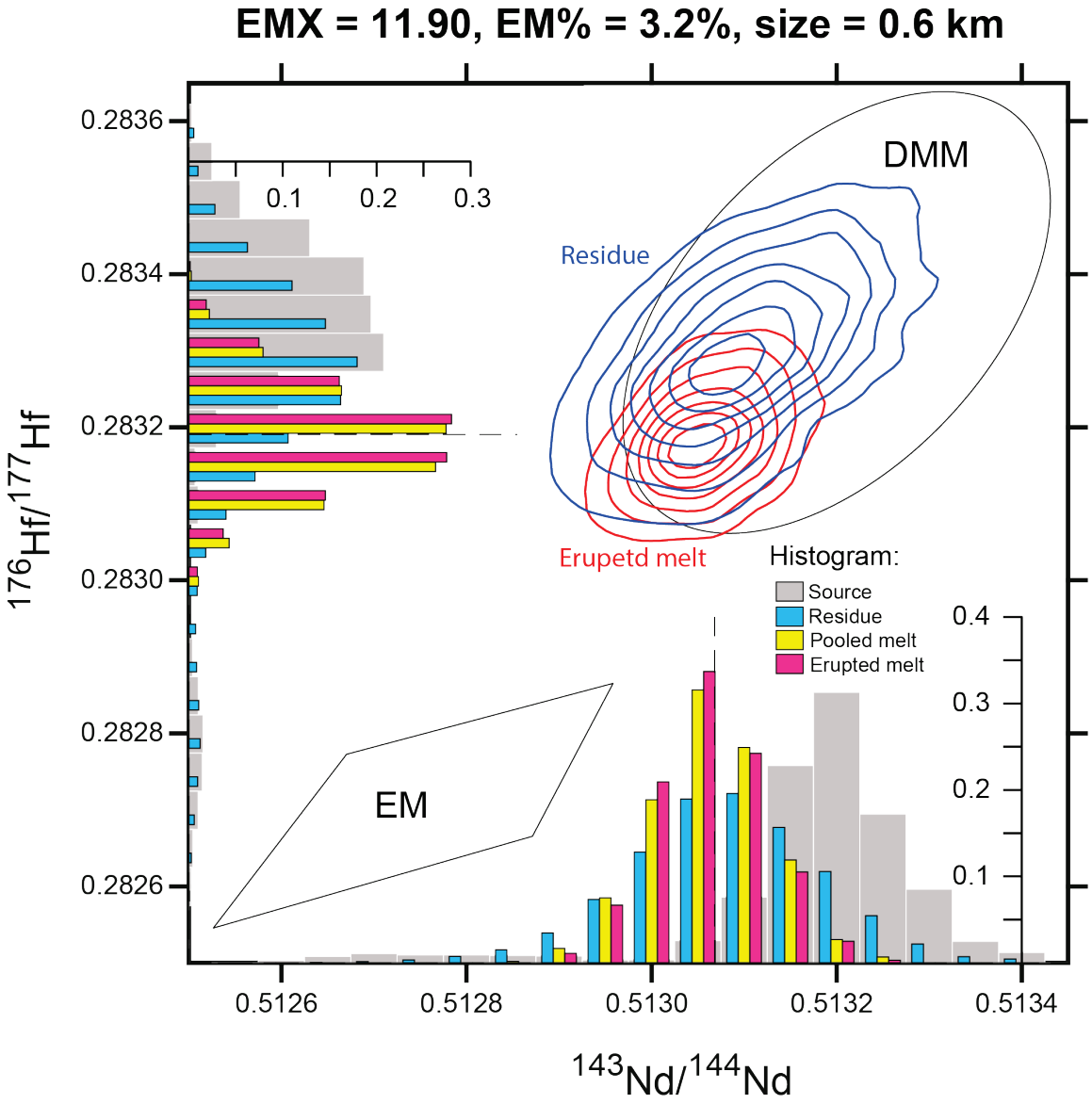

Supplementary Materials

Supplementary Table S2-1 Errors and numerical orders.

cells#	L_2		L_∞	
	error	order	error	order
12	2.61×10^{-4}		2.66×10^{-3}	
24	2.43×10^{-5}	3.43	3.42×10^{-4}	2.96
48	1.75×10^{-6}	3.79	3.16×10^{-5}	3.44
96	1.15×10^{-7}	3.93	2.42×10^{-6}	3.71
192	7.35×10^{-9}	3.97	1.67×10^{-7}	3.85

Supplementary Table S2-2 List of Physical Parameters

	Description	Related Expression	Value
A	Dimensionless along-ridge section area of the magma chamber	Eq. (A2-43)	1/200
C_ϕ	A constant in the expression of permeability[1]	Eq. (A2-18)	200
d	Mineral grain size used in the permeability	Eq. (A2-18)	3 mm
D_a	Damköhler number[2] describing the relative magnitude of melting versus chemical exchange	Eq. (A2-38)	0.01 to 0.04 for Nd, 0.05 to 0.2 for Hf
F_0	Reference degree of melting	Eq. (A2-37)	0.2
F	Degree of melting experienced by the bulk solid	Eq. (A2-9)	0 to 0.18
n	Exponent of porosity in the permeability[1]	Eq. (A2-18)	3
k_m	Bulk partition coefficient in the matrix		0.026 to 0.001 for Nd, 0.066 to 0.022 for Hf
k_p	Bulk partition coefficient for the melting reaction		0.06 for Nd, 0.24 for Hf
k_{ch}	Bulk partition coefficient in the channel		0
S	Melt suction rate	Eq. (A2-1)	0.80 to 1.00
V_0	Upwelling rate of the mantle source		5 cm/yr
z_0	Height of the melting column		50 km
η_f	Viscosity of the melt		10 Pa·s
ψ	Relative mass fraction of channel	Eq. (A2-3)	0.1
ϕ_{ch}	Porosity in the channel		0.02
ρ_f, ρ_s	Density of the melt or the solid		2700, 3300 kg/m^3

[1]Permeability model (Wark and Watson, 1998).

[2]also known as the disequilibrium parameter (Liang and Liu, 2016; Liu and Liang, 2017).

Supplementary Movie S2-1 Spatial variations of $^{143}Nd/^{144}Nd$ (a), $^{176}Hf/^{177}Hf$ (b), Nd (c), and Hf (d) as a function of the degree of melting are shown by blue lines (residue), red lines (matrix melt) and green lines (channel). The concentration in the melt is multiplied by the bulk partition coefficient to demonstrate the disequilibrium between the melt and the solid. The dashed lines in panel (c) and (d) show the depletion trend of equilibrium non-modal melting. The download link:

http://advances.sciencemag.org/highwire/filestream/199987/field_highwire_adjunct_files/0/1701872_MovieS1.mp4

CHAPTER 3

A two-dimensional double-porosity model for melting and melt migration beneath mid-ocean ridge spreading centers

Abstract

In this chapter, I study processes of partial meting and melt transport beneath mid-ocean ridge spreading centers using a double-porosity model that is constrained by geophysical and geochemical observations. The global mid-ocean ridge system is the primary location where new crust is produced. The magmatic processes at mid-ocean ridges may have continued for two billion years. Thus, the dynamics of mid-ocean ridges is an important problem for understanding the dynamic Earth. A plethora of observations have been made at current and relic mid-ocean ridges: compositions of the solidified melt and residual rocks, the seismic and magnetotelluric imaging, mapping of exposed ridge sections, etc. These independent observations can become more powerful if they can be jointly analyzed in a self-consistent model. The difficulty for such a model is to resolve and evaluate the effect of fine scale petrologic feature such as dunite channels in a tectonic-scale geodynamic model.

In an effort to address this first order problem, here I present a two-dimensional double-porosity model that consists of two overlapping continua made of high-porosity interconnected channel network and low-porosity lherzolite or harzburgite matrix. Melt generated in the matrix can be extracted to nearby channels and transport to the ridge axis. The porosity of the matrix and the dynamics of melt transport in the channel is controlled by the amount of melt extracted, the proportion of channels, and the permeability in the two continua. By using geochemically derived melt suction rate, field observed channel proportion and experimentally determined permeability model, the double-porosity model can make predictions of the porosity distribution, crustal thickness, REE in residual cpx, and U series concentration in extracted melts. These predictions will be compared with

observations to improve the understanding of the model and the melt generation processes beneath mid-ocean ridges.

A systematic study of the double-porosity ridge models over a range of cases has led to the following conclusions regarding the dynamics of the mid-ocean ridge. First, the orientation of high-porosity channels results in permeability anisotropy, which can enhance melt focusing by 50%. Second, the depth of the porosity maximum is controlled by the depth of melt extraction. The 60 km deep porosity maximum implied by magnetotelluric imaging on the East Pacific Rise is consistent with melt extraction into channels from 60 km depth and above. Third, depleted REE patterns in clinopyroxenes in abyssal peridotites is also consistent with melt extraction starting from 60 km depth. Fourth, the decrease of porosity due to melt extraction causes the Ra excess to grow in the matrix melt. And finally, the high Th excess is most likely produced by a combination of deep channels and high permeability. The approach taken here will serve future studies to synthesize more aspects of observations into a self-consistent ridge model based on which the local variation of mid-ocean ridge dynamics and general features of the global ridge system can be understood.

1. Introduction

The purpose of this study is to build a 2D double-porosity model that can be used to simulate channelized melt migration beneath mid-ocean ridges. I will show that the observed fine-scale channels which are suggested to be formed by various mechanisms can be integrated in a self-consistent geodynamic model. Results of this 2D double-porosity model can be tested by a range of first-order independent geochemical and geophysical observations. These observations include: 1) a porosity maximum deep below the ridge axis (Dunn and Forsyth, 2003; Baba et al., 2006; Yang et al., 2007; Key et al., 2013), 2) depleted REE patterns in clinopyroxenes in abyssal peridotites (Warren, 2016 and references therein), 3) excess of activity ratios of U-series (reviewed by Elliott and Spiegelman (2003)), and crustal thickness. The illustration of the double-porosity model and these three first-order observations are summarized in Fig. 3-1.

Current ridge models have demonstrated the general idea of melt migration in fractal networks of high-porosity channels beneath mid-ocean ridges (Kelemen et al., 1995; Kelemen et al., 1997; Weatherley and Katz, 2012; Keller et al., 2017). However, these models cannot produce fine-scale channel networks observed in the field. It is well known that mid-ocean ridge basalts are not in chemical equilibrium with residual mantle at low pressure (O'Hara, 1965; Stolper, 1980; Elthon and Scarfe, 1984; Klein and Langmuir, 1987). It has been inferred from petrological and geochemical observations that most melt generated in the upwelling mantle is transported through highly permeable dunite channels that occupy a small proportion of the melting region (Kelemen et al., 1997). Channelized melt migration is an effective mechanism to chemically isolated the melt from its surrounding harzburgite matrix, preserving geochemical signatures developed at depth.

According to a field compilation, the width of dunite channels ranges from 1 cm to ~100 m and sub-meter scale channels represent 99% the volume of all dunite channels (Braun and Kelemen, 2002).

One of the mechanisms of producing channelized melt migration is reactive infiltration instability (Daines and Kohlstedt, 1994; Aharonov et al., 1995; Aharonov et al., 1997; Spiegelman et al., 2001; Liang et al., 2011; Schiemenz et al., 2011; Peč et al., 2015; Peč et al., 2017). Numerical simulations of reactive infiltration in viscously deformable porous media have shown that high-porosity channel networks can be formed by fluxing reactive melt through partially molten mantle rocks (Spiegelman et al., 2001; Liang et al., 2011; Hesse et al., 2011; Weatherley and Katz, 2016; Keller et al., 2017). In a tectonic-scale simulation of channel networks beneath the mid-ocean ridge, the width of the thinnest channel produced by reactive infiltration instability is at least 1 km, which is only comparable to the widest channel observed in the field. Another mechanism of localizing melt for isolated transport is the shear-induced melt focusing that results in melt-rich bands (Stevenson, 1989; Holtzman et al., 2003; Katz et al., 2006). It has also been suggested that melt-filled hydro-fractures may be involved in the formation of some channels with sharp boundaries (Kelemen et al., 1995; Kelemen et al., 1997; Phipps Morgan and Holtzman, 2005). Explicit simulation of the aforementioned channel formation mechanisms in a tectonic-scale ridge model is still a computation challenge. Therefore, a model capable of analyzing the effect of fine-scale channels is needed to better understand geochemical and geophysical observations. Rather than working on the formation of channels, here I will focus on observational constraints on the distribution of channel networks.

The double-porosity model could reconcile a distribution of fine-scale channels and the tectonic-scale decompression melting. Such a model is first introduced to magma dynamics to solve trace element fractionation and U-series disequilibria in one dimension (Iwamori, 1993; Lundstrom, 2000; Jull et al., 2002; Liang and Parmentier, 2010). The model treats the highly-contrasted porosity in channels and surrounding residual rocks as two overlapping continua. One continuum, the interconnected melt channel network, has a small volume proportion but larger porosity and higher permeability. The other continuum, called the matrix, is the inter-channel region consisting of low porosity residual peridotites. Most melt generated from melting in the matrix is extracted to the channel (Iwamori, 1993).

An important parameter in the double-porosity model is the relative melt suction rate (S), defined as the ratio of melt extraction rate to the melting rate at a given location in the melting region (Iwamori, 1993a, 1993b). The relative melt suction rate should be at least 0.8 to satisfy REE patterns in abyssal peridotites from the Central Indian Ridge (Lundstrom, 2000; Liang and Peng, 2010). In Chapter one (also Liu and Liang, 2017), I presented sample-based inversion analysis of the melt extraction parameters using REE data in diopside in abyssal peridotites from five mid-ocean ridges (Salters and Dick, 2002; Hellebrand et al., 2005; Brunelli et al., 2006; Brunelli and Seyler, 2010; Warren and Shimizu, 2010; Lassiter et al., 2014; Mallick et al., 2014). The inversion result confirms that the melt extraction is efficient and the remaining melt flux in the residual matrix is small. Figure 3-2 shows the dependence of channel and matrix melt porosity and velocity on the dimensionless melt suction rate in an upwelling steady-state double porosity melting column. The porosity increases to a maximum of ~1% at the top of the melting column in

the matrix for a range of relative melt suction rate (Fig. 3-2). Larger melt suction rate results in smaller matrix porosity and matrix melt velocity, and faster channel melt velocity.

In more realistic cases, the melt suction rate and channel distribution may vary spatially in the melting column, which will affect the porosity in the melting region. In this chapter, I will examine the role of high-porosity channel on the distribution and transport of melts in the two-dimensional melting region beneath mid-ocean ridge spreading centers. I will examine six cases of possible channel distribution. I will test the model by comparing the result from all cases to independent geophysical and geochemical observations and will identify key features of the model that are important to explain the observations.

2. Method

2.1. The double-porosity ridge model

The double-porosity model has so far been applied to one-dimensional melting column (Iwamori, 1993; Jull et al., 2002; Liang and Parmentier, 2010), although the model is applicable to melt migration in higher dimensions. Here I consider a two-dimensional (2D) steady-state double-porosity ridge model. For simplicity, I assume that the solid in the channel and the matrix have the same velocity. The mass conservation equations for the matrix and channel continua are:

$$\nabla \cdot \left[\left(1-\psi\right) \rho_f \phi_m \mathbf{V}_f^m \right] = \left(1-\psi\right) \Gamma_m - \left(1-\psi\right) \Gamma_m S \ , \tag{3-1a}$$

$$\nabla \cdot \left[\left(1-\psi\right) \rho_s \left(1-\phi_m\right) \mathbf{V}_s^m \right] = -\left(1-\psi\right) \Gamma_m \ , \tag{3-1b}$$

$$\nabla \cdot \left(\psi \rho_f \phi_{ch} \mathbf{V}_f^{ch} \right) = \left(1-\psi\right) \Gamma_m S \ , \tag{3-1c}$$

$$\mathbf{V}_s^{ch} = \mathbf{V}_s^m \ , \tag{3-1d}$$

$$\Gamma_m = \rho_s \frac{dF}{dz} \frac{\left(1-\phi_m\right)\mathbf{V}_s^m \cdot \overrightarrow{\mathbf{n}_z}}{1-F}, \tag{3-1e}$$

where ψ is the volume fraction of channels (see section 2.3); ρ is the density; ϕ is the porosity; $\mathbf{V}$ is the velocity; Γ is the melting rate; S is the relative suction rate; subscript/superscript *m, ch, s, f* represent the matrix, channel, solid, and melt, respectively; F is the degree of melting; $\overrightarrow{\mathbf{n}_z}$ is the unit vertical vector, positive upward. Variables are listed in Table 3-1. To focus on the mechanics and chemistry of melt migration, here I use the degree of melting derived from pMELTS using DMM as the source composition (Asimow et al., 2001; Smith and Asimow, 2005; Workman and Hart, 2005). It is a first-order approximation valid when the geotherm of the asthenospheric mantle follows a melting adiabat (Turcotte and Schubert, 2002). Thus, I have implicitly assumed in Eq. (3-1e) that the degree of melting is a function of depth. To account for deeper final melting pressure for slower spreading ridges (Niu and Hékinian, 1997), I have suppressed melting in the shallowest 10 km for fast half-spreading rate (100 mm/yr) or in the shallowest 20 km for medium spreading rate (50 mm/yr).

Eq. (3-1a) states that the divergence or accumulation rate of melt in a representative elementary volume (REV) in the matrix continuum is due to matrix melting (first term on the right) and removal or extraction of melt from the matrix to the channel continuum in the REV (second term). The volume fraction of the REV participates in the melting is $1-\psi$, i.e., the proportion of matrix in the REV. Most melt generated by melting will be extracted to channels. Hence the relative melt suction rate is close to one on average.

However, the melt extraction rate can be larger than the melting rate in a restricted area where the matrix melting rate is low or vanishes ($S > 1$). Thus, not only the newly generated melt but also part of the existing matrix melt that flows into the REV from below will be extracted to the channel in the REV. Eqs. 3-1b and 3-1c state that changes in the divergence of solid in the matrix continuum and the divergence of melt in the channel continuum are due to matrix melting and extraction of matrix melt to the channel continuum, respectively. The sum of Eqs. 3.1a-3.1c recovers the global mass conservation for the REV (Liang and Parmentier, 2010).

The momentum equations for the matrix and the channel are (McKenzie, 1984; Jull et al., 2002):

$$\phi_m \left(\mathbf{V}_f^m - \mathbf{V}_s^m \right) = -\frac{1}{\eta_f} k_\phi^m \cdot \nabla P_{pz}, \tag{3-2a}$$

$$\phi_{ch} \left(\mathbf{V}_f^{ch} - \mathbf{V}_s^{ch} \right) = -\frac{1}{\eta_f} \mathbf{k}_\phi^{ch} \cdot \nabla P_{pz}, \tag{3-2b}$$

$$\nabla P_{pz} = \eta_s \nabla^2 \mathbf{V}_s^m + \left(\zeta_s + \frac{1}{3}\ \eta_s \right) \nabla \left(\nabla \cdot \mathbf{V}_s^m \right) + \Delta\rho \mathbf{g}, \tag{3-2c}$$

where $\mathbf{k}_f^{m,ch}$ is the permeability tensor (see section 2.2); P_{pz} is the piezometric pressure or the "pressure in excess of hydrostatic pressure" (Spiegelman and McKenzie, 1987); ζ_s and η_s are bulk and shear viscosity of the solid, respectively; η_f is the shear viscosity of the melt (Murase and McBirney, 1973); $\mathbf{g}$ is the gravitational vector; $\Delta\rho$ is the density difference between the solid and the melt. Eqs. (3-2a) and (3-2b) are the Darcy's law, accounting for the flow of melt relative to the solid. Eq. (3-2c) states that the gradient of

piezometric pressure arises from shear deformation in the solid (first term on the right hand side), compaction in the solid (the second term on the right hand side), and buoyancy (the third term on the right hand side). The viscosity of the solid is controlled by a number of competing effects (Braun et al., 2000). In this study, I will use uniform viscosity for the solid. Two values of η_s (10^{19} Pa·s or 10^{21} Pa·s) will be tested.

The model domain is 100 km deep and 200 km wide (Fig. 3-3a). The ridge axis is at the middle top. For simplicity, the lithosphere has a wedge shape. The angle of the wedge should decrease with the spreading rate because of the effect of half-space cooling (Turcotte and Schubert, 2002). Here, I use an angle of 13° for fast spreading ridge and 25° for medium spreading rate. The velocity of the solid at the lower boundary of the lithosphere is the half spreading rate. Melt can flow along the lithosphere-asthenosphere boundary near the axis because a decompaction boundary layer would form under fast crystallization rate (Sparks and Parmentier, 1991; Spiegelman, 1993; Hebert and Montési, 2010). If melt flow hit the LAB away from the axis, the melt freezes. The geometry and boundary condition are illustrated in Fig. 3-3.

Instead of simulating the formation of individual channel, the distribution and orientation of channels will be prescribed in the double-porosity model. This allows us to focus on porosity and the chemistry of channelized melt migration. There are three unknown scalars ($\phi_m, \phi_{ch}, P_{pz}$) and three unknown vectors ($\mathbf{V}_s^m, \mathbf{V}_f^m, \mathbf{V}_f^{ch}$). They can be solved from Eqs. (3-1a), (3-1b), (3-1c), (3-2a), (3-2b), and (3-2c) if the melting rate and the solid velocity in the channel are reduced by Eq. (3-1e) and (3-1d). The dimensionless form of the working equations and the numerical method are presented in the Appendix.

In the next two sections, I will discuss the orientation of channels and possible cases of channel distribution.

2.2. The orientation and permeability of channels

The orientation of individual channels in an upwelling mantle is not constrained. Intuitively one would expect that the average channel orientation be parallel to the melt flow direction, although this can be complicated by deformation (Baltzell et al., 2015). From Eq. (3-2a), we know that the direction of the melt flow in the channel depends on the velocity of the solid, the pressure gradient, and the permeability tensor. The velocity of the solid is much smaller than the velocity of the melt in the channel (Jull et al., 2002). Thus, it has little effect on the flow pattern in channels. The pressure gradient could be comparable to the buoyancy term only if the shear viscosity of the solid is greater than 10^{21} Pa·s (Morgan, 1987; Spiegelman and McKenzie, 1987). However, the rapid glacial rebound at Iceland suggests that the viscosity of oceanic mantle is less than 10^{19} Pa·s (Sigmundsson, 1991). The viscosity could increase by two orders of magnitude due to dehydration (Braun et al., 2000; Hirth and Kohlstedt, 2003). In this study, two values of η_s (10^{19} Pa·s or 10^{21} Pa·s) will be tested. Within this range, the pressure gradient is likely to be nearly vertical. If this is the case and the permeability is isotropic, nearly vertical melt channels would merge to the decompaction channel at LAB (Keller et al., 2017), suggesting that the active focusing by pressure gradient is not an effective mechanism to divert the channelized melt flow.

The melt flow can be tilted by anisotropic permeability (Morgan, 1987). The anisotropic permeability model used by Morgan (1987) aligns the easy-flow direction

along the maximum extension axis. This contradicts the rock deformation experiment where melt bands localized at a low angle to the maximum compression axis (Holtzman et al., 2003). The predicted melt band orientation shows great potential of focusing the melt (Katz et al., 2006). Fractures may also produce tilted channels, but the condition of brittle deformation is unlikely to be met in the asthenospheric mantle (Morgan, 1987). The grain size-induced barrier is another possibility of tilted channels (Turner et al., 2017). But it is unclear how the grain size varies with the presence of pyroxenes and reactive melt flow. Therefore, the mechanism of shear-induced melt band is a strong candidate of tilted channels because the strain state capable of producing the melt band is plausible beneath mid-ocean ridges (Morgan, 1987; Holtzman et al., 2003).

In the double-porosity model examined in this study, I assume that the permeability of the matrix continuum is isotropic, while the permeability of the channel continuum is anisotropic. I will use the orientation of the melt band produced in the shear deformation experiment to formulate the anisotropic permeability in the channel continuum. For vertical channels, anisotropic permeability is not required for the orientation of the melt flow because the pressure gradient is nearly vertical. The permeability tensor can be written as,

$$\mathbf{k}_\mathbf{f}^{\mathbf{ch}} = \Theta^T \begin{bmatrix} k_\phi^{iso} + k_\phi^{add} & 0 \\ 0 & k_\phi^{iso} \end{bmatrix} \Theta, \tag{3-3a}$$

$$\Theta = \begin{bmatrix} \cos(\theta) & \sin(\theta) \\ -\sin(\theta) & \cos(\theta) \end{bmatrix}, \tag{3-3b}$$

$$k_\phi^{iso} = \frac{d_{ch}^2 \phi_{ch}^n}{C_\phi}. \tag{3-3c}$$

where $\mathbf{k_f^{ch}}$ is the permeability tensor in the channel; k_ϕ^{iso} is the isotropic permeability which is a function of grain size and porosity (Wark and Watson, 1998; Miller et al., 2014); d_{ch} is the grain size in channel; n and C_ϕ are constants in the permeability model; k_ϕ^{add} is the magnitude of the anisotropic permeability on the easy-flow direction; Θ is the rotation or orientation tensor; and θ is the dip of the easy-flow direction.

Based on thermodynamic analyses and laboratory dissolution studies (Daines and Kohlstedt, 1994; Asimow and Stolper, 1999; Morgan and Liang, 2005), I assume that the dunite channels are pyroxene-free and have larger grain size than residual matrix. The presence of pyroxene could also increase the mean dihedral angle and reduce permeability (Zhu and Hirth, 2003). Thus, the permeability of channels should be larger than the matrix for the same porosity. For the purpose of demonstration, I test a range grain size in the matrix (0.4 mm-3 mm) and in the channel (1.4 mm-10 mm).

A rank-two tensor has three degrees of freedom. Here, $\mathbf{k}_\phi^{ch}$ is decomposed into an isotropic component (k_ϕ^{iso}) and a special anisotropic component with two degrees of freedom (k_ϕ^{add} and θ). The magnitude of the additional anisotropic component of the permeability increases with k_ϕ^{add} . Experiments show that the melt band form if the shear strain of the rock is greater than one (Holtzman et al., 2003). As a first attempt to add anisotropy to the channel permeability and for purpose of demonstration, I assume that θ is a function of the shear strain of the solid, γ, and takes on the simple expression:

$$\theta = \left(\theta_s - \frac{\pi}{2}\right) \cdot \frac{1}{2} erfc\left(\frac{0.5-\gamma}{0.2}\right) + \frac{\pi}{2} , \qquad (3\text{-}4a)$$

where θ_s is the predicted dip of the melt band; $erfc$ is the complementary error function. If the shear strain is small, the dip of the channel is vertical. If the shear strain is larger than one, the dip of the channel is consistent with the dip of the shear-induced melt band.

The factor k_ϕ^{add} should be zero when there is no strain. k_ϕ^{add} approaches a positive value when the fabric is fully developed after sufficient shear. Hence the additional permeability along the orientation of melt band is also a function of shear strain:

$$k_\phi^{add} = \frac{\beta k_\phi^{iso}}{2} erfc\left(\frac{0.5-\gamma}{0.2}\right), \tag{3-4b}$$

where β is an amplification factor of the additional anisotropic permeability in a fully developed melt-band fabric.

The bulk porosity and bulk melt flux of the double-porosity medium are defined as volume averages of the respective quantities in the matrix and channel continuum in the REV:

$$\phi_{bulk} = (1-\psi)\cdot\phi_m + \psi\phi_{ch}\ , \tag{3-5a}$$

$$\phi_{bulk}\mathbf{V}_f^{bulk} = (1-\psi)\phi_m\cdot\mathbf{V}_f^m + \psi\phi_{ch}\cdot\mathbf{V}_f^{ch}\ . \tag{3-5b}$$

2.3. Channel distribution

The first type of channel is the decompaction channel at LAB. Two inclined channels share the axis as the end point and have a finite length. According to Sparks and Parmentier (1991) and Spiegelman (1993), the decompaction layer arises as fast crystallization produces a boundary layer where buoyancy balances decompaction pressure.

The thickness of such channel is comparable to the "reduced compaction length" which is on the order of 100 m (Ribe, 1985; Sparks and Parmentier, 1991). I will treat the decompaction channels as part of boundary conditions in our modeling calculations. Any melt channel that merges to the decompaction channel will transfer its melt flux into the decompaction channel. In the numerical model, I place a thin layer with high permeability along the LAB to force the channel melt to flow to the axis. The length of the decompaction channel is based on Hebert and Montési (2010). I will test two cases of spreading rate. For 100 mm/yr half-spreading rate, the channel is 20 km wide at each side while for 50 mm/yr half-spreading rate, the width is 50 km on each side (Hebert and Montési, 2010). The region of LAB outside of the decompaction layer has no porosity.

There are two regions of large shear strain where tilted channels could form. The thickness of the regions increases from 10 km at the axis to 60 km at 100 km away from the axis (area highlighted in light green color in Fig. 3-3a). The proportion of tilted melt channels inside these two zones may be <10% according to the deformation experiment (Holtzman et al., 2003), with the caveat that the there is no melt flow in the experiment. For simplicity, the channel proportion in the region where both reactive infiltration and shear-induced melt localization are effective is set the same as that in regions where only one of the mechanism is effective.

Replacive channels are expected to be distributed in regions affected by melt-rock reaction. The proportion of replacive channels in the uppermost mantle, as indicated by the dunite proportion in mantle massifs, is 5% to 15% (Boudier and Coleman, 1981; Kelemen et al., 1997). The analysis on the solubility of pyroxenes in basalt has reached similar estimate on the proportion of channels produced by melt-rock reaction (Kelemen

et al., 1995). Because MORB is undersaturated in pyroxenes below 0.9-1 GPa (O'Hara, 1965; Stolper, 1980; Elthon and Scarfe, 1984), the isolated melt transport path has a minimum depth of 25 km. In other words, the existence of channels must extent to at least 25 km deep to limit the chemical interaction of the basalt and the surrounding harzburgite (Kelemen et al., 1997). In the deeper part of the melting region, the proportion of channels is not well constraint. Simulations show that there could be harzburgite channels in the lherzolite matrix at the lower part of the melting region (Liang et al., 2010; Liang et al., 2011). The proportion of harzburgite channels should be smaller than the that of overlying dunite channels because of the smaller melt flux and smaller capability of the melt generated at depth to dissolve pyroxenes.

2.4. Crustal thickness

Both the matrix and the channel contribute to the focused melt that forms the oceanic crust. The crustal thickness is calculated by dividing the volume flux of melt focused to the axis by the full-spreading rate (Forsyth, 1993). The total melt flux can be calculated by an integral of flux at the outflux boundary. However, this approach is subjected to unreliable solution near the singularity. Here I will use the volume integral to calculate the melt flux and crust thickness (Forsyth, 1993).

$$d_{crust} = d_{crust}^{m} + d_{crust}^{ch} \ , \tag{3-6a}$$

$$d_{crust}^{m} = \frac{1}{2\rho_f V_0} \int_{\Omega_m} dxdy \cdot \left[(1-\psi)\Gamma_m - (1-\psi)\Gamma_m S \right] \ , \tag{3-6b}$$

$$d_{crust}^{ch} = \frac{1}{2\rho_f V_0} \int_{\Omega_{ch}} dxdy \cdot (1-\psi)\Gamma_m S \, . \tag{3-6c}$$

where d_{crust} is the total crustal thickness; d_{crust}^{m} and d_{crust}^{ch} are contributions from the matrix melt and channel melt; V_0 is the half spreading rate; Ω_m and Ω_{ch} are regions of melt focusing zones for the matrix and the channel, from which matrix melt and channel melt are delivered to the ridge axis, respectively. In practice, $\Omega_{m,ch}$ is bounded by the decompaction channels beneath LAB, two melt streamlines on the sides, and the lower boundary. The width of the melt focusing zone depends on how the streamline of the melt is inclined to the ridge axis. The integrands in Eq. (3-6b) and Eq. (3-6c) are the right hand side of Eq. (3-1a) and Eq. (3-1c), respectively.

2.5. Trace element concentration

The steady state mass conservation equations for the concentration of a trace element in the matrix melt and the channel melt are modified after Liang and Parmentier (2010). In addition, the following equations are generalized for radiogenic parent or daughter isotope. For the purpose of demonstration, this section will be restricted to REE, ^{234}U, ^{230}Th, and ^{226}Ra. I assume that the solid and melt in the matrix are in local chemical equilibrium in the REV. For simplicity, the chemical flux in the solid of channels is neglected due to the very small olivine-melt partition coefficients for the aforementioned trace elements. Including radioactive decay and production, the mass conservation equations for a chemical species, *i*, in the matrix and channel are

$$\begin{aligned}
&\nabla\cdot\left(\rho_f\left(1-\psi\right)\phi_m\mathbf{V}_f^m C_f^{m,i}+\rho_s\left(1-\psi\right)\left(1-\phi_m\right)\mathbf{V}_s^m k^i C_f^{m,i}\right)\\
&=-\left(1-\psi\right)\Gamma_m S C_f^{m,i}-\left[\rho_s\left(1-\psi\right)\left(1-\phi_m\right)k^i+\rho_f\phi_m\left(1-\psi\right)\right]\lambda_i C_f^{m,i}\\
&+\left[\rho_s\left(1-\psi\right)\left(1-\phi_m\right)k^{i-1}+\rho_f\phi_m\left(1-\psi\right)\right]\lambda_{i-1}C_f^{m,i}
\end{aligned}, \quad \text{(3-7a)}$$

$$\nabla\cdot\left(\psi\rho_f\phi_{ch}\mathbf{V}_f^{ch}C_f^{ch,i}\right)=\left(1-\psi\right)\Gamma_m SC_f^{m,i}-\psi\rho_f\phi_{ch}\left(\lambda_i C_f^{ch,i}-\lambda_{i-1}C_f^{ch,i-1}\right). \quad (3\text{-}7b)$$

where C is the concentration of a trace element or isotope; C^i is the radiogenic daughter of C^{i-1}; k^i and λ_i are the bulk partition coefficient and the decay constant of isotope C^i, respectively.

The difference between the present model and the batch melting model of Spiegelman and Elliott (1993) is the chemical flux in extracted melt, i.e., the first term on the right-hand side of Eqs. (3-7a) and (3-7b). The left-hand side of Eq. (3-7a) is the net change (or the divergence) of chemical flux in the bulk matrix. The second term on the right-hand side of Eq. (3-7a) is the radiogenic loss in the melt and solid of the matrix, while the third term on the right-hand side is the radiogenic gain. The left-hand side of Eq. (3-7b) is the net change of the chemical flux in the channel where the chemical flux in the solid is neglected. The second term on the right-hand side of Eq. (3-7b) is the radiogenic loss in the channel melt, while the third term on the right-hand side is the radiogenic gain.

For non-radiogenic trace element, the concentration in the pooled melt can be calculated by dividing the total chemical flux by the sum of focused matrix melt flux and focused channel melt flux:

$$C^{pooled}=\frac{\int_{\Omega_m} dxdy\cdot\left(1-\psi\right)\left(1-S\right)\Gamma_m\cdot C_f^m+\int_{\Omega_{ch}} dxdy\cdot\left(1-\psi\right)\Gamma_m S\cdot C_f^m}{\int_{\Omega_m} dxdy\cdot\left(1-\psi\right)\left(1-S\right)\Gamma_m+\int_{\Omega_{ch}} dxdy\cdot\left(1-\psi\right)\Gamma_m S}. \quad (3\text{-}8a)$$

The numerator is the sum of the fluxes of the trace element in the matrix melt and the channel melt focused to the ridge axis. The two terms in the denominator have been used to derive the crustal thickness. The expression for radiogenic isotope concentration in

pooled melt is complicated because it needs to consider the radiogenic gain and loss during melt focusing (see the Appendix for calculating the concentration of radiogenic isotopes in focused melt).

3. Results: Porosity distribution, flow pattern, and crustal thickness

3.1. The reference case with no channels in the melting region

This case is comparable to Spiegelman and McKenzie (1987) except that the present setup includes the matrix melting and two decompression channels beneath the LAB (illustrated as case#1 in Fig. 3-3b). As shown in Fig. 3-4, the solid viscosity is small (1×10^{19} Pa·s). The porosity increases upward, and the melt (dashed lines) follows the solid flow (white solid lines) at the lower part of the domain. As the melt accelerates due to buoyancy, the pattern of melt flow has more vertical component than that of the solid flow. The active focusing by pressure gradient is negligible in this case of relatively weak solid rheology. The decompaction layer beneath the LAB is an effective melt focusing mechanism in this case. Melt focused to the ridge axis will form an 5.17 km thick crust.

3.2. Channelized melt flow with isotropic permeability

In this case, the channel network has a volume fraction of 10% and a relative suction rate of 0.9 in the partially molten region (illustrated as case#2 in Fig. 3-3b). The permeability in the channel is isotropic ($\beta = 0$). The melt porosity in the matrix is smaller than the reference case of no channelized melt migration. The smaller matrix porosity hinders Darcy flux. Consequently, the flow pattern of the melt in the matrix follows more closely to the solid flow in Fig. 3-5a. The melt focusing zone for the matrix melt is narrower

than the case with no channels. Active focusing of matrix melt is still negligible. Matrix melt delivered to the ridge axis will form an 0.42 km thick crust.

The permeability in the channel is higher than the matrix and the driving force of channel melt flow is dominated by buoyancy. Thus, the channel melt percolates fast in nearly vertical direction. The width of melt focusing zone for the channel is the same as the decompaction channel beneath LAB (Fig. 3-5b), which is considerably wider than that for the matrix (cf. Figs. 3-5a and 3-5b). Since 90% percent melt enters the channel at the place of melt generation ($S = 0.9$), we would expect that crust accumulated by channel melt should be more than nine times of that accumulated by the matrix melt. Indeed, channel melt focused to the axis will form a 5.10 km thick crust.

The bulk porosity of the double-porosity medium is slightly larger than the porosity in the matrix (cf. Figs. 3-5a and 3-5c). The contribution of channel melt to the bulk porosity is small because the proportion of channels is small (see section 4.1 for more discussion). A total of 5.53 km thick crust will be produced in this case.

3.3. Channelized melt flow with anisotropic permeability

In this case, the volume proportion of channels and the relative melt suction are the same as the previous case. The permeability in the channels is anisotropic ($\beta = 2$, illustrated as case#3 in Fig. 3-3b). The channel melt is diverted by the anisotropic permeability in the region of high strain. The melt focusing zone for the channel is expanded. The channel melt in this case will accumulate to a thicker crust compared to the isotropic case (5.10 vs. 5.46 km, cf. Figs. 3-5b and 3-6b), indicating that the melt flux in the channel is slightly larger than the case of isotropic permeability. Because of the

enhanced permeability along the easy flow direction, the melt velocity is faster and the porosity is smaller than the previous case (cf. Figs. 3-5b and 3-6b). The bulk porosity is smaller than the isotropic case due to the smaller channel porosity in this case. A total of 5.89 km thick crust will be produced in this case.

3.4. Cases with channel distribution

3.4.1. More dunite channels in the upper part of the melting region

This case explores the effect of more dunite channels in the upper part of the melting region and isotropic permeability in the channel. Here I assume that the proportion of channels increases from 5% in the lower 70 km to 10% in the upper 30 km (illustrated as case#4 in Fig. 3-3b). The relative melt suction rate increases from zero in the lower 70 km to 150% in the upper 30km. The depth of melt extraction and isolated melt transport satisfies the minimum depth of channels required by petrological constraints (O'Hara, 1965; Stolper, 1980; Elthon and Scarfe, 1984). The relative melt extraction rate in the upper part is greater than one so that melt retained in the matrix can be extracted into the channel as the matrix upwells above 30 km depth.

The distributed channel and melt extraction rate affect the melt distribution in the matrix and the channel. The lower part of the matrix melt distribution is comparable to the case with no channels inside the melting region (cf. Figs. 3-4 and 3-7a). In the upper part where matrix melt is extracted to channels, the porosity in the matrix is reduced. The contribution of matrix melt to the crustal thickness is reduced compared to the channel-free reference case (4.22 vs. 5.17 km).

In the deeper part of the channel continuum, the porosity is significantly reduced compared to the case with uniform melt extraction (cf. Figs. 3-6b and 3-7b). The porosity in channels is smaller than the case where melt extraction is ubiquitous in the partially molten mantle. The contribution of channel melt to crustal thickness is small (0.95 km) because most melt flux is retained in the matrix.

3.4.2. More channels in shear zone

This case has the same depth of channel as the previous case. The additional feature here is more channels in the region of high shear strain (illustrated as case#5 in Fig. 3-3b). Consequently, the porosity of matrix melt in regions of high shear strain is reduced (cf. Figs. 3-7a and Fig. 3-8a). The region of high matrix porosity (larger than 2%) is much narrower than the case without additional melt extraction due to shear (cf. 150 km in Fig. 3-7a and 50 km in Fig. 3-8a). Because of the additional melt extraction in regions of high strain, the melt flux in the channel is larger. The melt focusing area for channels is wider and the contribution of channel melt to crustal thickness is larger compared to the previous case without additional channels in regions of high shear strain.

3.4.3. Deep melt extraction starting from 60 km

In this case, melt extraction from the matrix to the channel initiates from 60 km depth (illustrated as case#6 in Fig. 3-3b). Above 60 km, the relative melt suction rate is greater than unity. The relative suction rate is adjusted so that all melts will be extracted to the channel. The porosity in the matrix has a maximum at 60 km and decreases to zero under LAB. Compared to the previous case with smaller area of melt extraction, the

maximum of bulk porosity decreases in magnitude and increases in depth (cf. Figs. 3-8c and 3-9c). The crustal thickness is 5.96 km in this case.

4. Discussion

4.1. Melt extraction reduces total porosity

Results presented in the preceding section demonstrate that extraction of melt from the matrix to the channel significantly reduces the total porosity. This porosity reduction is the sum of two competing effects: smaller matrix porosity and larger channel porosity. Here I use simple scaling relationships to explain why the bulk porosity decreases in the case of more melt extraction. The melt fluxes in the matrix and the channel in a one-dimensional steady state melting column are:

$$\left(1-\psi\right)\rho_f\phi_m V_f^m = \left(1-\psi\right)\Gamma_m z\left(1-X\right) , \tag{3-9a}$$

$$\psi\rho_f\phi_{ch} V_f^{ch} = \left(1-\psi\right)\Gamma_m zX . \tag{3-9b}$$

where z is the distance above the solidus. Here, X is the proportion of channel melt flux relative to the total melt flux and it should be smaller than one. Generally, the flux of channel melt increases with the integrated melt suction rate from below. For simplicity, I assume that the proportion of channels, the relative melt suction rate, and the melting rate are constant. Under these assumptions, X in Eq. (3-9b) is the relative melt suction rate, S, in the melting column. The REE patterns in abyssal peridotites require that S is between 0.6 to 1.0 in a melting model with constant relative melt suction rate (Lundstrom, 2000; Liang and Peng, 2010). Thus, the reasonable range for X is 0.6 to 1.0.

The Darcy's law for the matrix and the channel can be simplified if the melt velocity is sufficiently larger than the solid velocity and the driving force is dominated by buoyancy, viz.,

$$\phi_{m,ch} V_f^{m,ch} = \frac{d_{m,ch}^2 \phi_{m,ch}^n}{C} \cdot \frac{\Delta\rho |g|}{\eta_f} \ . \tag{3-9c}$$

I replace the velocity in Eqs. (3-8a) and (3-8b) using Eq. (3-9c) to solve for porosities in the matrix and the channel. The bulk porosity then takes the form:

$$\phi_{bulk} = \phi_0 \left[(1-X)^{1/n} (1-\psi) + \left(\frac{d_m}{d_{ch}} \right)^{2/n} X^{1/n} \psi^{\frac{n-1}{n}} (1-\psi)^{\frac{1}{n}} \right], \tag{3-10a}$$

$$\phi_0 = \left(\frac{\Gamma_m z C \eta_f}{d_m^2 \rho_f \Delta\rho |g|} \right)^{1/n}, \tag{3-10b}$$

where ϕ_0 is the reference porosity at a given height z when the channel volume fraction is zero (i.e., the porosity for batch melting). Both the total melt flux and ϕ_0 increase with height above the solidus (z).

For geologically reasonable range of ψ and X, the bulk porosity decreases with X to the first order (Fig. 3-10). The proportion of channels has little effect on the bulk porosity because the matrix porosity (the first term on the right hand side of Eq. (3-10a)) dominates. If the proportion of the flux of channel melt increases, the bulk porosity decreases. This conclusion is valid for more realistic 2D cases where the proportion of channels and the relative melt suction rate are spatially variable. If the relative melt suction rate increases locally, the flux of channel melt will increase downstream. Consequently,

the bulk porosity will decrease downstream. It has been shown that the region of high bulk porosity (larger than 2%) narrows due to the melt extraction into channels formed by shear in lateral areas (cf. Figs. 3-7c and 3-8c). And, the region of high bulk porosity shrinks vertically due to more melt extraction between 30 km and 60 km depth (cf. Figs. 3-8c and 3-9c)

The distribution of melt suction can reconcile geophysical observations. If the conductivity maximum at 60 km beneath the ridge is due to a porosity maximum at 60 km (Baba et al., 2006; Key et al., 2013), melt suction has to start from 60 km, otherwise the bulk porosity would increase from 100 km to above 60 km. The relative melt suction rate has to be greater than one above 60 km so that melt retained in the matrix can be effectively extracted to the channels. If the resistivity minimum of ~0.5 $\Omega \cdot m$ is due to the presence of melt, the porosity could be 10% (Key et al., 2013). However, Yang et al., (2007) suggests 0.5% porosity at the same depth based on reduction of shear wave velocity. I will further discuss the absolute porosity in section 4.4.3. The current model cannot fit the width of the high-conductivity region, probably because of the simplified nature of the present model. More realistic geometry of the lithosphere with parabolic LAB and horizontally variable melt productivity are needed to further test the shape of the high-porosity region.

4.2. Anisotropic permeability promotes focusing

The effect of anisotropic permeability on melt focusing is illustrated through the isotropic case#2 and anisotropic case#4 where the permeability in the easy-flow direction is up to three times that in the perpendicular direction (cf. Figs. 3-5 and 3-6). For a mantle viscosity of 10^{19} Pa·s, the gradient of piezometric pressure is almost vertical (Morgan, 1987; Spiegelman and McKenzie, 1987). If the permeability in the channel is isotropic, the melt

focusing is passive. The zone of melt focusing is as wide as the cap of the decompaction channel beneath the LAB. Because the cap is wider for medium-spreading ridges than fast-spreading ridges (Hebert and Montési, 2010), it is possible that the medium-spreading ridge produces thicker crust than the fast-spreading ridge even though the melting stops deeper for the medium-spreading ridge (Fig. 3-10). As the additional anisotropy increases, the velocity of channel melt will rotate from the vertical direction to the easy-flow direction. The lower part of the melt focusing region expands and the crustal thickness increases (Figs. 3-11 and 3-12). The medium-spreading ridge is less sensitive to the additional anisotropy than the fast-spreading ridge because the 100 km wide passive melt focusing zone for the channel under the medium-spreading ridge already includes most melt production. Once the additional anisotropy is greater than a threshold (5 for medium-spreading ridge), increase of the additional anisotropy does not translate to thicker crust because the extra area of melt focusing contains little melt production.

Active melt focusing is less important than anisotropic permeability. Current results confirm that the effective melt focusing due to the pressure gradient occurs only if the viscosity is 10^{21} Pa·s (Figs. 3-12c and 3-12d, see also Spiegelman and McKenzie (1987)). The width of active melt focusing is less than or equal to the cap of the decompaction channel beneath the LAB. Hence, active melt focusing does not expand the zone of melt focusing if the decompaction channels are on the top. But anisotropic permeability can still expand the melt focusing zone by tilting melt streamlines to the axis below the decompaction channel. When both the active melt focusing and anisotropic permeability are present, the streamline of channel melt could bend toward the middle beneath LAB in response to the pressure gradient (Figs. 3-12b and 3-12d). Consequently, the area of melt

focusing and the crustal thickness are reduced compared to the case with smaller mantle viscosity (Figs. 3-11 and S3-8). By changing the permeability from that of Wark and Watson (1998) to that of Miller et al. (2014), the crustal thickness slightly increases (Fig. S3-8). This is due to the higher permeability based on the model of Miller et al. (2014) that enhances the flow of channel melt with respect to the solid thus increases the melt focusing area.

4.3. The concentration of REE in MORB and residual mantle

The distribution of channel affects the REE pattern in the residual mantle. I will use the current 2D model to simulate the fractionation of trace element in the residual cpx and pooled melt. Because of the 5% garnet in the source, HREE could first increase and then decrease in the residual cpx (second row of Fig. 3-13). The 2D distribution of Ce in the matrix melt is stratified except for the case with shallow melt channels and shear-induced melt band (Fig. 3-13d). Melt extraction beneath the axis starts from 30 km while melt extraction away from the axis starts gradually deeper as the distance away from the axis increases. Less melt extraction has the same effect of smaller degree of melting (Iwamori, 1993a; Iwamori, 1993b). Thus, the greatest depletion of LREE happens at 20 km depth at LAB. In the case of batch melting with no channel (Fig. 3-12a) or the case with channels in the shallowest 30 km (Fig. 3-12c), the depletion of Ce in the residual mantle is less than one order of magnitude. In the case of uniform channel proportion (Fig. 3-12b) and the case with deep channels starting from 60 km depth (Fig. 3-12e), Ce can be depleted by three orders of magnitude in the mantle and the resulted REE pattern in residual cpx is depleted in LREE. These two cases are most consistent with REE patterns of cpx in residual abyssal peridotites (Johnson et al., 1990; Johnson and Dick, 1992; Dick and Natland, 1996;

Ross and Elthon, 1997; Hellebrand et al., 2002; Salters and Dick, 2002; Hellebrand and Snow, 2003; Cipriani et al., 2004; Brunelli et al., 2006; Seyler et al., 2007; Warren et al., 2009; Stracke et al., 2011; Mallick et al., 2014; D'Errico et al., 2016). However, the most depleted REE patterns cannot be found in these cases with a maximum degree of melting of 14%.

The abundance of incompatible trace element in the residual lithosphere and the REE pattern in cpx from the lithosphere also depend on the maximum degree of melting. As an endmember scenario, a ridge with a maximum degree of melting of 25% demonstrates the largest range of REE patterns that can be found in residual cpx (Fig. 3-14). For this maximum degree of melting, cpx will be consumed (Kinzler and Grove, 1992). So, cpx can only be found in lithosphere deeper than 17 km (Fig. 3-14). In the case of batch melting or the case with shallow channels, REE patterns in the cpx are still too flat compared to those observed in abyssal peridotites (Figs. 3-14a and 3-14c). The three cases with more melt extraction (Figs. 3-14b, 3-14d, and 3-14e) can produce LREE-depleted patterns similar to those observed in cpx in abyssal peridotites. However, only the case with deep channels starting from 60 km depth could produce a porosity maximum at depth that is consistent with geophysical inference. Therefore, these two cases with deep channels with different degree of melting shown in Figs. 3-13e and 3-14e are endmember cases that are capable of reconciling the normal crustal thickness, the depth of porosity maximum consistent with geophysical implications, and the full range of REE patterns in cpx in abyssal peridotites. Since the shallow and more easily exposed mantle in the case with 14% melting is cpx-bearing, the deep channel case with 14% melting (Fig. 3-12e) is more comparable to most abyssal peridotites which are cpx bearing (Warren, 2016).

The observed REE abundances in N-MORB (Hofmann, 1988; Sun and McDonough, 1989; Gale et al., 2013; White and Klein, 2014) are higher than the predicted REE abundances in the pooled melt for all cases (Fig 3-15). The pooled melt is thought to be primitive while the N-MORB has undergone crystallization. By adding the cumulates to the N-MORB, White and Klein (2014) obtained a composition of bulk oceanic crust that has ~50% less REE than the N-MORB. The REE pattern of the bulk oceanic crust is more consistent with the pooled melt. Thus, the effect of crystallization could be a key factor responsible for the misfit in comparing pooled melt with N-MORB. Moreover, I explore several other explanations for the misfit: variations in the composition of DMM, unfocused low degree melt, dissolution in the channel, and missing enriched components. The source composition used in these calculations of pooled melt is the average DMM of Workman and Hart (2005). The misfit cannot be accounted for by changing the source composition to E-DMM of Workman and Hart (2005) or DMM of Salters and Stracke (2004) (Fig. 3-15). In a case with 200 km wide decompaction channel at LAB, the low degree melt generated away from the axis will be focused to the axis. However, the contribution of these additional melts can only raise middle to light REE (Fig. 3-15b). After melting all pyroxenes and garnet to transform garnet-bearing lherzolite to harzburgite and eventually dunite channels, almost all REE budget is carried by the melt that is about 50% the mass of the source. Thus, the melt generated by forming dunite channels could have two times higher concentration than the source. Such melt will lower REE abundance in pooled melt instead of raising the REE to the level of N-MORB.

Alternatively, the misfit between N-MORB and the model that reproduces REE patterns in abyssal peridotites implies a source component potentially important to MORB

but less important to the residue. The source region of MORB may consist of 3%-10% of chemically enriched source (Liu and Liang, 2017). These enriched endmembers could have REE concentrations comparable or higher than the MORB (Hofmann, 2003). These enriched sources are probably consumed by melt-rock interaction, so they are not preserved in abyssal peridotites (Hirschmann and Stolper, 1996; Warren, 2016). But, they could have overprinted on the composition of MORB (Willbold and Stracke, 2006; Stracke and Bourdon, 2009; Rudge et al., 2013). The melt derived from melting a two-component mantle source consisting of DMM and enriched endmembers could raise the current estimate of REE abundances in pooled melt. Therefore, a two-component mantle source is required to fully account for trace element abundances in MORB. Nonetheless, the REE pattern in pooled melt is less sensitive than REE pattern in residue in terms of constraining the distribution of channels because of these factors mentioned in the above two paragraphs.

4.4. U-Th-Ra disequilibria

The activity ratio of ($^{230}Th/^{234}U$) and ($^{226}Ra/^{230}Th$) in fresh MORB carries valuable information about the dynamics of melt migration regardless of the absolute concentration of U, Th, and Ra (U series) in the source because modeling these activity ratios only assumes fixed concentration ratios in the source, known as secular equilibrium (McKenzie, 1985). Most models for U series are one dimensional (McKenzie, 1985; Qin, 1992; Spiegelman and Elliott, 1993; Iwamori, 1994; Lundstrom, 2000; Jull et al., 2002; Bourdon and Sims, 2003; Elliott and Spiegelman, 2003; Lundstrom, 2003; Van Orman et al., 2006). The 2D model of Richardson and McKenzie (1994) has not explicitly solved for the porous flow and the distribution of porosity because of their assumption of a critical porosity below which melt should not move with respect to the solid.

In this section, I will show the importance of spatially variable melting rate to the activity ratios in matrix melt. Simple approximated solution for the matrix melt will be used to highlight the most important parameters, partition coefficients and porosity. I will also show the importance of melt transport time to the activity ratios in extracted melts. The melt suction to channels starts at 60 km in all but one simulations presented in this section because previous sections suggest this case is most appropriate under constraints of the depth of high conductivity center beneath the axis and REE patterns in abyssal peridotites. For simplicity, I assume that the matrix melt is in equilibrium with the residue. The effect of disequilibrium will be assessed in the discussion using approximate solutions. Model predictions of (^{230}Th/^{234}U) and (^{226}Ra/^{230}Th) will be compared to observations (Lundstrom et al., 1995; Lundstrom et al., 1998; Lundstrom et al., 1999; Bourdon et al., 2000; Sturm et al., 2000; Peate et al., 2001; Sims et al., 2002; Cooper et al., 2003; Sims et al., 2003; Tepley et al., 2004; Bourdon et al., 2005; Russo et al., 2009; Russo et al., 2009; Standish and Sims, 2010; Elkins et al., 2011; Waters et al., 2011; Elkins et al., 2014) to put additional constraints on the ridge model.

4.4.1. The general behavior of (^{230}Th/^{234}U) and (^{226}Ra/^{230}Th)

To illustrate the general behavior of (^{230}Th/^{234}U) and (^{226}Ra/^{230}Th) in matrix melt, here I use a model with constant partition coefficients for U, Th, and Ra (2.3×10^{-3}, 1.9×10^{-3}, and 1×10^{-4} respectively (Wood et al., 1999; Jull et al., 2002). Initial excess of (^{230}Th/^{234}U) and (^{226}Ra/^{230}Th) are generated in the first fraction of melt. In the wet melting regime below ~70 km, (^{230}Th/^{234}U) and (^{226}Ra/^{230}Th) decreases (Fig. 3-16). Analysis of 1D approximate solution with small melting rate suggests that the decrease of (^{230}Th/^{234}U) and (^{226}Ra/^{230}Th) in the wet melting regime is due to the increase ofmatrix porosity (Eqs. (A3-34b) and (A3-

35), also illustrated in Figs. S3-9 and S3-10). As the melting rate increases in the dry melting regime between 20 km and 70 km depth, (^{230}Th/^{234}U) decreases to below unity while (^{226}Ra/^{230}Th) slightly increases (Fig. 3-16). Based on my simple analysis, the large melting rate acts like a negative driving force for (^{230}Th/^{234}U) because the radiogenic daughter is more incompatible, and thus depleted faster than the parent. The following expressions are approximated solutions for the activity ratios:

$$\begin{aligned}\left(^{230}\mathrm{Th}/^{238}\mathrm{U}\right) &\sim \frac{\phi_m + k_U}{\phi_m + k_{Th}} \cdot \left(1 - \delta + O\left(\delta^2\right)\right), \\ \left(^{226}\mathrm{Ra}/^{230}\mathrm{Th}\right) &\sim \frac{\phi_m + k_{Th}}{\phi_m + k_{Ra}},\end{aligned} \tag{3-11}$$

where δ is a correction term proportional to Γ_m / λ_{Th}. A detailed description of my simple analysis is presented in Appendix. When the perturbation term is neglected, these expressions recover the "no-melting limit" derived by McKenzie (1985).

(^{226}Ra/^{230}Th) is not sensitive to the negative effect of melting rate and maintains a ratio above unity in the example shown in Fig. 3-16 because the decay of Ra is faster thus minimizing the correction of melting rate. The increase of (^{226}Ra/^{230}Th) in the matrix melt above 60 km is due to the decrease of porosity. In the shallowest 20 km or near the LAB, the melting rate is zero and the porosity approaches zero. Thus, the approximation with small melting rate ($\delta = 0$ in Eq. (3-11)) is valid and activity ratios tend to return to the initial excess set by the relative incompatibility of the parent and the daughter.

Matrix melts are extracted to the channel and upwells rapidly to the ridge axis. Once the melt enters the channel, (^{230}Th/^{234}U) and (^{226}Ra/^{230}Th) in that fraction of extracted melt tends to recover unity (Figs. 3-16c and 3-16f). Because the transport time to the ridge axis

in channels from one point is generally shorter than another point below, the extent of recovering to unity is spatially variable. Besides, the melt extraction rate and the concentration of U, Th, and Ra are also spatially variable. In the next section, I will show a statistical assemble of melt fractions extracted from the melt focusing zone for the channel and then calculate the mean activity ratio in the pooled melt. The pooled melt will include the shallow matrix melt and all extracted melts after decay during melt extraction in the melt focusing zone for the channel (see the Appendix for modeling decay during melt extraction and transport in channels).

4.4.2. Deep channels and high permeability shorten transport time

The largest ($^{230}Th/^{234}U$) in the matrix melt is generated at the onset of melting. To produce the highest ($^{230}Th/^{234}U$) in MORB samples, k_U/k_{Th} at the onset of melting should be greater than 1.3 (LaTourrette et al., 1993). The ratio of partition coefficient of U to Th in cpx could be 1.3 at 3 GPa (Landwehr et al., 2001). But, such ($^{230}Th/^{234}U$) is likely to restore unity after melt transport as shown by the example in Fig. 3-16b. Thus, the largest ($^{230}Th/^{234}U$) observed in natural samples requires that garnet is present at the solidus and the melt transport time is fast (Beattie, 1993; LaTourrette et al., 1993; Klemme et al., 2002). In this section, I will explore the effect of melt transport time on activity ratios in melts extracted from the matrix within the melt focusing zone for the channel. The melting model is non-modal with partition coefficients of garnet, clinopyroxene, and orthopyroxene from the literature (Kinzler and Grove, 1992; Hauri et al., 1994; Wood et al., 1999; Klemme et al., 2002; Salters et al., 2002; Wood and Blundy, 2014). The bulk partition coefficient for Ra is set to be 1×10^{-4} (Jull et al., 2002). Details about the method can be found in the Appendix.

Preservation of large activity ratio in the matrix melt is favored by deep melt extraction to channels and large permeability. If melt extraction to channels only exist in the shallowest 30 km or in regions of high shear strain, melt extracted from the bottom half of the melt focusing zone for the channel would experience 100-200 Kyr of transport time in channels (Figs. 3-17a and 3-17b). The range of (^{230}Th/^{234}U) in extracted melts is limited to the range of 1 to 1.05 while the range of (^{226}Ra/^{230}Th) is between 1 and 1.1 (open dots in Fig. 3-18). If melt extraction extends to 60 km depth, the transport time for melt extracted from 60 km beneath the axis is reduced significantly (Figs. 3-17c and 3-17d). Thus, deep extracted melt is expected to have (^{230}Th/^{234}U) greater than 1.1. Melts extracted near the end of dry melting could have lower than unity (^{230}Th/^{234}U). (^{226}Ra/^{230}Th) higher than 1.2 are also sampled in melts extracted near the end of dry melting. (^{230}Th/^{234}U) and (^{226}Ra/^{230}Th) in extracted melts has a negative correlation due to the opposite sense of variation with depth as explained in the preceding section. The pooled melt is dominated by melt in the early stage of dry melting because of the high concentration and high melt extraction rate. Thus, the pooled melt has larger than unity (^{230}Th/^{234}U) with little, if any, (^{226}Ra/^{230}Th) excess.

The melt flow in the channel can be enhanced by the increase of grain size and porosity. The permeability formula is also model dependent. In an example with large permeability (Miller et al., 2014), the melt transport time is reduced (cf. Figs. 3-17d and 3-17f). The transport time from 100 km depth to the ridge axis is comparable to the half-life of ^{230}Th. Thus the (^{230}Th/^{234}U) of extracted melt extends to 1.2 (blue and green dots in Fig. 3-18). By further increasing the grain size or forcing the melt flux in the channel to be confined in smaller proportion of channels, the transport time in the channel can be further

reduced, producing larger ($^{230}Th/^{234}U$) and ($^{226}Ra/^{230}Th$) in extracted melts (Fig. 3-18). Shorter transport time does not increase the ($^{226}Ra/^{230}Th$) in pooled melt significantly because extracted melts with high ($^{226}Ra/^{230}Th$) has low concentration of Ra and Th compared to deeper melt. Thus, the pooled melt as a mixture of all extracted melt will be weighted to deep melt at the early stage of dry melting.

4.4.3. Comparison with MORB data

Simulations reported in this chapter cover a wide range of ($^{230}Th/^{234}U$) and ($^{226}Ra/^{230}Th$) in natural samples (Fig. 3-18). The highest ($^{226}Ra/^{230}Th$) in natural samples is higher than these simulations presented here. There are three possible explanations.

First, the high ($^{226}Ra/^{230}Th$) may suggest large grain size (>10 mm) in the channel or the permeability enhancement along the orientation of channels is underestimated here. To produce more Ra excess with grainsize smaller than 10 mm, the factor of additional anisotropic permeability (Eq. 3-4b) should be larger than two or the permeability constant (Eq. 3-3c) in the direction of channel orientation should be smaller than current experimental constraints on undeformed samples (Wark and Watson, 1998; Miller et al., 2014). If this is the reason, the porosity should be lower than the current predictions which are already on the lower end of geophysical interpretations (Fig. 3-18b).

Second, chemical disequilibrium could increase ($^{226}Ra/^{230}Th$) while making ($^{230}Th/^{234}U$) slightly smaller or unchanged (Qin 1992; Van Orman et al., 2006). Qin (1992) has shown that chemical disequilibrium between the matrix melt and the residue could increase ($^{226}Ra/^{230}Th$) in the melt. This effect could be qualitatively predicted by using the effective partition coefficient during disequilibrium melting (Liang and Liu, 2016) in the

"no-melting limit" of McKenzie (1985). The diffusivity of Ra is probably much faster than Th in cpx (Van Orman et al., 1998), thus the effective partition coefficient for Ra could be close to k_{Ra} whereas the effective partition coefficient for Th could be larger than k_{Th} (Liang and Liu, 2016). Thus, (^{226}Ra/^{230}Th) during disequilibrium melting will be higher (shown in Fig. 3-18a) than predicted by Eq. (3-11). For (^{230}Th/^{234}U), the effect of disequilibrium melting is difficult to predict because the diffusivity of U and Th are similar within experimental uncertainty (Van Orman et al., 1998). In the simulation of Van Orman et al. (2006) with $k_U / k_{Th} > 1$, larger extent of disequilibrium produces smaller (^{230}Th/^{234}U) for the same melting rate. This may be the effect of increasing the effective partition coefficient for both U and Th by the same increment. Therefore, disequilibrium melting could produce a trend towards larger (^{226}Ra/^{230}Th) and smaller (^{230}Th/^{234}U). The effect of chemical disequilibrium may be particularly important in reconciling the high (^{226}Ra/^{230}Th) in samples and the somewhat large porosity inferred from geophysical studies (Fig. 3-18b).

Third, shallow level processes could overprint on the disequilibria of U series in pooled melt. If the cumulate crystalizes from a melt that is relatively enriched with respect to the pooled melt, Ra could diffuse from the cumulates to the pooled melt in melt-cumulate interaction whereas Th is less modified (Saal and Van Orman, 2004; Van Orman et al., 2006). Thus, (^{226}Ra/^{230}Th) in the pooled melt could increase. After the solidification of MORB melt, hydrothermal alteration could also raise the (^{226}Ra/^{230}Th) (Volpe and Goldstein, 1993). However, the effect of hydrothermal fluid may be insignificant according to the analysis of other trace elements and isotope ratios (Lundstrom et al., 1999; Bourdon et al., 2000). Therefore, it is necessary to study samples with extreme (^{226}Ra/^{230}Th) on a case-by-case basis.

5. Conclusions

This chapter presents a platform for using independent geochemical and geophysical observations to constrain the dynamics of melt migration beneath mid-ocean ridges. The model treats the fine-scale channels and their surrounding matrix as two overlapping continua. The channel continuum interacts with the matrix continuum by means of melt extraction or suction. The permeability in the matrix is isotropic while the permeability in the channel is larger and possibly anisotropic due to the deformation of the solid and/or the orientation of dunite channels.

The anisotropic permeability in channel continuum due to the shear-localized melt band could enhance melt focusing, especially for fast spreading ridges with narrow horizontal range of decompaction channels at LAB. Fast spreading ridges can only produce 4.5-5.2 km thick crust without anisotropic permeability if the width of decompaction layer is 50 km as suggested by Hebert and Montési (2010) and the viscosity of the mantle is in the range of 10^{19}-10^{21}Pa·s (Sigmundsson, 1991). With anisotropic permeability, the crustal thickness can be increased from 4.6 km to 7.3 km. The melt focusing radius of active focusing is small or comparable to the melt focusing radius of passive focusing via the decompaction channel at LAB. Thus, active focusing has little, if any, additional contribution to the area of melt focusing zone for the channel. The anisotropic permeability can expand the width of the melt focusing area below the decompaction channel by 50%, and hence is an important mechanism for melt focusing.

Results from this study suggest that melt extraction to channels starting at 60 km can explain three independent observations listed below:

First, the depth of 60 km as the depth of channel initiation is consistent with the conductivity maximum at 60 km observed at EPR, which has been interpreted as a porosity maximum (Key et al., 2013). The porosity increases upwards from 100 km to 60 km depth because of melting. Once channel forms at 60 km and above, the newly generated melt and part of the retained melt in the matrix is efficiently extracted to the channel. The porosity is large and the melt velocity is fast in the channel. But the channel porosity has little contribution to the bulk porosity due to the small volume fraction of channels. The bulk porosity is controlled by the melt flux in the matrix. Thus, extracting melt from the matrix to the channel reduces bulk porosity.

Second, melt extraction to channels starting from 60 km can produce the depleted REE patterns in residual abyssal peridotites. Models with no channel or channels within the shallowest 30 km produces flat REE patterns whereas most REE patterns has depleted LREE. In the model with deep channels, the residue experiences more fractional melting so that the LREE can be efficiently fractionated.

Third, channels starting deep shorten the transport time of low degree matrix melt with high ($^{230}Th/^{234}U$). With channels in the shallowest 30 km, the transport time in channels from 100 km to the axis is ~200 Kyr. If channels form at 60 km, the transport time is reduced to ~80 Kyr, which is comparable to the half-life of ^{230}Th. Hence deep channels are more likely to preserve the high ($^{230}Th/^{234}U$) during melt transport in channels. A simulation with deep channels and large grain size in the matrix and the channel (3 mm and 10 mm, respectively) can produce the largest ($^{230}Th/^{234}U$) observed in natural samples. Disequilibrium melting and shallow level processes are required to produce the ($^{226}Ra/^{230}Th$) large than 2.5 seen in natural samples.

The 60 km depth is deeper than the requirement by disequilibrium between MORB and harzburgite at low pressure. Thus, channels above 30 km may be dunite whereas channels in between 30 km and 60 km may be harzburgite (Liang et al., 2010). To produce channels deeper than 30 km, the melt needs to be sufficiently reactive with the harzburgite and the melt-rock reaction needs to gain porosity. Such melt could be derived from melting heterogeneous mantle (Liang et al., 2010; Schiemenz et al., 2011; Weatherley and Katz, 2016; Keller et al., 2017). Future studies could test if melts derived from DMM at depth could also satisfy the physical requirement of forming deep channels.

The current model demonstrates the importance of variable melting rate on (^{230}Th/^{234}U) and (^{226}Ra/^{230}Th) in a 2D ridge section. (^{230}Th/^{234}U) in the matrix melt starts high and decreases quickly in the dry melting regime with fast melting rate. At the end of dry melting, (^{230}Th/^{234}U) in the matrix melt could be smaller than one. (^{226}Ra/^{230}Th) also starts high and decreases quickly in the wet melting regime but it can maintain above one in the dry melting regime. Due to the decrease of porosity associated with channelized melt extraction, (^{226}Ra/^{230}Th) could increase in the dry melting region. Therefore, there is an anti-correlation between (^{230}Th/^{234}U) and (^{226}Ra/^{230}Th) in the matrix melt. Such anti-correlation can be preserved if the melt transport time for the shallow high (^{226}Ra/^{230}Th) melt is comparable to the half-life of ^{226}Ra and the melt transport time for the deep high (^{230}Th/^{234}U) melt is comparable to the half-life of ^{230}Th.

The present model has limitations that naturally lead to some future directions for more comprehensive tests. Here, the 2D model assumes chemical equilibrium between the matrix melt and the residue. The next iteration of the model should use a similar approach applied in Chapter 2 to treat the potential chemical disequilibrium and the exchange

between the matrix melt and the residue. The more realistic geometry of the lithosphere and horizontally variable melt productivity could affect the distribution of porosity and the crustal thickness. These two issues can be resolved by coupling a thermal model with the mechanic model used in the present study. The present model assumes a homogeneous source composition of DMM, although an enriched component could affect the MORB composition. Future models need to consider the extraction of melt derived from enriched source and the chemical exchange between such melt and DMM-like source. All simulations presented here use a single F-depth path derived from pMELTS. The initial melting depth of this F-depth path is favored by the highest ($^{230}Th/^{234}U$) in MORB, the most depleted REE patterns in abyssal peridotites, and a normal range of crustal thickness, although these observations vary. It is very likely that melting could starts shallower than presented here. There are other observational constraints which can be used to test the current model, such as the major element composition of MORB, seismic velocity and attenuation of the mantle beneath mid-ocean ridges. Despite these limitations, the present model established a basic framework for integrating many observations made at the mid-ocean ridges.

Acknowledgement

We thank Don Forsyth, Marc Parmentier, Greg Hirth and Mark Behn for useful discussion.

References

Aharonov, E., M. Spiegelman and P. Kelemen (1997). "Three-dimensional flow and reaction in porous media: Implications for the Earth's mantle and sedimentary basins." Journal of Geophysical Research: Solid Earth **102**(B7): 14821-14833.

Aharonov, E., J. A. Whitehead, P. B. Kelemen and M. Spiegelman (1995). "Channeling instability of upwelling melt in the mantle." Journal of Geophysical Research: Solid Earth **100**(B10): 20433-20450.

Asimow, P. D., M. M. Hirschmann and E. M. Stolper (2001). "Calculation of Peridotite Partial Melting from Thermodynamic Models of Minerals and Melts, IV. Adiabatic Decompression and the Composition and Mean Properties of Mid-ocean Ridge Basalts." Journal of Petrology **42**(5): 963-998.

Asimow, P. D. and E. M. Stolper (1999). "Steady-state Mantle–Melt Interactions in One Dimension: I. Equilibrium Transport and Melt Focusing." Journal of Petrology **40**(3): 475-494.

Baba, K., A. D. Chave, R. L. Evans, G. Hirth and R. L. Mackie (2006). "Mantle dynamics beneath the East Pacific Rise at 17°S: Insights from the Mantle Electromagnetic and Tomography (MELT) experiment." Journal of Geophysical Research: Solid Earth (1978–2012) **111**(B2).

Baltzell, C., E. M. Parmentier, Y. Liang and S. Tirupathi (2015). "A high-order numerical study of reactive dissolution in an upwelling heterogeneous mantle: 2. Effect of shear deformation." Geochemistry, Geophysics, Geosystems **16**(11): 3855-3869.

Beattie, P. (1993). "Uranium-thorium disequilibria and partitioning on melting of garnet peridotite." Nature **363**(6424): 63-65.

Boudier, F. and R. G. Coleman (1981). "Cross section through the peridotite in the Samail Ophiolite, southeastern Oman Mountains." Journal of Geophysical Research: Solid Earth **86**(B4): 2573-2592.

Bourdon, B., S. Goldstein, D. Bourles, M. Murrell and C. Langmuir (2000). "Evidence from ^{10}Be and U series disequilibria on the possible contamination of mid-ocean ridge basalt glasses by sedimentary material." Geochemistry, Geophysics, Geosystems **1**(8).

Bourdon, B. and K. W. Sims (2003). "U-series constraints on intraplate basaltic magmatism." Reviews in Mineralogy and Geochemistry **52**(1): 215-254.

Bourdon, B., S. P. Turner and N. M. Ribe (2005). "Partial melting and upwelling rates beneath the Azores from a U-series isotope perspective." Earth and Planetary Science Letters **239**(1-2): 42-56.

Braun, M. G., G. Hirth and E. M. Parmentier (2000). "The effects of deep damp melting on mantle flow and melt generation beneath mid-ocean ridges." Earth and Planetary Science Letters **176**(3–4): 339-356.

Braun, M. G. and P. B. Kelemen (2002). "Dunite distribution in the Oman Ophiolite: Implications for melt flux through porous dunite conduits." Geochemistry, Geophysics, Geosystems **3**(11): 1-21.

Brunelli, D. and M. Seyler (2010). "Asthenospheric percolation of alkaline melts beneath the St. Paul region (Central Atlantic Ocean)." Earth and Planetary Science Letters **289**(3–4): 393-405.

Brunelli, D., M. Seyler, A. Cipriani, L. Ottolini and E. Bonatti (2006). "Discontinuous Melt Extraction and Weak Refertilization of Mantle Peridotites at the Vema Lithospheric Section (Mid-Atlantic Ridge)." Journal of Petrology **47**(4): 745-771.

Cipriani, A., H. K. Brueckner, E. Bonatti and D. Brunelli (2004). "Oceanic crust generated by elusive parents: Sr and Nd isotopes in basalt-peridotite pairs from the Mid-Atlantic Ridge." Geology **32**(8): 657-660.

Cooper, K. M., S. J. Goldstein, K. W. Sims and M. T. Murrell (2003). "Uranium-series chronology of Gorda Ridge volcanism: new evidence from the 1996 eruption." Earth and Planetary Science Letters **206**(3): 459-475.

D'Errico, M. E., J. M. Warren and M. Godard (2016). "Evidence for chemically heterogeneous Arctic mantle beneath the Gakkel Ridge." Geochimica Et Cosmochimica Acta **174**: 291-312.

Daines, M. J. and D. L. Kohlstedt (1994). "The transition from porous to channelized flow due to melt/rock reaction during melt migration." Geophysical Research Letters **21**(2): 145-148.

Dick, H. J. B. and J. H. Natland (1996). "6. Late-Stage Melt Evolution And Transport In The Shallow Mantle

Beneath The East Pacific Rise1." Proceedings of the Ocean Drilling Program, Scientific Results **147**: 32.

Elkins, L. J., K. W. W. Sims, J. Prytulak, J. Blichert-Toft, T. Elliott, J. Blusztajn, S. Fretzdorff, M. Reagan, K. Haase, S. Humphris and J. G. Schilling (2014). "Melt generation beneath Arctic Ridges: Implications from U decay series disequilibria in the Mohns, Knipovich, and Gakkel Ridges." Geochimica Et Cosmochimica Acta **127**: 140-170.

Elkins, L. J., K. W. W. Sims, J. Prytulak, T. Elliott, N. Mattielli, J. Blichert-Toft, J. Blusztajn, N. Dunbar, C. Devey, D. F. Mertz, J. G. Schilling and M. Murrell (2011). "Understanding melt generation beneath the slow-spreading Kolbeinsey Ridge using ^{238}U, ^{230}Th, and ^{231}Pa excesses." Geochimica Et Cosmochimica Acta **75**(21): 6300-6329.

Elliott, T. and M. Spiegelman (2014). "Melt migration in oceanic crustal production: a U-series perspective." Treatise on geochemistry **3**: 465-510.

Elthon, D. and C. M. Scarfe (1984). "High-pressure phase equilibria of a high-magnesia basalt and the genesis of primary oceanic basalts." Am Mineral **69**(1): 15.

Forsyth, D. W. (1993). "Crustal thickness and the average depth and degree of melting in fractional melting models of passive flow beneath mid-ocean ridges." Journal of Geophysical Research: Solid Earth **98**(B9): 16073-16079.

Hauri, E. H., T. P. Wagner and T. L. Grove (1994). "Experimental and natural partitioning of Th, U, Pb and other trace elements between garnet, clinopyroxene and basaltic melts." Chemical Geology **117**(1): 149-166.

Hebert, L. B. and L. G. J. Montési (2010). "Generation of permeability barriers during melt extraction at mid-ocean ridges." Geochemistry, Geophysics, Geosystems **11**(12).

Hellebrand, E., J. Snow, S. Mostefaoui and P. Hoppe (2005). "Trace element distribution between orthopyroxene and clinopyroxene in peridotites from the Gakkel Ridge: a SIMS and NanoSIMS study." Contributions to Mineralogy and Petrology **150**(5): 486-504.

Hellebrand, E. and J. E. Snow (2003). "Deep melting and sodic metasomatism underneath the highly oblique-spreading Lena Trough (Arctic Ocean)." Earth and Planetary Science Letters **216**(3): 283-299.

Hellebrand, E., J. E. Snow, P. Hoppe and A. W. Hofmann (2002). "Garnet-field Melting and Late-stage Refertilization in 'Residual' Abyssal Peridotites from the Central Indian Ridge." Journal of Petrology **43**(12): 2305-2338.

Hesse, M. A., A. R. Schiemenz, Y. Liang and E. M. Parmentier (2011). "Compaction–dissolution waves in an upwelling mantle column." Geophysical Journal International **187**(3): 1057-1075.

Hirschmann, M. M. and E. M. Stolper (1996). "A possible role for garnet pyroxenite in the origin of the "garnet signature" in MORB." Contributions to Mineralogy and Petrology **124**(2): 185-208.

Hirth, G. and D. Kohlstedt (2003). "Rheology of the upper mantle and the mantle wedge: A view from the experimentalists." Inside the subduction factory: 83-105.

Hofmann, A. (2003). "Sampling mantle heterogeneity through oceanic basalts: isotopes and trace elements." Treatise on geochemistry **2**: 61-101.

Holtzman, B. K., D. L. Kohlstedt, M. E. Zimmerman, F. Heidelbach, T. Hiraga and J. Hustoft (2003). "Melt Segregation and Strain Partitioning: Implications for Seismic Anisotropy and Mantle Flow." Science **301**(5637): 1227-1230.

Iwamori, H. (1993a). "Dynamic disequilibrium melting model with porous flow and diffusion-controlled chemical equilibration." Earth and Planetary Science Letters **114**(2): 301-313.

Iwamori, H. (1993b). "A model for disequilibrium mantle melting incorporating melt transport by porous and channel flows." Nature **366**(6457): 734-737.

Iwamori, H. (1994). "^{238}U-^{230}Th-^{226}Ra and ^{235}U-^{231}Pa disequilibria produced by mantle melting with porous and channel flows." Earth and Planetary Science Letters **125**(1–4): 1-16.

Johnson, K. T. M. and H. J. B. Dick (1992). "Open system melting and temporal and spatial variation of peridotite and basalt at the Atlantis II Fracture Zone." Journal of Geophysical Research: Solid Earth **97**(B6): 9219-9241.

Johnson, K. T. M., H. J. B. Dick and N. Shimizu (1990). "Melting in the oceanic upper mantle: An ion microprobe study of diopsides in abyssal peridotites." Journal of Geophysical Research: Solid Earth **95**(B3): 2661-2678.

Jull, M., P. B. Kelemen and K. Sims (2002). "Consequences of diffuse and channelled porous melt migration on uranium series disequilibria." Geochimica Et Cosmochimica Acta **66**(23): 4133-4148.

Katz, R. F., M. Spiegelman and B. Holtzman (2006). "The dynamics of melt and shear localization in partially molten aggregates." Nature **442**(7103): 676-679.

Kelemen, P. B., G. Hirth, N. Shimizu, M. Spiegelman and H. J. B. Dick (1997). "A Review of Melt Migration Processes in the Adiabatically Upwelling Mantle beneath Oceanic Spreading Ridges." Philosophical Transactions: Mathematical, Physical and Engineering Sciences **355**(1723): 283-318.

Kelemen, P. B., N. Shimizu and V. J. M. Salters (1995). "Extraction of mid-ocean-ridge basalt from the upwelling mantle by focused flow of melt in dunite channels." Nature **375**(6534): 747-753.

Kelemen, P. B., J. A. Whitehead, E. Aharonov and K. A. Jordahl (1995). "Experiments on flow focusing in soluble porous media, with applications to melt extraction from the mantle." Journal of Geophysical Research: Solid Earth **100**(B1): 475-496.

Keller, T., R. F. Katz and M. M. Hirschmann (2017). "Volatiles beneath mid-ocean ridges: Deep melting, channelised transport, focusing, and metasomatism." Earth and Planetary Science Letters **464**: 55-68.

Key, K., S. Constable, L. Liu and A. Pommier (2013). "Electrical image of passive mantle upwelling beneath the northern East Pacific Rise." Nature **495**(7442): 499-502.

Kinzler, R. J. and T. L. Grove (1992). "Primary magmas of mid-ocean ridge basalts 1. Experiments and methods." Journal of Geophysical Research: Solid Earth **97**(B5): 6885-6906.

Kinzler, R. J. and T. L. Grove (1992). "Primary magmas of mid-ocean ridge basalts 2. Applications." Journal of Geophysical Research: Solid Earth **97**(B5): 6907-6926.

Klein, E. M. and C. H. Langmuir (1987). "Global correlations of ocean ridge basalt chemistry with axial depth and crustal thickness." Journal of Geophysical Research: Solid Earth (1978–2012) **92**(B8): 8089-8115.

Klemme, S., J. D. Blundy and B. J. Wood (2002). "Experimental constraints on major and trace element partitioning during partial melting of eclogite." Geochimica Et Cosmochimica Acta **66**(17): 3109-3123.

Landwehr, D., J. Blundy, E. M. Chamorro-Perez, E. Hill and B. Wood (2001). "U-series disequilibria generated by partial melting of spinel lherzolite." Earth and Planetary Science Letters **188**(3–4): 329-348.

Lassiter, J. C., B. L. Byerly, J. E. Snow and E. Hellebrand (2014). "Constraints from Os-isotope variations on the origin of Lena Trough abyssal peridotites and implications for the composition and evolution of the depleted upper mantle." Earth and Planetary Science Letters **403**: 178-187.

LaTourrette, T. Z., A. K. Kennedy and G. J. Wasserburg (1993). "Thorium-Uranium Fractionation by Garnet: Evidence for a Deep Source and Rapid Rise of Oceanic Basalts." Science **261**(5122): 739-742.

Liang, Y. and B. Liu (2016). "Simple models for disequilibrium fractional melting and batch melting with application to REE fractionation in abyssal peridotites." Geochimica Et Cosmochimica Acta **173**: 181-197.

Liang, Y. and E. M. Parmentier (2010). "A Two-Porosity Double Lithology Model for Partial Melting, Melt Transport and Melt–rock Reaction in the Mantle: Mass Conservation Equations and Trace Element Transport." Journal of Petrology **51**(1-2): 125-152.

Liang, Y. and Q. Peng (2010). "Non-modal melting in an upwelling mantle column: Steady-state models with applications to REE depletion in abyssal peridotites and the dynamics of melt migration in the mantle." Geochimica Et Cosmochimica Acta **74**(1): 321-339.

Liang, Y., A. Schiemenz, M. A. Hesse and E. M. Parmentier (2011). "Waves, channels, and the preservation of chemical heterogeneities during melt migration in the mantle." Geophysical Research Letters **38**(20): n/a-n/a.

Liang, Y., A. Schiemenz, M. A. Hesse, E. M. Parmentier and J. S. Hesthaven (2010). "High-porosity channels for melt migration in the mantle: Top is the dunite and bottom is the harzburgite and lherzolite." Geophysical Research Letters **37**(15): n/a-n/a.

Liu, B. and Y. Liang (2017). "The prevalence of kilometer-scale heterogeneity in the source region of MORB upper mantle." Science Advances **3**(11).

Lundstrom, C. (2000). "Models of U-series disequilibria generation in MORB: the effects of two scales of melt porosity." Physics of the Earth and Planetary Interiors **121**(3–4): 189-204.

Lundstrom, C., J. Gill, Q. Williams and B. Hanan (1998). "Investigating solid mantle upwelling beneath mid-ocean ridges using U-series disequilibria. II. A local study at 33 S Mid-Atlantic Ridge." Earth and Planetary Science Letters **157**(3-4): 167-181.

Lundstrom, C., J. Gill, Q. Williams and M. Perfit (1995). "Mantle melting and basalt extraction by equilibrium porous flow." Science **270**(5244): 1958-1961.

Lundstrom, C., D. Sampson, M. Perfit, J. Gill and Q. Williams (1999). "Insights into mid-ocean ridge basalt petrogenesis: U - series disequilibria from the Siqueiros Transform, Lamont Seamounts, and East Pacific Rise." Journal of Geophysical Research: Solid Earth **104**(B6): 13035-13048.

Lundstrom, C. C. (2003). "Uranium-series Disequilibria in Mid-ocean Ridge Basalts: Observations and Models of Basalt Genesis." Reviews in Mineralogy and Geochemistry **52**(1): 175-214.

Mallick, S., H. J. B. Dick, A. Sachi-Kocher and V. J. M. Salters (2014). "Isotope and trace element insights into heterogeneity of subridge mantle." Geochemistry, Geophysics, Geosystems **15**(6): 2438-2453.

McKenzie, D. (1984). "The generation and compaction of partially molten rock." Journal of Petrology **25**(3): 713-765.

McKenzie, D. (1985). "^{230}Th-^{238}U disequilibrium and the melting processes beneath ridge axes." Earth and Planetary Science Letters **72**(2–3): 149-157.

Miller, K. J., W.-l. Zhu, L. G. J. Montési and G. A. Gaetani (2014). "Experimental quantification of permeability of partially molten mantle rock." Earth and Planetary Science Letters **388**: 273-282.

Morgan, J. P. (1987). "Melt migration beneath mid-ocean spreading centers." Geophysical Research Letters **14**(12): 1238-1241.

Morgan, Z. and Y. Liang (2005). "An experimental study of the kinetics of lherzolite reactive dissolution with applications to melt channel formation." Contributions to Mineralogy and Petrology **150**(4): 369-385.

Murase, T. and A. R. McBirney (1973). "Properties of some common igneous rocks and their melts at high temperatures." Geological Society of America Bulletin **84**(11): 3563-3592.

Niu, Y. and R. Hékinian (1997). "Spreading-rate dependence of the extent of mantle melting beneath ocean ridges." Nature **385**(6614): 326-329.

O'Hara, M. (1965). "Primary magmas and the origin of basalts." Scottish Journal of Geology **1**(1): 19-40.

Peate, D. W., C. J. Hawkesworth, P. W. van Calsteren, R. N. Taylor and B. J. Murton (2001). "^{238}U–^{230}Th constraints on mantle upwelling and plume–ridge interaction along the Reykjanes Ridge." Earth and Planetary Science Letters **187**(3): 259-272.

Peč, M., B. K. Holtzman, M. Zimmerman and D. L. Kohlstedt (2015). "Reaction infiltration instabilities in experiments on partially molten mantle rocks." Geology **43**(7): 575-578.

Peč, M., B. K. Holtzman, M. E. Zimmerman and D. L. Kohlstedt (2017). "Reaction Infiltration Instabilities in Mantle Rocks: an Experimental Investigation." Journal of Petrology **58**(5): 979-1003.

Phipps Morgan, J. and B. K. Holtzman (2005). "Vug waves: A mechanism for coupled rock deformation and fluid migration." Geochemistry, Geophysics, Geosystems **6**(8): n/a-n/a.

Qin, Z. (1992). "Disequilibrium partial melting model and its implications for trace element fractionations during mantle melting." Earth and Planetary Science Letters **112**(1): 75-90.

Ribe, N. M. (1985). "The deformation and compaction of partial molten zones." Geophysical Journal International **83**(2): 487-501.

Richardson, C. and D. McKenzie (1994). "Radioactive disequilibria from 2D models of melt generation by plumes and ridges." Earth and Planetary Science Letters **128**(3): 425-437.

Ross, K. and D. Elthon (1997). 13. Extreme Incompatible Trace-Element Depletion Of Diopside In Residual Mantle From South Of The Kane Fracture Zone1. Proceedings of the Ocean Drilling Program, Scientific Results.

Rudge, J. F., J. Maclennan and A. Stracke (2013). "The geochemical consequences of mixing melts from a heterogeneous mantle." Geochimica Et Cosmochimica Acta **114**: 112-143.

Russo, C. J., K. H. Rubin and D. W. Graham (2009). "Mantle melting and magma supply to the Southeast Indian Ridge: The roles of lithology and melting conditions from U-series disequilibria." Earth and Planetary Science Letters **278**(1-2): 55-66.

Russo, C. J., K. H. Rubin and D. W. Graham (2009). "Mantle melting and magma supply to the Southeast Indian Ridge: The roles of lithology and melting conditions from U-series disequilibria." Earth and Planetary Science Letters **278**(1–2): 55-66.

Salters, V. J. M. and H. J. B. Dick (2002). "Mineralogy of the mid-ocean-ridge basalt source from neodymium isotopic composition of abyssal peridotites." Nature **418**(6893): 68-72.

Salters, V. J. M., J. E. Longhi and M. Bizimis (2002). "Near mantle solidus trace element partitioning at pressures up to 3.4 GPa." Geochemistry, Geophysics, Geosystems **3**(7): 1-23.

Salters, V. J. M. and A. Stracke (2004). "Composition of the depleted mantle." Geochemistry, Geophysics, Geosystems **5**(5): Q05B07.

Schiemenz, A., Y. Liang and E. M. Parmentier (2011). "A high-order numerical study of reactive dissolution in an upwelling heterogeneous mantle-I. Channelization, channel lithology and channel geometry." Geophysical Journal International **186**(2): 641-664.

Seyler, M., J. P. Lorand, H. J. B. Dick and M. Drouin (2007). "Pervasive melt percolation reactions in ultra-depleted refractory harzburgites at the Mid-Atlantic Ridge, 15° 20′N: ODP Hole 1274A." Contributions to Mineralogy and Petrology **153**(3): 303-319.

Sigmundsson, F. (1991). "Post-glacial rebound and asthenosphere viscosity in Iceland." Geophysical Research Letters **18**(6): 1131-1134.

Sims, K., J. Blichert-Toft, D. Fornari, M. Perfit, S. Goldstein, P. Johnson, D. DePaolo, S. Hart, M. Murrell and P. Michael (2003). "Aberrant youth: Chemical and isotopic constraints on the origin of off-axis lavas from the East Pacific Rise, 9–10 N." Geochemistry, Geophysics, Geosystems **4**(10).

Sims, K., S. Goldstein, J. Blichert-Toft, M. Perfit, P. Kelemen, D. Fornari, P. Michael, M. Murrell, S. Hart and D. DePaolo (2002). "Chemical and isotopic constraints on the generation and transport of magma beneath the East Pacific Rise." Geochimica Et Cosmochimica Acta **66**(19): 3481-3504.

Smith, P. M. and P. D. Asimow (2005). "Adiabat_1ph: A new public front-end to the MELTS, pMELTS, and pHMELTS models." Geochemistry, Geophysics, Geosystems **6**(2): n/a-n/a.

Sparks, D. W. and E. M. Parmentier (1991). "Melt extraction from the mantle beneath spreading centers." Earth and Planetary Science Letters **105**(4): 368-377.

Spiegelman, M. (1993). "Physics of Melt Extraction: Theory, Implications and Applications." Philosophical Transactions: Physical Sciences and Engineering **342**(1663): 23-41.

Spiegelman, M. and T. Elliott (1993). "Consequences of melt transport for uranium series disequilibrium in young lavas." Earth and Planetary Science Letters **118**(1–4): 1-20.

Spiegelman, M., P. B. Kelemen and E. Aharonov (2001). "Causes and consequences of flow organization during melt transport: The reaction infiltration instability in compactible media." Journal of Geophysical Research: Solid Earth **106**(B2): 2061-2077.

Spiegelman, M. and D. McKenzie (1987). "Simple 2-D models for melt extraction at mid-ocean ridges and island arcs." Earth and Planetary Science Letters **83**(1): 137-152.

Standish, J. J. and K. W. Sims (2010). "Young off-axis volcanism along the ultraslow-spreading Southwest Indian Ridge." Nature Geoscience **3**(4): 286.

Stevenson, D. J. (1989). "Spontaneous small-scale melt segregation in partial melts undergoing deformation." Geophysical Research Letters **16**(9): 1067-1070.

Stolper, E. (1980). "A phase diagram for mid-ocean ridge basalts: Preliminary results and implications for petrogenesis." Contributions to Mineralogy and Petrology **74**(1): 13-27.

Stracke, A. and B. Bourdon (2009). "The importance of melt extraction for tracing mantle heterogeneity." Geochimica Et Cosmochimica Acta **73**(1): 218-238.

Stracke, A., J. E. Snow, E. Hellebrand, A. von der Handt, B. Bourdon, K. Birbaum and D. Günther (2011). "Abyssal peridotite Hf isotopes identify extreme mantle depletion." Earth and Planetary Science Letters **308**(3–4): 359-368.

Sturm, M. E., S. J. Goldstein, E. M. Klein, J. A. Karson and M. T. Murrell (2000). "Uranium-series age constraints on lavas from the axial valley of the Mid-Atlantic Ridge, MARK area." Earth and Planetary Science Letters **181**(1): 61-70.

Tepley, F. J., C. C. Lundstrom, K. W. Sims and R. Hékinian (2004). "U-series disequilibria in MORB from the Garrett Transform and implications for mantle melting." Earth and Planetary Science Letters **223**(1-2): 79-97.

Turcotte, D. L. and G. Schubert (2002). Geodynamics, Cambridge University Press.

Turner, A. J., R. F. Katz, M. D. Behn and T. Keller (2017). "Magmatic Focusing to Mid-Ocean Ridges: The Role of Grain-Size Variability and Non-Newtonian Viscosity." Geochemistry, Geophysics, Geosystems **18**(12).

Van Orman, J. A., T. L. Grove and N. Shimizu (1998). "Uranium and thorium diffusion in diopside." Earth and Planetary Science Letters **160**(3–4): 505-519.

Van Orman, J. A., A. E. Saal, B. Bourdon and E. H. Hauri (2006). "Diffusive fractionation of U-series radionuclides during mantle melting and shallow-level melt–cumulate interaction." Geochimica Et Cosmochimica Acta **70**(18): 4797-4812.

Wark, D. A. and E. B. Watson (1998). "Grain-scale permeabilities of texturally equilibrated, monomineralic rocks." Earth and Planetary Science Letters **164**(3–4): 591-605.

Warren, J. M. (2016). "Global variations in abyssal peridotite compositions." Lithos **248–251**: 193-219.

Warren, J. M. and N. Shimizu (2010). "Cryptic Variations in Abyssal Peridotite Compositions: Evidence for Shallow-level Melt Infiltration in the Oceanic Lithosphere." Journal of Petrology **51**(1-2): 395-423.

Warren, J. M., N. Shimizu, C. Sakaguchi, H. J. B. Dick and E. Nakamura (2009). "An assessment of upper mantle heterogeneity based on abyssal peridotite isotopic compositions." Journal of Geophysical Research: Solid Earth **114**(B12): B12203.

Waters, C. L., K. W. Sims, M. R. Perfit, J. Blichert-Toft and J. Blusztajn (2011). "Perspective on the genesis of E-MORB from chemical and isotopic heterogeneity at 9–10 N East Pacific Rise." Journal of Petrology **52**(3): 565-602.

Weatherley, S. M. and R. F. Katz (2012). "Melting and channelized magmatic flow in chemically heterogeneous, upwelling mantle." Geochemistry, Geophysics, Geosystems **13**(5): Q0AC18.

Weatherley, S. M. and R. F. Katz (2016). "Melt transport rates in heterogeneous mantle beneath mid-ocean ridges." Geochimica Et Cosmochimica Acta **172**: 39-54.

Willbold, M. and A. Stracke (2006). "Trace element composition of mantle end-members: Implications for recycling of oceanic and upper and lower continental crust." Geochemistry, Geophysics, Geosystems **7**(4): n/a-n/a.

Wood, B. J. and J. D. Blundy (2014). 3.11 - Trace Element Partitioning: The Influences of Ionic Radius, Cation Charge, Pressure, and Temperature. Treatise on Geochemistry (Second Edition). K. K. Turekian. Oxford, Elsevier**:** 421-448.

Wood, B. J., J. D. Blundy and J. A. C. Robinson (1999). "The role of clinopyroxene in generating U-series disequilibrium during mantle melting." Geochimica Et Cosmochimica Acta **63**(10): 1613-1620.

Workman, R. K. and S. R. Hart (2005). "Major and trace element composition of the depleted MORB mantle (DMM)." Earth and Planetary Science Letters **231**(1–2): 53-72.

Zhu, W. and G. Hirth (2003). "A network model for permeability in partially molten rocks." Earth and Planetary Science Letters **212**(3–4): 407-416.

Appendix

1. Nondimensionalized equations

The set of equations governing the conservations of mass and momentum in the double-porosity model are given as Eqs. (3-1) and (3-2) in the text. In this section, I present nondimensionalized equations. To begin with, I will define a set of characteristic scales for nondimensionalization. The characteristic length scale, L_0, is the height of the model domain (100 km). The characteristic velocity, V_0, is the half spreading rate. Thus, the characteristic time scale follows naturally:

$$t_0 = \frac{L_0}{V_0}. \tag{A3-1}$$

The following definitions will be used for nondimensionalization:

$$\begin{aligned} \nabla' &= L_0 \cdot \nabla, \\ z' &= z / L_0, \\ \mathbf{V'} &= \mathbf{V} \cdot \frac{t_0}{L_0}, \\ \Gamma_m' &= \frac{\Gamma_m \cdot t_0}{\rho}, \\ P_{pz}' &= \frac{P_{pz}}{\rho L_0^{\,2} t_0^{\,-2}}. \end{aligned} \tag{A3-2}$$

where the density of the solid and the melt are approximated as ρ.

The proportion of channel, ψ, the porosities in the matrix and the channel, $\phi_{m,ch}$, and the degree of melting, F, are dimensionless. Substituting Eq. (A3-2) into Eq. (3-1) and Eq. (3-2) leads to:

$$\nabla'\cdot\left[(1-\psi)\phi_m\mathbf{V}_f^m{}'\right]=(1-\psi)\Gamma_m{}'-(1-\psi)\Gamma_m{}'S\,, \tag{A3-3a}$$

$$\nabla'\cdot\left[(1-\psi)(1-\phi_m)\mathbf{V}_s^m{}'\right]=-(1-\psi)\Gamma_m{}'\ , \tag{A3-3b}$$

$$\nabla'\cdot\left(\psi\phi_{ch}\mathbf{V}_f^{ch}{}'\right)=(1-\psi)\Gamma_m{}'S\ , \tag{A3-3c}$$

$$\Gamma_m{}'=\frac{dF}{dz'}\frac{(1-\phi_m)\mathbf{V}_s^m{}'\cdot\mathbf{n_z}}{1-F}\ , \tag{A3-3d}$$

$$\phi_m\left(\mathbf{V}_f^m{}'-\mathbf{V}_s^m{}'\right)=-\frac{\phi_m^n}{C}\left(\frac{d_m}{L_0}\right)^2\cdot\nabla'P_{pz}{}', \tag{A3-3e}$$

$$\begin{aligned}&\phi_{ch}\left(\mathbf{V}_f^{ch}{}'-\mathbf{V}_s^m{}'\right)=\\&-\frac{\phi_{ch}^n}{C}\left(\frac{d_{ch}}{L_0}\right)^2\cdot\Theta^T\begin{bmatrix}1+\dfrac{\beta}{2}erfc\left(\dfrac{0.5-\gamma}{0.2}\right) & 0\\ 0 & 1\end{bmatrix}\Theta\cdot\nabla'P_{pz}{}',\end{aligned} \tag{A3-3f}$$

$$\nabla'P_{pz}{}'=\frac{\eta_s}{\eta_f}\nabla'^2\,\mathbf{V}_s^m{}'+\left(\frac{\zeta_s}{\eta_f}+\frac{1}{3}\frac{\eta_s}{\eta_f}\right)\nabla'\left(\nabla'\cdot\mathbf{V}_s^m{}'\right)+B, \tag{A3-3g}$$

where B is a dimensionless term describing the buoyancy forcing:

$$B=\frac{L_0t_0\Delta\rho\mathbf{g}}{\eta_f}. \tag{A3-4}$$

In the following derivation, I will drop the prime in Eq. (A3-3). Unknowns in Eq. (A3-3) are $\phi_m,\phi_{ch},P_{pz},\Gamma_m,\mathbf{V}_s^m,\mathbf{V}_f^m,\mathbf{V}_f^{ch}$. Accordingly, there are four scalar equations and three vector equations.

2. Solutions of the governing equations: simplifications, procedures and methods

First, I solve for the mass flux of the solid in an equation obtained by combining Eq. (A3-3b) and (A3-3d):

$$\nabla \cdot \mathbf{M}_s = -\frac{1}{1-F}\frac{dF}{dz}\mathbf{M}_s \cdot \mathbf{n}_z \ , \tag{A3-5a}$$

$$\mathbf{M}_s = (1-\psi)(1-\phi_m)\mathbf{V}_s^m \ . \tag{A3-5b}$$

One of the boundary condition is constrained at LAB. The corner-flow solution of Batchelor (2000) has the same boundary condition at LAB but considers no compressibility. To make use of the corner-flow solution, here I decompose the mass flux into the divergence-free corner-flow solution and a compressible component:

$$\mathbf{M}_s = \mathbf{M}^\alpha + \widetilde{\mathbf{M}} \ , \tag{A3-5}$$

where $\mathbf{M}^\alpha$ is the corner-flow solution with a wedge angle α; $\widetilde{\mathbf{M}}$ is the compressible component.

By choosing arbitrary boundary condition at the bottom and two sides, the compressible component could have both vertical and horizontal components. Instead of setting boundary condition for $\mathbf{M}_s$ at the bottom and two sides and solve for $\mathbf{M}_s$, I force the compressible component to have only vertical component and the boundary condition at the bottom and two sides are adjusted to this type of specific solution of $\mathbf{M}_s$. Then equation (A3-5a) is rearranged as an ordinary differential equation of the vertical component of $\widetilde{\mathbf{M}}$:

$$\frac{\partial \widetilde{\mathbf{M}}_z}{\partial z} = -\frac{1}{1-F}\frac{dF}{dz}\left(\mathbf{M}^\alpha{}_z + \widetilde{\mathbf{M}}_z\right), \tag{A3-6}$$

where subscript z denotes the vertical component of the vector. The degree of melting as a function as depth (Fig. S3-1) is given by the pMELTS calculation (Smith and Asimow, 2005) with source composition, DMM (Workman and Hart, 2005) and potential temperature, 1360 °C. $\widetilde{\mathbf{M}}_z$ can be solved from this equation using the four-stage Runge-Kutta method (Gustafsson et al., 1995). The boundary condition at the LAB is given at the bottom of the lithosphere:

$$\widetilde{\mathbf{M}}_z = 0, z = -x \cdot \tan\theta \tag{A3-7}$$

The next step is to solve for the porosity and the velocity of the melt in the matrix and the channel. I have included the time-dependent terms in the mass conservation equations for the matrix and channel continua and solve for the steady state distribution of porosities and melt velocities in the matrix and the channel. The equations of the time-dependent system are derived as:

$$\frac{\partial}{\partial t'}\left[\left(1-\psi\right)\phi_m\right] + \nabla' \cdot \left[\left(1-\psi\right)\phi_m \mathbf{V}_f^m{}'\right] = \left(1-\psi\right)\Gamma_m{}' - \left(1-\psi\right)\Gamma_m{}' S \ , \tag{A3-8a}$$

$$\frac{\partial\left(\psi\phi_{ch}\right)}{\partial t'} + \nabla' \cdot \left(\psi\phi_{ch}\mathbf{V}_f^{ch}{}'\right) = \left(1-\psi\right)\Gamma_m{}' S \ . \tag{A3-8b}$$

The initial condition is zero porosity in both the matrix and the channel. Eqs. (A3-8a) and (A3-8b) are solved iteratively until the porosities and melt velocities in the matrix and the channel reach steady-state. The iteration to solve for steady-state porosity distribution in the matrix and the channel has three steps:

- First, the solid velocity is updated using Eq. (A3-5b) given ϕ_m and $\mathbf{M}_s$.

- Then melt velocities can be updated using Eq. (A3-3) given the porosity and the solid velocity.
- The porosities at a new time step can be updated according to Eqs. (A3-8a) and (A3-8b).

The numerical scheme for the time-dependent equation is the upwind in space, Forward-Euler in time finite difference scheme (Gustafsson et al., 1995). The CFL constant is 0.01. The time step is updated in every time step because it is inversely proportional to the fastest velocity in each step. The time to approach steady state is typically two times of the solid upwelling time (i.e., $2t_0$).

3. Modelling trace element and radiogenic isotope

3.1. Governing equations for a chemical species in the matrix

In this section, I outline procedures for numerical solutions of the concentration of a trace element in the matrix and the pooled melt. The concentration in the matrix will be solved in the model domain while the concentration in the channel networks will not be solved spatially. There are two reasons why I will focus on the concentration of the pooled melt rather than the concentration in channel networks distributed in the model domain. First, the fast melt velocity in the channel slows numerical calculation. Second, the observation of MORB composition is comparable to the focused melt. To solve the concentration in the matrix, I use the steady-state matrix porosity and velocity fields obtained from the previous section. Including radioactive decay and production and chemical exchange between the melt and the solid, mass conservation equations for a chemical species in the solid residue and the interstitial melt in the matrix are:

$$\nabla\cdot\left(\left(1-\psi\right)\rho_f\phi_m\mathbf{V}_f^m C_f^{m,i}\right)=\left(1-\psi\right)\Gamma_m C_s^{p,i}-\left(1-\psi\right)\Gamma_m SC_f^{m,i}$$
$$-\left(1-\psi\right)\rho_f\phi_m\left(\lambda_i k^i C_f^{m,i}-\lambda_{i-1}k^{i-1}C_f^{m,i-1}\right)+\rho_s\left(1-\psi\right)\left(1-\phi_m\right)R^i\left(C_s^{m,i}-k^i C_f^{m,i}\right) \quad \text{, (A3-9a)}$$

$$\nabla\cdot\left(\rho_s\left(1-\psi\right)\left(1-\phi_m\right)\mathbf{V}_s^m C_s^{m,i}\right)=-\left(1-\psi\right)\Gamma_m C_s^{p,i}$$
$$-\rho_f\left(1-\psi\right)\left(1-\phi_m\right)\left(\lambda_i C_s^{m,i}-\lambda_{i-1}C_s^{m,i-1}\right)-\rho_s\left(1-\psi\right)\left(1-\phi_m\right)R^i\left(C_s^{m,i}-k^i C_f^{m,i}\right) \quad \text{, (A3-9b)}$$

where C_s^p is the bulk composition of the chemical species in minerals participated in the melting reaction; R^i is the exchange rate coefficient for the chemical species (Liang, 2003; Liang and Liu, 2016); superscript *i*-1 represents the radiogenic parent of *i*. After substituting Eq. (A3-2) to, we obtain the dimensionless forms of Eq. (A3-9):

$$\nabla'\cdot\left(\left(1-\psi\right)\phi_m\mathbf{V}_f^m{}' C_f^{m,i}\right)=\left(1-\psi\right)\Gamma_m{}' C_s^{p,i}-\left(1-\psi\right)\Gamma_m{}' SC_f^{m,i}$$
$$-\left(1-\psi\right)\phi_m\left(\lambda_i{}' C_f^{m,i}-\lambda_{i-1}{}' C_f^{m,i-1}\right)+\left(1-\psi\right)\left(1-\phi_m\right)R^i{}'\left(C_s^{m,i}-k^i C_f^{m,i}\right) \quad \text{, (A3-10a)}$$

$$\nabla'\cdot\left(\left(1-\psi\right)\left(1-\phi_m\right)\mathbf{V}_s^m{}' C_s^{m,i}\right)=-\left(1-\psi\right)\Gamma_m{}' C_s^{p,i}$$
$$-\left(1-\psi\right)\left(1-\phi_m\right)\left(\lambda_i{}' C_s^{m,i}-\lambda_{i-1}{}' C_s^{m,i-1}\right)-\left(1-\psi\right)\left(1-\phi_m\right)R^i{}'\left(C_s^{m,i}-k^i C_f^{m,i}\right) \quad \text{, (A3-10b)}$$

$$R^i{}'=R^i\cdot t_0 \quad \text{(A3-10c)}$$

$$\lambda_{i-1}{}'=\lambda_{i-1}\cdot t_0 \ . \quad \text{(A3-10d)}$$

To further simplify, here I assume that the melt and solid are in chemical equilibrium in the matrix, and their concentrations are related to each through the bulk partition coefficient, viz.,

$$C_m^{s,i}=k^i\cdot C_m^{f,i} \ . \quad \text{(A3-10e)}$$

Substituting into Eq. (A3-10), we have the dimensionless equation for the concentration in the matrix melt:

$$\left[(1-\psi)\phi_m \mathbf{V}_f^m + (1-\psi)(1-\phi_m)\mathbf{V}_s^m k^i\right]\cdot\nabla C_f^{m,i} = -(1-\psi)\Gamma_m\left(1-k_p^i\right)C_f^{m,i}$$
$$-\left[(1-\psi)(1-\phi_m)k^i + \phi_m(1-\psi)\right]\lambda_i' C_f^{m,i} + \left[(1-\psi)(1-\phi_m)k^{i-1} + \phi_m(1-\psi)\right]\lambda_{i-1}' C_f^{m,i}, \quad \text{(A3-11)}$$

where k_p^i is the bulk partition coefficient for minerals participated in melting. Primes on dimensionless parameters are dropped.

According to the pMELTS model, 5% garnet is present in the source and is consumed within the first 0.4% melting. For the purpose of demonstration, the modal abundance of garnet decreases linearly with the degree of melting while the modal abundance of other minerals vary according to the melting reaction of Kinzler and Grove (1992). The partition coefficients of REE in opx and cpx are from Sun and Liang (2012), Yao et al. (2012) and Sun and Liang (2014). The partition coefficients of REE in olivine, garnet and spinel are from Kelemen et al. (2003). The partition coefficients of U and Th in cpx and opx are from Hauri et al. (1994) and Wood et al. (1999). The partition coefficients of U and Th in garnet are from Salters et al. (2002). The bulk partition coefficient for Ra is set to 1×10^{-4} (Jull et al., 2002).

Given the matrix porosity and flow fields, Eq. (A3-11) can be solved by the method of characteristics (Gustafsson et al., 1995). For REE, the source composition is the average DMM from Workman and Hart (2005).

Eq. (A3-11) can be applied to radiogenic isotopes in a chain of decays:

$$N_1 \xrightarrow{\lambda_1} N_2 \xrightarrow{\lambda_2} N_3 \xrightarrow{\lambda_3} \ldots \qquad \text{(A3-12)}$$

where N_1, N_2, and N_3 can be ^{234}U, ^{230}Th, and ^{226}Ra, respective;y. If N_1 is ^{234}U, the decay of ^{234}U should be buffered by the decay of ^{238}U because the activity ratio of ^{238}U to ^{234}U is unity in natural samples. The activity is defined as usual,

$$\left(N_i\right) = \lambda_i \cdot C^i . \qquad \text{(A3-13)}$$

For ^{234}U, ^{230}Th, and ^{226}Ra, their concentration in the source is in secular equilibrium:

$$^{234}\mathrm{U} \cdot \lambda_1 = {}^{230}\mathrm{Th} \cdot \lambda_2 = {}^{226}\mathrm{Ra} \cdot \lambda_3 = \kappa \ , \qquad \text{(A3-14a)}$$

where the constant, κ is determined by the Uranium concentration in DMM (Workman and Hart, 2005) and the proportion of ^{234}U in terrestrial samples (Böhlke et al., 2005), viz.,

$$\kappa = C_U^{DMM} \cdot \left(\frac{^{234}U}{U} \right) \cdot \lambda_1 \ . \qquad \text{(A3-14b)}$$

3.2. Concentration in pooled channel melt

I will derive the solution in one dimension and generalize the solution to two dimensions. The solution for unradiogenic trace element in the pooled melt is given by Eq. (3-8). Here, the solution for radiogenic isotopes in the pooled channel melt will be derived. The expression for the solution for radiogenic isotopes in the pooled melt will be given at the end of this section. The transport time in the channel will be shown to have potential impact on the concentration of radiogenic isotope in focused channel melt. Before solving the concentration in focused channel melt, the concentration of matrix melt should be given

by the previous section. In one dimension, the chemical flux of N_1, N_2, and N_3 in the channel melt are described by Eq. (3-6b):

$$\frac{d\left(\psi\rho_f\phi_{ch}V_f^{ch}C_f^{ch,1}\right)}{dz}=\left(1-\psi\right)\Gamma_m SC_f^{m,1}, \tag{A3-15a}$$

$$\frac{d\left(\psi\rho_f\phi_{ch}V_f^{ch}C_f^{ch,2}\right)}{dz}=\left(1-\psi\right)\Gamma_m SC_f^{m,2}-\psi\rho_f\phi_{ch}\left(\lambda_2 C_f^{ch,2}-\lambda_1 C_f^{ch,1}\right), \tag{A3-15b}$$

$$\frac{d\left(\psi\rho_f\phi_{ch}V_f^{ch}C_f^{ch,3}\right)}{dz}=\left(1-\psi\right)\Gamma_m SC_f^{m,3}-\psi\rho_f\phi_{ch}\left(\lambda_3 C_f^{ch,3}-\lambda_2 C_f^{ch,2}\right), \tag{A3-15c}$$

The concentration of a radiogenic isotope depends on the concentrations of its parent and grandparent. Hence $C_f^{ch,1}$, $C_f^{ch,2}$, and $C_f^{ch,3}$ need to be solved sequentially. It is convenient to define the characteristics as:

$$t\left(z\right)=\int_0^z\frac{dz}{V_f^{ch}}\ , \tag{A3-16a}$$

$$dt\left(z\right)=\frac{dz}{V_f^{ch}}. \tag{A3-16b}$$

The solution of $C_f^{ch,1}$ is obtained by integrating Eq. (A3-15a).

$$\psi\rho_f\phi_{ch}V_f^{ch}C_f^{ch,1}=\int_0^z d\zeta\cdot C_f^{m,1}\cdot\left(1-\psi\right)\Gamma_m S, \tag{A3-17}$$

The left-hand side is the chemical flux of isotope N_1 in the channel at height z. Because ^{234}U is buffered by ^{238}U, ^{234}U behaves like a stable trace element. Next, I solve the flux of isotope N_2 in the channel.

$$\psi\rho_f\phi_{ch}V_f^{ch}C_f^{ch,2} = \int_0^z d\zeta\cdot\left[e^{-\lambda_2\left(t(z)-t(\zeta)\right)}C_f^{m,2}+\frac{1-e^{-\lambda_2\left(t(z)-t(\zeta)\right)}}{\lambda_2}\lambda_1 C_f^{m,1}\right]\cdot\left(1-\psi\right)\Gamma_m S, \quad \text{(A3-18)}$$

where the second term in the square bracket is the contribution from the decaying of isotope N_1 in the channel melt. Finally, I solve the flux of isotope N_3 in the channel.

$$\psi\rho_f\phi_{ch}V_f^{ch}C_f^{ch,3} = \int_0^z d\zeta\cdot\left[\begin{array}{l} e^{-\lambda_3\left(t(z)-t(\zeta)\right)}C_f^{m,3}+\dfrac{e^{-\lambda_2\left(t(z)-t(\zeta)\right)}-e^{-\lambda_3\left(t(z)-t(\zeta)\right)}}{\lambda_3-\lambda_2}\lambda_2 C_f^{m,2} \\ +\left(\dfrac{1-e^{-\lambda_3\left(t(z)-t(\zeta)\right)}}{\lambda_3}-\dfrac{e^{-\lambda_2\left(t(z)-t(\zeta)\right)}-e^{-\lambda_3\left(t(z)-t(\zeta)\right)}}{\lambda_3-\lambda_2}\right)\lambda_1 C_f^{m,1}\end{array}\right]\cdot\left(1-\psi\right)\Gamma_m S, \quad \text{(A3-19)}$$

where the second term in the square bracket is the contribution from the decay of isotope N_2 to the flux of isotope N_3 in the channel melt, while the third term in the square bracket is the contribution from the decay of isotope N_1 to the flux of isotope N_3 in the channel melt.

Eqs. (A3-17), (A3-18), and (A3-19) demonstrate the importance of melt transport on the flux of radiogenic isotope. Once melt is extracted to the channel, the amount of radiogenic isotope in the channel has the contribution from the remaining undecayed isotope and the contribution from decayed parental or grandparental isotope. By tracking the transport of each fraction of matrix melt that is extracted into the channel, the flux of radiogenic isotope in a two dimensional melting region can be calculated as follows:

$$\overline{C_f^{ch,1}}\int_{\Omega_{ch}} dxdy\cdot\left(1-\psi\right)\Gamma_m S = \int_{\Omega_{ch}} dxdy\cdot e^{-\lambda_1\tau(x,y)}C_f^{m,1}\cdot\left(1-\psi\right)\Gamma_m S, \quad \text{(A3-20)}$$

$$\overline{C_f^{ch,2}} \int_{\Omega_{ch}} dxdy \cdot (1-\psi)\Gamma_m S = \int_{\Omega_{ch}} dxdy \cdot \left[e^{-\lambda_2 \tau(x,y)} C_f^{m,2} + \frac{1-e^{-\lambda_2 \tau(x,y)}}{\lambda_2} \lambda_1 C_f^{m,1} \right] \cdot (1-\psi)\Gamma_m S, \quad \text{(A3-21)}$$

$$\overline{C_f^{ch,3}} \int_{\Omega_{ch}} dxdy \cdot (1-\psi)\Gamma_m S = \int_{\Omega_{ch}} dxdy \cdot \left[\begin{array}{l} e^{-\lambda_3 \tau(x,y)} C_f^{m,3} + \frac{e^{-\lambda_2 \tau(x,y)} - e^{-\lambda_3 \tau(x,y)}}{\lambda_3 - \lambda_2} \lambda_2 C_f^{m,2} \\ + \left(\frac{1-e^{-\lambda_3 \tau(x,y)}}{\lambda_3} - \frac{e^{-\lambda_2 \tau(x,y)} - e^{-\lambda_3 \tau(x,y)}}{\lambda_3 - \lambda_2} \right) \lambda_1 C_f^{m,1} \end{array} \right] \cdot (1-\psi)\Gamma_m S, \quad \text{(A3-22)}$$

where $\overline{C_f^{ch,i}}$ is the concentration of isotope N_i in the pooled channel melt flux; $\tau(x,y)$ is the melt transport time through the channel networks from (x, y) to the decompaction channel at LAB. $\tau(x,y)$ will be solved on 20 streamlines in the melt focusing zone and interpolated to the melt focusing zone. The transport time in the decompaction channel is assumed to be negligibly small.

Then, the concentration of pooled melt is given by:

$$C^{MORB} = \frac{\overline{C_f^m} \cdot \int_{\Omega_m} dxdy \cdot (1-\psi)(1-S)\Gamma_m + \overline{C_f^{ch}} \cdot \int_{\Omega_{ch}} dxdy \cdot (1-\psi)\Gamma_m S}{\int_{\Omega_m} dxdy \cdot (1-\psi)(1-S)\Gamma_m + \int_{\Omega_{ch}} dxdy \cdot (1-\psi)\Gamma_m S}, \quad \text{(A3-23)}$$

where $\overline{C_f^m}$ is the concentration of the matrix melt near the axis (5km beneath the ridge axis); $\overline{C_f^{ch}}$ is calculated using Eq. (A3-20), (A3-21), or (A3-22).

4. The effect of variable melting rate on (^{230}Th/^{238}U): an analysis of 1D model

The melting rate competes with radiogenic decay to dictate the fractionation of U series (Eq. (A3-11)). While the decay rate or the radiogenic constant is precisely known, the melting rate varies spatially in the melting region (Fig. S3-9c). In this section, I will compare numerical solution of U series with an approximate solution. The approximate solution is obtained by solving a model with constant matrix porosity, matrix melt velocity, and melting rate. These constant values are chosen to be local values. Unlike the single-porosity model of Spiegelman and Elliott (1993) and Bourdon and Sims (2003), the current model deal with a scenario in which the melt flux in the matrix is smaller than all melt generated in the matrix because of melt extraction to the channel. The current model for U series has the same double-porosity set-up as the model of Lundstrom (2000) and Jull et al. (2002) except that the matrix melt in earlier models is instantaneously extracted to the channel at the depth of channel formation. The constant, κ, in the secular equilibrium is set to be unity because only the activity ratio will be discussed in this section. Due to the similarity in the approximate solution, only the result of (^{230}Th/^{238}U) will be discussed in detail.

The approximate solution of ^{234}U, ^{230}Th, and ^{226}Ra in matrix melt are obtained by solving Eq. (A3-11) in one dimension with constant coefficients.

$$C_U = \frac{1}{\lambda_U k_U} \cdot e^{-a_U z}, \tag{A3-23}$$

$$C_{Th} = \frac{1}{k_U V_{Th}} \cdot \frac{\phi_m + (1-\phi_m) k_U}{\phi_m + (1-\phi_m) k_{Th}} \cdot \frac{e^{-a_U z} - e^{-a_{Th} z}}{a_{Th} - a_U} + \frac{1}{k_{Th} \lambda_{Th}} \cdot e^{-a_{Th} z}, \tag{A3-24}$$

$$C_{Ra} = \frac{1}{k_{Ra}\lambda_{Ra}} \cdot e^{-a_{Ra}z} + \frac{\lambda_{Th}}{V_{Ra}} \cdot \frac{\phi_m + (1-\phi_m)k_{Th}}{\phi_m + (1-\phi_m)k_{Ra}} \cdot$$
$$\left[\frac{\frac{1}{k_U V_{Th}} \cdot \frac{\phi_m + (1-\phi_m)k_U}{\phi_m + (1-\phi_m)k_{Th}} \cdot \frac{1}{a_{Th} - a_U}}{a_{Ra} - a_U} \left(e^{-a_U z} - e^{-a_{Ra} z} \right) + \right. \tag{A3-25}$$
$$\left. \frac{\frac{1}{k_{Th}\lambda_{Th}} - \frac{1}{k_U V_{Th}} \cdot \frac{\phi_m + (1-\phi_m)k_U}{\phi_m + (1-\phi_m)k_{Th}} \cdot \frac{1}{a_{Th} - a_U}}{a_{Ra} - a_{Th}} \left(e^{-a_{Th} z} - e^{-a_{Ra} z} \right) \right],$$

where the decay factors and effective velocities are defined as:

$$\begin{aligned} a_U &= \frac{\Gamma_m (1-k_U)}{V_U \left[\phi_m + (1-\phi_m)k_U \right]}, \\ a_{Th} &= \frac{\Gamma_m (1-k_{Th})}{V_{Th} \left[\phi_m + (1-\phi_m)k_{Th} \right]} + \frac{\lambda_{Th}}{V_{Th}}, \\ a_{Ra} &= \frac{\Gamma_m (1-k_{Ra})}{V_{Ra} \left[\phi_m + (1-\phi_m)k_{Ra} \right]} + \frac{\lambda_{Ra}}{V_{Ra}}, \end{aligned} \tag{A3-26}$$

$$\begin{aligned} V_U &= \frac{\phi_m V_f^m + (1-\phi_m) V_s^m k_U}{\phi_m + (1-\phi_m)k_U}, \\ V_{Th} &= \frac{\phi_m V_f^m + (1-\phi_m) V_s^m k_{Th}}{\phi_m + (1-\phi_m)k_{Th}}, \\ V_{Ra} &= \frac{\phi_m V_f^m + (1-\phi_m) V_s^m k_{Ra}}{\phi_m + (1-\phi_m)k_{Ra}}. \end{aligned} \tag{A3-27}$$

Knowing that ($^{234}U/^{238}U$) is always unity, ($^{230}Th/^{238}U$) can be expressed as ($^{230}Th/^{234}U$):

$$\left({}^{230}\mathrm{Th}/{}^{238}\mathrm{U} \right) =$$
$$\frac{\lambda_{Th}}{V_{Th}} \cdot \frac{\phi_m + (1-\phi_m)k_U}{\phi_m + (1-\phi_m)k_{Th}} \cdot \frac{1 - \exp\left(-(a_{Th} - a_U)z\right)}{a_{Th} - a_U} + \frac{k_U}{k_{Th}} \cdot \exp\left(-(a_{Th} - a_U)z\right). \tag{A3-28}$$

4.1. Wet melting regime

At the onset of melting and the following wet melting regime between 100 km and 70 km depth, the ratio of the melting rate to the porosity is small in the simulation of melting and melt migration. This ratio is much smaller than the radiogenic decaying constant of Th and Ra. Thus, the first term in the decay factor of Th and Ra can be neglected (Eq. (A3-26)). The decay factor in (^{230}Th/^{238}U) can be approximated by:

$$\left(a_{Th}-a_{U}\right)\sim\frac{\lambda_{Th}}{V_{Th}}. \tag{A3-29}$$

The effective velocity of Th is in between the solid velocity and the melt velocity. Considering that the melt velocity is close to the solid velocity due to the small porosity, the effective velocity of Th should be similar to the solid velocity. An estimate for the decay factor can be obtained as:

$$\left(a_{Th}-a_{U}\right)\sim\frac{\lambda_{Th}}{V_{Th}}\sim\frac{\lambda_{Th}}{V_{s}}. \tag{A3-30}$$

For a medium spreading rate of 50 mm/yr, Eq. (A3-30) states that (^{230}Th/^{238}U) in the matrix melt should approach the asymptotic value after upwelling a distance larger than 5 km. The height of wet melting regime is greater than this length scale. Thus, it is meaningful to acquire the asymptotic value of (^{230}Th/^{238}U) in wet melting regime, which is obtained by dropping all exponential terms in Eq. (A3-28):

$$\left(^{230}\mathrm{Th}/^{238}\mathrm{U}\right)=\frac{\lambda_{Th}}{V_{Th}}\cdot\frac{\phi_{m}+\left(1-\phi_{m}\right)k_{U}}{\phi_{m}+\left(1-\phi_{m}\right)k_{Th}}\cdot\frac{1}{a_{Th}-a_{U}}\ . \tag{A3-31}$$

Because of the fast decaying rate of ^{226}Ra, (^{226}Ra/^{230}Th) has an even shorter decay length scale. Similarly, the asymptotic value of (^{226}Ra/^{230}Th) is given by the expression:

$$\left(^{226}\mathrm{Ra}/^{230}\mathrm{Th}\right)=\frac{\lambda_{Ra}}{V_{Ra}}\cdot\frac{\phi_m+\left(1-\phi_m\right)k_{Th}}{\phi_m+\left(1-\phi_m\right)k_{Ra}}\cdot\frac{1}{a_{Ra}-a_U}\ . \tag{A3-32}$$

By noting $\phi_m \ll 1$ in Eq. (A3-31), (^{230}Th/^{238}U) can be approximated by a constant:

$$\left(^{230}\mathrm{Th}/^{238}\mathrm{U}\right)\sim\frac{\lambda_{Th}}{V_{Th}}\cdot\frac{\phi_m+k_U}{\phi_m+k_{Th}}\cdot\frac{1}{\frac{\lambda_{Th}}{V_s}}\sim\frac{\phi_m+k_U}{\phi_m+k_{Th}}\ . \tag{A3-33}$$

Eq. (A3-33) suggests that the ^{230}Th and ^{238}U in the two-phase matrix is in secular equilibrium. Because the parent and daughter are partitioned into the matrix melt, ^{230}Th and ^{238}U in the matrix melt will not be in secular equilibrium. The activity ratio in the matrix melt is greater than one if U is less incompatible than Th. (^{230}Th/^{238}U) in the matrix melt after wet melting will start from $\frac{k_U}{k_{Th}}$ and approach $\frac{\phi_m+k_U}{\phi_m+k_{Th}}$. Therefore, Eq. (A3-33) sets an initial condition for the following dry melting regime with larger melting rate. The current approximation is the same as the slow-melting limit proposed by McKenzie (1985). The larger than unity ratio of k_U/k_{Th} is required to produce the larger than unity (^{230}Th/^{238}U) in the slow melting regime. Next, we will examine if (^{230}Th/^{238}U) will grow in the dry melting regime.

4.2. Dry melting regime

When the melting rate increases in the dry melting regime, Eq. (A3-31) can be rearranged as a perturbation from the slow-melting approximation, Eq. (A3-33).

$$\left(^{230}\mathrm{Th}/^{238}\mathrm{U}\right)=\frac{\phi_m+k_U}{\phi_m+k_{Th}}\cdot\left(1-\delta+O\left(\delta^2\right)\right)\ , \tag{A3-34a}$$

$$\delta=\frac{\Gamma_m}{\lambda_{Th}\left(\phi_m+k_{Th}\right)}\frac{V_s^m\left(k_U-k_{Th}\right)}{\phi_m V_f^m+V_s^m k_U}\ . \tag{A3-34b}$$

The sense of changing (^{230}Th/^{238}U) in the dry melting regime depends on the relative compatibility of U and Th. If U is less incompatible than Th and the effective velocity of U and Th are similar, (^{230}Th/^{238}U) in the matrix melt will decrease in the dry melting regime. The asymptotic value of (^{230}Th/^{238}U) could be smaller than unity. However, the opposite case where (^{230}Th/^{238}U) will grow in the dry melting regime are also plausible if U is more incompatible than Th. In such a case, (^{230}Th/^{238}U) starts from below unity in the wet melting regime and then increases in the dry melting regime. At the end of the dry melting, (^{230}Th/^{238}U) could increase to above unity. Thus, larger than unity k_U/k_{Th} is not required by the larger than unity (^{230}Th/^{238}U) as long as k_U/k_{Th} is smaller than unity from wet solidus to the end of dry melting. The relative compatibility of U and Th below 2 GPa is still controversial given existing experimental measurements (Hauri et al., 1994; Wood et al., 1999; Blundy and Wood, 2003; Wood and Blundy, 2014), though the data shows a trend that k_U/k_{Th} decreases from larger than unity at ~2.5 GPa to around unity at ~1 GPa. Thus, the previous case where (^{230}Th/^{238}U) decreases from $\frac{k_U}{k_{Th}}$ to $\frac{\phi_m+k_U}{\phi_m+k_{Th}}$ in the wet melting regime and then to $\frac{\phi_m+k_U}{\phi_m+k_{Th}}\cdot\left(1-\delta\right)$ in the dry melting regime should be more consistent with experimental constraints on the partition coefficients of U and Th.

A similar analysis on (^{226}Ra/^{230}Th) with correction of melting rate can be done. Because the decay constant of Ra is 50 times faster than Th, the correction of (^{226}Ra/^{230}Th) for the melting rate is small. Thus, (^{226}Ra/^{230}Th) in the matrix melt is well approximated by the following expression (Fig. S3-10):

$$\left(^{226}\mathrm{Ra}/^{230}\mathrm{Th}\right) \sim \frac{\phi_m + k_{Th}}{\phi_m + k_{Ra}}. \tag{A3-35}$$

Results shown in Fig. 3-8 suggest that the porosity maximizes at 60 km. So, the minimum of (^{226}Ra/^{230}Th) is at 60 km (Fig. S3-10). Above 60 km, the porosity decreases. (^{226}Ra/^{230}Th) increases towards $\frac{k_{Th}}{k_{Ra}}$ while (^{230}Th/^{238}U) decreases due to that the negative correction term for melting is still valid. Hence (^{226}Ra/^{230}Th) inversely correlates with (^{230}Th/^{238}U) in the matrix melt above 60 km. It is possible to preserve such anticorrelation if melt transport is fast in the channels.

Melt extracted from dry melting regime dominates the pooled melt. The melt extraction time for the melt generated at depth could be enough for the matrix melt to restore secular equilibrium of (^{230}Th/^{238}U) during the transport in channels. Most natural samples have (^{230}Th/^{238}U) from 0.9 to 1.3. Therefore, these two values: $\frac{k_U}{k_{Th}}$ in the wet melting regime and $\frac{\phi_m + k_U}{\phi_m + k_{Th}} \cdot (1-\delta)$ in the dry melting regime should bracket the range of data, viz.

$$\frac{k_U}{k_{Th}} > 1.3 \ , \tag{A3-36a}$$

$$\frac{\phi_m + k_U}{\phi_m + k_{Th}} \cdot (1 - \delta) < 0.9 \qquad \text{(A3-36b)}$$

4.3. Top non-melting layer

The melting rate decreases to zero at the base of LAB. The asymptotic value for (^{230}Th/^{238}U) can be approximated by Eq. (A3-31). (^{230}Th/^{238}U) in the matrix melt just below the base of LAB should restore or even overshoot the value at the end of wet melting regime. However, these matrix melt has much lower volume flux and concentration of U and Th than deeper melts. Therefore, the matrix melt in the top-non-melting layer is not important to the activity ratio of pooled melt.

Figure captions

Figure 3-1 The motivation for the double-porosity model and four independent observational constraints. Observation #0 is the mapping of dunite channels as tabular veins within harzburgite at exposed ridge section (Braun and Kelemen, 2002). This observation motivates the double-porosity model where the harzburgite matrix and dunite channels are treated as two layers of continua. Observation #1 is the deep low resistivity center beneath the ridge axis at 9.5°N EPR (Key, et al., 2013). The depth of the resistivity minimum, 50-70 km, is consistent with another magnetotelluric study by Baba et al. (2006) at 17°S EPR. Observation #2 is depleted REE patterns in clinopyroxene in abyssal peridotites (Johnson et al., 1990; Johnson and Dick, 1992; Dick and Natland, 1996; Ross and Elthon, 1997; Hellebrand et al., 2002; Salters and Dick, 2002; Hellebrand and Snow, 2003; Cipriani et al., 2004; Brunelli et al., 2006; Seyler et al., 2007; Warren et al., 2009; Stracke et al., 2011; Mallick et al., 2014; D'Errico et al., 2016). Blue field shows the range of REE pattern generated by batch melting model with degree of melting between 0% and 18%. Observation #3 is excess of ($^{230}Th/^{234}U$) and ($^{226}Ra/^{230}Th$) in MORB (Lundstrom et al., 1995; Lundstrom et al., 1998, 1999; Bourdon et al., 2000; Sturm et al., 2000; Peate et al., 2001; Sims et al., 2002, 2003; Cooper et al., 2003; Tepley et al., 2004; Bourdon et al., 2005; Kokfelt et al., 2005; Rubin et al., 2005; Russo et al., 2009; Standish and Sims, 2010; Elkins et al., 2011; Waters et al., 2011; Elkins et al., 2014).

Figure 3-2 One-dimensional porosity profiles (a) and velocity profiles (b) in the matrix and the channel. The relative melt suction rates are 0.80, 0.85, 0.90, and 0.95. The

velocity is normalized by the upwelling rate of the mantle (V_0). The permeability model is from Wark and Watson (1998). The grain size in the matrix and the channel are 1 mm and 3 mm, respectively. The proportion of channels is 10%.

Figure 3-3 Model setup (a) and cases of different channel distribution (b). The model domain is 200 km wide and 100 km deep. Blue lines are streamlines of the solid. The lithosphere has a wedge shape. The angle depends on the spreading rate. Here it is 25°, corresponding to a half-spreading rate of 50 mm/yr. On the left half-space, circles with red and black clock hands are placed at the bottom. The shape of the circle and the angle between clock hands are used to illustrate the extent of deformation as the solid mantle flows. The interval between nearest clock face in a streamline is 0.2 Myr. The rim of the clock is originally gray but gradually changes to orange as the shear strain reaches one. The area where the shear strain is greater than one is filled by green. On the right half-space, magenta bars indicate the predicted dip of shear-induced melt band. The dip is obtained by rotating the shear plane 20° in the same direction of the sense of the shear. The pink cap on the top of the melting region are two decompaction channels. The width of this cap is from Hebert and Montési (2010). In four panels of (b), only the right half-space is illustrated. Case#1 is a reference case with no channels. This case will be labeled with "Batch, no channels" in the later discussion. Case#2 has uniform channel distribution, ψ , and relative melt suction rate, S . The channels in case#2 has isotropic permeability. This case will be labelled with "Uniform channel distribution, isotropic $\mathbf{k}_{\phi}^{ch}$ ". Case#3 has the same uniform channel distribution and relative melt suction rate as case #2. But the channel has anisotropic permeability.

This case will be labelled with "Uniform channel distribution, anisotropic $\mathbf{k}_{\phi}^{ch}$". Case#4 considers larger proportion of channels and strong melt extraction in the shallowest 30 km. Because the melt suction rate is zero in the lower part, there is no melt in the channel in the lower part. So, this case considers effective channels only in the shallowest 30 km. This case will be labelled with "RII channel <30km". Case#5 considers additional channels formed by shear deeper than 30 km. This case will be labelled with "RII channel <30km + shear band". And finally, case#6 considers larger proportion of channels and strong melt extraction in the shallowest 60 km. This case will be labelled with "RII channel <60km + shear band".

Figure 3-4 The melt distribution, flow fields of the melt and the solid mantle in a reference case with no channels (case#1 in Fig. 3-3b). The permeability model is from Wark and Watson (1998). The grain size is 0.4 mm in the matrix. The viscosity of the melt and the mantle are 1 Pa·s and 10^{19} Pa·s respectively (Murase and McBirney, 1973; Sigmundsson, 1991). The porosity is shown in the color map. The flow of the solid is illustrated by white lines while the melt flow is illustrated by black dashed lines. Two thick lines along the LAB are decompaction channels. The zone of melt focusing is highlighted. The resulted crustal thickness is labeled on the upper right of the plot. In this case, the zone of melt focusing is slightly narrower than the decompaction channel at LAB.

Figure 3-5 The melt distribution, flow fields of the melt and the solid mantle in a case with uniform channel distribution (case#2 in Fig. 3-3b). The viscosities and permeability model are the same as the case shown in Fig. 3-4. The grain size is 0.4 mm and 1.3 mm in the matrix and the channel respectively.The permeability of channels is

isotropic. Panel (a) shows the porosity in the matrix. The dashed line is the streamline of the matrix melt. Panel (b) shows the porosity in the channel. The dashed line is the streamline of the channel melt. Panel (c) shows the bulk porosity. The dashed line is the streamline of the bulk melt flux. The channel melt flows nearly vertical. The zone of melt focusing is as wide as the cap of the decompaction channel at LAB.

Figure 3-6 The melt distribution, flow fields of the melt and the solid mantle in a case with uniform channel distribution (case#3 in Fig. 3-3b). The permeability of channels is anisotropic in regions of high shear strain. The grain size, viscosities, and permeability model are the same as the case shown in Fig. 3-5. The channel melt is effectively focused under the cap of the decompaction channel at LAB.

Figure 3-7 The melt distribution, flow fieldss of the melt and the solid mantle in a case where the proportion of channels is larger and the melt extraction is stronger in the shallowest 30 km (case#4 in Fig. 3-3b). The grain size, viscosities, and permeability model are the same as the case shown in Figure 3-5.

Figure 3-8 The melt distribution, flow fields of the melt and the solid mantle in a case where additional channels are formed by shear deeper than 30 km (case#5 in Fig. 3-3b). The grain size, viscosities, and permeability model are the same as the case shown in Fig. 3-5. These additional channels help melt focusing compared to case#4 (Fig. 3-7).

Figure 3-9 The melt distribution, flow fields of the melt and the solid mantle in a case where replacive channels form at 60 km depth (case#6 in Fig. 3-3b). The grain size,

viscosities, and permeability model are the same as the case shown in Fig. 3-4. The porosity in the matrix has a maximum at 60 km and is near zero beneath LAB. The matrix melt has essentially no contribution to the crustal thickness.

Figure 3-10 The bulk porosity as a function of the channel proportion, ψ and the proportion of channel melt flux, X. The grain size, viscosities, and permeability model are the same as the case shown in Fig. 3-4. The highlighted region with $X > 0.6$ and $\psi < 0.15$ is most geologically relevant.

Figure 3-11 The effect of anisotropic permeability on the crustal thickness. The grain size, viscosities, and permeability model are the same as the case shown in Fig. 3-4. Red symbols are for fast half-spreading rate (100 mm/yr) while blue symbols are for medium half-spreading rate (50 mm/yr). The proportion of channels and the relative melt suction rate are uniform in each case. The crustal thickness is calculated by dividing the integral of melt production inside the zone of melt focusing by the full spreading rate (see Eq. 3-6).

Figure 3-12 The melt focusing zone for the channel in four cases of different half-spreading rate and mantle viscosity. The grain size, viscosity of the melt, and permeability model are the same as the case shown in Fig. 3-4. The colormap is for the melting rate. The red lines are the streamline of channel melt in the isotropic case. The magenta lines are two sides of the melt focusing zone for various permeability anisotropy (0, 1, 2, 3, 5, 10, 15). The inner most pair brackets the melt focusing zone for isotropic permeability. To the first order, the lateral extent of the

melt focusing zone increases as the additional anisotropy increases. See Fig. S3-8 for the resulted crustal thickness.

Figure 3-13 The concentration of Ce normalized by the source in the matrix solid (first row) and the REE pattern in clinopyroxenes sampled along two lines in the lithosphere for five cases of channel distribution (a, b, c, d, e). The lithosphere is left blank. The Ce concentration in the wedge-shape lithosphere is horizontally layered and continuous at LAB. The REE pattern is normalized by CI chondrite (Anders and Grevesse, 1989). According to the pMELTS model, 5% garnet is present in the source and is consumed within 0.4% melting. This interval of melting in the vertical bar beneath the axis is filled with black stripe pattern. REE patterns in color are from cpx during spinel-lherzolite melting while REE patterns in dashed line are from garnet-lherzolite melting. The gray lines are REE pattern in cpx in residual abyssal peridotites (the same data shown in Fig. 3-1). See the text for trace element modeling. The case for of the first column of panels (a) has no channels (case#1 in Fig. 3-3b). The case of the second column of panels (b) has uniform melt channels (case#3 in Fig. 3-3b). The case of the third column of panels (c) has replacive channels (or "reaction-infiltration instability", RII channels) in 0-30 km depth (case#4 in Fig. 3-3b). The case of the fourth column of panels (d) has RII channels in 0-30 km depth and melt localization bands in high shear strain region (case#5 in Fig. 3-3b). The case of the fourth column of panels (e) has RII channels in 0-60 km depth and melt localization bands in high shear strain region (case#6 in Fig. 3-3b).

Figure 3-14 The concentration of Ce normalized by the source in the matrix solid and the REE pattern in clinopyroxenes sampled along two lines in the lithosphere for five cases of channel distribution (a, b, c, d, e). The same as Fig. 3-13 except that the angle of the lithosphere wedge is smaller (13° compared to 25° in Fig. 3-13) and the maximum degree of melting is larger (25% compared to 14% in Fig. 3-13). Thus, cpx will be consumed at 17 km depth. The interval of cpx-exhaustion in the vertical bar beneath the axis is filled with black dots pattern.

Figure 3-15 Comparisons of REE patterns predicted by the current model with N-MORB (Hofmann, 1988; Sun and McDonough, 1989; Gale et al., 2013; White and Klein, 2014) and the bulk oceanic crust (White and Klein, 2014). The DMM of Salters and Stracke (2004) and the range of DMM of Workman and Hart (2005) are plotted as black dashed lines and black solid lines for reference. The black dotted lines are for the E-DMM and D-DMM from Workman and Hart (2005). Compositions of pooled melt in panel (a) and panel (b) are calculated using a maximum degree of melting of 25% (the same as Fig. 3-13) and 14% (the same as Fig. 3-14) respectively. The mean value of *F* (Forsyth, 1993) in the pooled melt is 12.2% in the case with F_max = 25% whereas the mean value of *F* is 7.1% in the case with F_max = 14%. The color code for the predicted REE pattern in the pooled melt is for different cases of channel distribution, the same color code for REE patterns in Fig. 3-13 and Fig. 3-14. The dashed orange line in panel (b) is the predicted REE patterns of the pooled melt if the width of the cap of decompaction channels doubles to 200 km.

Figure 3-16 Panel (a) and (d) are ($^{230}Th/^{234}U$) and ($^{226}Ra/^{230}Th$), respectively, in the matrix melt. Panel (b) and (e) are ($^{230}Th/^{234}U$) and ($^{226}Ra/^{230}Th$), respectively, in the matrix melt after this fraction of melt is extracted to the channel transports to the axis. Only the region of melt focusing is shown. Panel (c) and (f) are ($^{230}Th/^{234}U$) and ($^{226}Ra/^{230}Th$), respectively, in the middle line of melting region. The solid line is the activity ratio in the matrix melt while the dashed line is the activity ratio after melt extraction and transport. I use a modal-melting model with constant partition coefficients for U, Th, and Ra (2.3×10^{-3}, 1.9×10^{-3}, and 1×10^{-4} respectively). The partition coefficients of U and Th in cpx are from Wood et al. (1999). I assume 10% cpx is present on average during melting. The bulk partition coefficient of Ra is set to be that of Ba (Jull et al., 2002). The distribution of channels is the same as the deep channel case in Fig. 3-9. The grain size in the matrix and the channel are 1 mm and 3 mm, respectively.

Figure 3-17 The effect of the distribution of channels on the bulk porosity (a, c, e) and the melt transport time to the axis (b, d, f) for three different cases. The case in the first row has RII channels in 0-30 km depth and melt localization bands. The grain size in the matrix and the channel are 1 mm and 3 mm, respectively. Th permeability model is from Wark and Watson (1998). The case in the second row has RII channels in 0-60 km depth and melt localization bands. The grain size and the permeability model are the same as the case in the panel (a). The case in the third row has RII channels in 0-60 km depth and melt localization bands. The grain size is the same as the case in the panel (a) and (c) but the permeability model is from Miller et al. (2014).

Figure 3-18 (a) ($^{230}Th/^{234}U$) and ($^{226}Ra/^{230}Th$) in extracted melts and pooled melt for different channel distribution, permeability model, and grain sizes in the matrix and the channel, (b) Porosity profile in the middle line beneath the axis. The arrow in panel a is the effect of disequilibrium using a disequilibrium parameter of $\varepsilon_{La} = 0.01$, which is a reasonable value according to Chapter 1. The highest ($^{226}Ra/^{230}Th$) can be extended to 5. The gray box in panel b is the range of porosity at ~60km beneath the ridge axis estimated by Baba et al., (2006), Yang et al., (2007), and Key et al., (2013). The dashed gray line and the solid dark gray line are two cases with channels in the shallowest 30 km. Partition coefficients used in these simulations are summarized in Table 3-2. "WW" and "Miller" represent the permeability models of Wark and Watson (1998) and Miller et al. (2014), respectively. Numbers inside the parentheses are the grain size of the matrix and the channel in millimeter. One case labeled with "small ψ" has a maximum channel proportion of 5% while others has a maximum channel proportion of 10%. The range of global data is from Elkins et al. (2014) and references therein.

Supplementary figure captions

Figure S3-1 The degree of melting as a function of depth for two choices of spreading rate. The degree of melting is calculated using pMELTS (Smith and Asimow, 2005). The final melting depth is chosen according to the spreading rate (Niu and Hékinian, 1997). For fast half-spreading rate (100 mm/yr), melting ceases at 10 km and the maximum degree of melting is 25%. For medium half-spreading rate (50 mm/yr), melting ceases at 20 km and the maximum degree of melting is 14%.

Figure S3-2 The melt distribution, flow fields of the melt and the solid mantle in a reference case with no channels. It is the same as Fig. 3-4 except that the angel of the lithosphere wedge is smaller (13° compared to 25° in Fig. 3-4) and the maximum degree of melting is larger (25% compared to 14% in Fig. 3-4).

Figure S3-3 The melt distribution, flows of the melt and the solid mantle in a case with uniform channel distribution. It is the same as Fig. 3-5 except that the angel of the lithosphere wedge is smaller and the maximum degree of melting is larger.

Figure S3-4 The melt distribution, flows of the melt and the solid mantle in a case with uniform channel distribution. The permeability of channels is anisotropic. It is the same as Fig. 3-6 except that the angel of the lithosphere wedge is smaller and the maximum degree of melting is larger.

Figure S3-5 The melt distribution, flows of the melt and the solid mantle in a case where the proportion of channels is larger and the melt extraction is stronger in the shallowest 30 km. It is the same as Fig. 3-7 except that the angel of the lithosphere wedge is smaller and the maximum degree of melting is larger.

Figure S3-6 The melt distribution, flows of the melt and the solid mantle in a case where additional channels are formed by shear deeper than 30 km. It is the same as Fig. 3-8 except that the angel of the lithosphere wedge is smaller and the maximum degree of melting is larger.

Figure S3-7 The melt distribution, flows of the melt and the solid mantle in a case where replacive channels form at 60 km depth. It is the same as Fig. 3-9 except that the angel of the lithosphere wedge is smaller and the maximum degree of melting is larger.

Figure S3-8 The effect of mantle viscosity and permeability model on the crustal thickness. The proportion of channels is uniform in these runs. The grain size, viscosities, and permeability model are the same as the case shown in Fig. 3-4. "WW" and "Miller" represent the permeability model of Wark and Watson (1998) and Miller et al. (2014), respectively.

Figure S3-9 The matrix porosity (a), velocities (b), dimensionless melting rate (c), and (^{230}Th/^{238}U) in the matrix melt (d) as a function of depth. The red lines in panel (a), (b) and (c) are sampled along the vertical line beneath the ridge axis in the 2D model shown in Fig. 3-16. Melt extraction starts at 60 km depth. Melting stops at 20 km depth. The dashed lines in panel (a), (b), and (c) are from a one dimension melting column with constant melting rate. Results of (^{230}Th/^{238}U) in matrix melt are calculated using two different sets of k_U and k_{Th}. The red lines in panel d are calculated using the variable melting rate while the black lines are calculated using

constant melting rate. The blue lines are calculated using the approximation of Eq. (A3-31).

Figure S3-10 ($^{226}Ra/^{230}Th$) in the matrix melt as a function of depth. The bulk partition coefficient of Ra is 1×10^{-4}. The bulk partition coefficient for Th is 1.9×10^{-3}. The red line is calculated with variable melting rate on the same middle line in the 2D model shown in Fig. 3-15. The blue line is calculated using the approximate solution of Eq. (A3-34). The black line is calculated using the same constant melting rate in Fig. S3-2c.

Figures

Figure 3-1 The double-porosity model and observational constraints

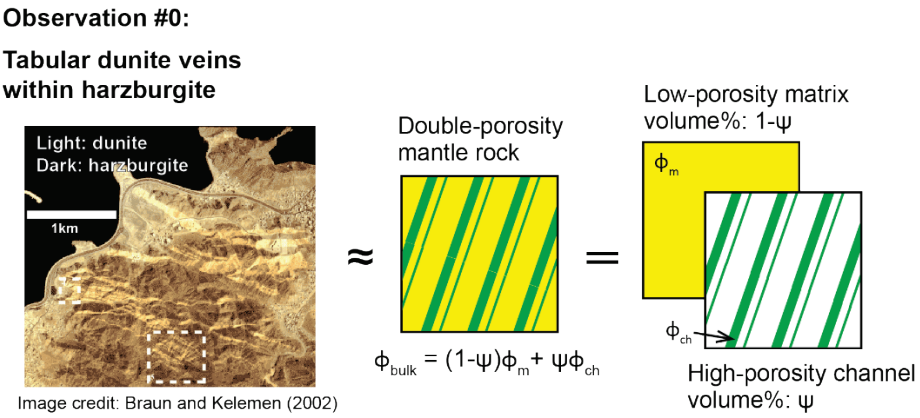

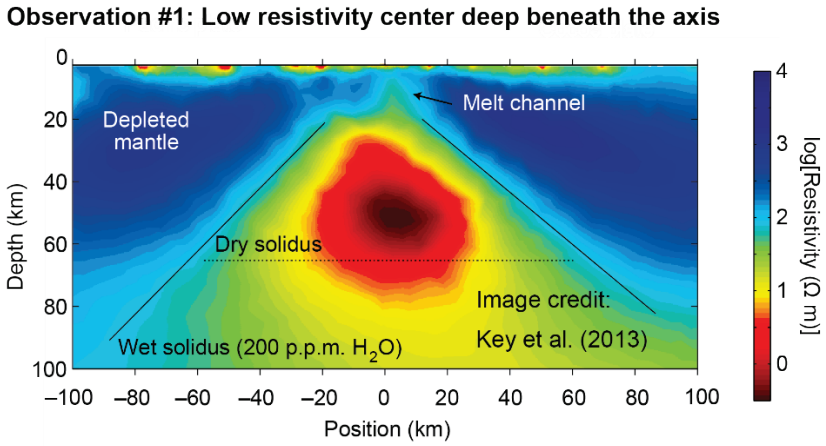

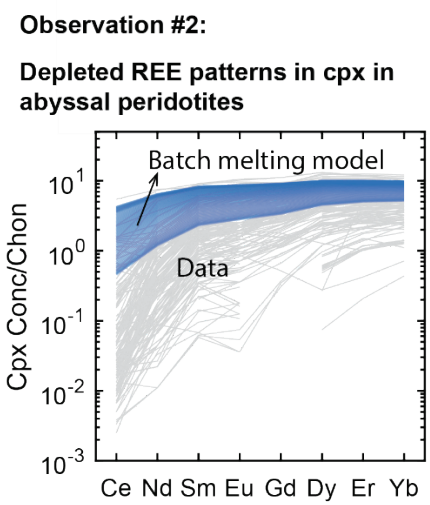

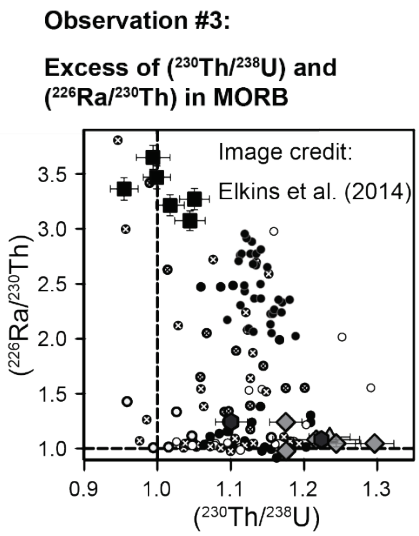

Figure 3-2 One-dimensional porosity profile (a) and velocity profile (b) in the matrix and channel

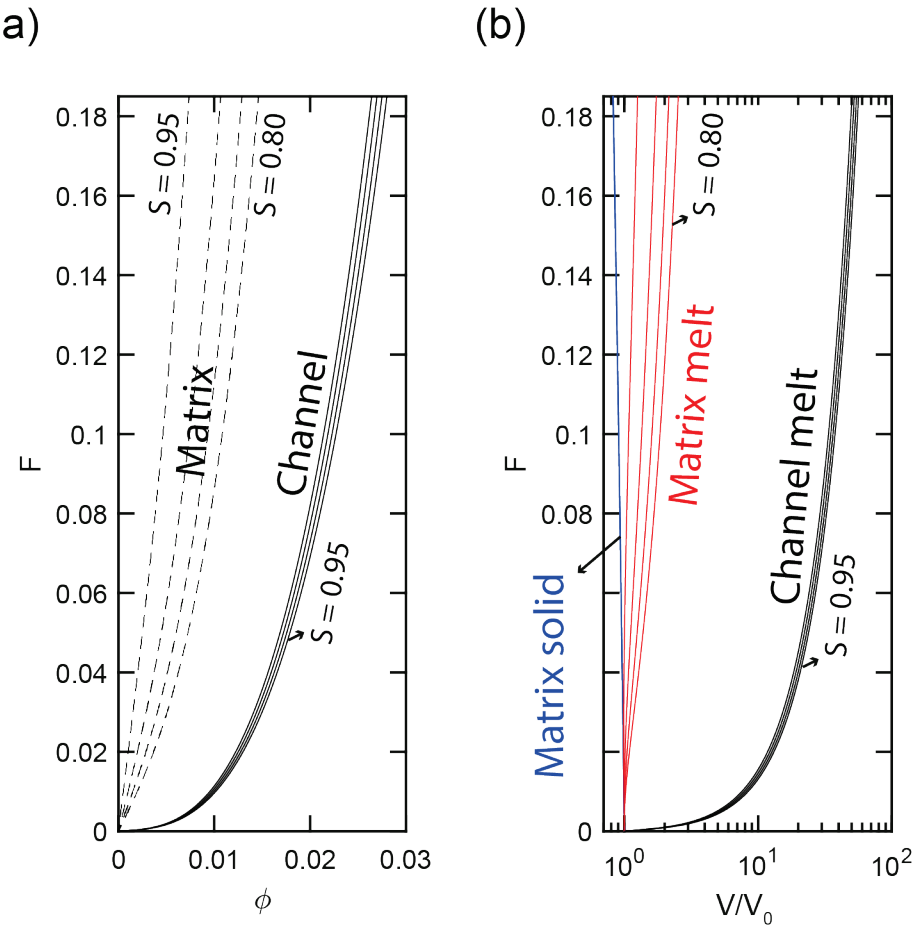

Figure 3-3 Model setup of the model (a) and cases of different channel distribution (b)

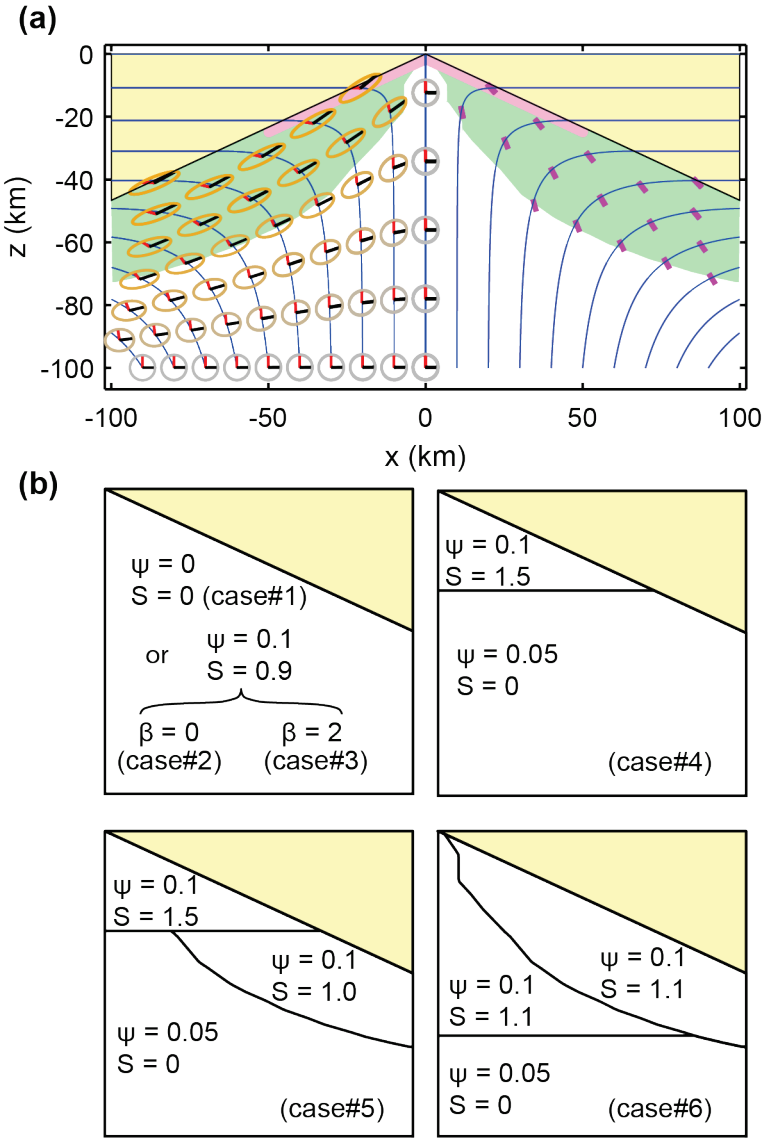

Figure 3-4 The melt distribution, flow fields of the melt and the solid mantle in a reference case with no channels (F_max = 14%)

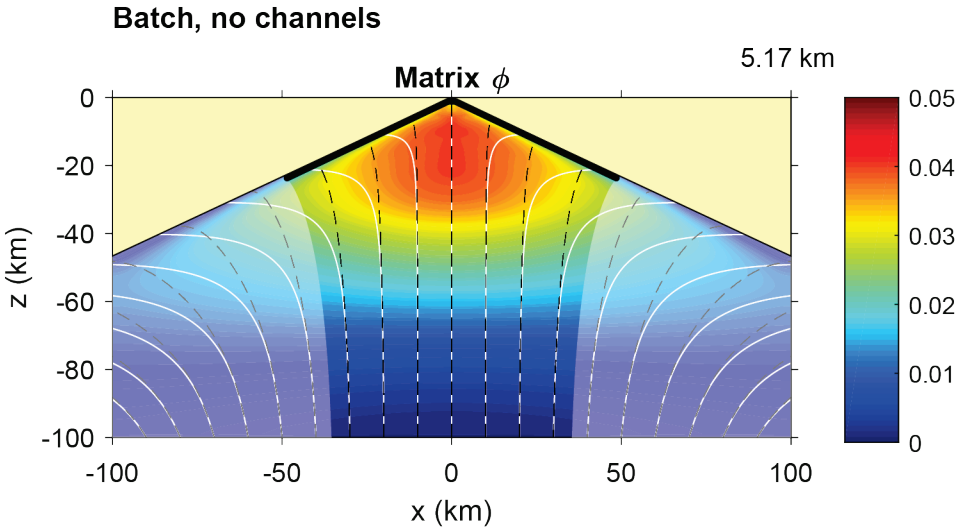

Figure 3-5 The melt distribution, flow fields of the melt and the solid mantle in a case with uniform channel distribution (F_max = 14%)

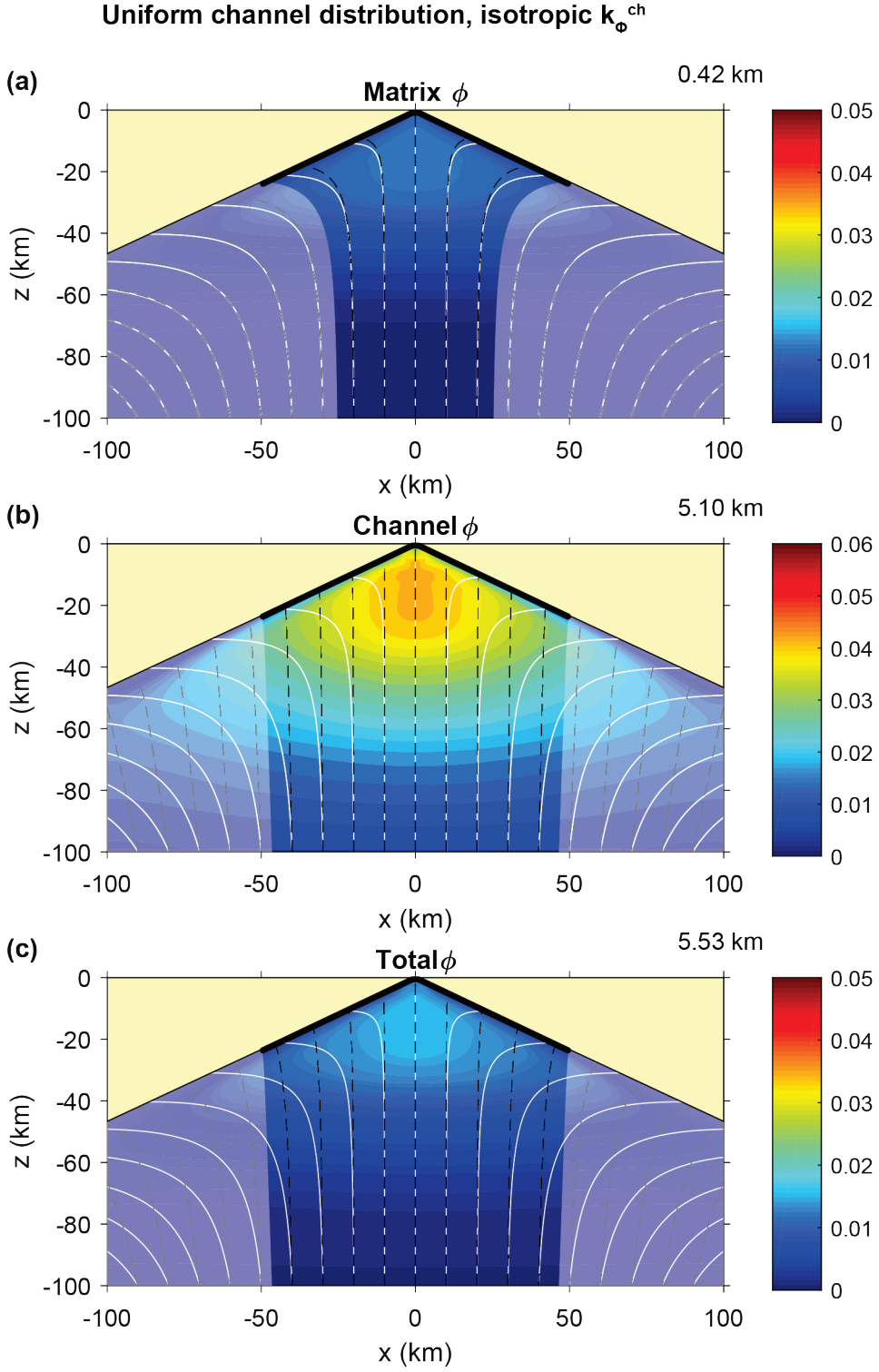

Figure 3-6 The melt distribution, flow fields of the melt and the solid mantle in a case with uniform channel distribution (F_max = 14%)

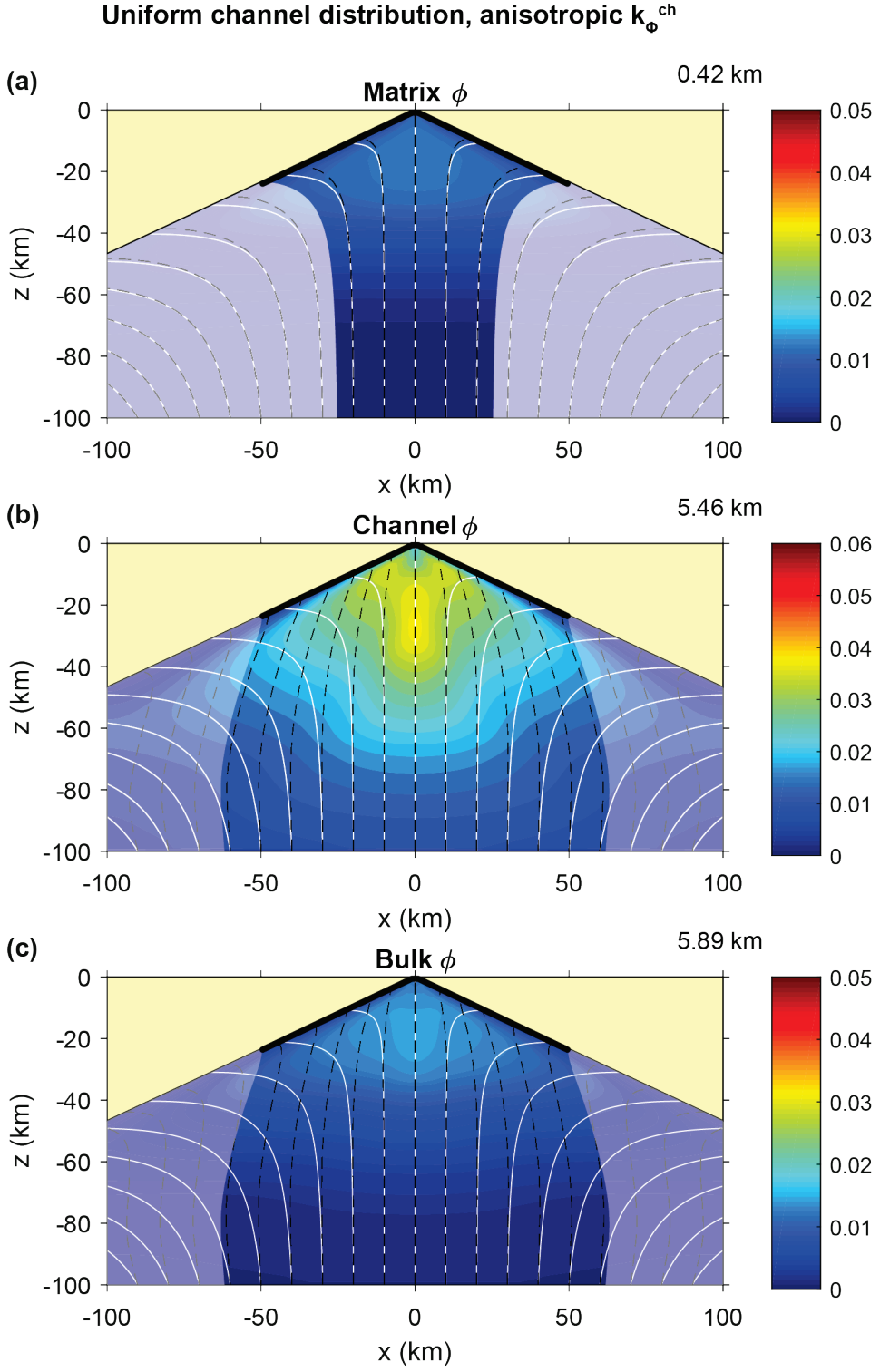

Figure 3-7 The melt distribution, flow fields of the melt and the solid mantle in a case where the proportion of channels is larger and the melt extraction is stronger in the shallowest 30 km (F_max = 14%)

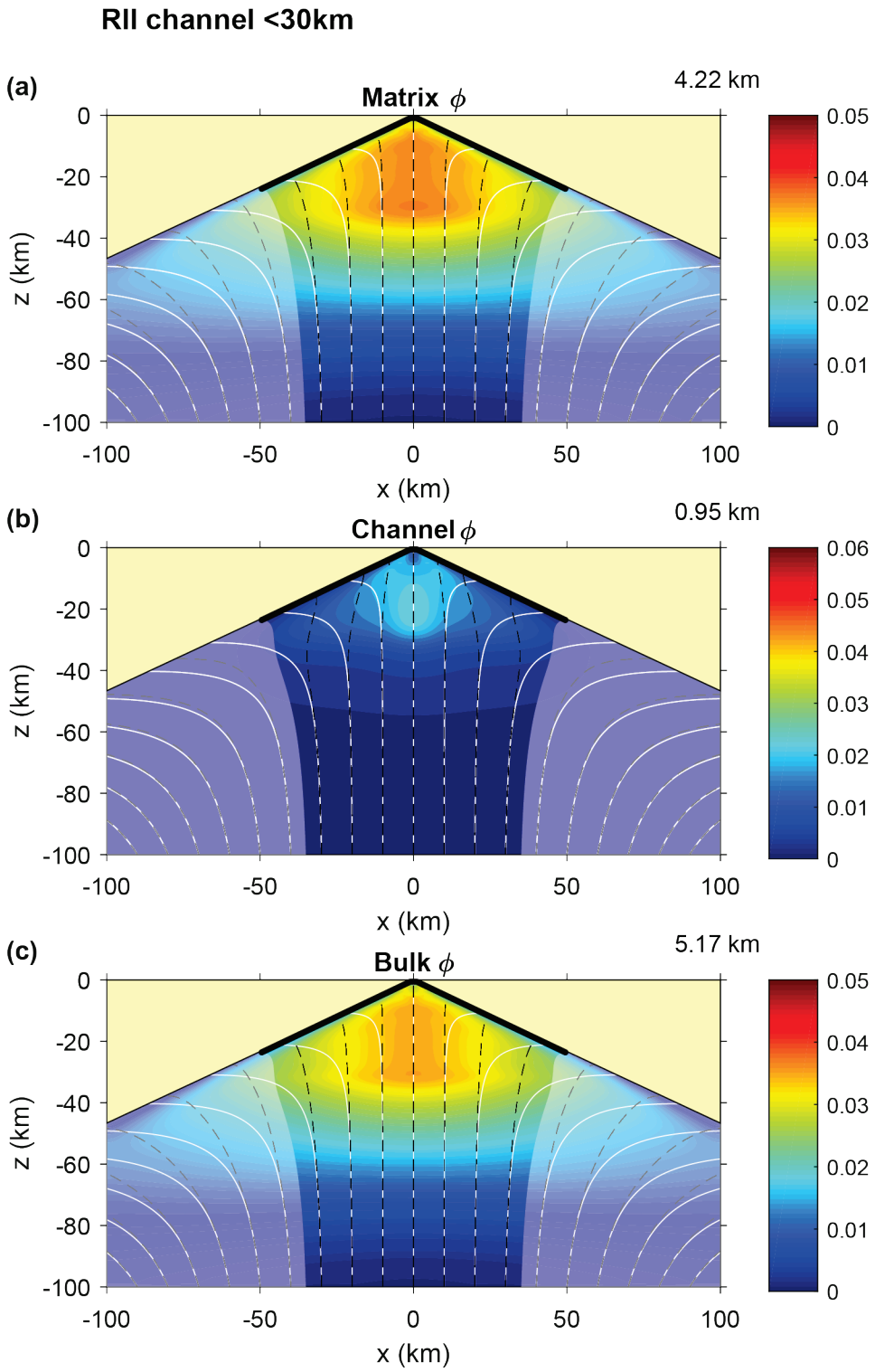

Figure 3-8 The melt distribution, flow fields of the melt and the solid mantle in a case where additional channels are formed by shear deeper than 30 km (F_max = 14%)

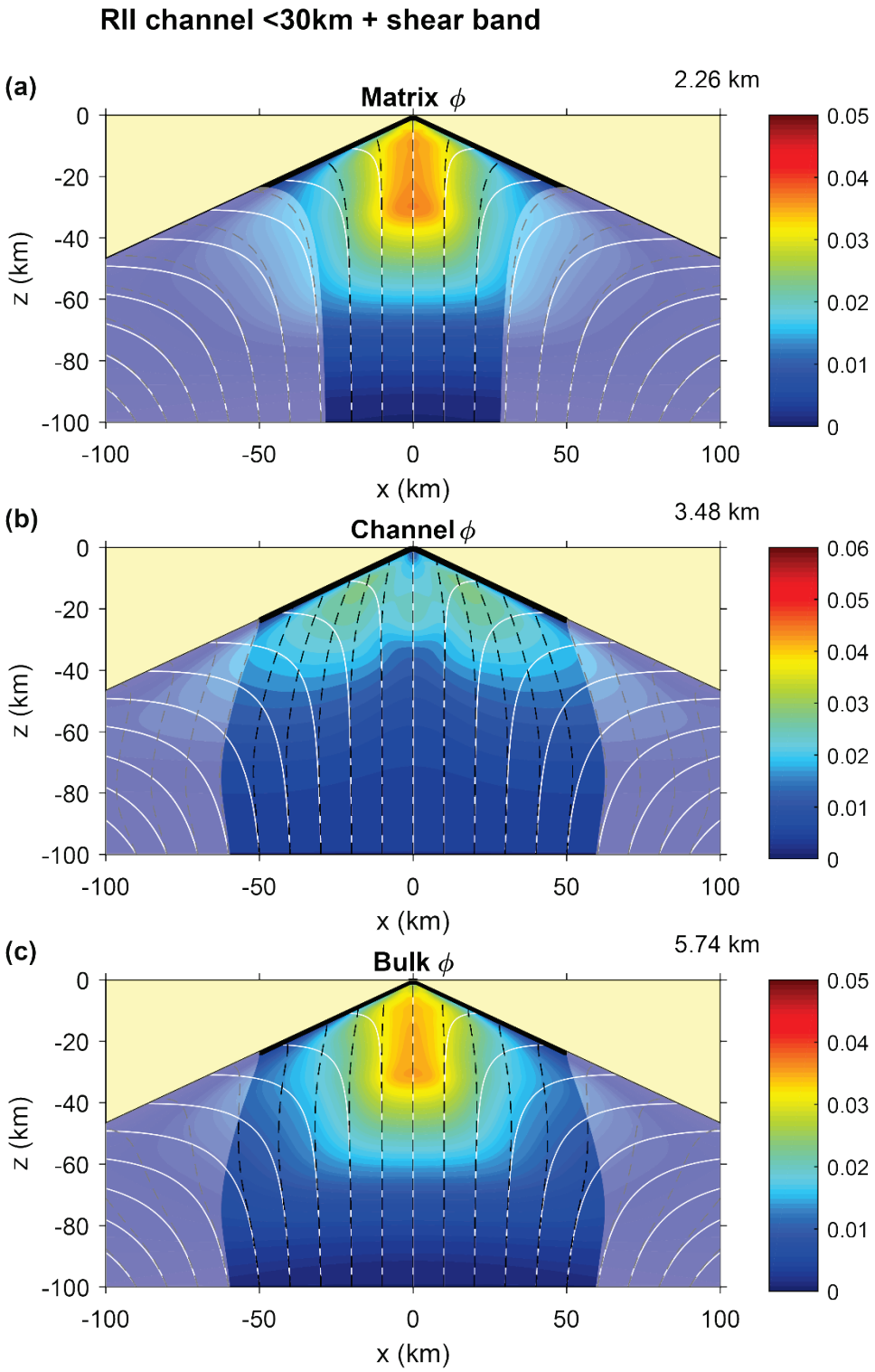

Figure 3-9 The melt distribution, flow fields of the melt and the solid mantle in a case where replacive channels form at 60 km depth (F_max = 14%)

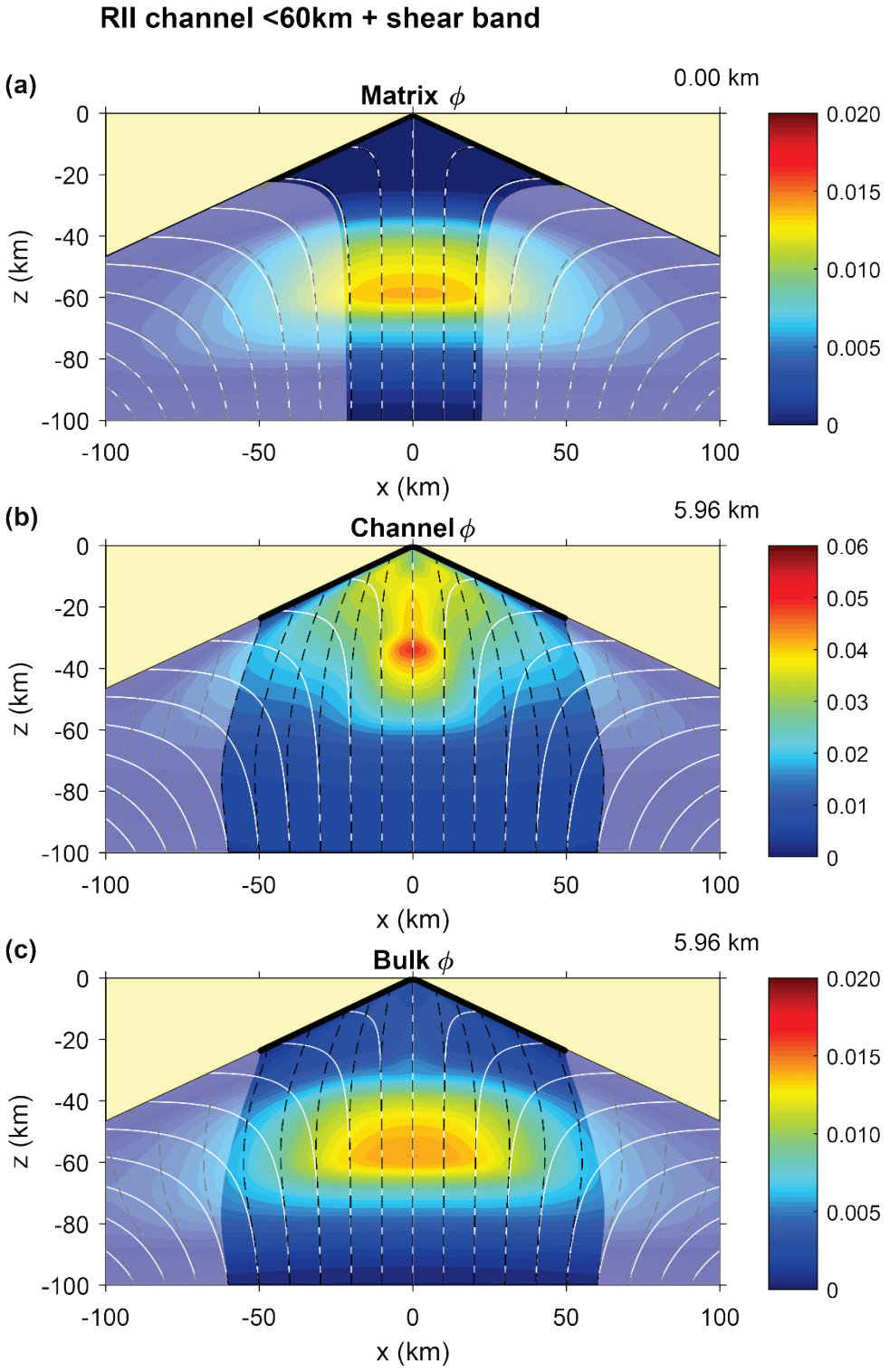

Figure 3-10 The bulk porosity as a function of the channel proportion, ψ and the proportion of channel melt flux

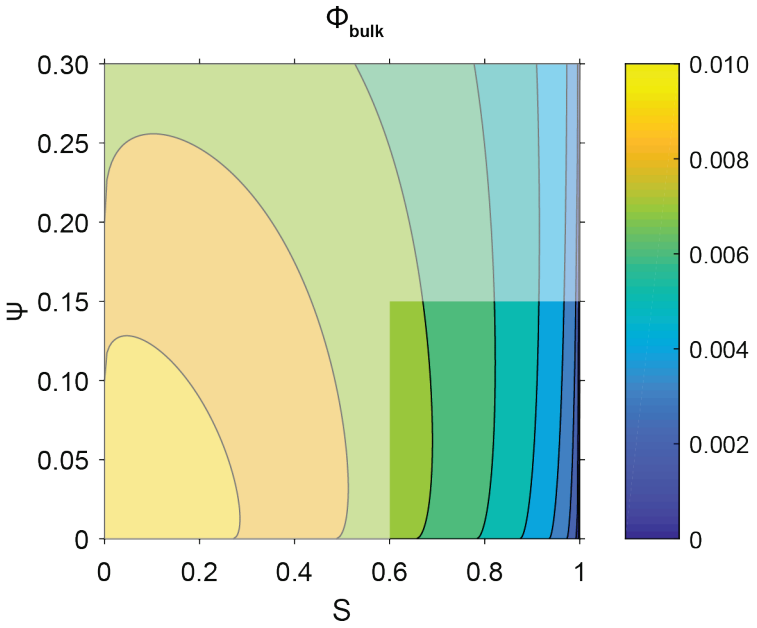

Figure 3-11 The effect of anisotropic permeability on the crustal thickness

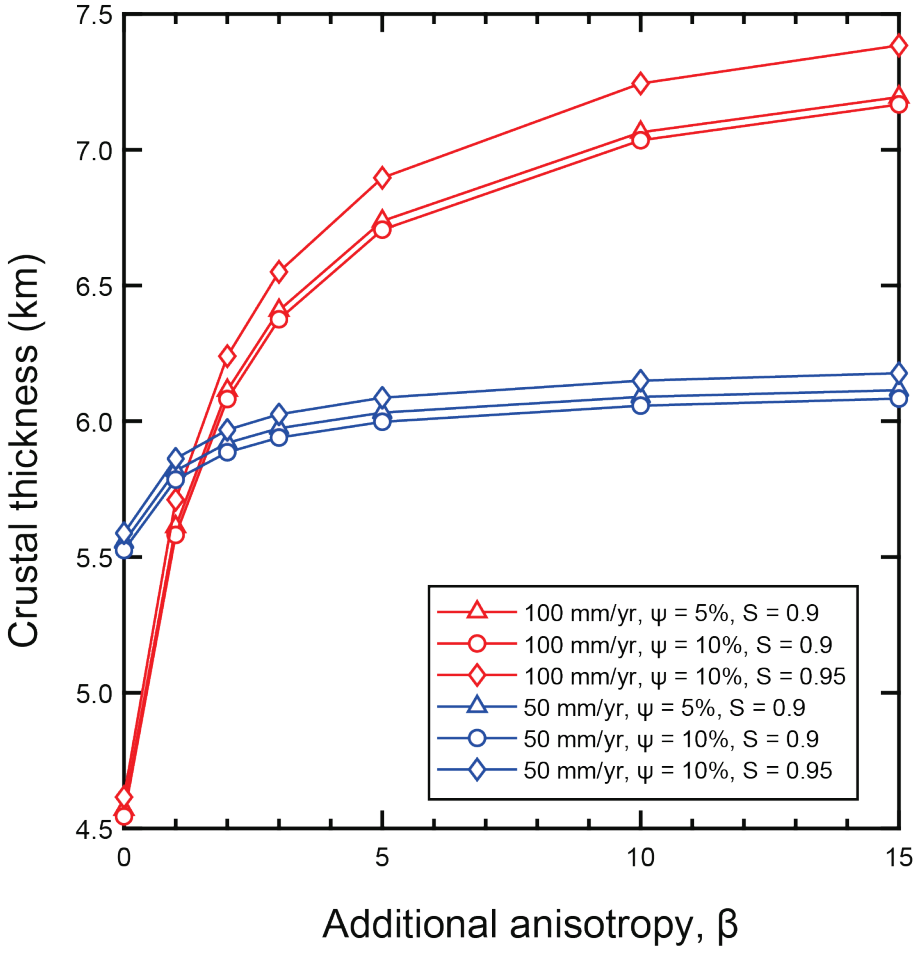

Figure 3-12 The melt focusing zone for the channel in four cases of different half-spreading rate and mantle viscosity

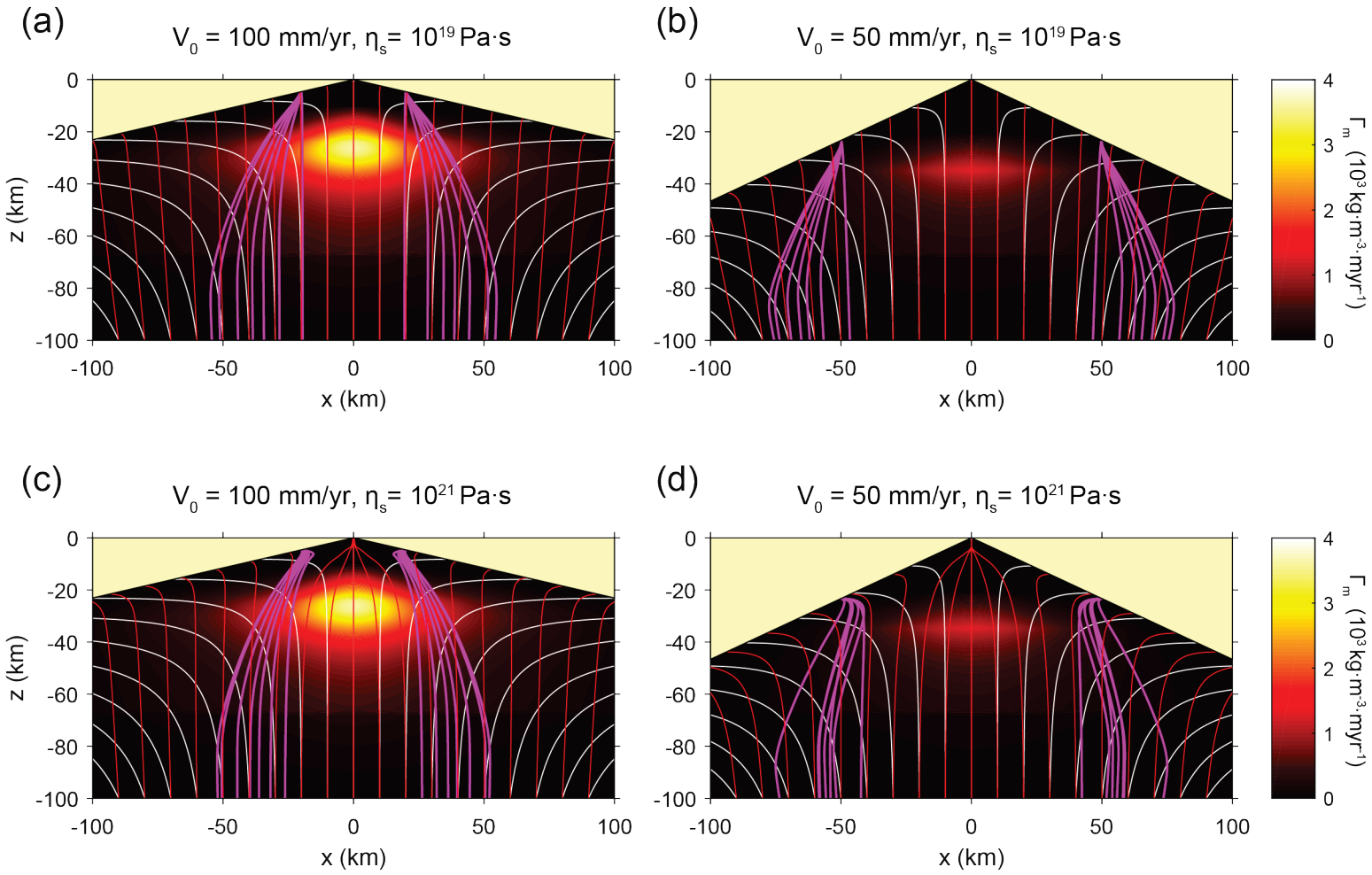

Figure 3-13 The concentration of Ce normalized by the source in the matrix solid and the REE pattern in clinopyroxenes (F_max = 14%)

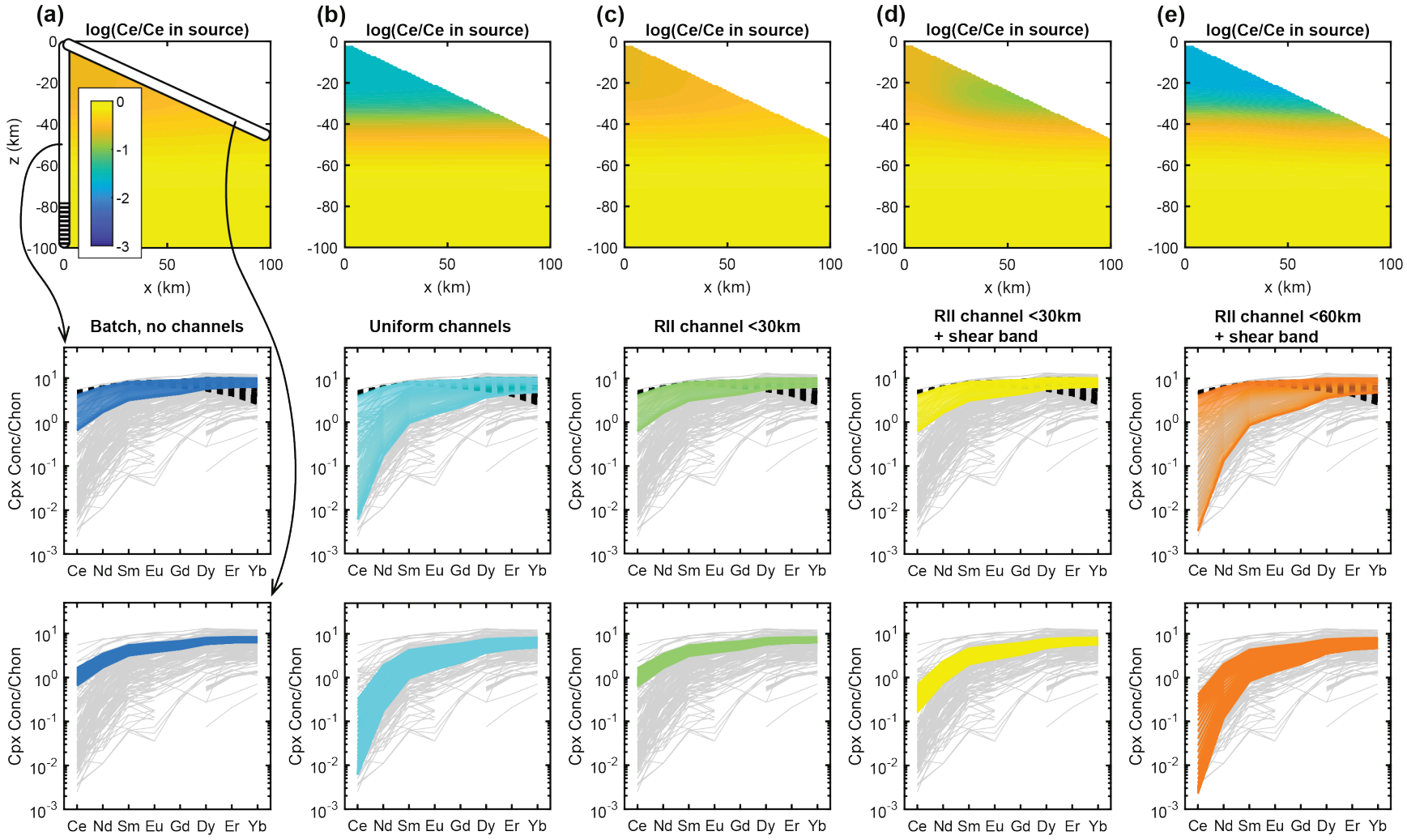

Figure 3-14 The concentration of Ce normalized by the source in the matrix solid and the REE pattern in clinopyroxenes (F_max = 25%)

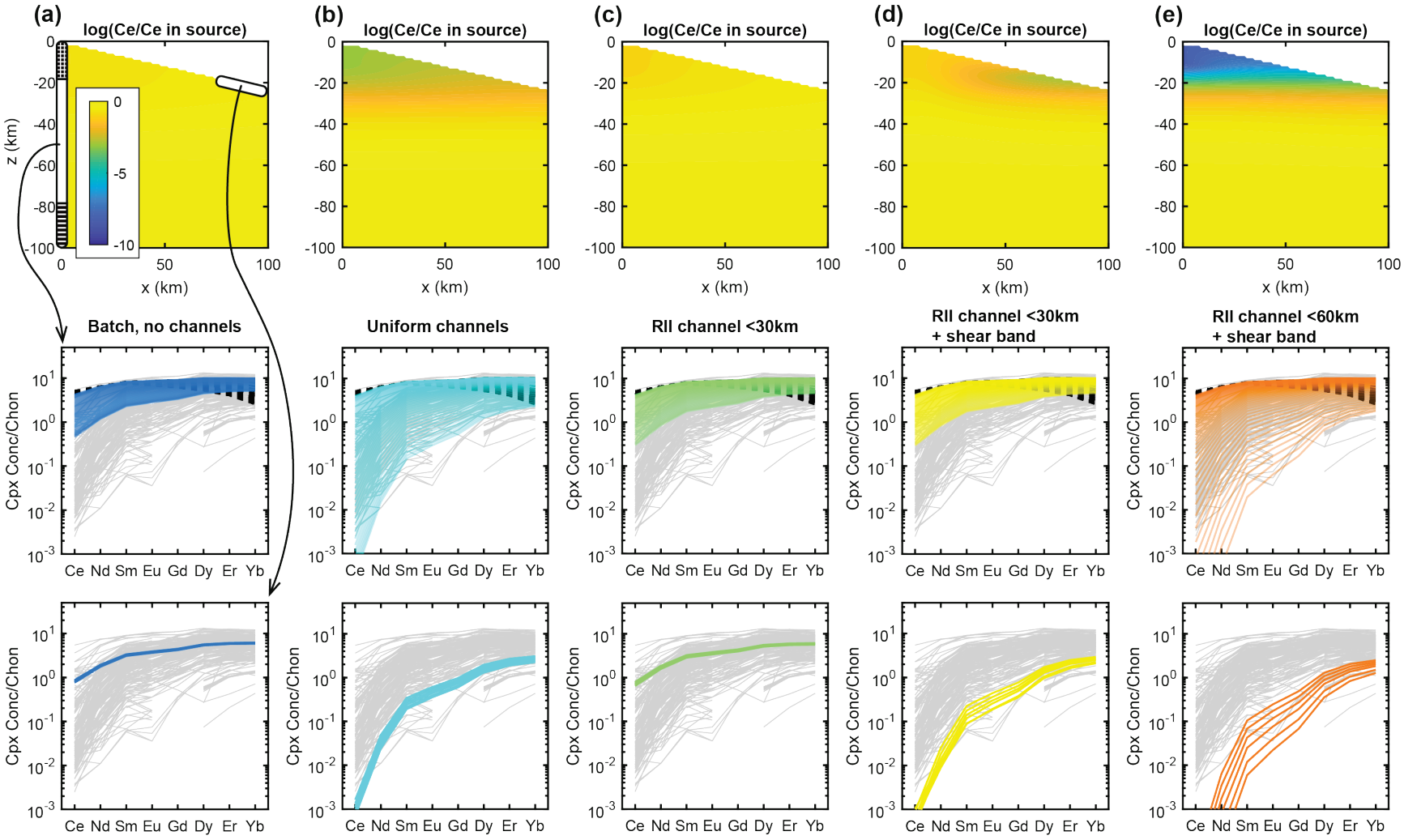

Figure 3-15 Comparisons of REE patterns predicted by the current model with N-MORB and the bulk oceanic crust

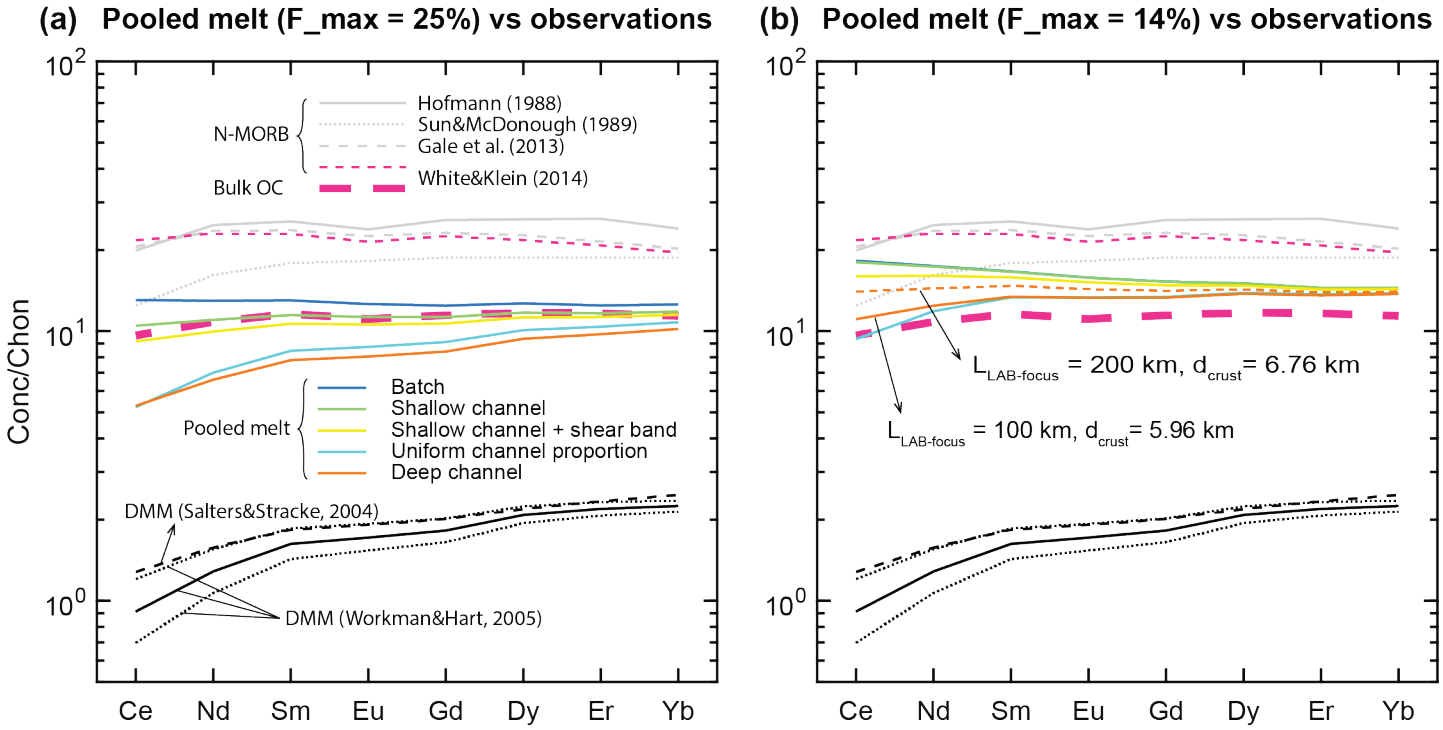

Figure 3-16 ($^{230}Th/^{234}U$) and ($^{226}Ra/^{230}Th$) in the matrix melt (a, d), in the matrix melt after this fraction of melt is extracted to the channel transports to the axis (b, e), and in the middle line of the melting region (c, f)

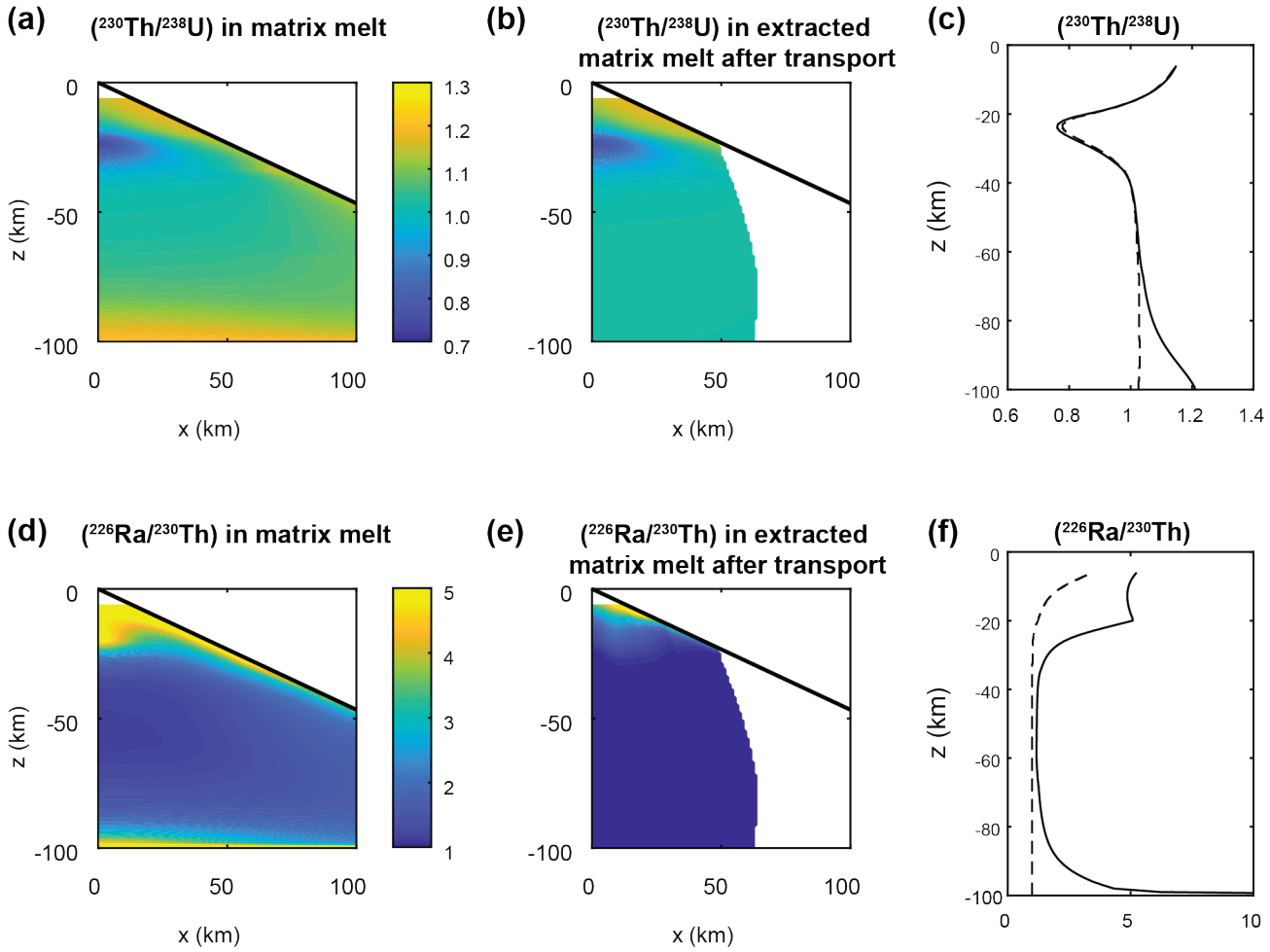

Figure 3-17 The effect of the distribution of channels on the bulk porosity and the melt transport time to the axis

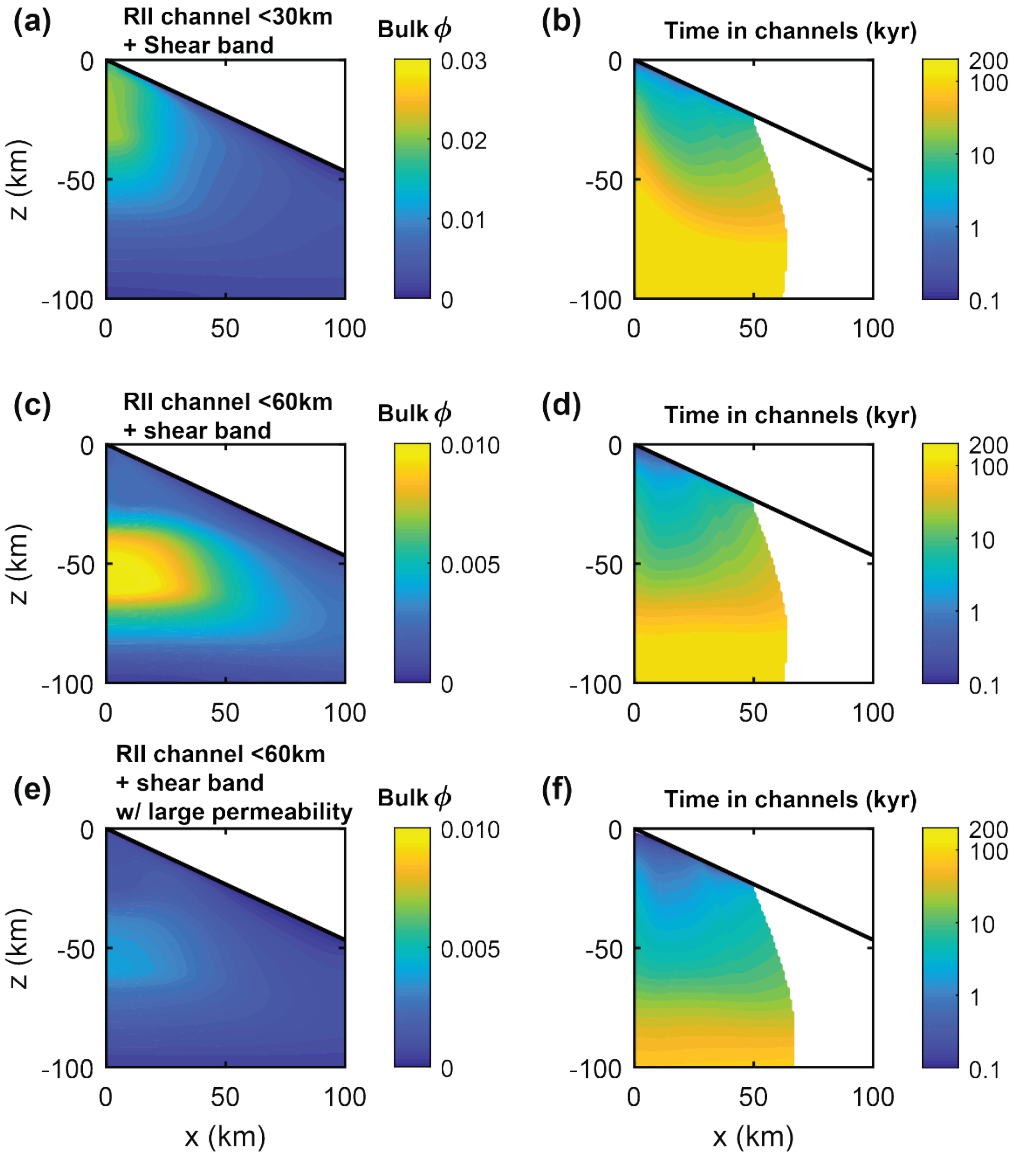

Figure 3-18 ($^{230}Th/^{234}U$) and ($^{226}Ra/^{230}Th$) in extracted melts and pooled melt for different channel distribution, permeability model, and grain size (a) and the porosity profile in the middle line beneath the axis (b)

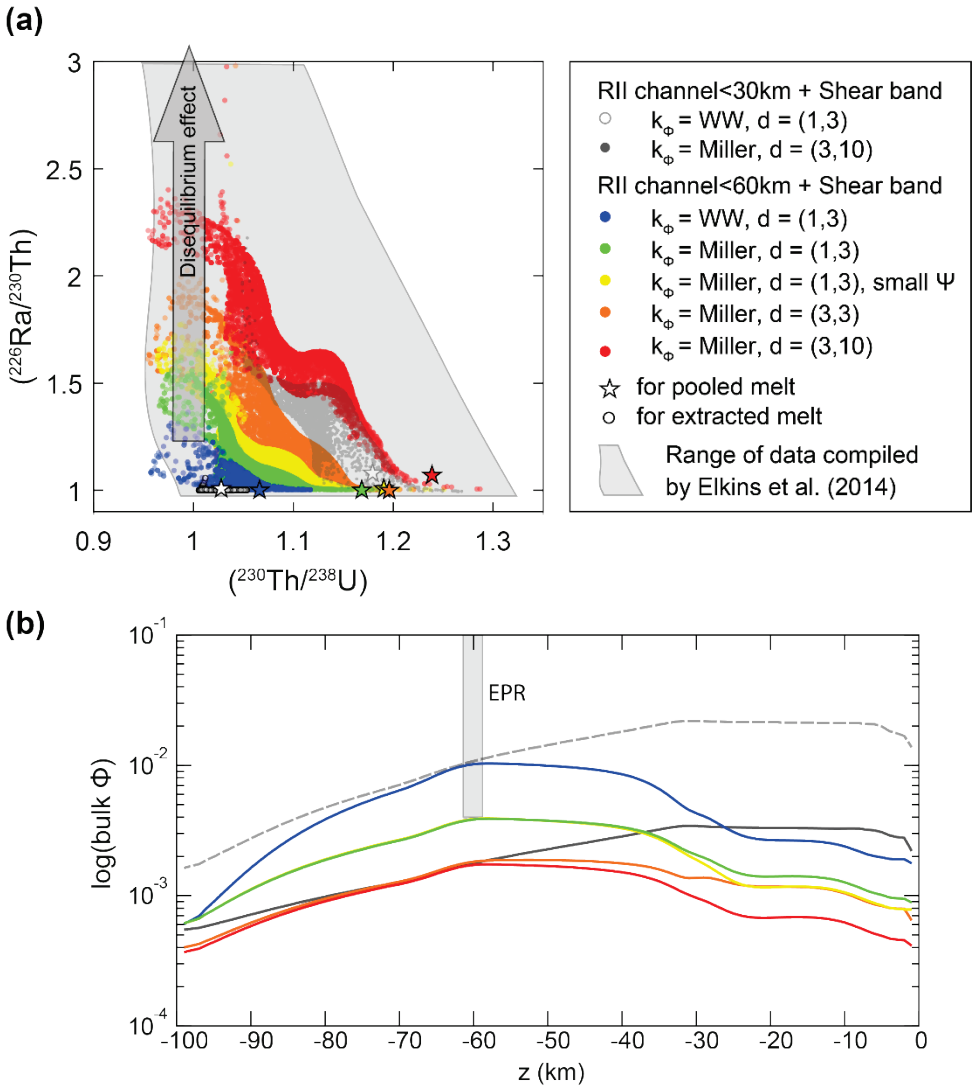

Figure S3-1 The degree of melting as a function of depth for variable spreading rate

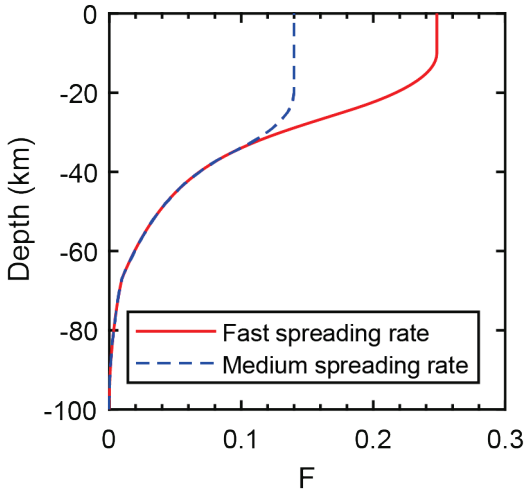

Figure S3-2 The melt distribution, flow fields of the melt and the solid mantle in a reference case with no channels (F_max = 25%)

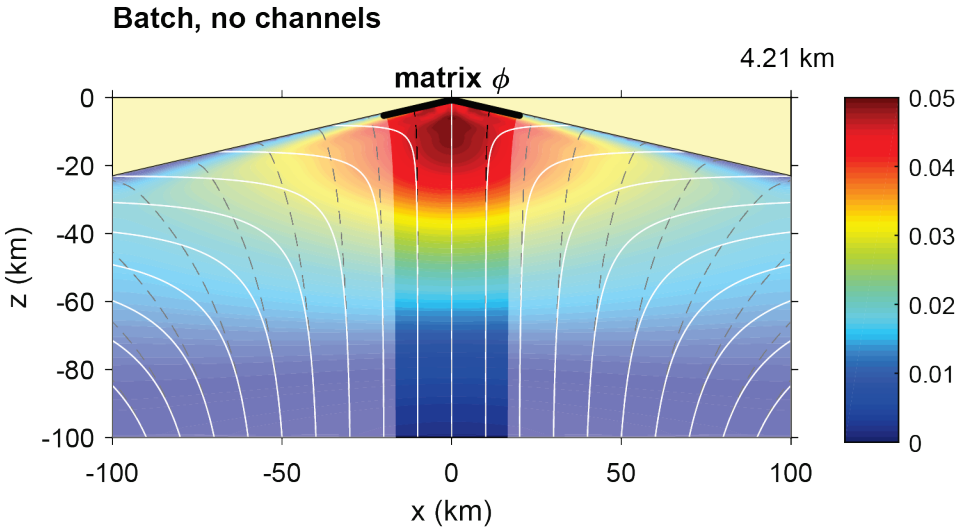

Figure S3-3 The melt distribution, flow fields of the melt and the solid mantle in a case with uniform channel distribution (F_max = 25%)

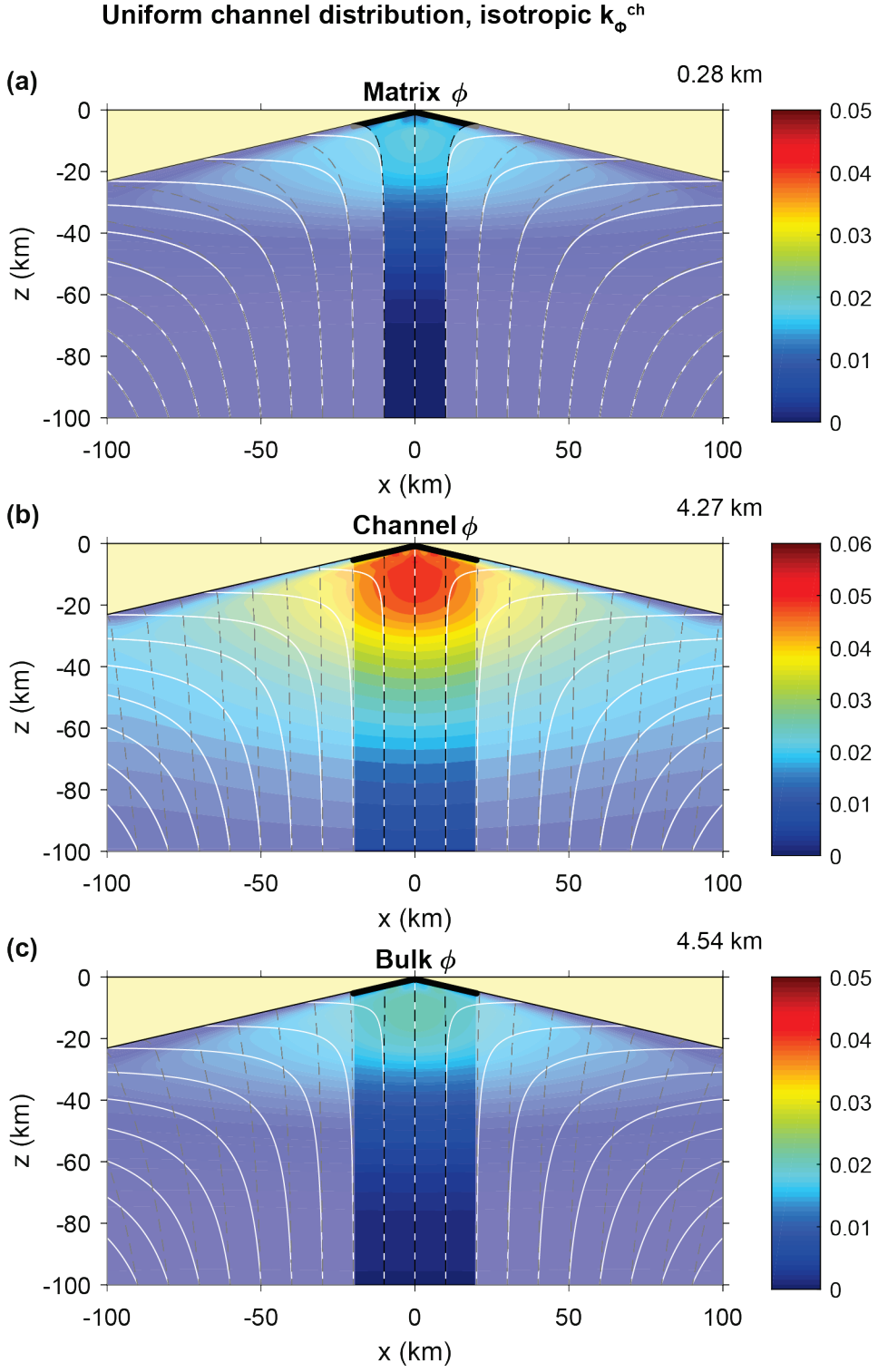

Figure S3-4 The melt distribution, flow fields of the melt and the solid mantle in a case with uniform channel distribution (F_max = 25%)

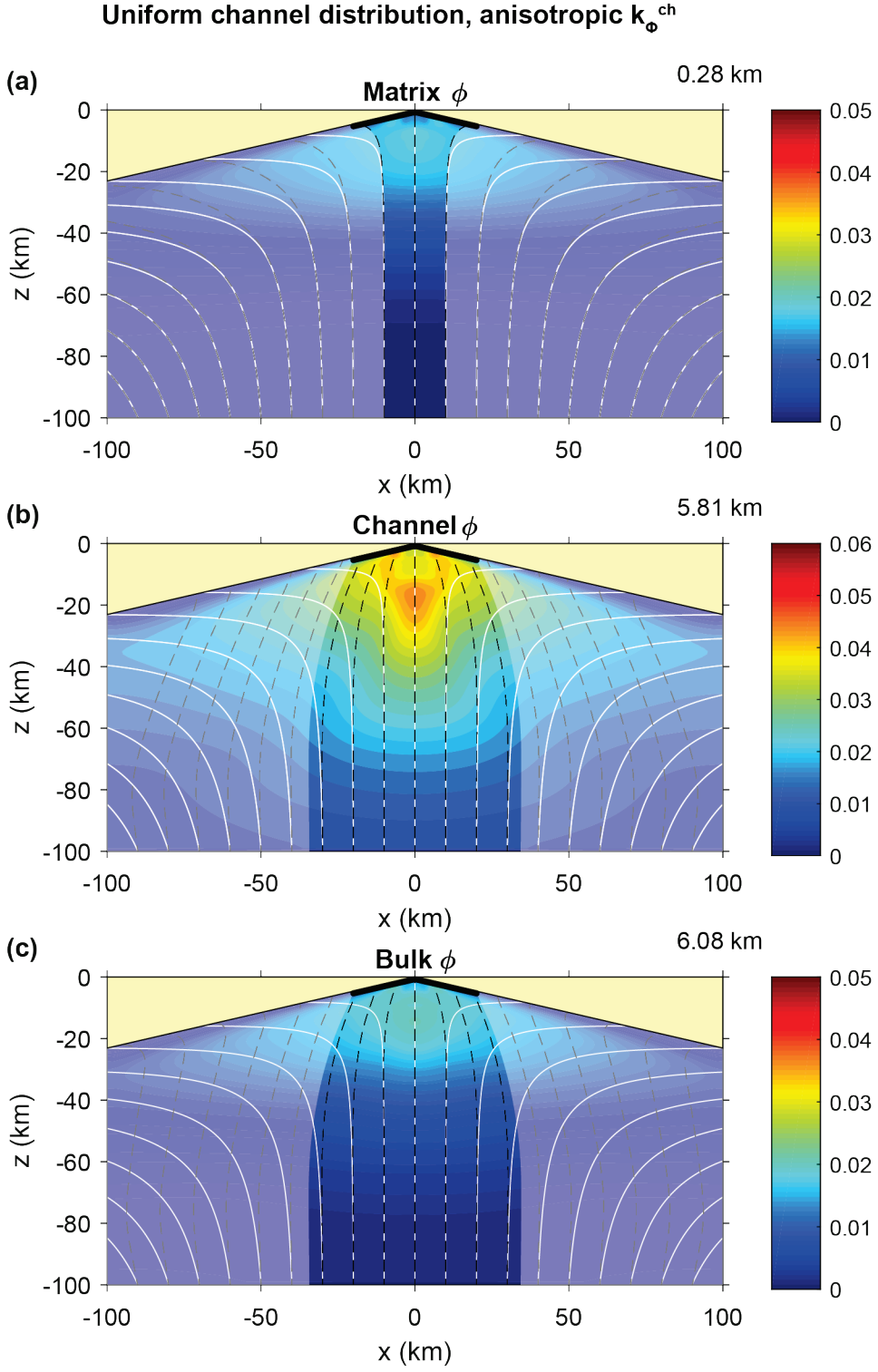

Figure S3-5 The melt distribution, flow fields of the melt and the solid mantle in a case where the proportion of channels is larger and the melt extraction is stronger in the shallowest 30 km (F_max = 25%)

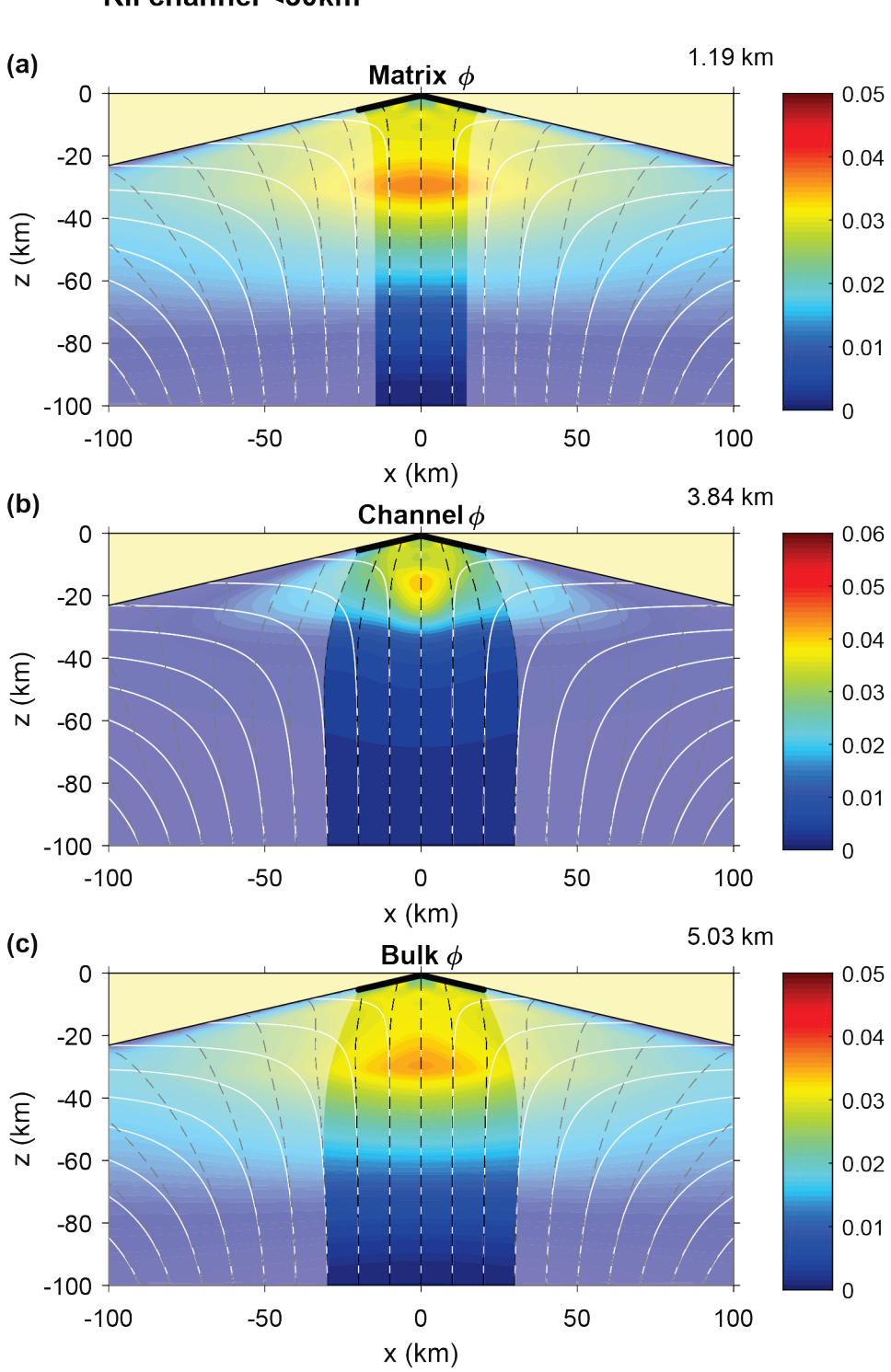

Figure S3-6 The melt distribution, flow fields of the melt and the solid mantle in a case where additional channels are formed by shear deeper than 30 km (F_max = 25%)

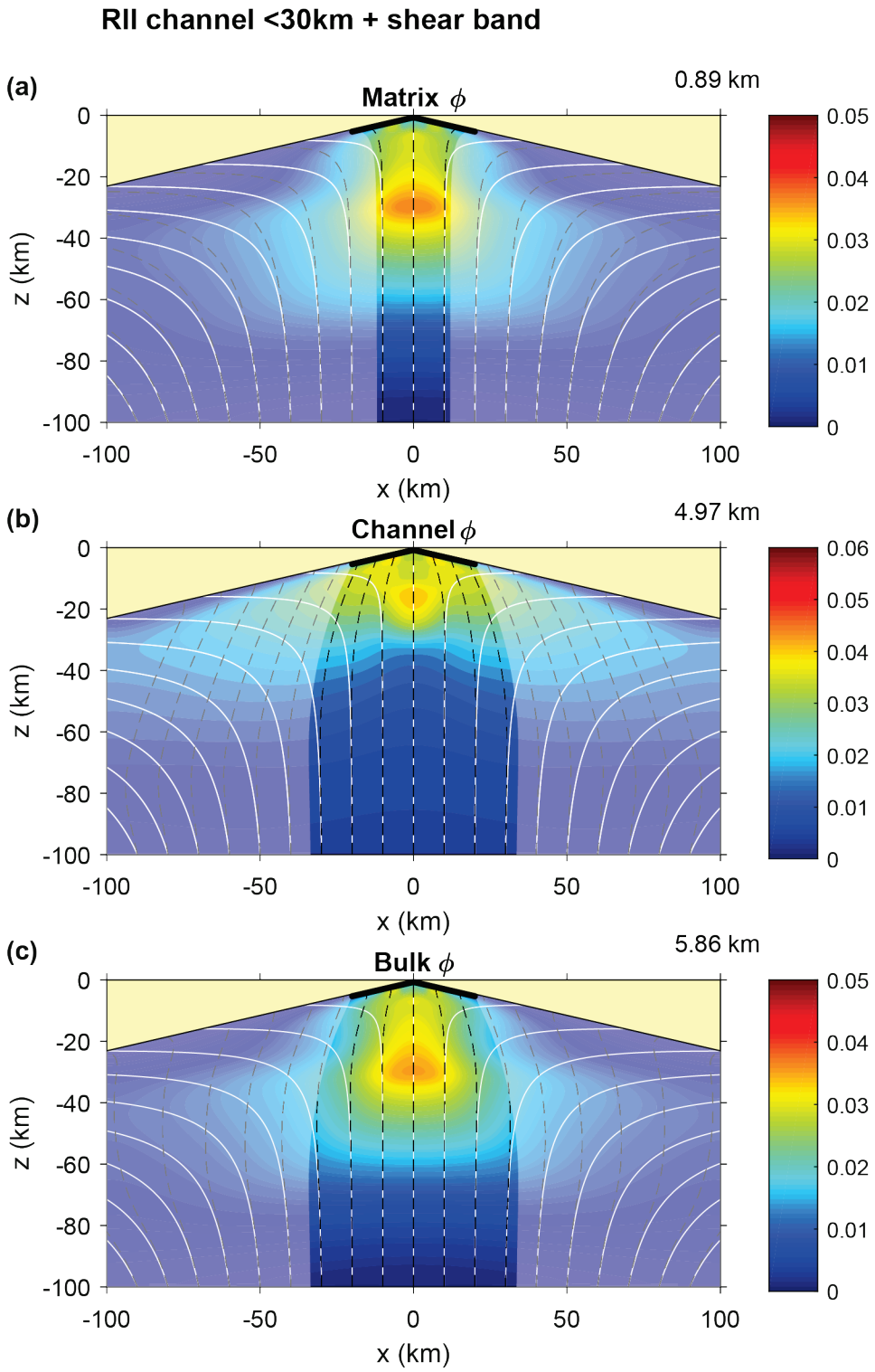

Figure S3-7 The melt distribution, flow fields of the melt and the solid mantle in a case where replacive channels form at 60 km depth (F_max = 25%)

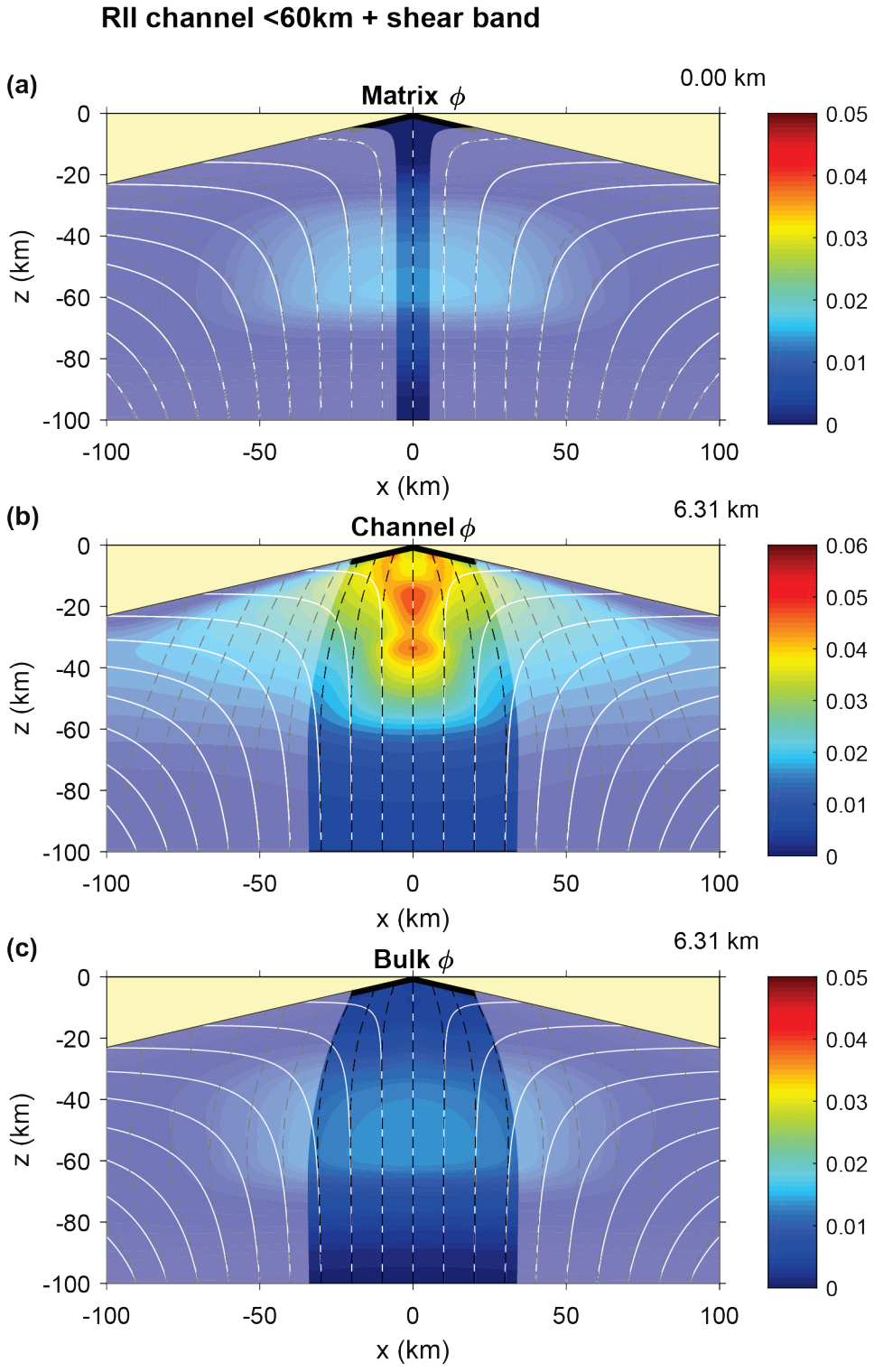

Figure S3-8 The effect of mantle viscosity and permeability model on the crustal thickness. The proportion of channels is uniform in these runs

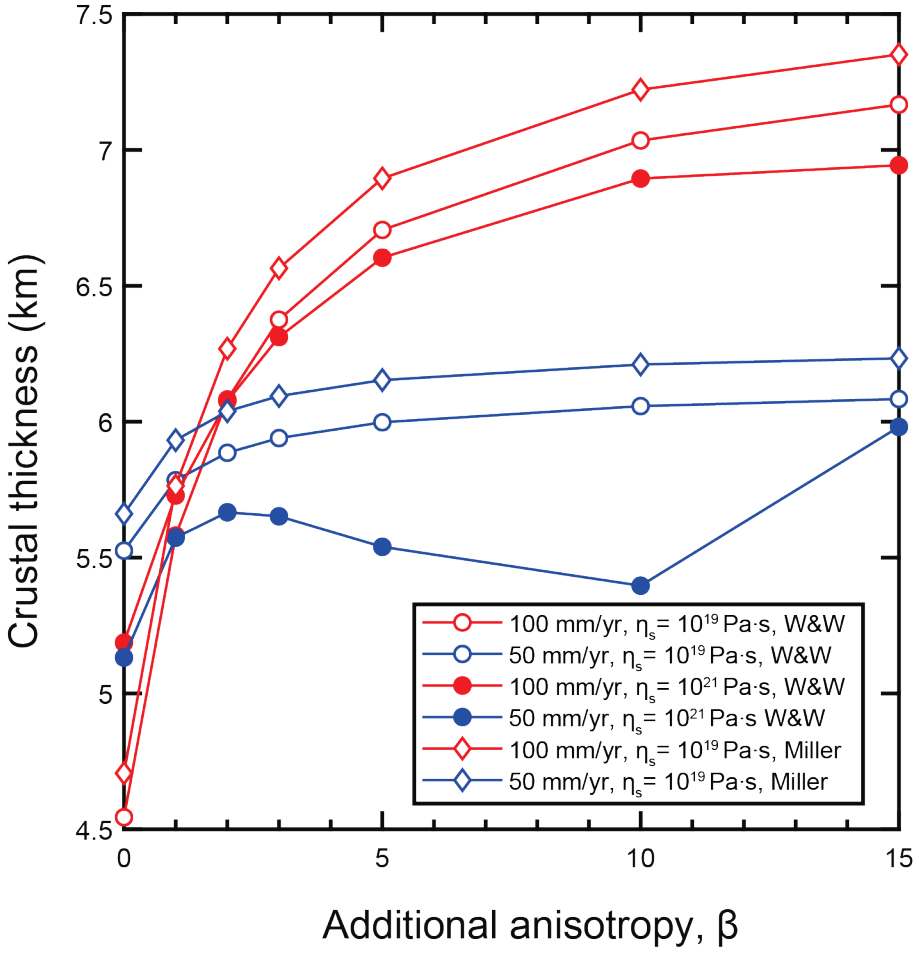

Figure S3-9 The matrix porosity (a), velocities (b), dimensionless melting rate (c), and (^{230}Th/^{238}U) in the matrix melt (d) as a function of depth

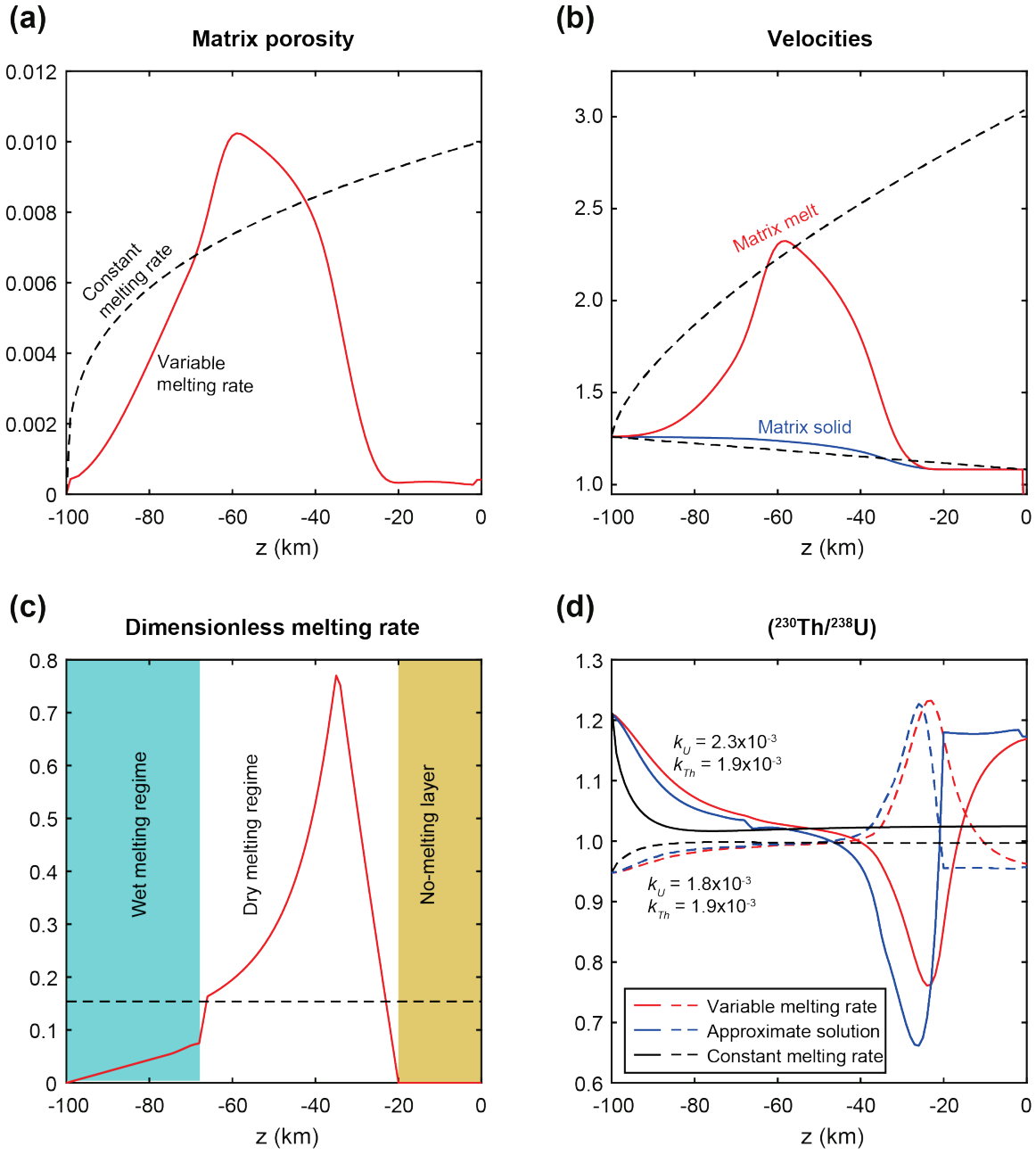

Figure S3-10 ($^{226}Ra/^{230}Th$) in the matrix melt as a function of depth

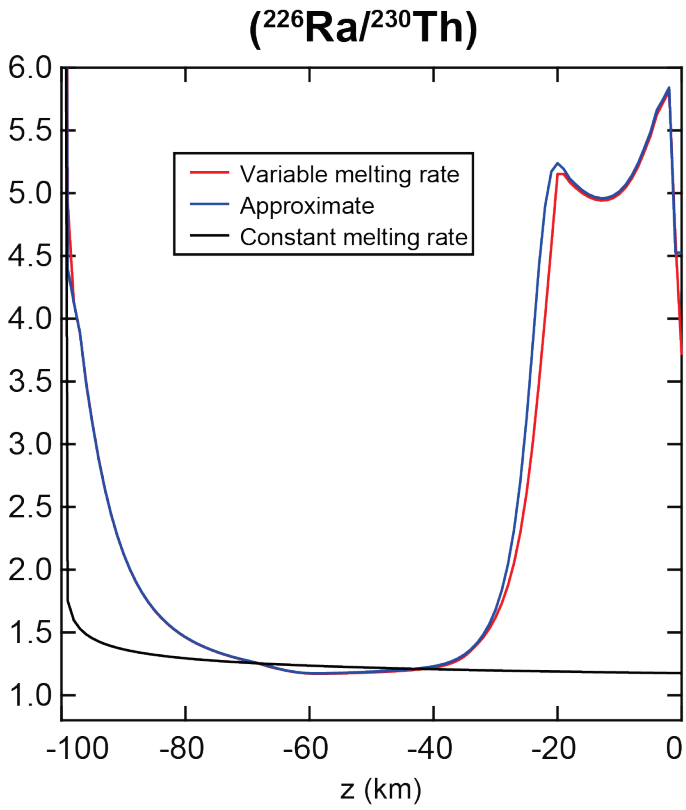

Tables

Table 3-1 List of key symbols

Variable	Meaning	Value used
a_U, a_{Th}, a_{Ra}	Decay factor in the solution of matrix melt	
α	Dip of the lithosphere-asthenosphere boundary	13° or 25°
β	An amplification factor of the additional anisotropic permeability in a fully developed melt-band fabric	0 - 15
$C_s^{m,i}$	Concentration of the chemical species, i, in the residue	
$C_f^{m,i}, C_f^{ch,i}$	Concentration of the chemical species, i, in the matrix melt and the channel melt	
C^{MORB}	Concentration of pooled melt	
C_ϕ	A constant in the expression of permeability[1,2]	200 or 58
d_{crust}	Crustal thickness	
$d_{crust}^m, d_{crust}^{ch}$	Contribution of the matrix melt and channel to d_{crust}	
d_m, d_{ch}	Grain size of the matrix or channel	0.4 – 10 mm
F	Degree of melting experienced by the bulk solid	<0.25
ϕ_m, ϕ_{ch}	Porosity in the matrix or the channel	
$\mathbf{g}$	Gravity	10 m/s^2 downward
γ	Shear strain	
Γ_m	Melting rate of the matrix	
η_f	Shear viscosity of the melt[3]	1 Pa·s
η_s	Shear viscosity of the mantle[4]	10^{19} or 10^{21} Pa·s
k_ϕ^{iso}	Isotropic permeability	
k_ϕ^{add}	Additional anisotropic permeability on the easy-flow direction	
$\mathbf{k}_\mathbf{f}^{\mathbf{ch}}$	Permeability tensor for the channel	
k^i	Bulk partition coefficient for the chemical species, i	
k_{ch}	Bulk partition coefficient in the channel	0
L_0	Length scale used for nondimensionalization	100 km
λ_i	Decay constant for the chemical species, i	
$\mathbf{M}^\alpha$	Corner-flow solution[5] with a wedge angle α	
$\mathbf{M}_s$	Flux of mantle solid	
$\widetilde{\mathbf{M}}$	compressible component of the flux of mantle solid	
n	Exponent of porosity in the permeability[1,2]	2 or 3

Ω_m, Ω_{ch}	Melt focusing zone for the matrix and channel melt	
P_{pz}	Piezometric pressure	
R^i	Exchange rate coefficient[6] for the chemical species	
ρ_f, ρ_s	Density of the melt and the solid	2700 and 3300 kg/m^3
$\Delta\rho$	Density difference of the melt and the solid	600 kg/m^3
S	Relative melt suction rate	<1.5
t_0	Time scale used for nondimensionalization	2 Myr or 1Myr
θ	Local orientation of the channel	
θ_s	Predicted dip of the shear-induced melt band	
Θ	Rotation tensor	
V_0	Half spreading rate	50 or 100 mm/yr
V_U, V_{Th}, V_U	Effective velocity of U, Th, and Ra in the matrix	
$\mathbf{V}_s^m, \mathbf{V}_f^m$	Velocity of the solid and melt in the matrix	
$\mathbf{V}_s^{ch}, \mathbf{V}_f^{ch}$	Velocity of the solid and melt in the channel	
ψ	Volume proportion of channel	<0.10
ζ_s	Bulk viscosity of the mantle	Same as η_s

[1]Wark and Watson (1998)

[2]Miller et al. (2014)

[3]Murase and McBirney (1973)

[4]Sigmundsson (1991)

[5]Batchelor (2000)

[6]Liang (2003)

Table 3-2 Partition coefficients[1]

	D ol/liq	D opx/liq	D cpx/liq	D sp/liq	D gt/liq
Ce	0.0000	0.0016	0.0876	0.0006	0.008
Nd	0.0001	0.0060	0.1878	0.0006	0.057
Sm	0.0003	0.0158	0.3083	0.0006	0.217
Eu	0.0005	0.0227	0.3638	0.0006	0.45
Gd	0.0010	0.0315	0.4169	0.0006	0.9
Dy	0.0029	0.0549	0.5034	0.0015	2
Er	0.0066	0.0808	0.5437	0.0030	3.5
Yb	0.0121	0.1036	0.5453	0.0045	7
U	-	0.0017	0.0103, P<1.5GPa linearly changes to 0.023, P>1.9GPa	-	0.038
Th	-	0.0008	0.012, P<1.5GPa linearly changes to 0.019, P>1.9GPa	-	0.017

[1] The bulk partition coefficient is calculated using mineral partition coefficients and mineral modes. The mineral mode of olv, opx, cpx, sp in DMM are from Workman and Hart (2005). According to the pMELTS model, 5% grt is in the source and is consumed within the first 0.4% melting. For the purpose of demonstration, the modal abundance of garnet decreases linearly with the degree of melting while the modal abundance of other minerals follows the reaction trend from Kinzler and Grove (1992). The partition coefficients of REE in opx and cpx are from Sun and Liang (2012), Yao et al. (2012) and Sun and Liang (2014). The partition coefficients of REE in olivine, garnet and spinel are from Kelemen et al. (2003). The partition coefficients of U and Th in cpx and opx are from Hauri et al. (1994) and Wood et al. (1999). The partition coefficients of U and Th in garnet are from Salters et al. (2002). The bulk partition coefficient for Ra is set to be 1×10^{-4}.